Eidgenössische Technische Hochschule Zürich
Swiss Federal Institute of Technology Zurich

Diss. ETH No. 27501

Precision Spectroscopy of Positronium Using a Pulsed Slow Positron Beam

A thesis submitted to attain the degree of
Doctor of Sciences
(Dr. sc. ETH Zurich)

presented by
Michael Wolfgang Heiss
MSc ETH, ETH Zurich

born on 13th June, 1986
citizen of Austria

accepted on the recommendation of
Prof. Dr. Paolo Crivelli, examiner
Prof. Dr. Klaus Stefan Kirch, co-examiner
Prof. Dr. Anna Sótér, co-examiner
Prof. Dr. Dylan Yost, co-examiner

2021

I. Abstract

Positronium is the lightest known atom and comprises a structureless point-like electron and its anti-particle, the positron. As such, it is purely leptonic and can be described to very high precision by bound-state QED without the inherent complications given by the finite size and quark substructure of protonic atoms. Furthermore, being a true onium atom, recoil effects are strongly enhanced and its quantum numbers sum to zero, making it an ideal candidate to test fundamental symmetries like CPT-invariance.

However, positronium is also a very challenging system for precision measurements due to its ephemeral nature. Being a bound state of anti-particles it tends to self-annihilate quickly and due to its lightness it exhibits much larger velocities than other atoms. Nevertheless, being a precision test-bench for QED with many unique features, it represents a particularly interesting system for spectroscopic measurements. This thesis presents the efforts towards precise determinations of the $1^3\mathrm{S}_1 \rightarrow 2^3\mathrm{S}_1$ transition and both the hyperfine and fine structure of positronium in the $n = 2$ state.

The pulsed slow positron beamline at ETH Zurich, being a key prerequisite for these measurements, was optimized and a new beam transport and bunching system was developed. It was found that the efficiencies were comparable to similar beamlines and several further possible improvements were identified.

This thesis includes a measurement of the $1^3\mathrm{S}_1 \rightarrow 2^3\mathrm{S}_1$ transition by Doppler-free two-photon laser spectroscopy of $1\,233\,607\,210.5\,\mathrm{MHz} \pm 49.6\,\mathrm{MHz}$, which paves the way towards a new precision determination of this interval. Improvements by roughly two orders of magnitude on this result are suggested and discussed.

The design of an experiment to measure the hyperfine transition in the first excited state is presented. A microwave system supporting more than 100 kW of circulating power was developed and tested. Extensive simulations of the excitation and detection show the expected sensitivity to be 9.9 ppm (statistical) and 2.8 ppm (systematic) and further envisioned improvements are presented. This measurement will constitute the first measurement of this transition and the first determination of a hyperfine interval of positronium in vacuum altogether.

It was found that the experimental setup directly supports a determination of the $2^3\mathrm{S}_1 \rightarrow 2^3\mathrm{P}_0$ interval. Minor changes allow also for the measurement of the $2^3\mathrm{S}_1 \rightarrow 2^3\mathrm{P}_1$ and $2^3\mathrm{S}_1 \rightarrow 2^3\mathrm{P}_2$ transitions. Simulations show the expected sensitivities to be approximately 7 ppm (statistical) and 0.5 ppm (systematic), which will allow to shed light on a 4.5σ discrepancy of the most precise fine structure measurement in positronium with theory calculations.

II. Zusammenfassung

Positronium ist das leichteste bekannte Atom und besteht aus dem strukturlosen punktförmigen Elektron und seinem Antiteilchen, dem Positron. Als solches ist es rein leptonisch und kann durch die Quantenelektrodynamik mit sehr hoher Präzision beschrieben werden, ohne die inhärenten Komplikationen, die durch die endliche Grösse und Quark-Substruktur protonischer Atome entstehen. Da es sich um ein echtes Onium-Atom handelt, sind die Rückstosseffekte stark verstärkt und seine Quantenzahlen summieren sich zu Null. Dies macht es zu einem idealen Kandidaten, um fundamentale Symmetrien wie die CPT-Invarianz zu testen.

Positronium ist jedoch aufgrund seiner kurzlebigen Natur auch ein sehr herausforderndes System für Präzisionsmessungen. Da es sich um einen gebundenen Zustand von Antiteilchen handelt, neigt es dazu, innerhalb kürzester Zeit zu annihilieren und weist aufgrund seiner geringen Masse viel höhere Geschwindigkeiten auf als andere Atome. Als Präzisions-Testumgebung für die Quantenelektrodynamik, mit vielen einzigartigen Merkmalen, stellt es dennoch ein besonders interessantes System für spektroskopische Messungen dar. In dieser Arbeit werden die Bemühungen um eine präzise Bestimmung des $1^3\mathrm{S}_1 \rightarrow 2^3\mathrm{S}_1$ Übergangs sowie der Hyperfein- und Feinstruktur von Positronium im Zustand $n = 2$ vorgestellt.

Der gepulste langsame Positronenstrahl an der ETH Zürich, der eine wesentliche Voraussetzung für diese Messungen ist, wurde optimiert und ein neues Strahltransport- und Kompressionssystem wurde entwickelt. Es hat sich gezeigt, dass die Wirkungsgrade mit jenen von ähnlichen Aufbauten vergleichbar waren, und es wurden mehrere weitere mögliche Verbesserungen identifiziert und präsentiert.

Diese Arbeit beinhaltet eine Messung des $1^3\mathrm{S}_1 \rightarrow 2^3\mathrm{S}_1$ Übergangs durch Doppler-freie Zwei-Photonen-Laserspektroskopie von $1\,233\,607\,210{,}5$ MHz $\pm$ $49{,}6$ MHz, die den Weg für eine neue Präzisionsbestimmung dieses Intervalls ebnet. Verbesserungen dieses Ergebnisses um ungefähr zwei Grössenordnungen werden vorgeschlagen und diskutiert.

Der Aufbau eines Experiments zur Messung des Hyperfeinübergangs im ersten angeregten Zustand wird vorgestellt, wofür ein Mikrowellensystem mit einer zirkulierenden Leistung von mehr als 100 kW entwickelt und getestet wurde. Umfangreiche Simulationen der Anregung und Detektion zeigen eine erwartete Sensitivität von $9{,}9$ ppm (statistisch) and $2{,}8$ ppm (systematisch) und weitere geplante Verbesserungen werden vorgestellt. Diese Messung würde die erste Messung dieses Übergangs und die erste Bestimmung eines Hyperfeinintervalls von Positronium im Vakuum überhaupt darstellen.

Es wurde festgestellt, dass der entwickelte Versuchsaufbau ebenso eine Bestimmung des $2^3\mathrm{S}_1 \rightarrow 2^3\mathrm{P}_0$ Intervalls unterstützt. Kleinere Änderungen ermöglichen ausserdem die Messung der Übergänge $2^3\mathrm{S}_1 \rightarrow 2^3\mathrm{P}_1$ und $2^3\mathrm{S}_1 \rightarrow 2^3\mathrm{P}_2$. Simulationen zeigen, dass die erwarteten Sensitivitäten bei ungefähr 7 ppm (statistisch) and $0{,}5$ ppm (systematisch) liegen, was es ermöglichen wird, eine $4{,}5\sigma$-Diskrepanz der momentan genauesten Feinstrukturmessung mit theoretischen Berechnungen zu überprüfen.

III. Acknowledgements

Whenever I near the conclusion of a momentous chapter of my life – which the pursuit of a PhD certainly is – I can't help but look back and reminisce. Increasingly, I find that the most important part is not the final destination, but the journey. And what is a journey without great people to walk with and guide you along the path?

My sincere gratitude goes to Prof. Paolo Crivelli, who guided me in my professional career like no one else, always willing to share his immense knowledge and to help find solutions to problems which might have seemed insurmountable at first. I would like to express my appreciation for the encouragement and introduction provided by Prof. Eberhard Widmann, without whom I might not have taken this particular direction. I would also like to thank Prof. André Rubbia for his supervision in the early phases and Prof. Klaus Kirch, Prof. Anna Sótér, and Prof. Dylan Yost for examining this thesis and thereby acting as gatekeepers for my destination.

I was truly fortunate to work with so many extremely talented people over the years. Among them, Dr. Dave Cooke and Dr. Pauline Comini, who introduced me to the intricacies of the pulsed positron beamline and the pulsed dye amplifier. I also had the great pleasure to work with Dr. Carlos Vigo Hernandez and Dr. Lars Gerchow and enjoy their many insights into positron beams, MCPs and much more. My gratitude also goes out to Dr. Artem Golovizin for sharing his expertise of all things laser-related and for being the best guide of Moscow one could wish for. I would also like to thank Dr. Balint Radics, Dr. Ben Ohayon and Dr. Zak Burkley for many enlightening discussions and help along the way.

A great pleasure and learning experience was the chance to supervise highly curious and talented Master students. Without a doubt many of them will go on to become great physicists. I would especially like to thank Lucas de Sousa Borges for his support in the late stages of the 1S-2S measurement and for taking up the torch of positronium spectroscopy at ETH.

What made life much more enjoyable, were the amazing colleagues at ETH: Mr. Dr. Emilio Depero, Gianluca Janka, Alexander Stauffer, Johannes Wüthrich, Paul Prantl, Ibâa El-Maïs, Philipp Blumer, Dr. Laura Molina Boleno, Henri Sieber, Irene Cortinovis, Mark Rajmaakers, Benjamin Banto Oberhauser and so many more with whom I had great conversations about physics, life, and Rick and Morty – not necessarily in that order.

My deepest gratitude goes to my family, to my aunt Karin for sparking my curiosity in physics and to my parents Renate and Wolfgang for always supporting me in times of need. Without them, going on this adventure would not have been possible. Sadly, my mother did not live to see me reach this milestone, but I know she would be very proud.

Finally, and most importantly, I want to thank my wife Carina for her unwavering love and support. Putting up with me and my quirks for more than a decade is surely a bigger achievement than writing this thesis.

Contents

1. Introduction

1.1. Positronium: the fleeting atom

1.1.1. The history of the positron and positronium

Paul Dirac postulated the famous Dirac equation in the quest to create a relativistic version of Quantum Mechanics in 1928 [1]. The importance of this work was immediately clear, since it finally allowed to successfully explain the origin of electron spin. Despite being a very compelling theory, it seemed to have one fatal flaw, namely the existence of negative energy solutions. This suggested the simultaneous existence of electrons with negative and positive charge and possibly even oscillations from one to the other.

It took Dirac three more years and multiple attempts to explain this peculiar feature by postulating that in fact the theory does not only describe electrons, but also another type of particle, which he called the anti-electron [2] – and hence, the idea of the positron was born. It did not even take a full year for Carl Anderson to discover [3] this anti-electron, or as he named it[1] – the positron – taking thousands of photographs using his Wilson cloud chamber (see figure 1).

The year following Andersons publication, Stjepan Mohorovičić postulated a bound state of electron and positron [5], which he initially called Electrum and suggested to look for it via astronomical spectroscopy. After this flurry of activity it would take more than a decade until Arthur Ruark proposed a spectroscopic measurement of this bound state [6] – which he called Positronium – using intense positron beams that have become available with the introduction of the betatron. He already noted the exceptional difficulty such a measurement posed due to the inherent properties of positronium, which we will discuss later in this section.

Finally, in 1951 Martin Deutsch experimentally showed the formation of long-lived positronium states in nitrogen gas [7] using a ^{22}Na source and PALS – Positron Annihilation Lifetime spectroscopy – a detection method he pioneered. This technique, which has been continuously developed and is still widely used, measures the time between a start signal relative to the formation of positronium and a signal compatible with either the annihilation of the positron or the decay of positronium. In the original experiment Deutsch took advantage of the fact that when ^{22}Na undergoes β^+ decay and emits a positron, the daughter isotope (^{22}Ne*) decays to its ground state via the emission of a 1275 keV photon with a lifetime of only 3.7 ps. A scintillator was placed close to the source to detect this nuclear de-excitation photon and another scintillator, placed in a lead cylinder to shield from the source, was used to monitor the decay volume. Deutsch showed that the relatively high energy positrons could ionize the gas atoms and pick up an electron and thereby forming positronium. Three quarters of those atoms were formed in long-lived states (due to the respective spin states, see next section), which produced a delayed signal in the scintillator when they decayed. To make sure this delayed signal was indeed from positronium and not some unexpected background, he

---

[1] To be precise, it should be noted that the name positron was actually coined by Watson Davis, the editor in charge of Andersons publication in Science [4].

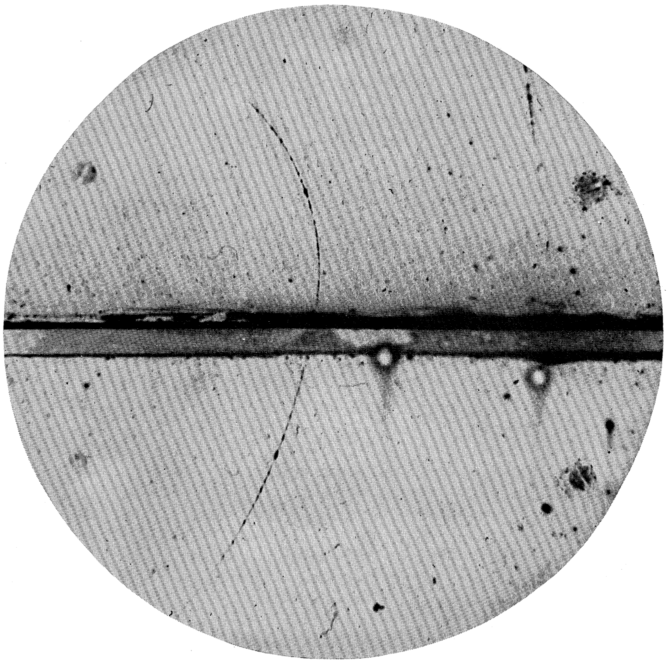

Figure 1: Discovery of the positron – the picture shows a photograph taken in Andersons cloud chamber of a 63 MeV positron, entering from the lower left, passing a 6 mm lead plate and emerging with approximately 23 MeV. From the direction and length of the curve one can see that this is indeed a positive particle, which is found to be significantly lighter than a proton. (*source:* [3])

added a small admixture of NO gas which was likely to interact with the spin states of positronium and thereby shortening their lifetime considerably.

1.1.2. Properties of positronium

Positronium (often abbreviated Ps) is a purely leptonic atom comprising an electron and a positron, which also makes it the lightest known atom, being around 1000 times lighter than hydrogen. While positronium is in many regards very similar to hydrogen and can be described using the same theoretical models, there are major differences (see also section 1.2). One of the most obvious is that positronium is very short-lived, since its constituents are antimatter counterparts of each other.

Electron and positron are the lightest charged fermions and – to our current understanding – point-like with no substructure. This means that the dynamics of the bound state of these particles including decay modes and the energy level structure is only governed by the electromagnetic interaction[2], which can be very precisely calculated

---

[2] Note that they also interact via the weak interaction, e.g. decays to photons violating C-parity and decays to neutrinos, but those are suppressed by at least 19 orders of magnitude [8]. Similarly, the strong interaction enters only in higher order corrections, which are also strongly suppressed.

within the framework of bound state QED. Furthermore, the system is free from finite size effects which plague protonic atoms (see next section).

The specific decay channels of positronium are determined by C-parity of the multi-particle spin state. Since both electron and positron are fermions, they can combine to an asymmetric singlet (S=0) state (called para-positronium - pPs)

$$|0,0\rangle = {}^1\!/\!\sqrt{2}\,(|\uparrow\rangle\,|\downarrow\rangle - |\downarrow\rangle\,|\uparrow\rangle) \tag{1}$$

and a symmetric triplet (S=1) state (called ortho-positronium - oPs):

$$|1,1\rangle = |\uparrow\rangle\,|\uparrow\rangle \tag{2}$$

$$|1,0\rangle = {}^1\!/\!\sqrt{2}\,(|\uparrow\rangle\,|\downarrow\rangle + |\downarrow\rangle\,|\uparrow\rangle) \tag{3}$$

$$|1,-1\rangle = |\downarrow\rangle\,|\downarrow\rangle \tag{4}$$

Assuming positronium in the ground state (n=1, L=0) we find C-parity for those states to be:

$$\eta_C(\mathrm{pPs}) = (-1)^{L+S}(\mathrm{pPs}) = (-1)^0 = +1 \tag{5}$$

$$\eta_C(\mathrm{oPs}) = (-1)^{L+S}(\mathrm{oPs}) = (-1)^1 = -1 \tag{6}$$

Given the intrinsic parity of a photon

$$\eta_C(\gamma) = -1 \tag{7}$$

we find that parity conservation dictates that pPs can only decay to an even number, while oPs can only decay to an odd number.

The decay into one photon is kinematically forbidden, since in the center of mass system the photon would have zero momentum by definition, but carry the mass of electron and positron. Furthermore, already the decay into 4 (pPs), respectively 5 (oPs) photons is highly suppressed to the order $\alpha^2 \approx 5 \times 10^{-5}$. Proper calculations taking into account the phase space factor find the relative branching ratio to be even lower with [9]:

$$\frac{\Gamma\left(pPs \to 4\gamma\right)}{\Gamma\left(pPs \to 2\gamma\right)} \approx \frac{\Gamma\left(oPs \to 5\gamma\right)}{\Gamma\left(oPs \to 3\gamma\right)} \approx 10^{-6} \tag{8}$$

To a good approximation we can therefore assume within the scope of this thesis that positronium decays exclusively via pPs → 2γ and oPs → 3γ respectively. The leading order QED graphs responsible for those decays can be found in figure 2.

The lifetime of pPs was first calculated by Wheeler [10] and Pirenne [11] at leading order to be:

$$\tau_{\mathrm{pPs}}^{\mathrm{LO}} = \frac{2\hbar}{m_e c^2 \alpha^5} = 124.5\,\mathrm{ps} \tag{9}$$

The most precise theoretical value to date including second loop order corrections is [12]

$$\tau_{\mathrm{pPs}}^{\mathrm{th}} = 125.1624327(63)\,\mathrm{ps} \tag{10}$$

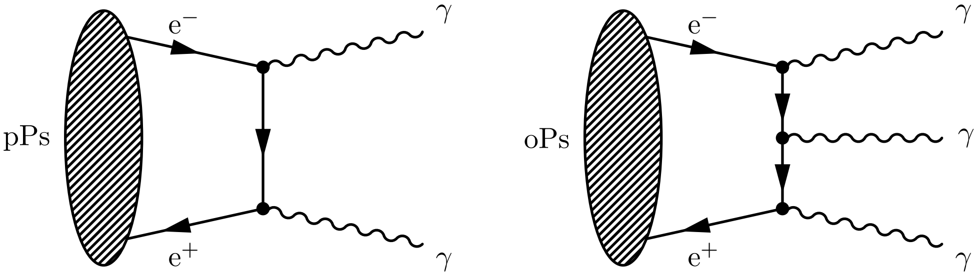

Figure 2: Leading order QED Feynman diagrams responsible for para-positronium (left) and ortho-positronium decays (right). The inherently non-perturbative bound state dynamics is hinted at by the shaded region in the initial state.

while the experimental value agrees well with [13]:

$$\tau_{\mathrm{pPs}}^{\mathrm{exp}} = 125.142(53)\,\mathrm{ps} \tag{11}$$

The first calculation of the oPs lifetime by Ore and Powell [14] at leading order yielded:

$$\tau_{\mathrm{oPs}}^{\mathrm{LO}} = \frac{9\pi\hbar}{2\left(\pi^2-9\right) m_e c^2 \alpha^6} = 138.7\,\mathrm{ns} \tag{12}$$

In this case the loop corrections are somewhat more significant. The most precise theoretical value is given by [15]:

$$\tau_{\mathrm{oPs}}^{\mathrm{th}} = 142.04588(44)\,\mathrm{ns} \tag{13}$$

The best experimental value is also in good agreement[3] with [18]:

$$\tau_{\mathrm{oPs}}^{\mathrm{exp}} = 142.043(28)\,\mathrm{ns} \tag{14}$$

1.2. Precision test bench for QED

Hydrogen has been the most prominent atomic system to test quantum theories to incredibly high precision – a few parts per *trillion* [19, 20] – for almost a century, but those tests are inherently limited by our understanding of the low energy behavior of Quantum chromodynamics which binds quarks in the proton. Therefore, positronium – as a purely leptonic system – is an excellent candidate to complement tests of bound state QED to high precision without these issues. This section shall discuss the energy level structure and history of spectroscopic studies of this exotic atom.

When discussing energy levels in this thesis we will use the common spectroscopic notation used for positronium

$$\mathrm{n}^{(2\mathrm{S}+1)}\mathrm{L}_\mathrm{J} \tag{15}$$

---

[3] This agreement is actually a rather recent development [16, 17]. For almost 4 decades significant differences between theoretical predictions and experimental values were found [12]. This was known as the ortho-positronium lifetime puzzle.

where n is the principal quantum number, S is the spin angular momentum, L the orbital angular momentum[4] and J = L+S the total angular momentum. For example, the states discussed in the last section are therefore written as:

$$\mathrm{pPs}\,(\mathrm{n}=1,\mathrm{L}=0)=\mathrm{Ps}\left(1^1\mathrm{S}_0\right) \tag{16}$$

$$\mathrm{oPs}\,(\mathrm{n}=1,\mathrm{L}=0)=\mathrm{Ps}\left(1^3\mathrm{S}_1\right) \tag{17}$$

1.2.1. The theory of the positronium atom

The gross energy structure of positronium can be easily understood in terms of the non-relativistic Schrödinger equation

$$H=-\frac{\hbar^2}{2\mu}\nabla^2+V(r) \tag{18}$$

for the reduced mass (where M is the mass of the nucleus and m the mass of the electron)

$$\mu=\frac{mM}{m+M} \tag{19}$$

and the electromagnetic Coulomb potential

$$V(r)=-\frac{Ze^2}{4\pi\epsilon_0 r}=-\hbar c\frac{Z\alpha}{r} \tag{20}$$

where Z is the total charge of the nucleus. The well known energy eigenstates are given by

$$E_{\mathrm{n}}=-\frac{Z^2\alpha^2}{2\mathrm{n}^2}\mu c^2 \tag{21}$$

where the nuclear charge $Z=1$ both for hydrogen and positronium. The correction of the reduced mass to the electron mass for hydrogen is very small with

$$\frac{m-\mu_H}{m}=\frac{m}{m+M}\approx\frac{m}{M}\approx 5\times 10^{-4}\quad , \tag{22}$$

while the same correction for positronium is maximal with

$$\frac{m-\mu_{Ps}}{m}=\frac{m}{m+M}=\frac{m}{2m}=\frac{1}{2} \tag{23}$$

due to the fact that electron and positron have the same mass[5]. The gross energy structure of positronium therefore scales the hydrogen spectrum by a factor ≈ 2. We find (using equation 21)

$$E\left(\mathrm{n}_i\rightarrow\mathrm{n}_f\right)=\frac{m_e\alpha^2c^2}{4}\left(\frac{1}{{\mathrm{n}_f}^2}-\frac{1}{{\mathrm{n}_i}^2}\right)\approx 6.8028\,\mathrm{eV}\left(\frac{1}{{\mathrm{n}_f}^2}-\frac{1}{{\mathrm{n}_i}^2}\right) \tag{24}$$

---

[4] For historic reasons this is given in letters, e.g. S for L = 0 (as in sharp) , P for L = 1 (as in principal), D for L = 2 (as in diffuse), etc.

[5] The *exact* same mass is a consequence of CPT invariance. However, CPT might ultimately be violated at some level (see next section).

for the transition frequencies in positronium within the picture of non-relativistic quantum mechanics.

All the known corrections to this result can be described within the theoretical framework of bound state QED. The energy levels for all states up to the order[6] $m\alpha^6$ have been calculated. We will present the most important corrections for calculations up to order $m\alpha^5$ following Ley and Werth [21]. The full expression for the energy levels reads:

$$E_{\mathrm{n,L,S,J}} = -\frac{m_e\alpha^2c^2}{4\mathrm{n}^2} + \tag{25a}$$

$$+\frac{m_e\alpha^4c^2}{2n^3}\left[\frac{11}{32\mathrm{n}} - \frac{1}{2\mathrm{L}+1} + \frac{7}{6}\delta_{1\mathrm{S}}\delta_{0\mathrm{L}} + \right. \tag{25b}$$

$$\left. + \frac{\delta_{1\mathrm{S}}\left(1-\delta_{0\mathrm{L}}\right)}{2\mathrm{L}\left(\mathrm{L}+1\right)\left(2\mathrm{L}+1\right)} \cdot \left\{ \begin{array}{lll} \dfrac{\mathrm{L}\left(3\mathrm{L}+4\right)}{2\mathrm{L}+3} & \text{for} & \mathrm{J}=\mathrm{L}+1 \\ -1 & \text{for} & \mathrm{J}=\mathrm{L} \\ -\dfrac{\left(\mathrm{L}+1\right)\left(3\mathrm{L}-1\right)}{2\mathrm{L}-1} & \text{for} & \mathrm{J}=\mathrm{L}-1 \end{array} \right] + \right. \tag{25c}$$

$$+\frac{m_e\alpha^5c^2}{2\pi n^3}\left[-\left(\frac{3}{2}\ln\alpha\right)\delta_{0\mathrm{L}} - \frac{4}{3}\ln k_0\left(\mathrm{n},\mathrm{L}\right) + \right. \tag{25d}$$

$$+\left\{\frac{203}{180} + \frac{7}{12\mathrm{n}} + \frac{7}{3}\ln 2 + \frac{7}{6}\left(\sum_{k=1}^{\mathrm{n}}\frac{1}{k} - \frac{1}{\mathrm{n}} - \ln\mathrm{n}\right)\right\}\delta_{0\mathrm{L}} - \tag{25e}$$

$$-\frac{7\left(1-\delta_{0\mathrm{L}}\right)}{12\mathrm{L}\left(\mathrm{L}+1\right)\left(2\mathrm{L}+1\right)} - \left(\frac{16}{9} + \ln 2\right)\delta_{1\mathrm{S}}\delta_{0\mathrm{L}} + \tag{25f}$$

$$\left. + \frac{\delta_{1\mathrm{S}}\left(1-\delta_{0\mathrm{L}}\right)}{4\mathrm{L}\left(\mathrm{L}+1\right)\left(2\mathrm{L}+1\right)} \cdot \left\{ \begin{array}{lll} \dfrac{\mathrm{L}\left(4\mathrm{L}+5\right)}{2\mathrm{L}+3} & \text{for} & \mathrm{J}=\mathrm{L}+1 \\ -1 & \text{for} & \mathrm{J}=\mathrm{L} \\ -\dfrac{\left(\mathrm{L}+1\right)\left(4\mathrm{L}-1\right)}{2\mathrm{L}-1} & \text{for} & \mathrm{J}=\mathrm{L}-1 \end{array} \right] \right. \tag{25g}$$

where δ is the Kronecker delta and the Bethe logarithm $\ln k_0\left(\mathrm{n},\mathrm{L}\right)$ is a term arising in non-relativistic Lamb shift corrections. For S states this term is roughly $\ln k_0\left(\mathrm{n},0\right) \approx e$, while for small $\mathrm{L} > 0$ the value is approximately $\ln k_0\left(\mathrm{n},\mathrm{L}\right) \approx -0.1\, e^{\text{-L}}$. Precise values can be found in the literature [22, 23].

It is interesting to note that while the gross energy structure has a $1/n^2$ dependence, corrections generally scale with $1/n^3$. This feature appears also in higher order ($m\alpha^6$ and $m\alpha^7$) terms [21]. Furthermore, positronium has the peculiar property that there is no dependence on a second mass term[7] or the charge radius of the nucleus, like in most

---

[6] Note that the results from non-relativistic QM are already of the order $m\alpha^2$ as one can easily read off equation 21.

[7] Assuming CPT invariance, which is an inherent property of (standard) QED.

other atomic systems.

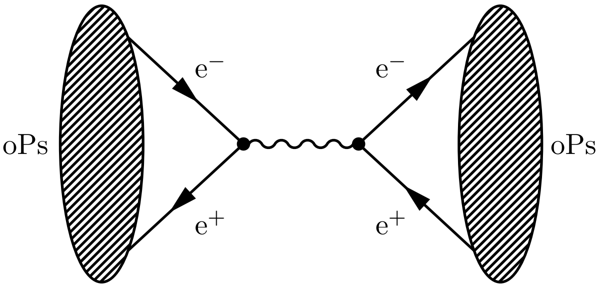

Figure 3: Leading order QED Feynman diagram responsible for the virtual annihilation correction to the positronium energy levels.

As expected, the leading order result (equation 25a) is the same as the non-relativistic QM result in equation 21. Corrections of the order $m\alpha^4$ in equations 25b and 25c arise due to several different sources. Most of them can be understood in analogy with the standard relativistic perturbative treatment of hydrogen. The terms arise due to relativistic corrections, the spatial uncertainty of the charge[8], and the coupling of the spins among themselves (hyperfine structure) and with the orbital angular momentum (fine structure) [24].

However, it should be noted that in contrast to hydrogen already at this order in α there is no remaining degeneracy[9] in the energy levels with respect to any of the quantum numbers n, L, S or J. Furthermore, since $M/m = 1$ there is no suppression in recoil and nuclear effects, which leads to the peculiar effect that the hyperfine structure is on the same size scale as the fine structure. Another correction that arises in positronium, contrary to protonic atoms, is a contribution due to virtual annihilation (see figure 3) [11]. Note that this only contributes a non-zero value when there is sufficient overlap between the electron and positron wave functions, i.e. in S-states, and is only allowed for states where $\eta_C = -1$ (see section 1.1.2). Therefore, this correction only affects oPs with arbitrary n and L = 0.

The $m\alpha^5$ order terms in equations 25d-25g are contributions arising in first loop order corrections within the bound state QED framework [25], similar to the lamb shift in hydrogen. In addition to the graphs commonly found in protonic atoms (vertex correction, vacuum polarization and two photon exchange box diagrams) there is another class related to virtual annihilation processes in positronium. They can be grouped in vacuum polarization (see figure 4), vertex correction (see figure 5), and two-photon virtual annihilation (see figure 6) diagrams. As discussed above for the one-photon virtual annihilation, each diagram must respect C-parity and therefore the one-photon virtual annihilation including vertex correction or vacuum polarization only contributes to oPs

---

[8] This leads to an effective charge distribution on the order of the Compton wavelength of the electron/positron, even if they can otherwise be seen as point charges.

[9] There is a peculiar degeneracy for n^3P_2 and n^3D_2 for $n > 2$ [21], which seems to be accidental and disappears at one order higher in α.

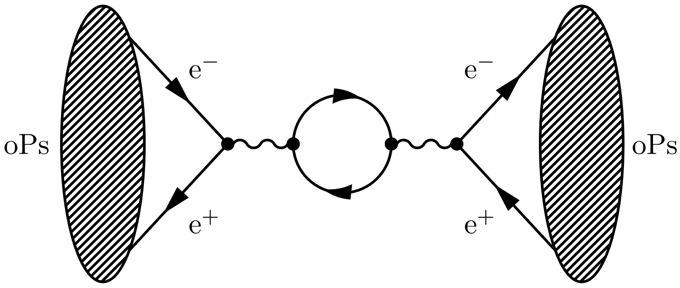

Figure 4: QED Feynman diagram responsible for the virtual annihilation channel including vacuum polarization to the positronium energy levels.

states and two-photon virtual annihilation only contributes to pPs states. Furthermore, both contributions need overlap of the wave functions and are therefore only non-zero for S states.

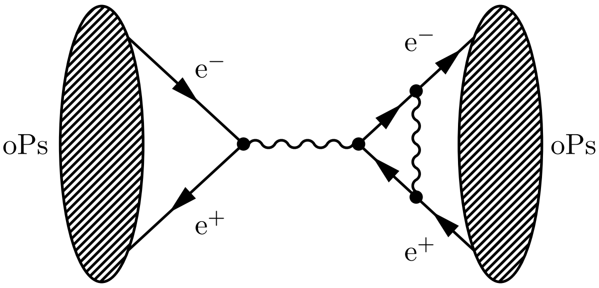

Figure 5: QED Feynman diagram responsible for the virtual annihilation channel including vertex correction to the positronium energy levels. The corresponding diagram with the vertex modification on the initial state also contributes to this correction.

Corrections at order $m\alpha^6$ can be found in the literature (e.g. Ley and Werth [21] tabulate these corrections including the leading-log $m\alpha^7$ for all S and P states up to n = 3). The order of magnitude of the theoretical uncertainty on these calculations are often estimated by the leading-log contribution of the calculations in $m\alpha^7$, which is given by

$$h\Delta E_n = \mathcal{O}\left(\frac{m\alpha^7 hc^2 \ln^2 \alpha}{2\pi n^3}\right) \approx \frac{1}{2\mathrm{n}^3}\,\mathrm{MHz} \quad . \tag{26}$$

However, there is a great ongoing theoretical effort to calculate the remaining terms in $m\alpha^7$ [26–36], which will be crucial if the experimental accuracy in optical spectroscopy can be pushed below the ppb level (see chapter 3) and the sensitivity of fine structure measurements reach a few kHz (see chapter 4). Since the hyperfine structure is particularly sensitive on higher order corrections, a ppm level measurement of the excited state hyperfine structure further motivates continuing theoretical developments.

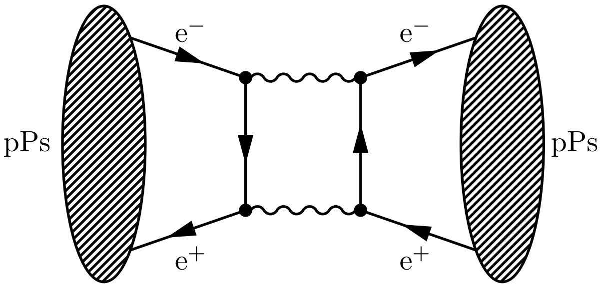

Figure 6: QED Feynman diagram responsible for the two-photon virtual annihilation correction to the positronium energy levels. The diagram with crossed photon lines also contributes to this correction.

1.2.2. The excited state lifetime

The lifetime of excited states with $n > 1$ is limited both by annihilation and radiative decay, such that

$$\tau_{\mathrm{n}^{(2S+1)}\mathrm{L}_\mathrm{J}} = \left[\Gamma^a_{\mathrm{n}^{(2S+1)}\mathrm{L}_\mathrm{J}} + \Gamma^r_{\mathrm{n}^{(2S+1)}\mathrm{L}_\mathrm{J}}\right]^{-1} \tag{27}$$

where Γ^a is the decay rate due to annihilation and Γ^r is the radiative decay rate. The annihilation cross-section crucially depends on the overlap of the wave-functions of the positron and the electron. Therefore, the lifetime of S states (L = 0) scales with n^3 [14]. For the same reason annihilations are highly suppressed for states with L > 0. The shortest annihilation lifetime of such a state [37] is

$$\tau^a_{2^3\mathrm{P}_2} = 99.57 \times 10^{-6}\,\mathrm{s} \tag{28}$$

which is still two orders of magnitude higher than

$$\tau^a_{2^3\mathrm{S}_1} = 2^3 \cdot 142.05 \times 10^{-9}\,\mathrm{s} = 1.136 \times 10^{-6}\,\mathrm{s} \tag{29}$$

for the equivalent S state (see equation 13). Annihilation lifetimes of P states scale with $\frac{n^5}{n^2-1}$ [37], which for large n becomes approximately n^3, analogously to the S states.

The radiative decay rate is given by the sum of the Einstein coefficients of spontaneous decay to all lower lying states [38], such that

$$\Gamma^r_{\mathrm{n}^{(2S+1)}\mathrm{L}_\mathrm{J}} = \sum A_{\mathrm{n'L'}\to\mathrm{nL}} = \sum \frac{16\pi\alpha\left(E_{\mathrm{n'L'}\to\mathrm{nL}}\right)^3}{\hbar^3 c^2} \left|\langle\mathrm{n'L'}|r|\mathrm{nL}\rangle\right|^2 \tag{30}$$

where $E_{\mathrm{n'L'}\to\mathrm{nL}}$ is the transition energy (see equations 24-25) and $\langle\mathrm{n'L'}|r|\mathrm{nL}\rangle$ the transition matrix element.

Figure 7 shows the lifetime (see equation 27) for S (L = 0), P (L = 1) and D (L = 2) states. For S states with n > 1, the lifetime of pPs is dominated by annihilation due to it decaying predominantly to two photons (see section 1.1.2), while oPs is mainly governed by radiative decay. However, an important exception is oPs in the 2S state, which is radiatively meta-stable. In fact, due to the small fine-structure splitting, the decay rate

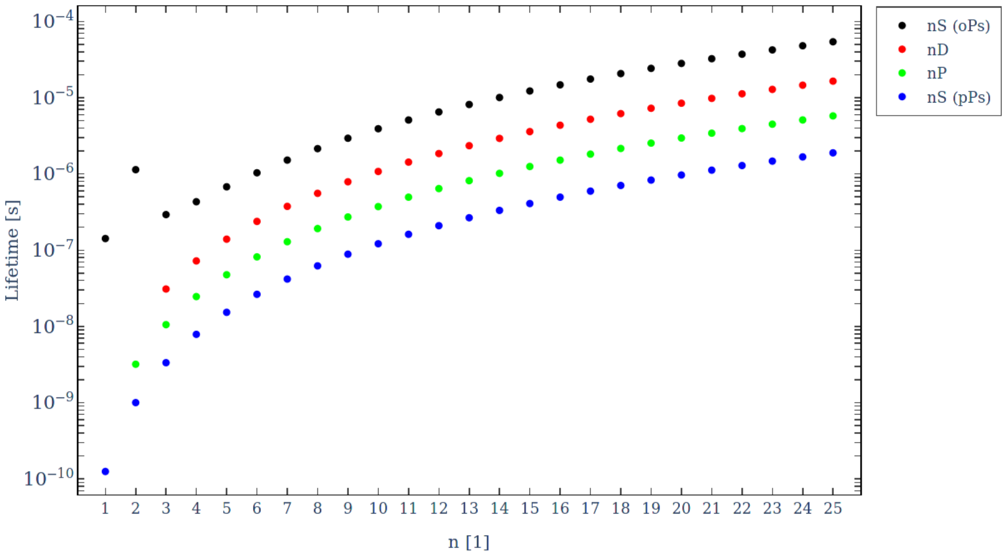

Figure 7: Lifetime for positronium states with n $<$ 26 including annihilation (for n $<$ 3) and radiative decay. Numerical values for radiative lifetimes were taken from [39] and scaled by a factor 2 to account for the reduced mass.

to 2P is minuscule and the main contribution is the electric dipole transition directly to the 1S, by the simultaneous emission of two photons [40]. For P and D states the total spin does not play a significant role, since the radiative decay rates are many orders of magnitude larger than the respective annihilation decay rates.

1.2.3. The experimental history of positronium spectroscopy

From the very beginning of experimental efforts related to positronium, spectroscopic measurements were front and center. Just half a year after Deutsch published the first evidence for positronium formation in gases [7], he completed the first measurement of its hyperfine[10] structure [41]. The technique he developed served as a basis for virtually all subsequent hyperfine measurements in positronium.

Over the following decades the ground state hyperfine interval was measured with increasing precision [42–49], culminating in a 3.6 ppm measurement by Ritter et al. [50]. However, when theory calculations caught up in precision, it became clear that there was a discrepancy of almost 4σ with those calculations. This prompted further experimental activity, including one of the measurements presented in this thesis (see chapter 4 for the recent history and current efforts).

The first experiment involving positronium in the excited state n = 2 [51] led to the measurement of the fine structure of positronium [52]. Subsequent measurements determined the different splittings [53–56] to varying accuracy, the most precise being the

---

[10] Note that there is historical ambiguity about the convention of naming the respective corrections in positronium fine or hyperfine structure. Over the years different authors used both those terms to describe the shift due to spin-spin coupling in positronium.

$2^3S_1 \rightarrow 2^3P_1$ (170 ppm) and the $2^3S_1 \rightarrow 2^3P_2$ (225 ppm) transitions. The availability of slow positron beams and efficient laser excitation to the excited state allows for significant improvements on these measurements [57]. Most recently, a new (33 ppm) measurement of the $2^3S_1 \rightarrow 2^3P_0$ interval showed a 4.5σ discrepancy with the corresponding theoretical calculation [58]. This clearly shows the importance of additional, more precise measurements to be conducted. One such improvement is presented in chapter 4.

Finally, with the advent of high power, narrow-band lasers at the required wavelengths, optical spectroscopy of positronium was realized by Chu and Mills measuring the optical $1^3S_1 \rightarrow 2^3S_1$ transition in 1982 [59]. This was continually improved upon, to be the benchmark QED test in positronium, reaching 12 ppb using pulsed lasers [60] and a final precision of 3.2 ppb [61–63] using CW lasers. After almost two decades of absence in positronium laser experiments, the last ten years saw a resurgence of experiments using lasers for a number of precise measurements in positronium (for an excellent overview see [57]). However, the 1993 value for the $1^3S_1 \rightarrow 2^3S_1$ transition is still the most precise to date and significant improvements in our understanding of bound state QED (see preceding section) call for a new, more precise measurement of this transition. One such measurement is presented in chapter 3.

1.3. A window to the world beyond the Standard Model

The Standard Model of particle physics, which incorporates QED (and therefore also bound state QED), is an incredibly successful theoretical framework. It has led to many great insights into the makeup of our universe, culminating in the recent experimental discovery of the Higgs boson [64, 65]. Notwithstanding the success, it is clearly not the most fundamental description of nature, seeing as it neglects to describe one of the four known forces in nature – gravity. Furthermore, it does not explain phenomena such as dark matter, dark energy or the extreme baryon asymmetry in our universe.

A fundamental property of the Standard Model is that it is invariant under the combined transformations of C (charge), P (parity) and T (time). This is a consequence of the CPT-theorem [76, 77], which is valid in any quantum field theory respecting unitarity, Lorentz invariance and locality [78]. However, CPT invariance can be naturally broken in theories incorporating quantum gravity, e.g. string theory [79, 80].

Even if we do not know the "full" theory yet and scales at which it would become apparent are not accessible, effective field theories are a powerful tool to study the dynamics of a system at lower energy scales. In fact, in this context a quantum field theory might well be non-renormalizable but still have predictive power and operators of mass dimension $d > 4$ can be seen as an effective result of the unknown large energy scale dynamics [81].

One such effective field theory is the Standard Model Extension (SME), which as the name suggests, is built as an extension to the Standard Model incorporating General Relativity and all possible terms breaking Lorentz invariance [82]. Since a violation of CPT implies Lorentz violation [83], the SME also includes terms breaking CPT invariance. If the model is restricted to operators of mass dimension $d \leq 4$, the theory

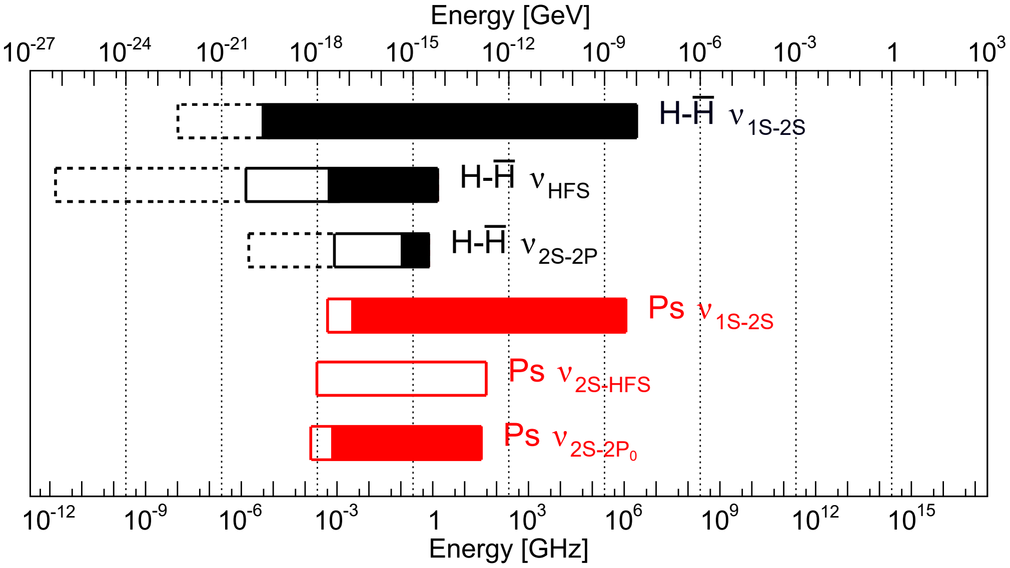

Figure 8: Sensitivity for CPT violation in hydrogen and positronium: The left edge of the bars represents the absolute accuracy of the respective measurements, while the right edge represents the absolute value. The length of the bar gives the relative precision. Solid bars are given for the most precise past measurements [55, 62, 66–68] in the exotic atom system – anti-hydrogen and positronium respectively – while non-filled bars represent expected accuracies [69–72] (see also chapter 3 and 4). Dotted bars show the most precise value in hydrogen [19, 73, 74]. (*adapted from:* [75])

is renormalizable and referred to as the minimal Standard Model Extension.

The coefficients for Lorentz violation in the SME can not be found from first principles, but must be necessarily measured. Constraints for these coefficients have been extracted from a multitude of different experimental disciplines, including Astrophysics, particle colliders, optical experiments, and atomic spectroscopy [84]. Comparisons of atomic systems consisting of antimatter or a combination of matter and antimatter are excellent candidates to test CPT, due to the achievable precision in such experiments. Non-zero coefficients of Lorentz violating operators in the Standard Model extension lead to observable effects, such as shifts from bound state QED values and varying shifts depending on sidereal time [85].

In general, one is interested in measurements with the highest absolute precision and not the relative one, since all non-relativistic coefficients carry mass dimensions [85]. The most stringent limits are extracted from the hydrogen sector, but measurements in positronium are competitive with anti-hydrogen (see figure 8). Furthermore, positronium depends on a different combination of Lorentz violating coefficients than hydrogen, allowing one to use the measurements to disentangle CPT-even and CPT-odd effects [85]. In this sense positronium studies complement those in hydrogen and anti-hydrogen respectively.

2. Pulsed slow positron beamline

2.1. Overview

The pulsed slow positron beamline at ETH Zurich (see figures 9 and 10) is designed to supply up to 10^5 positrons per second in nanosecond scale bunches at typically 1 Hz to 10 Hz repetition rate. The positron beam can be focused down to approximately 1 mm and guided onto a target to form positronium (details in section 3).

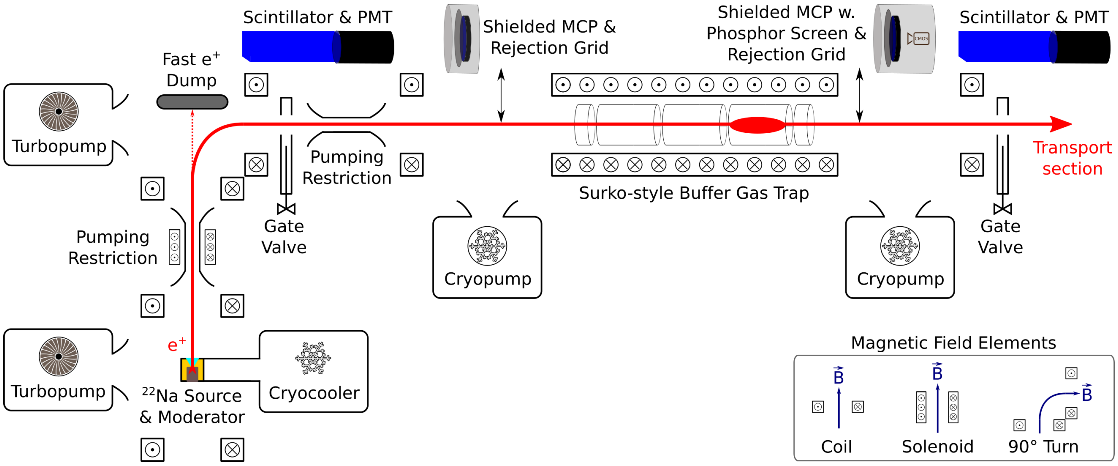

Figure 9: Schematic overview of the pulsed slow positron beamline at ETH Zurich. The drawing is not to scale and orientations might differ. For a detailed description of this part see section 2.1 and for an annotated picture of the physical setup, see figure 10. For further information about the pulsed beam handling up to the target implantation, refer to section 2.4 and figure 31.

Positrons are created in the β^+ decay of the radioactive isotope ^{22}Na and moderated using a solid rare gas moderator to approximately 40 eV. They are then guided through a velocity selector to remove unmoderated positrons from the beam, and further transported to the buffer gas trap. Section 2.2 discusses this part of the beam in detail.

There they lose energy by inelastic collisions with N_2 gas atoms to be trapped in an electric potential with magnetic radial confinement. In the last stage of the trap the positron plasma is compressed by a rotating electric field and cooled by collisions with CF_4 gas. A thorough description of the buffer gas trap can be found in section 2.3.

When the trap gate potential is opened, the cloud of positrons leaves the trap with an energy on the order of 10 eV and is then magnetically guided to a drift tube, which is pulsed to a potential of around 200 V to increase the beam energy. The positrons are then transported through a beam extension of approximately 4 m, connecting the buffer gas trap and the spectroscopy chamber in a dedicated laser room. Finally, a time-varying potential on a second long cylindrical electrode compresses the time spread to a few nanoseconds, before it is pulsed to high voltage. This accelerates the bunch to the required implantation energy, which can be varied from approximately 1 keV to 6 keV, depending on the experimental requirements. After leaving the electrode, the beam is extracted to a field-free region and focused spatially by an electrostatic einzel-lens. A more in-depth description of this stage can be found in section 2.4.

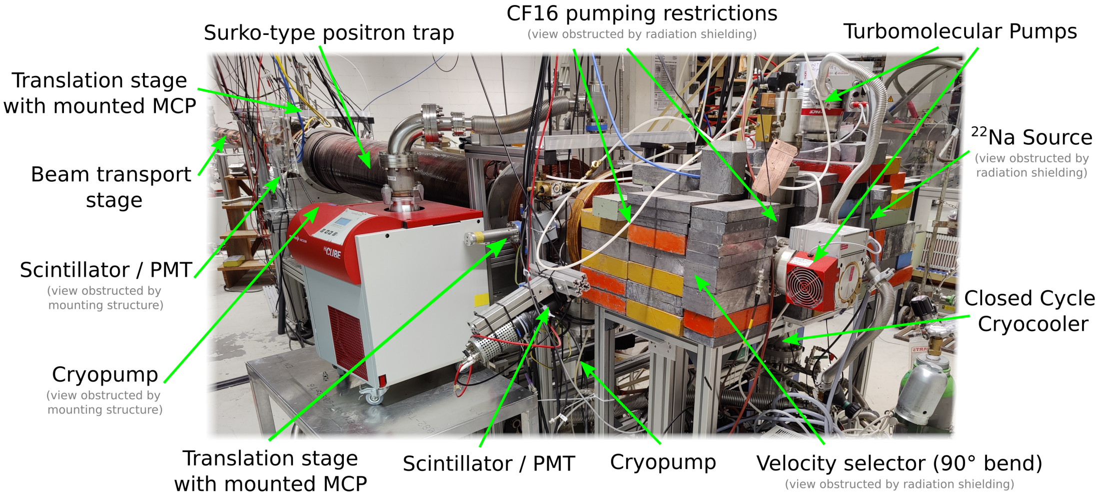

Figure 10: Picture of the pulsed slow positron beamline at ETH Zurich seen from the source side. The reimplantation electrode and source chamber are located in a separate room, which is connected by a transport section. The source chamber itself cannot be seen due to the radiation shielding that is required when the source is in place.

2.2. Positron source and moderation

Positrons are usually created using radioactive isotopes undergoing β^+ decay or by pair-production using accelerators. While accelerator [86, 87] and nuclear reactor [88, 89] based systems offer high constant brightness sources of positrons, they are inherently limited to large facilities, difficult to operate and can be prohibitively expensive. Therefore, a large number of experimental efforts involving slow positron beams are employing a closed radioactive isotope source, which is easy to operate and mostly maintenance free. However, the drawback is that the activity is usually limited to around 2 GBq for radiation safety reasons and that the isotope decays according to its half-life (e.g. 951 days for ^{22}Na [90]) and needs to be replaced at regular intervals according to individual rate needs.

The source employed on the pulsed slow positron beamline at ETH Zurich is a commercial 463 MBq (January 2016) ^{22}Na capsule produced by iThemba LABS using a magnesium target irradiated by a 66 MeV proton beam and subsequent chemical extraction [91]. The titanium capsule (see figure 11) is closed and sealed after production. Positrons can escape through a 5 μm thick titanium foil covering the ^{22}Na salt deposition on a tantalum reflector.

Figure 11: Picture (left) and drawing of ^{22}Na source capsule (*from:* [91])

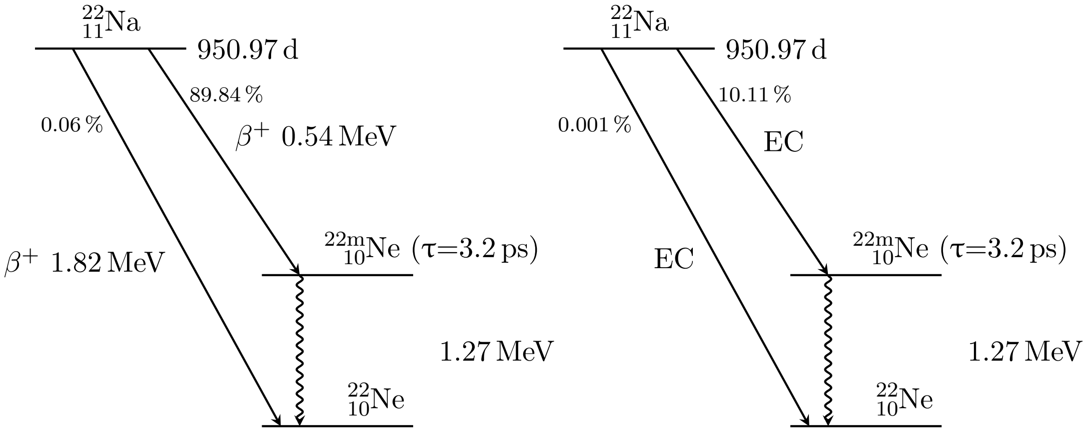

Figure 12: β^+ (left) and electron capture (right) decay channels of ^{22}Na including branching ratios and positron endpoint energies [92]

There are four relevant decay channels (see figure 12) for ^{22}Na. Positrons are emitted in approximately 90 % of all decays with endpoint energies of 546 keV (89.84 %) and 1821 keV (0.06 %), respectively [92]. The remaining decays proceed via electron capture and therefore do not contribute to the positron flux, which needs to be taken into account by appropriately scaling the activity, when calculating fluxes or efficiencies. Therefore, the scaled positron flux of the source is expected to be

$$\Phi_{e^+}(t) = 0.9 \cdot A_0 \cdot e^{-t\cdot\frac{\ln 2}{\tau}} \approx 416 \times 10^6 \cdot e^{-\frac{t}{1371.3}}\ {}^{1}\!/\!{}_{\mathrm{s}} \tag{31}$$

where t is the age of the source in days. At the time of this writing (June 2020) the positron flux of the source is therefore taken to be approximately $126 \times 10^6\ {}^{1}\!/\!{}_{\mathrm{s}}$. Note that this does not take losses on the reflector, window or bulk material of the source into account. This is usually included in the value of the moderator efficiency ε (see end of this section).

Since β-decay is a three body process, the positron energy is distributed over a wide range. However, trapping requires a quite narrow energy spread on the order of a few eV (see section 2.3) and using positrons directly emitted from the source would be extremely inefficient. Therefore, a number of techniques to moderate beams of positrons have been developed, which reduce the mean positron energy drastically (see figure 14). However, the drawback with all these methods is that they are quite inefficient due to the high probability of annihilation of positrons on matter. The ideal moderator for a given application depends on the requirements on the achievable efficiency and energy spread [93].

The most common choices in transmission geometry are metal foil/mesh (most commonly Ni or W) or solid rare gas moderators (most commonly Kr, Ar or Ne). With appropriate preparation and annealing procedures, tungsten foils or meshes can reach efficiencies of $\varepsilon \approx 0.1\,\%$ and an energy spread on the order of a few hundred meV [94, 95]. Solid neon moderators [96] are able to provide efficiencies which are an order of magnitude higher at the cost of a slightly larger energy spread of approximately 2 eV and the additional requirement for a cryogenic system, capable of achieving temperatures below approximately 8 K. The slightly larger energy spread results in a loss of achievable trapping efficiencies (see section 2.3) of around a factor 2 [97], but this is more than offset by the increase in moderator efficiency. Contrary to metal moderators, solid rare gas moderators tend to degrade over time and need to be regularly regrown (see below in this section).

Positrons implanted in metals rapidly thermalize to approximately 40 meV (room temperature) by inelastic collisions on a picosecond timescale and can be reemitted from the surface after diffusion, if the metal has a negative positron workfunction [93]. In solid rare gases however, positrons will lose energy efficiently only down to a certain threshold energy below which the only loss mechanism proceeds via very inefficient phonon emission [96]. The diffusion length and the moderation efficiency is therefore higher in these materials. Due to the fact that most of these positrons are not completely thermalized, the energy spread is correspondingly higher.

The pulsed slow positron beam at ETH Zurich employs a cryogenic solid rare gas moderator using neon or alternatively argon[11]. An overview of the moderator assembly can be found in figure 13. The source is mounted on the second stage of an ARS DE-204 closed cycle cryocooler capable of reaching 4 K with a cooling power of 0.2 W at 4.2 K via a sapphire disc. This allows for good thermal contact, while providing electrical isolation for applying a bias voltage to the source. The source is placed in such a way that the window is flush with a conical aperture where a film of solid rare gas is frozen onto. This geometry allows for strongly increased moderation efficiencies [98].

An overview of the main elements of the slow pulsed positron beam can be found in figure 10. A CF160 turbopump (Pfeiffer HiPace 700M - approximately 700 l/s pumping speed) is mounted directly on top of the source chamber. A second chamber, connected by a CF16 pumping restriction (ID 16 mm), is pumped separately by a CF100 turbopump (Pfeiffer HiPace 300M - approximately 250 l/s pumping speed). This chamber is

---

[11] Argon can be used to extend the service lifetime of the coldhead, since it allows for temperatures significantly higher than neon, at the cost of around a factor 4 to 5 of moderation efficiency.

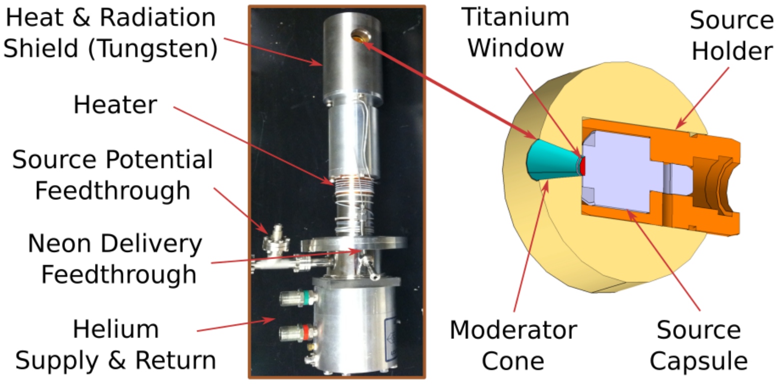

Figure 13: Picture of coldhead assembly with mounted heat shield, source holder and mount (left) and CAD drawing of cross-section of source holder in mount with with moderator cone (right). Note that the wire heater shown here was exchanged for a kapton foil heater in the current configuration.

connected to the trapping region by another CF16 restriction and a gate valve. This setup allows for continuous operation of all pumps, even while evaporating and growing the moderator. Furthermore, the gate valve to the trapping chamber can be left open during all phases, with only minor impact on operating pressures. The final pressure[12] reached during operation is below 5×10^{-9} mbar.

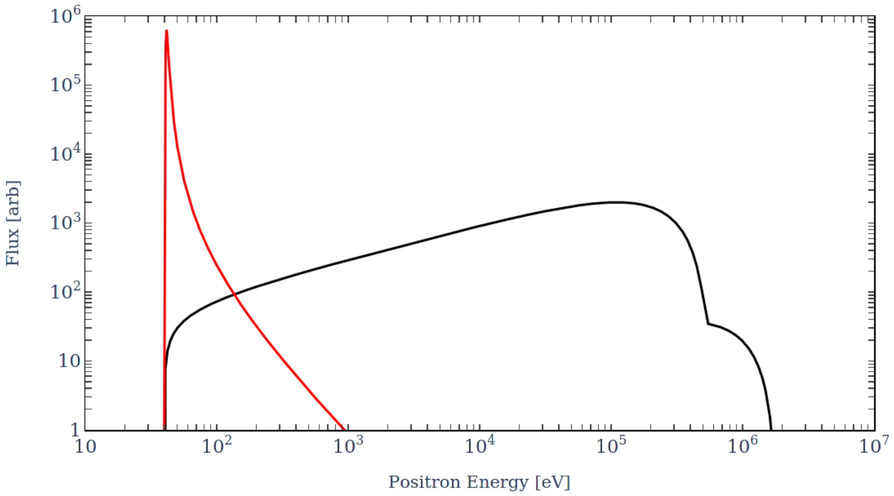

Figure 14: Calculated energy distribution of unmoderated (black) and solid neon moderated (red, assuming a Landau distribution) positrons in ^{22}Na β^+ decay for 40 V source voltage and 0.5 % moderation efficiency

To monitor the parameters and performance several detectors are placed along the

---

[12] The employed pressure sensor (Pfeiffer PKR 261) shows a minimum pressure of 5×10^{-9} mbar, so the achievable end pressure is likely significantly lower.

beamline (see figure 9). Both before the trap inlet and after the trap outlet a large solid angle plastic scintillator, coupled to a photo-multiplier tube (PMT), is placed close to the respective gate valve, which can be closed to serve as an annihilation plate. Additionally, two fully shielded custom design multi channel plate (MCP) detectors can be inserted into the beam path by means of linear actuators. Both MCP mounts incorporate a grid electrode that can be used to bias off moderated positrons of arbitrary energy. The detector on the trap outlet side can be used both in CW and pulsed mode and is also equipped with a phosphor screen to allow for visual inspection and beam size measurements.

To determine the total rate of positrons, or equivalently the moderation efficiency, the scintillator at the trap inlet was calibrated for rate and solid angle using a radioactive source. To measure the losses due to magnetic mirroring on the trap solenoid, another scintillator was placed at the trap outlet and likewise calibrated. A lead tungstate ($PbWO_4$) scintillator[13] was additionally placed there to determine the trapping efficiency in pulsed mode (see section 2.3).

For the calibration of the scintillators a closed ^{22}Na source with an activity of

$$A_S(t = 4505\,\mathrm{d}) = A_0 \cdot e^{-t\cdot\frac{\ln 2}{\tau}} \approx 413\,\mathrm{kBq} \cdot e^{-\frac{4505}{1371.3}} = 15.46\,\mathrm{kBq} \tag{32}$$

was used. The fractional coverage is given by

$$\omega = \frac{4\pi}{\Omega} \tag{33}$$

where Ω is the subtended solid angle of the scintillator. While the detection efficiency often strongly depends on the incident energy of the particle, for the used group of plastic scintillators and range of energies the response is quite flat [99–101] and one can assume the same detection efficiency ε_s for all photons. Therefore, the discussion of the calibration factor can be limited to the probability to pick up at least one photon from either a beam positron annihilation or one ^{22}Na decay of the calibration source. The measured rate from beam positrons is given by

$$R_{e^+} = \varepsilon_s N_{e^+} \cdot [1 - (1 - 2 \cdot \omega)] = 2\omega\varepsilon_s N_{e^+} \tag{34}$$

where N_{e^+} is the rate of positrons on the annihilation point. On the other hand, one needs to correct for the fact that in addition to the 511 keV photons from positron annihilation, the calibration source additionally emits a 1275 keV neon de-excitation gamma. Additionally, approximately 10 % of the ^{22}Na decays of the calibration source proceed via electron capture without the emission of 511 keV gammas (see figure 12). The rate for the calibration source is therefore given by

$$R_S = \varepsilon_s A_S \left\{1 - [0.1(1-\omega) + 0.9(1-\omega)(1-2\omega)]\right\} = 2\omega\varepsilon_s A_S\,(1.4 - 0.9\omega) \tag{35}$$

---

[13] Multiple lead tungstate scintillators were graciously supplied by Dr. Nessi-Tedaldi of the ETH CMS group.

and for the special case of the calibration source directly placed on top of the scintillator ($\omega \approx 0.5$):[14]

$$R_0 = R_S(d = 0) = \varepsilon_s A_S \cdot 0.95 \tag{36}$$

with d being the distance between source and scintillator.

Therefore three count rate measurements are needed to calculate the calibration factor, namely one with the calibration source placed directly on top of the scintillator centred on the active area (R_0), one with the source placed at the distance of the annihilation point (R_S), and one measurement without source and moderator grown (R_B). The fractional coverage can be calculated from the ratio

$$\frac{R_S}{R_0} = \frac{2.8\omega - 1.8\omega^2}{0.95} \quad \Rightarrow \quad \omega = \frac{2.8 - \sqrt{7.84 - 6.84\frac{R_S}{R_0}}}{3.6} \tag{37}$$

and the detection efficiency

$$\varepsilon_s = \frac{R_0}{0.95 A_S} \tag{38}$$

then gives the calibration factor

$$CF = \frac{N_{e^+}}{R_{e^+}} = \frac{1}{2\omega\varepsilon_s} = \frac{0.95 A_S}{2\omega R_0} \tag{39}$$

which has to be multiplied with the count rate to arrive at the total positron rate annihilating close to the scintillator position. Uncertainties in the exact position of the annihilation point result in errors on the order of 15 % for the calibration factor. This is purely a scale error and can be neglected for comparing various growth parameters, but has to be included for absolute values, e.g. the moderation efficiency.

The calibration factors for the scintillators were found to be

$$CF_{\text{inlet}} = 67 \pm 10 \tag{40}$$

and

$$CF_{\text{outlet}} = 23.0 \pm 3.4 \tag{41}$$

for the scintillators placed before the trap inlet and after the trap outlet respectively.

A typical procedure to prepare the solid neon moderator is shown in figure 15 and consists of four distinct phases. In the first phase (evaporation) the second stage is heated up via a 50 Ω kapton foil heater, mounted to the second stage of the closed cycle cryostat, to a peak temperature of approximately 40 K.[15] This leads to the evaporation and pumping out of the old neon moderator. Additionally, the neon line is flushed to ensure that there are no impurities which would impact the quality of the fresh moderator. The flow rate is set such that the chamber pressure does not exceed 10^{-3} mbar to avoid

---

[14] This is a good approximation due to the small size of the source relative to the large surface area of the scintillator.

[15] Note that at this temperature not all gas species completely evaporate. To avoid degrading moderator performance due to buildup of other gas species, the second stage is heated to approximately 80 K at regular intervals, i.e. after 20 - 30 regrowth cycles.

excessive gas loads on the turbopump. After two minutes heating and flushing is stopped to allow the second stage to cool down and the chamber to be pumped out to a base level of approximately 5×10^{-9} mbar. Once this pressure level is reached, the kapton heater is used to stabilize the second stage temperature to approximately 9.7 K (see below).

In the second phase (Growth) neon is admitted to the chamber via a small nozzle adjacent to the moderator cone. The number of slow positrons increases significantly before plateauing and subsequently slightly decreasing. The flow rate and duration is chosen such that the final count rate is maximized (see below). Once the appropriate amount of neon has been admitted to the chamber, the flow rate is set to zero, leading to an immediate increase in count rate due to the smaller chance of positrons annihilating on the gas. For the next phase (Annealing) the temperature is held constant to allow for slow annealing of the moderator, while excess neon is pumped out of the chamber. After up to 20 minutes of annealing, the temperature PID control is disabled and the second stage is allowed to cool down to around 6 K, while the chamber pressure settles to below 10^{-8} mbar. The complete procedure can be conducted during operation of the rest of the system without closing any gate valves. However, to avoid an increase of pressure in the trapping region and buffer gas impurities on the moderator, usually the gate valve separating the moderator and trapping region is closed for the evaporation, growth and annealing phase.

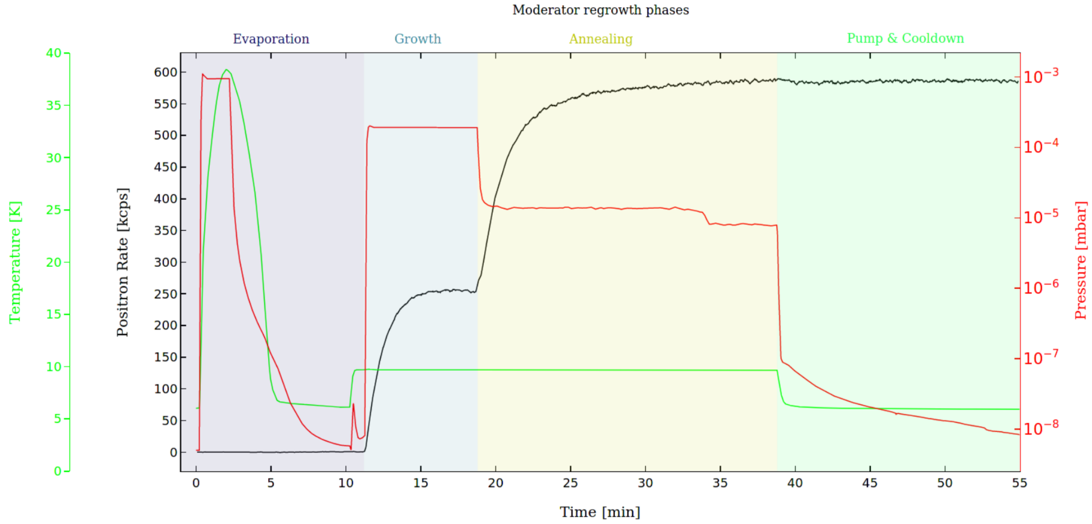

Figure 15: Solid neon moderator regrowth procedure including measurements of the positron rate at the trap inlet (black), second stage coldhead temperature (green) and moderator chamber pressure (red). The respective phases of the procedure are marked above the graph. A scale error of approximately 15 % on the positron rate is not shown.

The efficiency of the moderator and therefore the final positron flux depend strongly on the specific parameters used for the growth procedure. These were investigated in depth and the results are presented in the following section.

Total admitted gas mass: To find the optimal thickness of the neon moderator, the mass flow rate was set to an intermediate value of approximately 3 mg/min using a MKS M100B mass flow meter and the time of admission was varied between 3 to 20 minutes. The positron rate at the end of the growth cycle was measured with a calibrated scintillator to ascertain the moderation efficiency (see figure 16). The count rate initially significantly increases until the moderator is thick enough that the dominant loss mechanism becomes phonon scattering, which leads to a plateauing above a total admitted neon mass of approximately 44 mg. There is no discernible advantage to having significantly thicker neon layers, so to avoid excessive loads on the vacuum pumps the growth phase should be stopped when this threshold is reached. It is interesting to note that for larger admitted neon masses the count rate at the end of the growth phase (see figure 15) actually starts to decrease, while the final count rate still increases due to a larger rise in the annealing phase.

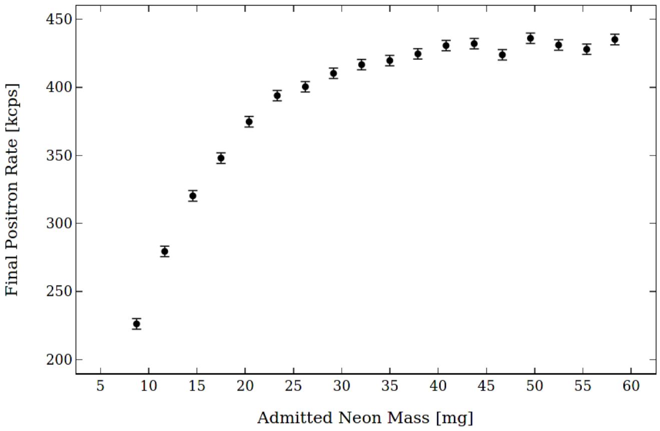

Figure 16: Dependence of final positron count rate on total neon mass admitted to the chamber via the mass flow meter. A scale error of approximately 15 % on the final positron rate is not shown.

Mass flow rate: The influence of the mass flow rate on the moderator efficiency was tested, keeping the total mass admitted to the chamber constant. As can be seen in figure 17 the final count rate is only weakly dependent on this parameter for sufficiently high flow rates. For very long growth phases it is likely that the moderator film incorporates more impurities due to remaining background gas atoms, leading to a slightly degraded performance. While higher flow rates are preferred to shorten the amount of time spent regrowing the moderator while data-taking, excessively high values should be avoided to keep the gas load on the vacuum pumps below an acceptable level.

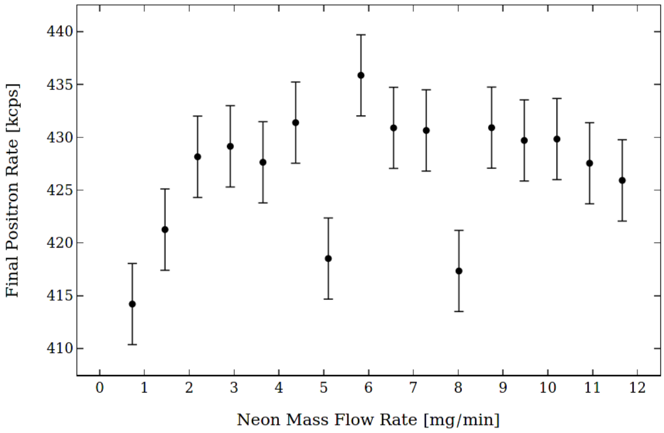

Figure 17: Dependence of final positron count rate on neon mass flow rate, keeping the total mass constant. A scale error of approximately 15 % on the final positron rate is not shown.

Source temperature: The source holder is mounted on the second stage of an ARS DE-204 closed cycle cryocooler using a sapphire disc as an electrical isolator. Using a temperature sensor mounted on top of the holder and a kapton heater wrapped around the second stage, the temperature can be stabilized to arbitrary temperatures between approximately 6 to 300 K. If the temperature is stabilized just below the sublimation temperature, this leads to the annealing [102] of crystal defects in the moderator, thereby increasing the efficiency. This process can already be exploited during the growth phase by increasing and stabilizing to a higher temperature before admitting neon to the chamber. Figure 18 shows the final count rate increasing with temperature until plateauing at approximately[16] 9.7 K up to the sublimation point, which was measured to be slightly above 10 K sensor reading at approximately 10^{-5} mbar ambient pressure. It was found that keeping the temperature stabilized for a few more minutes after stopping the gas flow was beneficial, leading to a further increase on the order of 3 % of the final positron count rate.

A disadvantage of solid rare gas moderators is that the moderation efficiency degrades over time. Several mechanisms for this degradation have been identified and studied. Background gas atoms are deposited on the moderator surface as impurities on which positrons can scatter, thereby reducing the probability that positrons get remitted epithermally. Similarly, defects in the crystal structure, which can be caused over time due to radiation damage, allow positrons to localize and annihilate, reducing the reemitted positron rate [103]. Furthermore, surface charging of impurities can also negatively impact the moderation efficiency over time [104]. Clearly, depending on the specific

---

[16] Note that the temperature on the surface of the cone, where the moderator is actually frozen onto, is likely slightly lower ($\sim 0.3\,\mathrm{K} - 0.4\,\mathrm{K}$) due to a temperature gradient on the moderator structure mounted on the second stage of the cryostat, as evidenced by a temperature difference of 0.7 K in two sensors mounted on opposite ends of the structure.

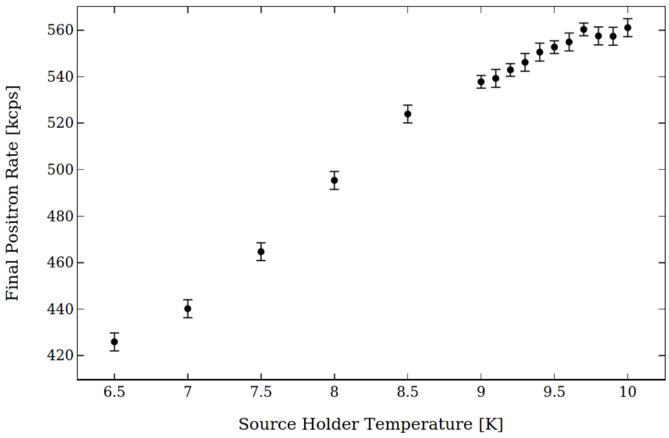

Figure 18: Dependence of final positron count rate on the source temperature during the growth phase. A scale error of approximately 15, % on the final positron rate is not shown.

thermal conditions, continuous sublimation of moderator atoms can also be of concern.

The moderator lifetime was measured by continuously monitoring the positron count rate over 60 hours (see figure 19). While the lifetime of the moderator can simply be given in terms of the half-life of 36 hours, a closer look is warranted. A reasonable fit of the positron rate after the regrowth procedure requires three components of the form

$$R(t) = R_1 \cdot e^{-t/\tau_1} + R_2 \cdot e^{-t/\tau_2} + R_3 \tag{42}$$

and the best fit parameters given in table 1. The moderator decay is mainly driven by an exponential decay time of approximately 40 hours (75 %), a constant[17] offset (20 %) and a small fast decaying component with a decay time of approximately 1.5 hours (5 %), which is responsible for the slightly faster decay over the first few hours.

Name	**Best Fit**
R_1	441.37 ± 0.33 kcps
τ_1	39.66 ± 0.11 h
R_2	31.65 ± 0.66 kcps
τ_2	1.488 ± 0.055 h
R_3	116.97 ± 0.51 kcps

Table 1: Moderator lifetime best fit parameters. A scale error of approximately 15 % on the rate parameters is not shown.

Another crucial property of the slow positron beam is its energy spread, which was measured with the same calibrated scintillator as used for the moderation efficiency

---

[17] While it is likely that this component would also decay exponentially, the decay time is clearly much larger than the measurement window, which makes a constant offset an appropriate approximation.

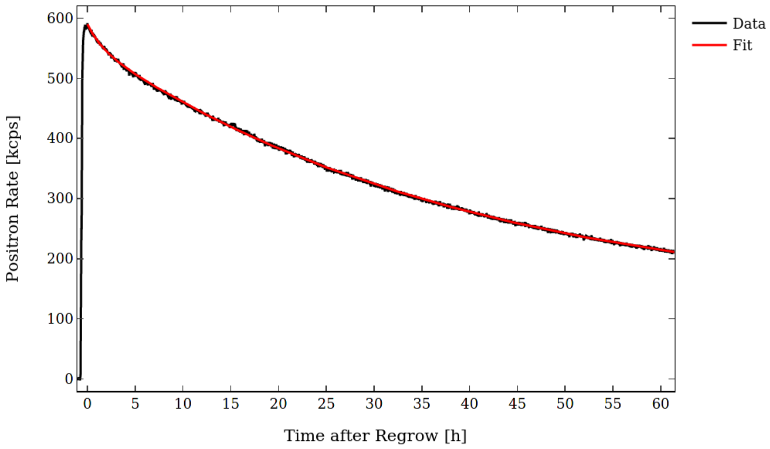

Figure 19: Long term moderator efficiency measurement. A scale error of approximately 15 % on the positron rate is not shown.

measurements. A rejection electrode upstream of the annihilation point next to the scintillator allows for the rejection of positrons with energies smaller than the electrode voltage, which therefore translates to the measured positrons minimum energy (see figure 20 for one such measurement). In terms of the energy distribution this translates to an expression for the count rate in terms of the energy E:

$$R(E) = R_t \cdot [1 - CDF(E)] \tag{43}$$

where R_t is the total rate of positrons irrespective of energy and CDF is the cumulative distribution function of positron energies. It was found that a skew normal distribution[105]

$$CDF\left(E, \mu, \sigma, \alpha\right) = \Phi\left(\frac{E-\mu}{\sigma}\right) - 2T\left(\frac{E-\mu}{\sigma}, \alpha\right) \tag{44}$$

which depends on the location of the distribution μ, a scale parameter σ, and a skewness parameter α, fits the data quite well. In the case of $\alpha = 0$ the distribution is just given by

$$CDF\left(E, \mu, \sigma, 0\right) = \Phi\left(\frac{E-\mu}{\sigma}\right) \quad , \tag{45}$$

where Φ is just the cumulative distribution function of the standard normal distribution. In this case μ corresponds to the mean energy and σ to the energy spread. For non-zero α there is an asymmetric correction given by the Owen's T-function

$$T(x, a) = \frac{1}{2\pi} \int_0^a \frac{e^{-\frac{1}{2}x^2(1+y^2)}}{1+y^2} dy \tag{46}$$

which also leads to a correction in the mean energy of

$$\overline{E} = \mu + \sqrt{\frac{2}{\pi}} \frac{\sigma\alpha}{\sqrt{1+\alpha^2}} \tag{47}$$

and similarly in the energy spread

$$\Delta E_\sigma = \sigma\sqrt{1 - \frac{2\alpha^2}{\pi(1+\alpha^2)}} \tag{48}$$

given by the variance in the distribution.

The FWHM value in this case has no closed solution, but can readily be calculated numerically. The energy distribution is then simply given by the total positron rate multiplied by the probability distribution function for the skew normal distribution

$$p(E) = R_t \cdot PDF(E, \mu, \sigma, \alpha) = \frac{2R_t}{\sigma}\phi\left(\frac{E-\mu}{\sigma}\right)\Phi\left(\alpha\frac{E-\mu}{\sigma}\right) \tag{49}$$

where ϕ and Φ are the probability distribution function and the cumulative distribution function of the standard normal distribution respectively.

The energy spread obtained is comparable with recently obtained measurements in a similar setup [106], where the asymmetric shape has been attributed to magnetic mirroring on the trap inlet due to the significant differences in magnetic field flux density at the source (approximately 20 mT) versus the trapping region (approximately 70 mT). A specific difference in the setup presented in this thesis is that it incorporates a 90° bend in the magnetic field as a velocity selector to reject unmoderated positrons. This explains the slightly higher measured energy spread compared to other systems.

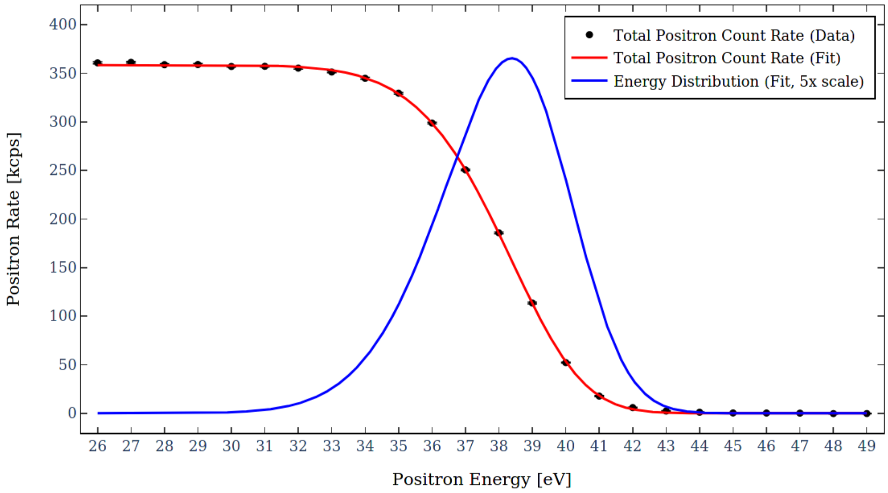

Figure 20: Single energy spread measurement. A scale error of approximately 15 % on the positron rate is not shown.

The energy profile was continually measured for several hours to ascertain the evolution of the mean energy and the energy spread (FWHM) of the distribution. Figure 21 shows that the mean energy decreases over time with $-51.8 \pm 1.6\,\mathrm{mV/h}$, while the energy spread (FWHM) increases with $19.1 \pm 2.6\,\mathrm{mV/h}$. Both these effects significantly decrease the trapping efficiency over the moderator lifetime, which leads to a significantly faster degradation in the number of available positrons in pulsed mode (see section 2.3). Furthermore, it makes tuning trapping parameters extremely challenging, since ideal values indeed change over time. Ideally those parameters would be continually matched to the moderator life cycle, which could drastically increase the time until a moderator needs to be regrown.

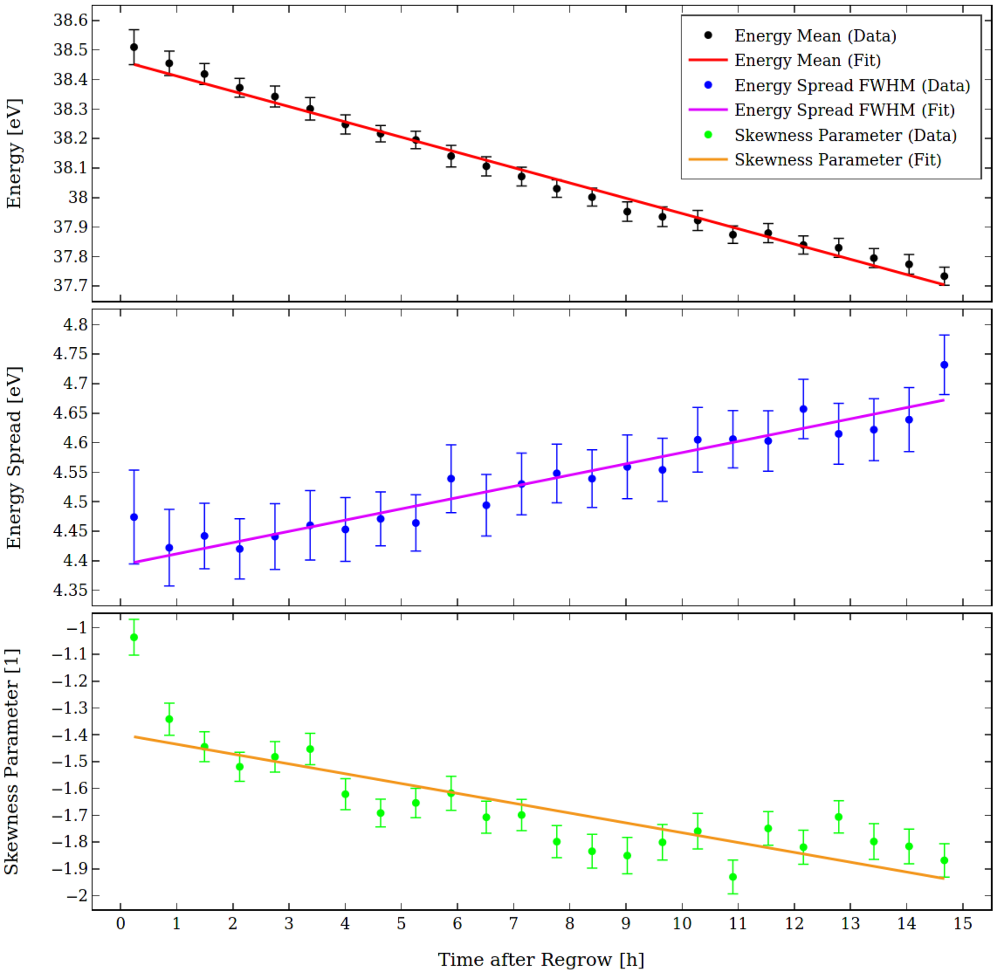

Figure 21: Long term moderator energy evolution.

In addition to the energy distribution, the spatial distribution of the CW beam was measured using a phosphor screen MCP (multi channel plate) and a CMOS sensor. The size reference was given by the active area of the phosphor screen of 27.1 mm. The resulting beam profile can be seen in figure 22. The shape is a result of the conical geometry of the source holder. This allows for significant increases in overall moderation efficiencies [98], but leads to a doughnut-like shaped beam, since most of the slow positron flux is generated on the cone surface and not on the source window itself. Another apparent feature of the beam profile is that there is some asymmetry on the horizontal axis, which is a result of a slight misalignment of the magnetic field of the source coils and the axis of the first pumping restriction leading to annihilation losses on the pipe. By symmetry arguments the overall rate losses incurred due to this mismatch can be calculated to be approximately 10 %. Since this region of the apparatus is not accessible once the radiation shielding and source is installed and there is no mechanism to steer positrons in this part of the beam, recovering these losses proves challenging.

The beam widths[18] in terms of standard deviations of the distribution are found to be

$$\sigma^{cw}_{\text{hor}} = 3.46\,\text{mm} \tag{50}$$

$$\sigma^{cw}_{\text{ver}} = 4.34\,\text{mm} \tag{51}$$

for the horizontal and vertical axis respectively. An interesting feature of the profile is that the horizontal beam size is significantly smaller than the vertical size. The losses described in the preceding paragraph only account for roughly a quarter of this difference, while the remaining effect is most likely caused by a compression in the horizontal axis due to the 90° bend employed as a velocity selector.

After optimization, the best final positron count rate was found to be

$$N_{e+} = R_{e+} \cdot CF_{\text{inlet}} = 67 \cdot 8888\,\text{kcps} = (592 \pm 89)\,\text{kcps} \quad , \tag{52}$$

which can be corrected for the losses due to beam transportation from the moderator to the annihilation point (see above), yielding the total rate of emitted moderated positrons

$$N^m_{e+} = (651 \pm 98)\,\text{kcps} \tag{53}$$

which finally leads to a moderation efficiency of

$$\varepsilon = \frac{N^m_{e+}}{\Phi_{e+}} = (0.519 \pm 0.078)\,\% \tag{54}$$

neglecting transportation losses. This value is comparable to that achieved in other experiments with similar moderation stages [107, 108].

The positron rate was also measured with another scintillator placed after the trap outlet in CW mode and was found to be

$$N^t_{e+} = R^t_{e+} \cdot CF_{\text{outlet}} = 23 \cdot 18883\,\text{kcps} = (433 \pm 65)\,\text{kcps} \tag{55}$$

which corresponds to the number of positrons available for trapping. After accounting for the 10 % of losses on the first beam restriction, it can be seen that around 25 % of the remaining positrons are lost on the trap inlet. This is due to magnetic mirroring caused by the large difference in magnetic fields between the positron source and trapping region. While these losses could at least partially be recovered by producing a higher field with the source coils, this would involve a substantial redesign due to thermal constraints.

---

[18] Note that this value is dependent on the magnetic field value where the measurement is taken. For this measurement the magnetic flux density at the position of the MCP was on the order of 10 mT, while it is approximately 20 mT at the source.

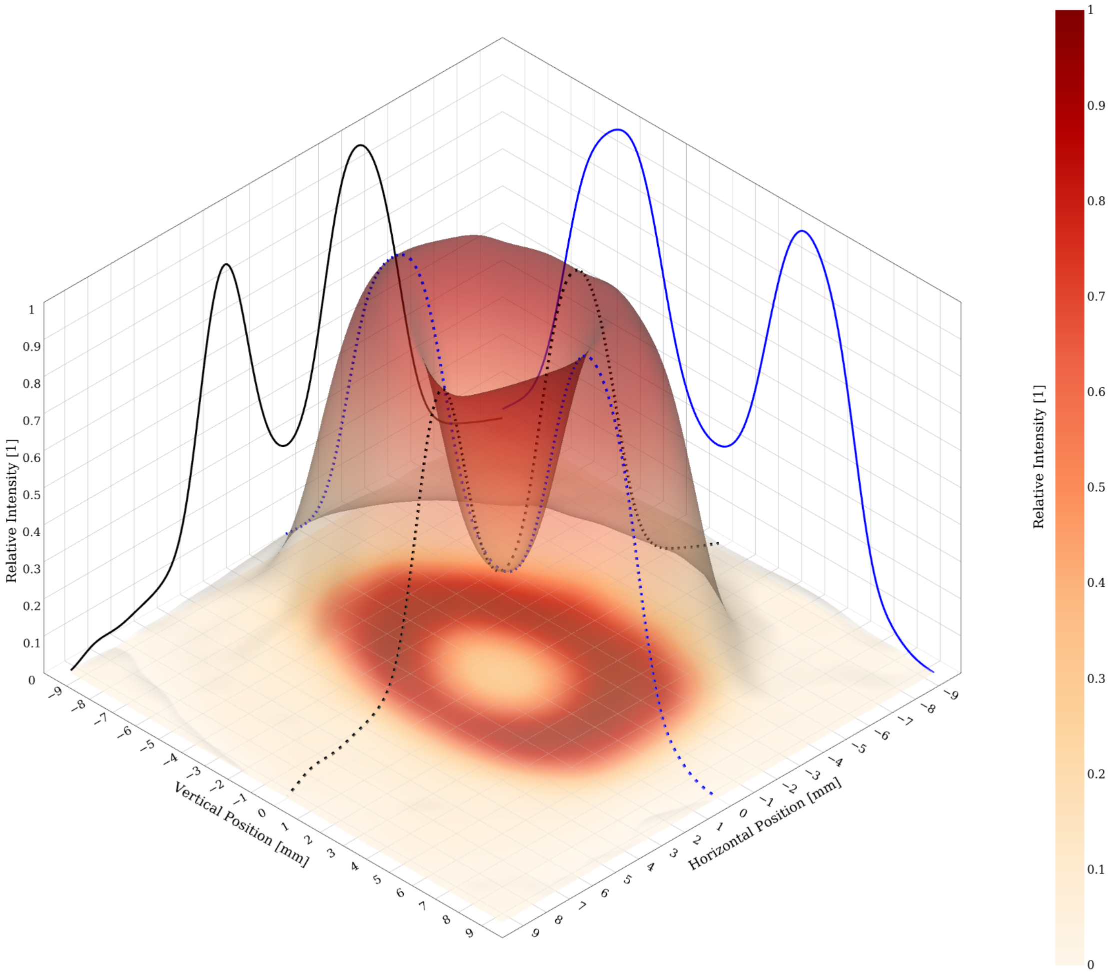

Figure 22: 3D surface plot of spatial CW positron beam profile, with 2D color space projection on the z-plane and 2D contour projections of the beam center for the horizontal (black) and vertical (blue) planes.

2.3. Buffer gas trap

Buffer gas traps are used to convert conventional slow positron beams from continuous to pulsed emission with superior beam parameters at the disadvantage of reducing the rate of positrons by approximately one order of magnitude. The working principle of these traps is based on a Penning-Malmberg trap [109] additionally employing a buffer gas (usually N_2) to facilitate trapping of charged particles [110]. Such traps confine plasmas of particles using an electrostatic well potential created using ring electrodes that allow experimental access from both sides. The radial confinement is achieved using a strong, uniform magnetic field along the center axis of the electrode structure. The buffer gas is responsible to introduce an energy loss mechanism that allows the trap to be loaded.

The two relevant[19] interactions for nitrogen in the energy region of interest are electronic excitations and positronium formation (see figure 23). While the former leads to a desirable reduction in kinetic energy, the latter removes positrons from the trap. This restricts the useful window for trapping to the energy range between 8.6 eV (threshold energy of the $a^1\Pi$ electronic state) to approximately 12 eV, where positronium formation becomes dominant. Therefore, the potentials should be chosen approximately 10 eV below the expected kinetic energies of the positrons to be trapped. The process most likely to occur then is the electronic excitation in N_2 of the $a^1\Pi$ state, leading to a reduction in the kinetic energy of 8.8 eV per inelastic collision [111].

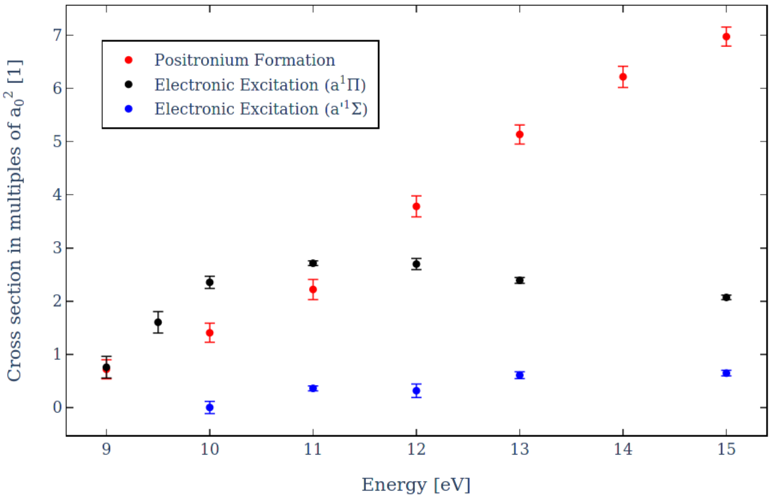

Figure 23: Measured cross-sections of positronium formation and relevant electronic excitations in N_2, given in multiples of the squared Bohr radius as determined by Marler and Surko [111].

The trap is segmented in three stages (see figure 24) with decreasing electrostatic potentials optimized for best trapping efficiency according to the these cross-section and energy loss considerations. Additionally, the trap is closed with ring electrodes representing an inlet and outlet. The inlet electrode is set to a voltage such that the initial positron energy (including spread) is just large enough to allow positrons to pass into the first stage, while positrons that underwent an inelastic collision will be trapped upon reflection. To facilitate the reflection, the outlet electrode potential needs to be high enough to block all incoming positrons. To eject positrons out of the trap, the outlet electrode is ramped to ground. The time and energy distribution of the pulse can be optimized, depending on the specifics of the ramp waveform (see section 2.4).

Nitrogen is admitted to the first stage at a relatively high pressure on the order of 10^{-3} mbar. Differential pumping is then used to gradually decrease the ambient pressure to approximately 10^{-4} mbar in the second and 10^{-6} mbar in the third stage. This ensures

---

[19] Vibrational excitations of N_2 also contribute, but they have negligible cross-sections compared to these effects. Direct ionization does not occur below a threshold of 15.6 eV.

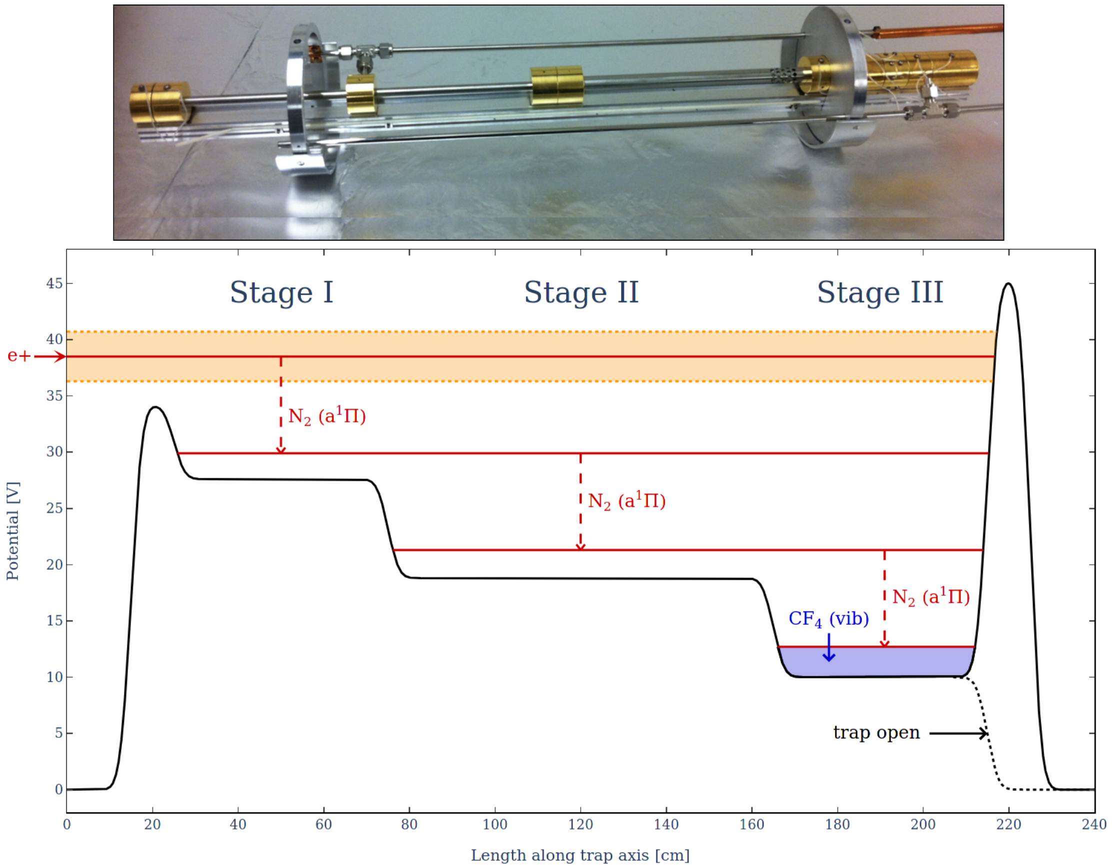

Figure 24: Picture of trap electrodes (above) and plot of electrostatic potential along the trapping axis in a buffer gas trap (below). Positron energy levels are given in red, including the FWHM for the initial energy in orange. The levels are separated by 8.8 eV. The quasi-continuous cooling in the final stage is hinted at by the shaded blue region. The dotted black line represents the change in potential when the trap is opened.

that there is a high probability for an incoming positron to undergo at least one inelastic collision, without too drastically impacting the lifetime of positrons in later stages due to annihilation. Positrons trapped in the lowest potential well of the third stage further cool down via inelastic collisions on gas atoms exciting vibrational states. Since this is a rather inefficient process in nitrogen, a small amount of CF_4 (approximately 10^{-6} mbar) is added. This allows for quasi-continuous ($\Delta E = 160\,\text{meV}$ per collision [112]) cooling down to the electrostatic potential.

The electrodes of the last stage are azimuthally segmented in four equally large parts. This allows for applying a quadrupole rotating electric field with relative phases of 90° to radially compress the positron cloud. This technique is known as rotating wall compression in the single particle regime (due to the low density of trapped positrons)

[113]. While this process does lead to increased heating of the positron cloud, the CF_4 in the last stage counteracts this effect by collisional cooling. This does not only lead to a significantly smaller beam size, but also prevents a major loss mechanism, namely the annihilation of positrons on the electrode walls.

The trapping efficiency is given by

$$\varepsilon_t = \frac{N^b_{e+} \cdot f_{\mathrm{rep}}}{N^t_{e+}} \tag{56}$$

where N^t_{e+} is the number of positrons per second available to be trapped (see equation 55), N^b_{e+} is the number of positrons per bunch in pulsed mode and f_{rep} is the operating frequency of the trap. The setup presented here is designed to be operated at repetition rates of 2-10 Hz, to match with the requirements of other parts of the system (laser, HV switching and DAQ). In this regime the trapping efficiency is largely independent of the operating frequency, since the lifetime of positrons in the trap is significantly longer than the storage time. However, there is a strong dependence on the energy profile of incoming positrons, buffer gas flows, and potentials set on the trap electrodes. These were investigated by measuring the total charge deposited in a $PbWO_4$ scintillator operating the trap at 5 Hz. The results are presented in the following section and an absolute determination of the trapping efficiency is presented thereafter.

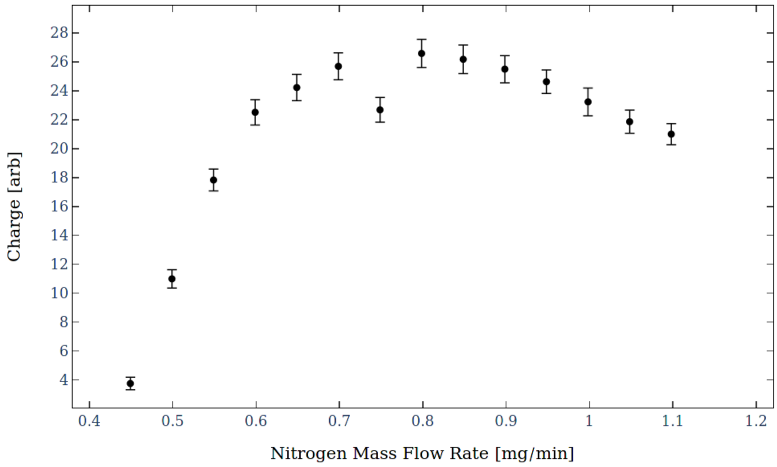

Figure 25: Dependence of number of positrons per bunch on nitrogen mass flow rate to first stage of the trap via the mass flow meter.

Nitrogen gas flow: Nitrogen is constantly admitted to the chamber via an Aalborg GFC 17 S – 10 sscm – mass flow meter and due to constant pumping speed a steady state pressure is reached in the trapping region after a few seconds. The total charge, which is directly proportional to the number of positrons, of a single bunch annihilating on the gate valve was measured with the $PbWO_4$ scintillator (see figure 25). For small mass flow rates the trapping efficiency sharply increases until the probability for an incoming positron to undergo at least one inelastic collision approaches unity, which is found to be at approximately 0.8 mg/min. Further increasing the pressure in the chamber leads to a slow decrease in efficiency due to the higher annihilation rate of positrons on nitrogen molecules.

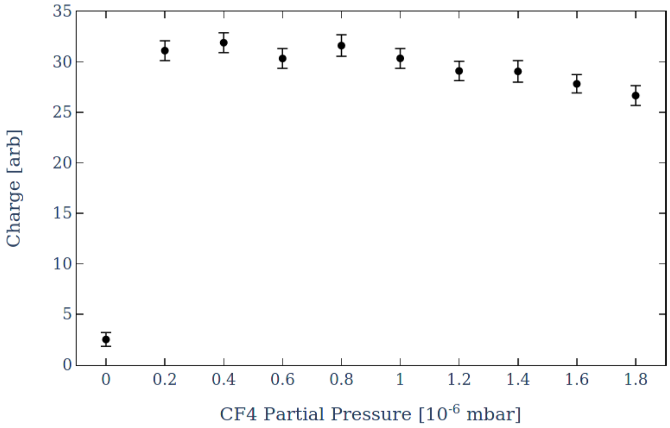

Figure 26: Dependence of number of positrons per bunch on CF_4 partial pressure in trap outlet chamber.

CF4 gas flow: A constant flow of CF_4 is admitted via an Agilent Variable Leak Valve, allowing precise manual control of very low flow rates. However, in this case the mass flow rate is not measured, but the pressure increase in the trap outlet chamber is used as a proxy value[20]. As before, the total charge deposited in the lead tungstate scintillator per bunch is measured (see figure 26). If the valve is completely closed, large losses are evident, which are due to the positron cloud expanding and annihilating on the chamber walls. Admitting even a modest amount of CF_4 counteracts this effect and increases the trapping efficiency by an order of magnitude. After plateauing, the losses due to annihilation start to dominate at around 10^{-6} mbar and decrease the number of positrons per bunch. In general, slightly higher amounts of CF_4 can be beneficial if small beam diameters are preferred, losing only slightly in trapping efficiency.

Potential differences: Figure 27 shows the number of positrons per bunch versus the difference between the mean positron energy entering the trapping region (see figure 21) and the electrostatic potential set on the first stage electrode. This corresponds to the mean kinetic energy of positrons in the first stage region. The other potentials were held constant during the measurement. The trapping efficiency increases sharply up to approximately 10 eV due to the increase in the cross-section of electronic excitations in N_2 and then slowly decreases due to the dominance of the positronium production cross-section (see paragraph above in this section and figure 23). Note that due to

---

[20] Due to the placement of the pressure sensor, it is likely that the pressure in the trapping region is slightly higher.

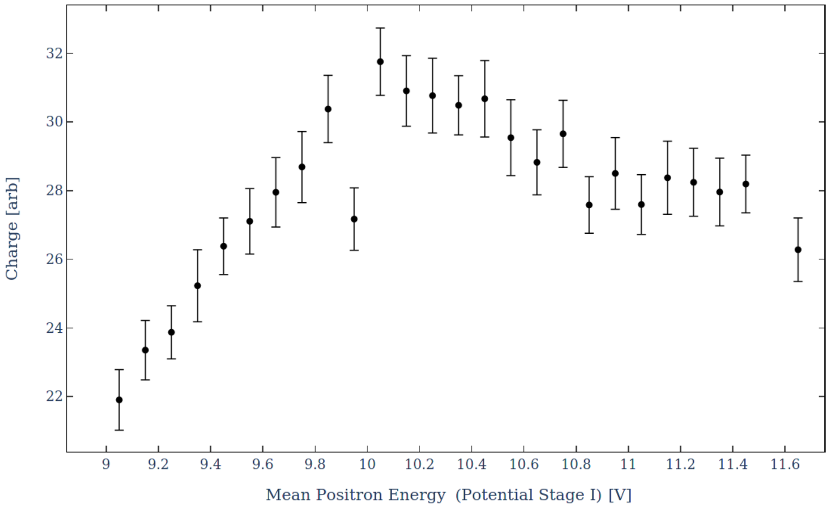

Figure 27: Dependence of number of positrons per bunch on difference between mean incoming positron energy and the electrostatic potential of stage I.

the relatively large energy spread of the incoming positrons the onset of the respective effects is not completely sharp with respect to the mean kinetic energy. Similar behavior is observed for potential differences in subsequent stages.

To determine the absolute trapping efficiency, a lead tungstate scintillator was used to determine the average deposited charge in the PMT per single event in CW mode, which, multiplied by the trigger rate, gives a good estimator of the total charge deposited per second. Then the same scintillator is used to measure the total charge deposited in the PMT per positron bunch when the trap is operated. Since the scintillator and PMT are used in a regime where there is no saturation expected, the charge measured is proportional to the number of positrons incident on the annihilation point. Therefore equation 56 can be rewritten

$$\varepsilon_t = \frac{N^b_{e+} \cdot f_{\text{rep}}}{N^t_{e+}} = \frac{Q^b_{e+} \cdot f_{\text{rep}}}{\overline{Q}_{e+} \cdot \overline{R}_{e+}} \tag{57}$$

where Q^b_{e+} is the total charge deposited due to a single bunch in pulsed mode, $\overline{Q}_{e+}$ is the average charge deposited due to a single positron in CW mode, and $\overline{R}_{e+}$ is the count rate in the same scintillator in CW mode. This was measured at a repetition rate of 1 Hz to be

$$\varepsilon_t = \frac{-4.0\,\text{nAs} \cdot 1\,\text{Hz}}{-6.9\,\text{nAs} \cdot 10.6\,\text{kcps}} = (5.4 \pm 0.1)\ \% \tag{58}$$

where the error is an estimation based on the linearity specifications (2 % below 25 mA of anode current) of the XP2020 photomultiplier tube used in conjunction with the lead tungstate scintillator.

The spatial distribution of the pulsed beam was measured analogously to the CW beam (see section 2.2), where the same phosphor screen MCP and CMOS sensor was

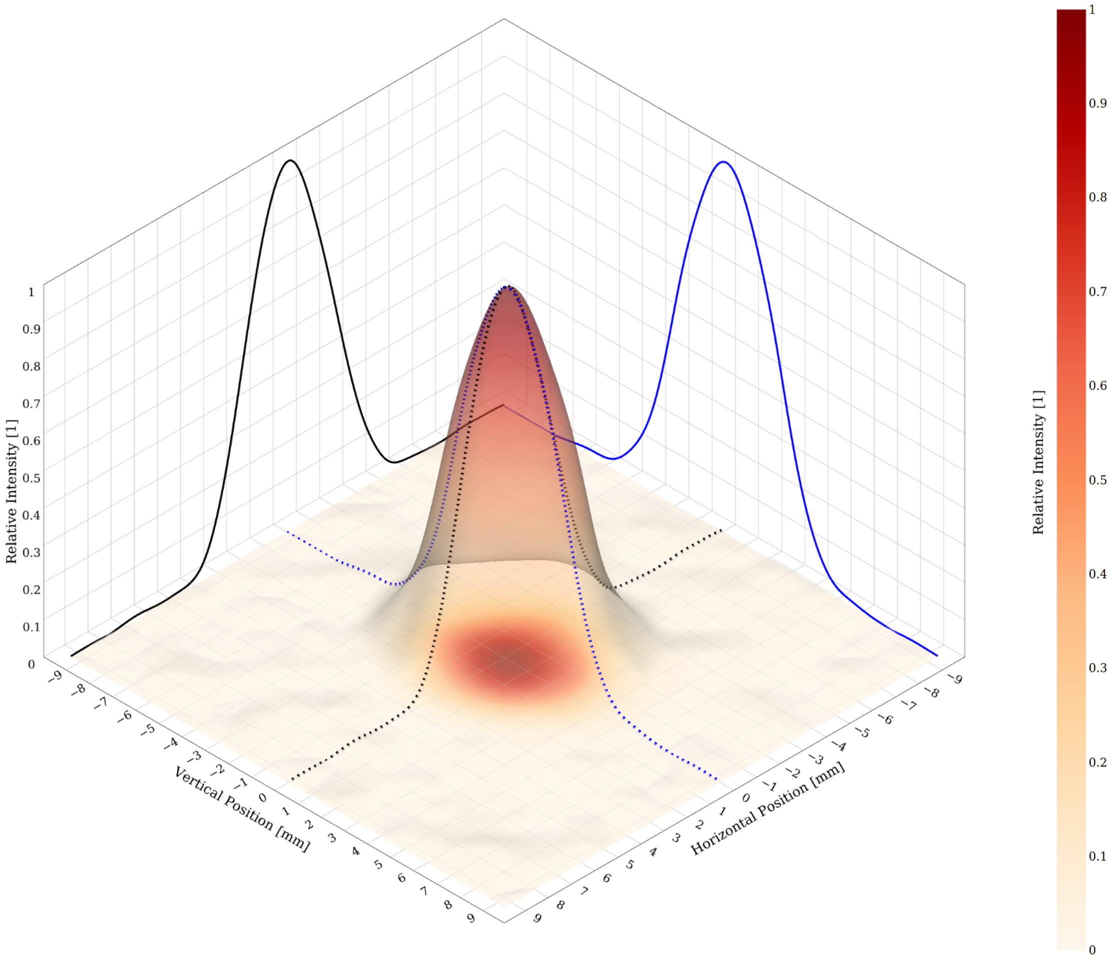

Figure 28: 3D surface plot of spatial pulsed positron beam profile, with 2D color space projection on the z-plane and 2D contour projections of the beam center for the horizontal (black) and vertical (blue) planes.

used. The resulting beam profile is close to an axially symmetric Gaussian profile (see figure 28). The beam widths[21] in terms of standard deviations of the distribution are found to be

$$\sigma_{\text{hor}} = 1.81\,\text{mm} \tag{59}$$

$$\sigma_{\text{ver}} = 1.92\,\text{mm} \tag{60}$$

for the horizontal and vertical axis respectively. This is significantly smaller than the corresponding values for the CW beam (see equations 50 and 51), due to the rotating

---

[21] Note that this value is dependent on the magnetic field value where the measurement is taken. For this measurement the magnetic flux density at the position of the MCP was on the order of 10 mT, while it is approximately 70 mT at the trap gate.

wall compression with collisional cooling via CF_4 vibrational states in the third stage (see above).

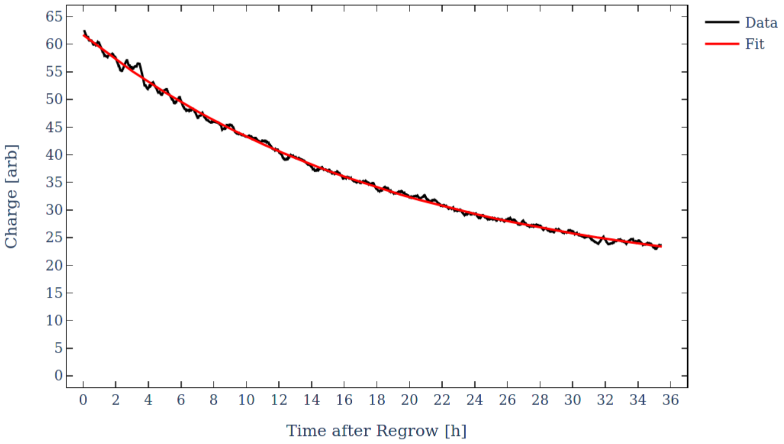

Figure 29: Long term measurement of the number of positrons per bunch. The time is given relative to the end of the regrowth procedure after the gate valve opens and when measurements can commence.

The number of positrons per bunch supplied by the trap was continuously measured over 36 hours starting immediately after the regrow procedure finshed (see figure 29). A good fit requires only one exponential component with a constant offset[22] of the form

$$Q(t) = Q_0 \cdot e^{-t/\tau} + Q_c \tag{61}$$

and the best fit parameters given in table 2. The measured half-life of the pulsed beam is therefore approximately 22 hours, which is significantly less than the measured moderator lifetime of 36 hours (see section 2.2). This is due to the changes in the mean energy and energy spread over time (see figure 21). As mentioned, appropriate corrections over time to the source and trap potentials could lead to significant improvements on this lifetime. However, these corrections are not trivial and would most likely depend on the exact conditions during moderator growth.

Name	**Best Fit**
Q_0	45.61 ± 0.13
τ	$19.37 \pm 0.15\,\text{h}$
Q_c	16.09 ± 0.16

Table 2: Pulsed beam lifetime best fit parameters. The amplitude of the charge Q_0 and Q_c are given in arbitrary units matching figure 29.

---

[22] Note that the constant component is likely to decay exponentially as well, with a lifetime that is much larger than the measurement window.

To maximize the number of positrons on the target per unit measurement time, the ideal length between subsequent regrows was determined. Numerical integration of the lifetime fit function (see equation 61 and table 2) yields the cumulative number of positrons on target. If this value is divided by the length of the integration window plus one hour, a value for the mean number of positrons on the target per unit measurement time is gained, assuming a regrow procedure as described in section 2.2 and figure 15 of approximately one hour. Varying the upper limit for the integration then yields the number of positrons relative to the time between subsequent regrowths (see figure 30). Therefore, when taking data continuously for multiple days, the moderator should be regrown every 5-10 hours to gather the largest set of statistics possible.

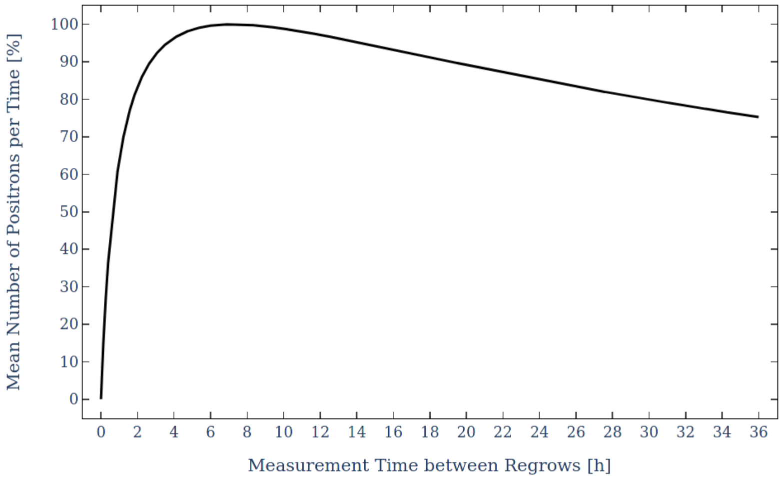

Figure 30: Mean number of positrons on target per unit measurement time depending on time between regrows (normalized to 1).

2.4. Pulsed beam transportation and implantation

Since all of the spectroscopic experiments presented here require at least one pulsed laser source, proper timing and synchronization of the pulsed positron bunches is crucial. Further complicating matters is that positrons need to be implanted onto the target with energies on the order of a few keV (see section 3.2) within a mostly electromagnetic field free region to avoid Zeeman and Stark shifts of energy levels.

Figure 31 shows the main components used to deliver pulsed bunches to the target. Bunches of positrons are prepared in the last stage of the buffer gas trap using the rotating wall technique and collisional cooling with CF_4 molecules (see section 2.3). The bunch is extracted from the trap by ramping down the potential of the gate electrode (see figure 24). Crucial beam parameters can be measured by a phosphor screen MCP, which can be lowered into the beam path by a pneumatic manipulator, which is placed in the chamber used to connect to the outlet cryopump. Additionally, a scintillator is placed outside of the chamber, which can be used to monitor rates and trapping efficiency. The beam then traverses the first drift tube which is pulsed to 100-200 V once most of the bunch is inside the tube. This increases the mean kinetic energy of the bunch by 100-200 eV without significantly impacting the energy spread. This step is required to avoid large spatial spreads of the bunch in the several meters long transport section connecting the trap and the experimental area. While the positron bunch enters the second drift tube, a time-varying potential is used to time-bunch. Subsequently, when most of the bunch is inside the drift tube, the electrode is pulsed to high voltage between 1 kV and 6 kV, depending on the experimental requirements (see section 3.2). After being accelerated upon exiting the drift tube, the positrons are extracted non-adiabatically from the magnetic field, by means of a sharp transition into a low field region via a mu-metal shield encompassing the experimental region. An electrostatic einzel lens is used to focus the beam at a variable distance. The final beam parameters can be monitored with a phosphor screen MCP and $PbWO_4$ scintillator.

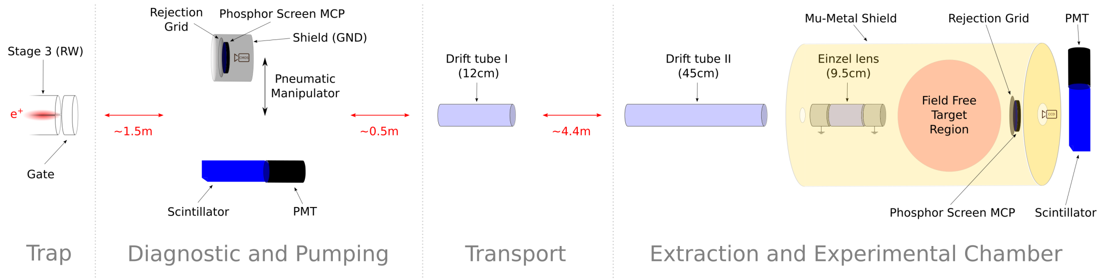

Figure 31: Schematic overview of the pulsed beamline from the extraction of the trap to the experimental chamber, including diagnostic elements and approximate distances (drawing not to scale). An overview for the electronics used to drive the electrodes, can be found in figure 32.

This technique is based on earlier work [114], but the implementation had to be redesigned to take the additional several meter long transport section into account and use the same electrode both for time-bunching and elevation, due to constraints present in the current setup. A new integrated electronics system was developed, based on custom logic delay lines, a 2-channel arbitrary waveform generator, several amplifiers and switches. A schematic overview of the electronics setup can be found in figure 32.

A Spectra-Physics Quanta-Ray Lab 190 laser is used as the main timing source, since its lamps need to be fired at a fixed rate of 10 Hz and all remaining devices need to be synchronized with it. However, depending on the specific measurement it is usually advantageous to run the experiment at a lower frequency, e.g. for reduced data rates in the DAQ system or to increase the lifetime of the employed dye in the pulsed dye amplifier (see section 3.3). For very low operating frequencies, annihilation losses in the trap limit the rate of positrons that can be supplied by the trap (see section 2.3), which is why the lower rate limit for practical purposes is around 1-2 Hz. Thus, a timer is used to skip a specific number of triggers from the lamp subsystem, effectively acting as an integer frequency divider providing a selectable rate from 1-10 Hz. This then triggers an arbitrary waveform generator supplying all required analog and digital signals to the rest of the system.

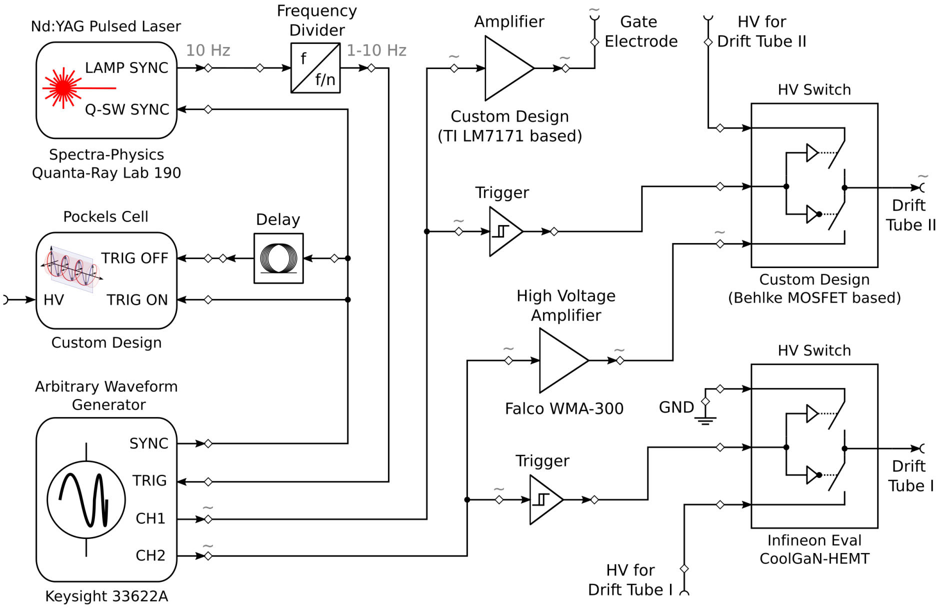

Figure 32: Schematic overview of electronics used in the pulsed beamline for extraction, bunching and timing. Schematics for timing, logic and HV switching are considerably simplified (detailed schematics for parts of the system can be found in Appendix C). Analog signals are marked with a grey tilde symbol where appropriate. Unmarked signals are digital or DC voltages for HV supply pins, respectively. The “SYNC” output and the logic triggers supply digital synchronization signals to additional devices not shown here, e.g. DAQ devices, shutters, etc.

The following section will present the specific subsystems shown in figures 31 and 32 including calculations and performance results, where appropriate. While the laser subsystem will be treated in more detail in section 3.3, it should be noted here that it is synchronized to the positron system by the digital “SYNC” output of the waveform generator. This drives both the internal Q-switch of the Quanta-Ray Nd:YAG and the Pockels cell, which is used to isolate the laser system against back-reflection and to stabilize the power output of the pulsed dye amplifier.

Positron extraction from the trap: As mentioned in section 2.3, the traps highest electrostatic potential is on the last electrode to create the potential well necessary for trapping. However, when this gate electrode is ramped down to below the potential in the last stage (see figure 24), positrons will escape the trap, guided by the magnetic field. Depending on the specific waveform used in the opening of the trap, the pulsed beam can have a wide range of properties. For example, a slow ramp on the order of

$0.1\,\mathrm{V}/\mu\mathrm{s}$ can provide extremely low energy spreads down to $\Delta E_{\mathrm{FWHM}} \approx 50\,\mathrm{meV}$ [115], but will spread out the bunch on the microsecond timescale. While this spread in time could in principle be counteracted by a similar time-bunching scheme as used (see below in this section), practical limits on the required voltage make this infeasible. However, if a very fast ramp on the order of $1000\,\mathrm{V}/\mu\mathrm{s}$ is employed, all positrons leave the trap within a few tens of nanoseconds. This comes at a cost of a generally increased energy spread (see figure 33) and potential instabilities depending on noise, ringing and other specifics of the supplied waveform. An intermediate slew rate can be used, which can achieve slight time-bunching due to the difference of potentials entering and exiting the gate electrode, without significant increases of the energy spread (see figure 34). Slight differences in the mean energy over time on the order of a few hundred meV lead to a significant reduction in time spread after being allowed to propagate the approximately 2 m to the first drift tube electrode.

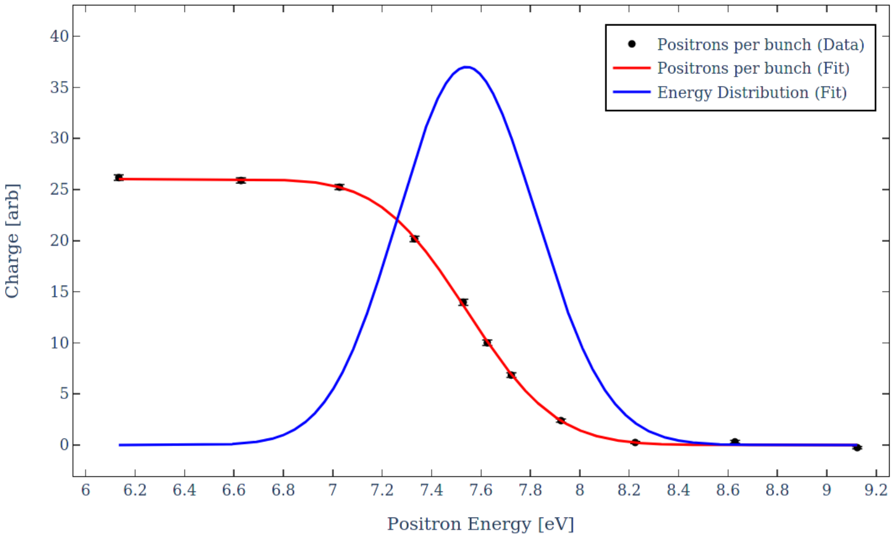

Figure 33: Pulsed mode energy spread measurement for fast ramp speed without time bunching.

A measurement of the energy spread of the pulsed beam is conducted completely analogously to the CW case, the only difference being that instead of the count rate, the total charge deposited per pulse in the scintillator/PMT is measured. Just as with the cumulative distribution function obtained in CW mode, a skewed Gaussian distribution (see equation 44) gives an appropriate fit. The mean energy and energy spread in terms of standard deviation is then given by equation 47 and 48, respectively. The FWHM value of the energy spread can be computed numerically from the obtained energy distribution of equation 49, where the total positron rate R_t is replaced by the charge deposited per bunch Q^b_{e+}. The measured values and best fit for a fast gate ramp can be found in figure 33. The measured parameters for this energy distribution are thus found to be

$$\overline{E}^f = (7.55 \pm 0.17)\ \mathrm{eV} \tag{62}$$

and

$$\Delta E^{f}_{\mathrm{FWHM}} = (660 \pm 160)\ \mathrm{meV} \tag{63}$$

respectively. The fit shows no skew in the distribution above the uncertainty of the fit.

The linear ramp speed resulting in the minimum time spread at the first drift tube was found to be approximately $50\,\mathrm{V}/\mu\mathrm{s}$ in this configuration and the energy spread was re-measured. The resulting data points and best fit are shown in figure 34. The parameters of the energy distribution were found to be

$$\overline{E} = (7.26 \pm 0.02)\ \mathrm{eV} \tag{64}$$

and

$$\Delta E_{\mathrm{FWHM}} = (760 \pm 40)\ \mathrm{meV} \tag{65}$$

with a clear skew towards higher energy due to the time-bunching on the gate electrode.

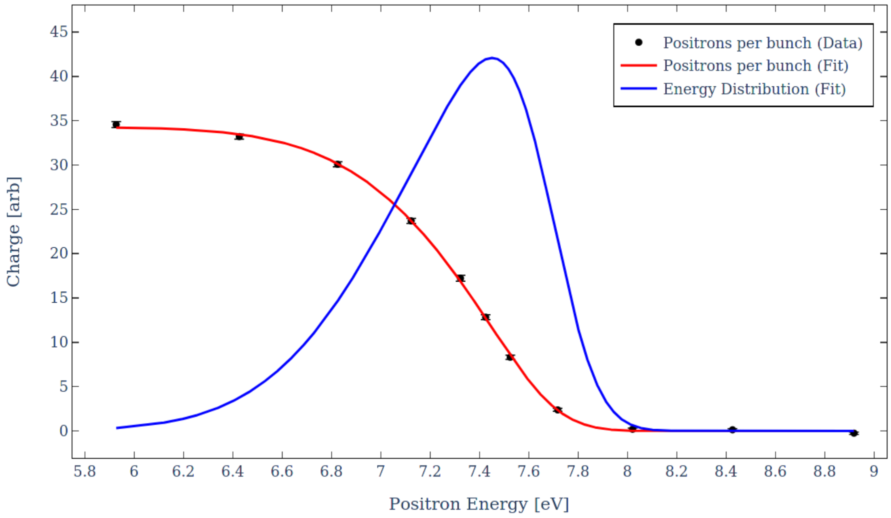

Figure 34: Pulsed mode energy spread measurement for medium ramp speed with slight time bunching.

Due to the limited length of the first drift tube of 12 cm, only a limited time window of positrons can be accepted. Since the positron bunches traverse approximately 2 m of apparatus before reaching the electrode (see figure 31), even perfectly time-bunched pulses will be limited by the energy spread causing a time spread, which can not be corrected for.

To optimize the parameters of the system, a Monte-Carlo simulation was written, where individual positrons were created at $t = 0$, with a random energy sampled from a standard normal distribution using the energy spread from equation 63. For the evolution to the first drift tube this is equivalent to a perfectly bunched beam with an initially symmetric energy profile. This is a good approximation for situations where the relative energy spread $\Delta E/\overline{E}$ is comparably high and errors due to imperfect bunching waveforms are not the limiting factor. Higher beam energy reduces the time spread on the location of the first drift tube, which is slightly offset by limiting the time positrons spend inside the electrode and the fixed transition time of the Infineon CoolGAN high voltage switch of approximately[23] 10 ns.

In practice, the mean beam energy can be increased by a few volts without significantly impacting the energy spread or trapping efficiency by incrementing all potentials on the trap and source simultaneously. The simulated efficiency of the elevation procedure in the first electrode is shown in figure 35. While this would suggest that the initial energy of the bunches extracted out of the trap should be above approximately 14 eV, it was found that there were no improvements above 10.5 eV. This is likely due to the limited effectiveness of a linear ramp for the bunching.

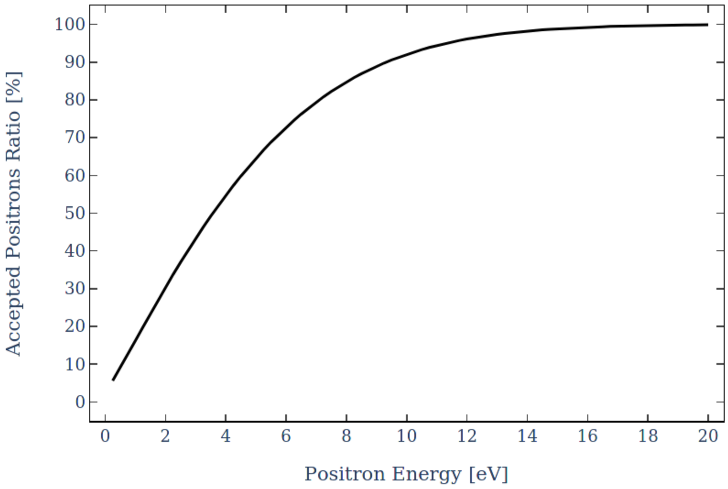

Figure 35: Monte-Carlo simulation of ratio of properly elevated positrons in first drift tube depending on initial mean energy, assuming perfectly bunched positrons extracted from the trap.

The time spread (FWHM) on the first drift tube entrance using a mean positron energy of 10.5 eV was optimized within the parameter space of the minimum gate voltage and the linear ramp speed. A wide range of combinations with similar time spread was found. The final value of $\Delta t_{\mathrm{FWHM}} = 36.8\,\mathrm{ns}$ was found using +5.5 V offset on the gate voltage and a linear ramp speed of $180\,\mathrm{V}/\mu\mathrm{s}$. Simulation is in reasonably good agreement for the time spread, yielding 32.7 ns. The slightly higher measured value is caused by the ramp waveform not being optimized for ideal bunching. Adjusting the energy spread parameter in the simulation to match the experimental time spread, one finds an effective value of

$$\Delta E_{\mathrm{FWHM}}^{\mathrm{MC}} = 742\,\mathrm{meV} \tag{66}$$

for the mean energy

$$\overline{E}^{\mathrm{MC}} = 10.5\,\mathrm{eV} \tag{67}$$

---

[23] The 10-90 % rise time for this device is specified as 7 ns by Infineon.

that was used for subsequent simulations. Approximately 10 % of positrons are not properly elevated and therefore lost for subsequent stages, due to the limited spatial overlap in the electrode (see figure 36).

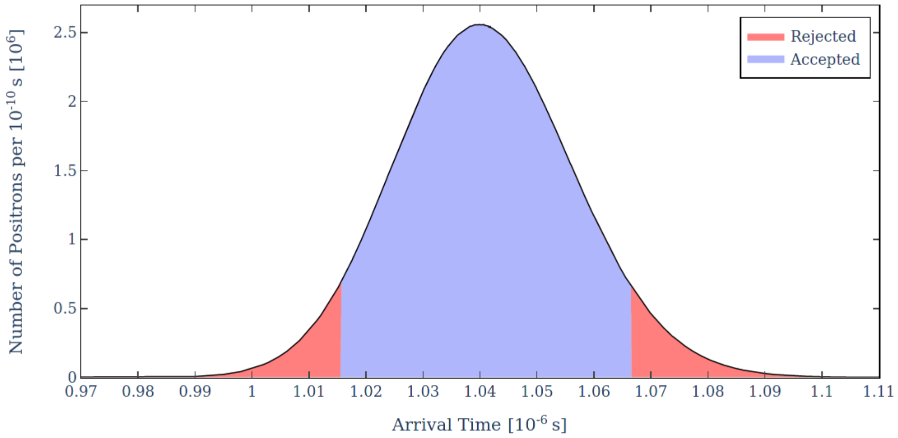

Figure 36: Monte-Carlo simulation of arrival time and acceptance of 10^9 positrons for elevation in first drift tube, assuming perfectly bunched positrons extracted from the trap. Source of time spread is given only by initial energy spread and propagation. Positrons enclosed within electrode while switching to HV are marked “Accepted” (light blue) and “Rejected” (light red) otherwise.

Positron transportation to experimental area: Positrons that are within the first drift tube when it is switched to high voltage, will be accelerated by the potential difference upon exiting the electrode without significantly impacting their energy spread. This is used to further reduce the relative energy spread $\Delta E/\overline{E}$, which is necessary to avoid excessively large time spreads on entering the second electrode. These would lead to issues with both the necessary voltage swing for bunching (see below) and acceptance similar to the first drift tube (see text below and figures 39 and 41).

Figure 37 shows the resulting time spread (FWHM) further propagating the sample of the Monte-Carlo simulation to the entry of the second drift tube approximately 4.4 m downstream. To remain agnostic of the exact time structure of the energy profile (or equivalently the precise exit time and bunching waveform) the energy profile is reset upon exiting the first drift tube using the original energy spread. Note that the FWHM value of the time spread does not change during elevation itself, since the part of the distribution that is rejected is well below the half-height points (see figure 36). Therefore, the time spread after transportation asymptotically approaches the time spread on the exit of the first drift tube of 39 ns (FWHM) with increasing elevation potentials. Voltages on the order of 100 V are required to avoid large increases in time spread. However, as long as the value is sufficiently high, a wide range of values can be chosen according to the specifics of the bunching waveform on the second drift tube (see next paragraph).

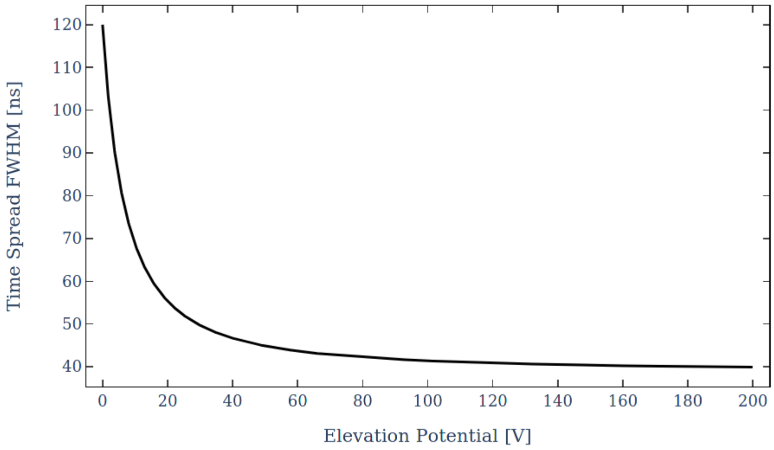

Figure 37: Monte-Carlo simulation of time spread on second drift tube depending on elevation potential, assuming perfectly bunched positrons extracted from the trap.

Positron bunching and extraction from magnetic field: The bunching waveform is supplied to the second drift tube by a Falco WMA-300 high voltage amplifier with a voltage swing of ±150 V. The device is frequency limited and therefore a large voltage swing is needed for high slew rates. It was found that due to the relatively high capacitive load of the electrode, the amplifier was too slow to accurately follow the waveforms supplied by the waveform generator. Instead, the fastest and largest swing without ringing effects of approximately ±140 V was requested from the device (see figure 38) by using a step function of the waveform generator. Instead of tailoring the bunching waveform to given initial conditions, the voltages and timings were optimized using the Monte-Carlo simulation to find a region where the optimal bunching waveform fitted the amplifier response well.

A custom device switches the electrode from the amplifier signal to a DC voltage between 1-6 keV (see figure 32), depending on the experimental requirements on the implantation (see section 3.2). The rise time of this switch is approximately 100 ns. However, contrary to the elevation step on the first drift tube, positrons exiting the electrode while the ramp is not complete, are not lost in subsequent stages. They will have a lower implantation energy and will also be somewhat out of focus on the target, but will nevertheless be implanted and produce positronium. Depending on the specific requirements of the experiment, the bunching waveform can therefore be optimized for minimum time spread, final energy spread or efficiency.

A χ^2 minimization algorithm was used to find the best fit parameters for the elevation potential, the mean energy in the buncher and the time offset for the bunching waveform. For the mean energy in the buncher an upper limit was chosen such that the mean traversal time was approximately 140 ns to avoid large energy spreads in the final bunch or acceptance losses on the incoming bunch, at the cost of a slightly higher time spread on implantation. This is the preferred situation for experiments where high statistics

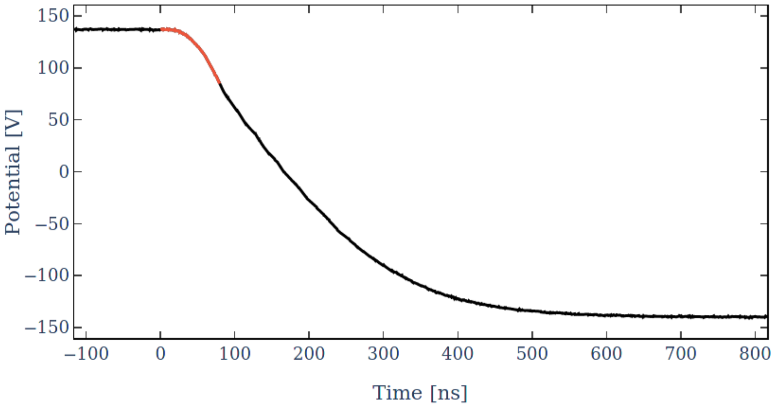

Figure 38: Bunching amplifier (Falco WMA-300) step function response connected to high voltage switch and second drift tube (see figure 32). The part of the waveform that can potentially be used for bunching is marked in red.

and a narrow velocity spread in the emitted positronium is preferred (see section 3.2) to avoid systematic effects due to Doppler shifts and a small time spread can be tolerated.

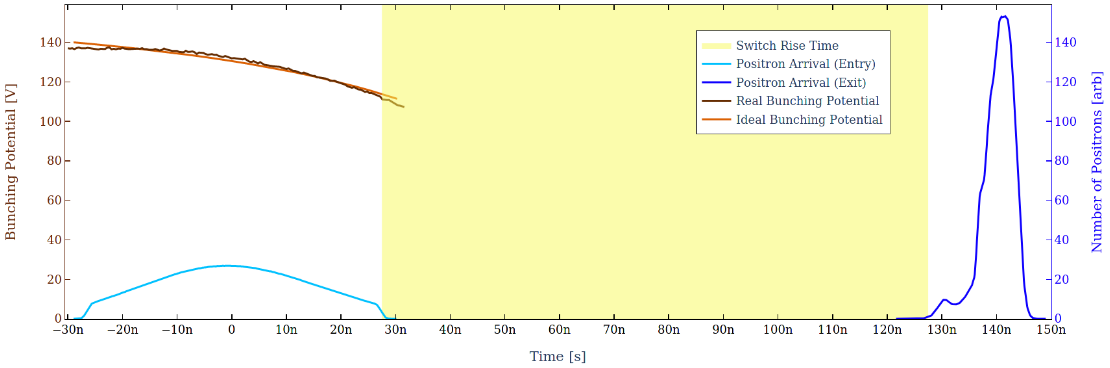

Figure 39: Monte-Carlo simulation of the bunching procedure using a limit of 140 ns mean traversal time of the second drift tube and fixed peak-to-peak bunching waveform. Both the incoming and the exiting time profiles of the positron bunch are shown (incoming – light blue, outgoing – dark blue). The specific part of the measured bunching waveform (see figure 38) used is shown in dark brown and the corresponding best fit of the ideal bunching waveform in light brown. The switching time of the high voltage switch is hinted at by the shaded yellow region.

Figure 39 shows the result of the Monte-Carlo simulation using these optimized values. The incoming time spread (FWHM) of 38.9 ns is compressed to 6.0 ns on the electrode outlet. Even employing a perfect bunching waveform would result in time spread of approximately 1.7 ns due to the initial energy spread of the bunch. The remaining spread is due to the mismatch of the real and ideal bunching waveforms. The best fit values found for the bunching parameters were 150.1 V for the elevation potential on the first drift tube and 30.0 eV for the mean energy inside the second drift tube. The ideal time delay between the bunching waveform and the mean arrival time of positrons on the second drift tube was found to be 22.0 ns. Losses are negligible for the incoming bunch and there is virtually no added energy spread on the outgoing positrons due to the switch rise time.

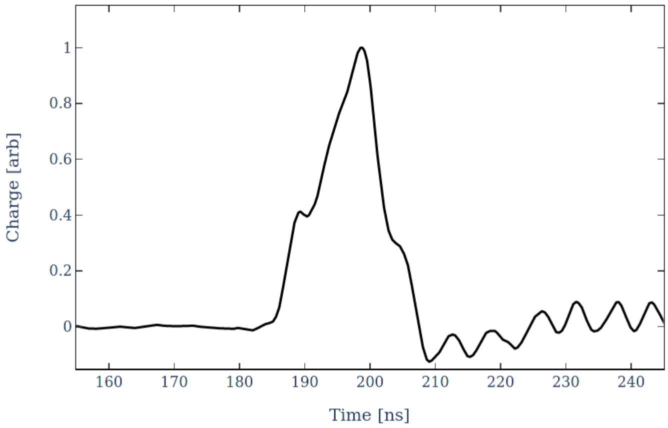

Figure 40: Measurement of time distribution of positrons incident on the target per bunch using backscattered positrons collected in an MCP. The offset of the time axis refers to the common DAQ trigger and is arbitrary here. The ringing of the signal evident starting at 210 ns is a common artefact of MCP signals and is not indicative of positrons arriving in this time frame.

The values found were used as initial parameters in the experimental setup. It was found that measured time spreads for bunches incident on the first and second drift tube (with and without elevation) matched the predictions from the Monte-Carlo to better than 10 % difference after careful tuning. The final time spread of the positrons incident on the target for an energy of 6 keV was measured using an MCP monitoring backscattered positrons, averaging over 2000 shots (see figure 40). The FWHM of the pulse was found to be 9.45 ns, and while this is slightly higher than predicted by simulation, it is in reasonably good agreement. The measured value includes the rise time of the detector on the order of 1 ns and time jitter in the drive electronics and DAQ. Furthermore, positrons backscattered from the target can have significantly lower energies than the original beam energy and therefore slightly enlarge the time spread.

To ascertain the lowest theoretically achievable time spread of the system, a slightly higher mean energy was allowed in the Monte-Carlo, corresponding to a traversal time of 120 ns. Additionally, a new variable was introduced allowing to scale the bunching waveform by a constant factor, which experimentally corresponds to reducing the voltage swing on the waveform generator supplying the bunching amplifier. The results of the simulation after the χ^2 minimization is shown in figure 41. The incoming time spread (FWHM) of 38.9 ns is compressed to 1.8 ns on the electrode outlet. The value is mainly

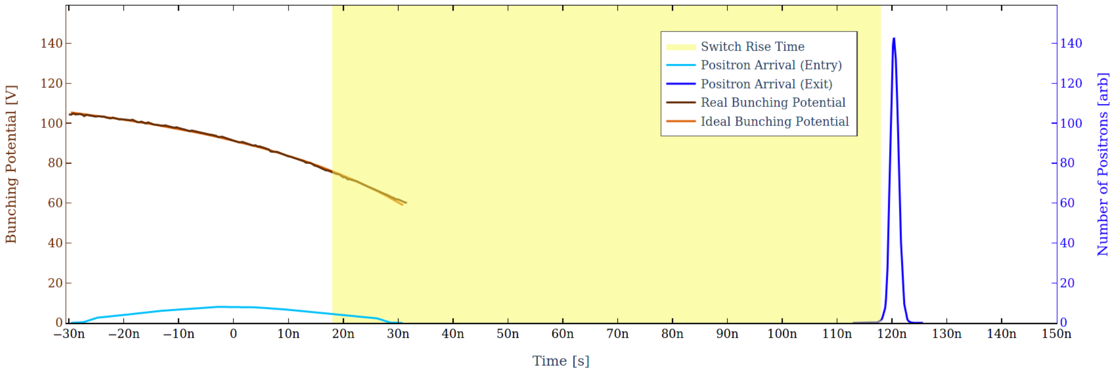

Figure 41: Monte-Carlo simulation of the bunching procedure using a limit of 120 ns mean traversal time of the second drift tube and variable peak-to-peak bunching waveform. Both the incoming and the exiting time profiles of the positron bunch are shown (incoming – light blue, outgoing – dark blue). The specific part of the measured bunching waveform (see figure 38) used is shown in dark brown and the corresponding best fit of the ideal bunching waveform in light brown. The switching time of the high voltage switch is hinted at by the shaded yellow region.

limited by the initial energy spread, which would produce approximately 1.1 ns spread with perfect bunching. The best fit values found for the bunching parameters were 120.6 V for the elevation potential on the first drift tube and 39.8 eV for the mean energy inside the second drift tube. The ideal time delay between the bunching waveform and the mean arrival time of positrons on the second drift tube was found to be 42.8 ns. The voltage swing of the bunching waveform was reduced by the factor 0.77. It was found that the reduced acceptance would lead to approximately 10 % losses of positrons, without significantly impacting the final energy profile.

3. Laser spectroscopy of Positronium

3.1. Overview

The pulsed slow positron beamline provides less than 10 ns (FWHM) wide bunches of approximately 2×10^4 positrons per second at a repetition rate of 1-10 Hz, which are re-accelerated to 1-6 keV and focused spatially via an electrostatic einzel lens to approximately $\sigma_d = 1.5\,\mathrm{mm}$ beam diameter (see section 2). The positrons impinge on a porous silica thin film target and form ortho-positronium, which is then emitted into vacuum, with a probability of 10-30 % depending on the implantation energy (see section 3.2).

The emitted positronium then interacts with one or multiple laser beams to be excited to higher energy levels or be photo-ionized. This chapter will focus specifically on the 1S → 2S → 20P two stage process, in addition to the photo-ionization of the 2S state. The excitation to the metastable 2S state (see section 3.3) is being driven by a modified Radiant-Dyes Pulsed Dye Amplifier (PDA), which is seeded at approximately 486 nm using a Toptica TA pro 972 nm diode laser and an included second harmonic generation stage. The Coumarin 102 dye [116] in the pulsed dye amplifier is pumped by the frequency-tripled output of a Spectra-Physics Quanta-Ray Lab 190 seeded Nd:YAG laser, which is synchronized to the pulsed positron beam (see section 2.4). Using a retro-reflecting mirror, this allows for two counter-propagating pulses of up to 20 mJ with a time spread of approximately 6 ns FWHM, centered approximately 3 mm away from the target. Power stabilization is achieved by varying the transmission on a polarizing beam-splitter using a Pockels cell. Alternatively, CW excitation is possible using a high finesse cavity locked to the same Toptica TA pro diode laser as used for pulsed excitation (see section 5.2).

Due to the relatively high photo-ionization cross-section (see section 3.3) a significant fraction of positronium atoms is ionized in the same laser by a third photon and the positron can be detected[24] either by detecting their annihilation in a scintillator [71] or by measuring them directly in an MCP placed approximately 4 cm from the target. To guide the positrons from photo-ionization to the detector a bias potential on the order of 100 V is usually applied to the target holder.

Two methods for detecting the surviving 2S positronium fraction have been developed. Using a laser far off-resonance of the 1S → 2S, with photon energies above the ionization threshold of approximately 1.7 eV, allows for delayed photo-ionization independent of the exciting laser. For this purpose, approximately 30 mJ of the frequency-doubled 532 nm output of the Nd:YAG, used for pumping the PDL-3 dye laser, and a delay line on the order of 10 ns were used. This ionizes the excited state positronium fraction with a probability close to unity.

Alternatively, the excited state positronium atoms can further be excited to a Rydberg state, using a modified Spectra-Physics Quanta-Ray PDL-3 pulsed dye laser pumped

---

[24] In principle, the electron from ionization can also be detected, but photo-electrons originating from scattered light are produced at virtually the same time with similar energies and prove to be an overwhelming background.

by the second harmonic of the Nd:YAG. The 20P state was selected as a compromise between polarizability, fluorescence lifetime and losses due to collisions with residual gas atoms in our vacuum environment (see section 3.3). Pulses at 736 nm of energies up to 10 mJ at approximately 7 ns FWHM were produced using Styryl 7 dye [117]. Since the transition 2S → 20P is a one-photon process, the first order Doppler shift due to the distribution of the emission angles had to be covered by enlarging the laser bandwidth to values on the order of 300 GHz (FWHM).

Positronium atoms in Rydberg states then ionize in the strong electric field between a grounded grid and the MCP front plate of approximately $4\,\mathrm{kV/cm}$ after a time of flight of a few hundred nanoseconds. This allows for the additional measurement of the velocity distribution of positronium atoms, which can be used to correct for the second order Doppler shift (see section 3.6). Further details about the detection system and mechanisms can be found in section 3.4.

The pulsed excitation experiment was conducted in two stages, a first measurement in the early months of 2018 and a second one in the fall of 2020. The first dataset[25] was acquired as a proof-of-principle without an absolute frequency standard or measurement of the laser chirp (see section 3.3). For the second run a Menlo FC1500-250-WG optical frequency comb and online laser chirp measurements were added to accurately determine the absolute laser frequency. Additionally, the target and detector systems were redesigned for the second run (see sections 3.2 and 3.4 for details) to reduce the background due to backscattered positrons.

It was found that the signal-to-noise ratio for the field-ionization signal of Rydberg states was significantly worse for run 2 (see section 3.6). Since this detection channel provides time-of-flight data in addition to pure line-shape information (see section 3.4), it was decided to take only direct photo-ionization and Rydberg excitation data to increase statistics for these events. Therefore, delayed photo-ionization data is only available for run 1.

3.2. Positronium formation

A wide variety of materials are known to produce positronium and have been used in experimental studies before, among them various gases, metals, semiconductors and insulators. They each offer different advantages and drawbacks and have to be selected according to experimental requirements [57]. For laser spectroscopy experiments the most widely used type of converters are thin silica films, which are produced by spin coating a glass substrate with a silica precursor and a surfactant, which is removed while calcinating the sample at 450 °C, leaving a mesoporous silica structure [119].

When positrons are implanted on these targets with kinetic energies on the order of a few keV, they can either be backscattered or penetrate the bulk and stop stochastically at a depth on the order of a few hundred nanometer. It was found that the probability distribution of implantation depth in most materials can be empirically described by the

---

[25] Results of this run were partly reported previously in references [72] and [118].

Makhovian distribution [120] which has the form

$$P\left(z,E\right) = \frac{m \cdot z^{m-1}}{{z_0}^{m}} \cdot e^{-\left({}^{z}\!/_{z_o}\right)^{m}} \tag{68}$$

with

$$z_0 = \frac{A}{\rho \cdot \Gamma\left(1 + {}^{1}\!/_{m}\right)} E^{\nu} \tag{69}$$

where E is the implantation energy given in keV, Γ is the gamma function and the parameters A, m and ν can be determined experimentally [121] or using Monte-Carlo simulation [120].

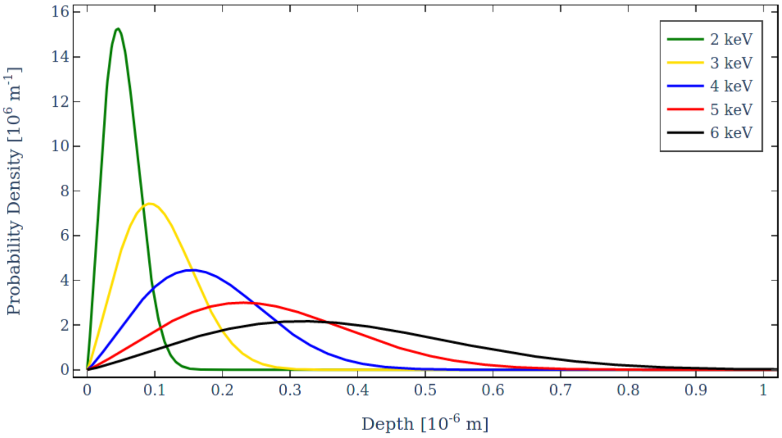

Figure 42: Probability density of implantation depth of positrons on F127-TEOS targets for several impact energies given by the Makhovian distribution using parameters from Dryzek et al. [122] and $\rho = 1.5\,{}^{\mathrm{g}}\!/_{\mathrm{cm}^3}$ [123].

Given the implantation profile in equation 68, the mean implantation depth is given by

$$\overline{z} = \frac{A}{\rho} E^{\nu} \tag{70}$$

or equivalently the median depth by

$$z_{1/2} = \frac{A_{1/2}}{\rho} E^{\nu} \tag{71}$$

where the respective A parameters are related by

$$A = A_{1/2} \cdot \frac{\Gamma\left(1 + {}^{1}\!/_{m}\right)}{\ln 2^{1/m}} \quad . \tag{72}$$

The most recent Monte-Carlo results for SiO_2 [122] were found to be

$$A_{1/2} = 22.2\,\mathrm{nm}\,{}^{\mathrm{g}}\!/_{\mathrm{cm}^3}\,\mathrm{keV}^{-\nu} \quad , \quad m = 2.19 \quad \text{and} \quad \nu = 1.774 \quad . \tag{73}$$

Using these parameters and the density $\rho = 1.5\,\mathrm{g/cm^3}$ for the specific type of samples (F127-TEOS) [123] in use for the experiments presented here, the probability density profiles of implantation are plotted for several energies in figure 42. Clearly, if deeper implantation is desired, which is generally the case to allow for sufficient time for the cooling of the produced positronium (see below in this section), a significantly broader implantation profile has to be accepted and there is always a significant fraction of positrons, which stop close to the surface. This is also evident from figure 43 which shows the mean implantation depth and width in terms of the standard deviation of the distribution as a function of the positron energy.

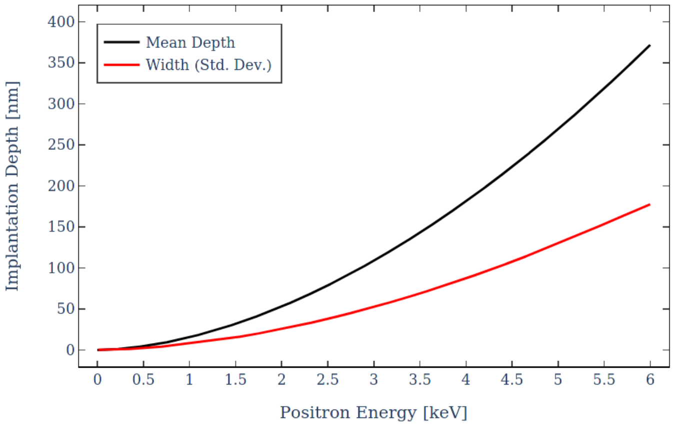

Figure 43: Mean value and width (standard deviation) of the implantation depth distribution of positrons on F127-TEOS target given by the Makhovian distribution using parameters from Dryzek et al. [122] and $\rho = 1.5\,\mathrm{g/cm^3}$ [123].

To reduce the amount of backscattered positrons on the detection MCP it is advantageous to tilt the target and implant positrons at an angle (see section 3.4). To implant at the same depth[26], a correspondingly higher incident positron energy needs to be used. Equation 70 can readily be extended to include the angle of incidence α:

$$\overline{z}\,(\alpha) = \frac{A}{\rho} E^{\nu} \cos\alpha \quad . \tag{74}$$

If one requires $\overline{z}\,(\alpha) = \overline{z}\,(0)$ it follows that

$$E_{\alpha} = \frac{E_0}{\sqrt[\nu]{\cos\alpha}} \tag{75}$$

which yields

$$E_{45^\circ} = 1.216\,E_0 \tag{76}$$

for the special case $\alpha = 45^\circ$. Therefore, tilting the target by 45° and increasing the implantation energy by 21.6 % is equivalent[27] for implantation purposes, which allows

---

[26] Depth in this context means the perpendicular distance to the surface of the target.

[27] Assuming there is no uncertainty on the energy scaling parameter ν and the implantation profile does not change significantly with the angle of incidence.

to compare measurements with a different angle of incidence. However, the spatial size of the beam spot will be elongated in the plane that is tilted, which needs to be taken into account.

When positrons stop in the bulk of the insulator they either directly annihilate or form positronium within a few picoseconds. They are mainly formed[28] in the radiation “spur” left in the wake of the positron slowing down in the material, which provides the free electrons needed [125]. Positronium will be formed equally likely in all available spin states according to equations 1 to 4, therefore 25 % pPs and 75 % oPs. The lifetime of pPs in the bulk is so short as to be indistinguishable from direct annihilation, so only oPs is relevant for the processes described hereafter.

The positronium atoms rapidly thermalize and diffuse to the large internal surface area given by the porous structure of the target. The emission into the pores is then governed by the work function of positronium for the bulk given by

$$\phi_{Ps} = -\mu_{Ps} + E_{bulk} - E_B \tag{77}$$

where μ_{Ps} is the chemical potential, E_{bulk} and E_B are the binding energy of positronium inside the bulk and in vacuum, respectively. For SiO_2 this was measured to be approximately $-1\,\mathrm{eV}$ [126], where $E_B = 6.8\,\mathrm{eV}$ and $E_{bulk} < 6.8\,\mathrm{eV}$.

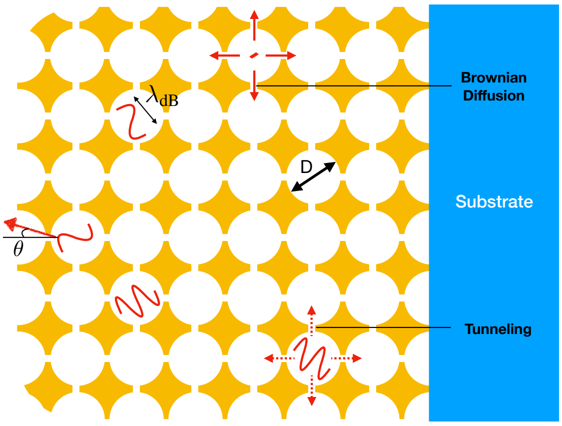

Figure 44: Positronium diffusion processes in mesoporous silica films. Hot positronium will diffuse classically and cool down rapidly due to collisions with the pore walls. When the thermal de Broglie wavelength becomes comparable with the pore size positronium is quantum confined and will diffuse via tunnelling. Emission from these films follows an angular distribution of the ideal diffuse emitter. (*source:* [127])

Positronium atoms ejected into the pore network (see figure 44) with 1 eV will diffuse through the material and rapidly cool down due to collisions with the pore walls [128].

---

[28] There is another mechanism by which positronium can be formed in the bulk of insulators, known as Ore gap formation [124], which plays virtually no role for implantations in the keV region.

This classical process will only continue as long as the de Broglie wavelength

$$\lambda_{dB} = \frac{h}{\sqrt{4\pi m_e k_B T}} \approx \sqrt{\frac{0.24\,\mathrm{eV}}{E_{\mathrm{kin}}}} \cdot 1\,\mathrm{nm} \tag{78}$$

is significantly smaller than the pore size of approximately 4 nm [123]. As positronium is approaching room temperature, the de Broglie wavelength becomes comparable to the pore size and the atom is confined quantum mechanically. Classical diffusion is not possible anymore and the atom will move from pore to pore via quantum tunneling instead, which implies a significantly smaller diffusion coefficient [129]. Experimental studies showed that the cooling from the classical to the quantum regime is completed within 5 ns and that the time for positronium to diffuse out of the sample depends linearly on implantation energy with approximately 3 ns/keV [130]. For the case of implantation at 45° angle of incidence this translates to approximately 2.5 ns/keV as per equation 76.

Due to the quantum nature of positronium in the pores, the minimum energy of positronium cooling down in the network is not given by the thermal limit (approximately 30 meV for room temperature), but the ground state energy of the particle confined to the pore. For the simple model of a particle of mass $2m_e$ in an infinite spherical well potential, the ground state energy is given by [131]:

$$E_0 = \frac{h^2}{4 m_e d^2} \approx \left(\frac{27.4\,\mathrm{nm}}{d}\right)^2 \cdot 1\,\mathrm{meV} \tag{79}$$

which yields $E_0 = 47\,\mathrm{meV}$ for $d = 4\,\mathrm{nm}$ pore size in good agreement with measured values [123, 129, 130] for implantation energies above 4 keV.

However, positronium emitted from these porous targets is not purely mono-energetic. For example, positronium which is formed close to the surface due to positrons stopping early, can be emitted epithermally before it cools down to the ground state energy of the pore. A distribution in pore sizes or positronium interacting on the target surface might also lead to smaller emission energies than the calculated ground state limit. In fact, while the exact velocity distribution is unknown, earlier experiments using the same type of target found that it could be well represented by a Maxwell-Boltzmann distribution with $T = 900\,\mathrm{K}$ for 3 keV implantation energy [130, 132]. Similarly, we found excellent agreement with a Maxwell-Boltzmann distribution for 550-700 K at implantation energies of 4-5 keV (see section 3.6). The most probable velocity of the distribution scales roughly like one would expect from earlier measurements of the mean emission energy [123, 129, 130].

It is usually assumed that the angular distribution of positronium from these films follows Lambert's law for ideal diffuse emitters, which is reasonably well justified by data [129]. The angular probability density for emission is then given by

$$\mathrm{P}\left(\theta\right) \mathrm{d}\theta \, \mathrm{d}\phi = \frac{\cos\theta}{2\pi} \, \mathrm{d}\theta \, \mathrm{d}\phi \tag{80}$$

where θ is the angle between the target surface plane and the emission direction and ϕ is the angle relative to an arbitrary plane perpendicular to the target.

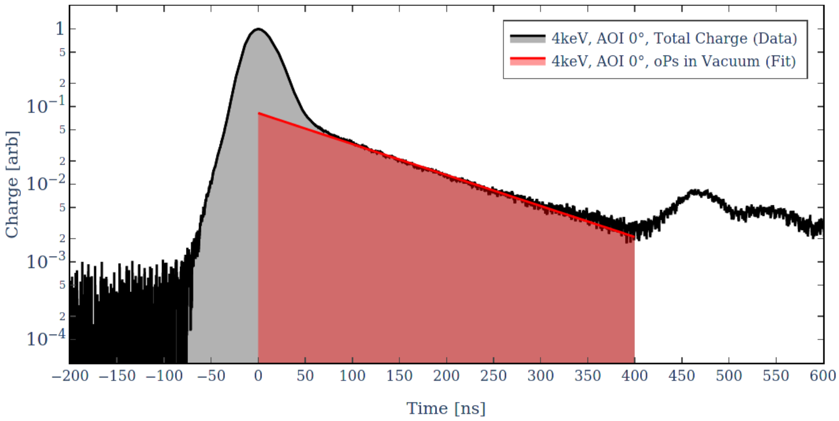

Figure 45: SSPALS spectrum obtained during run 1 using 4 keV implantation energy at 0° angle of incidence. The time axis is referenced to the peak position and the height is normalized to unity. The data is shown in black and the shaded region (from −100 ns to +400 ns) corresponds to the total charge. Shown in red is the best fit for the oPs component of the spectrum fitted in the window from +100 ns to +400 ns. The red shaded region from 0 ns to +400 ns serves as an estimator of the charge deposited due to oPs decays. Note that the implantation time spread for this run was significantly larger, due to issues with an earlier version of the bunching system. Ion feedback afterpulses [133] of the PMT are evident in the spectrum above approximately 400 ns.

The conversion efficiency of impinging positrons to oPs emitted into vacuum, depends on the implantation depth or conversely the positron energy. At 4-6 keV the conversion efficiency for these types of targets is expected to be approximately 20 % [123]. Using this value, the expected rate of oPs emitted into vacuum per second can then be calculated to be

$$N_{oPs} = N^t_{e+} \cdot \varepsilon_t \cdot \varepsilon_e \cdot \varepsilon_b \cdot \varepsilon_c \approx 4.2 \times 10^3 \, {}^1\!/\!_\mathrm{s} \tag{81}$$

where N^t_{e+} is the rate of positrons available for trapping (see equation 55), ε_t is the trapping efficiency (see equation 58), $\varepsilon_e = 0.9$ and $\varepsilon_b = 1.0$ is the elevator and buncher acceptance respectively (see section 2.4), and $\varepsilon_c \approx 0.2$ is the positronium conversion efficiency.

The fraction of oPs emitted into vacuum can be measured by positron annihilation lifetime spectroscopy (PALS). This technique was pioneered by Deutsch for the first experimental proof of formation of positronium in gases (see section 1.1.1) and is an excellent tool to study properties of mesoporous silica films [134]. However, this requires tagging individual positrons and measuring their decay products, which is not possible for pulsed beams where many thousands of positrons arrive at the target on the nanosecond timescale. In this case, the pulsed equivalent, single-shot positron annihilation lifetime spectroscopy (SSPALS) [135] can be used. To this end, a monolithic $PbWO_4$ scintillator, coupled to a PMT, is placed next to the experimental chamber and measures annihilation time spectra of incoming positron bunches. After averaging many pulses and subtracting

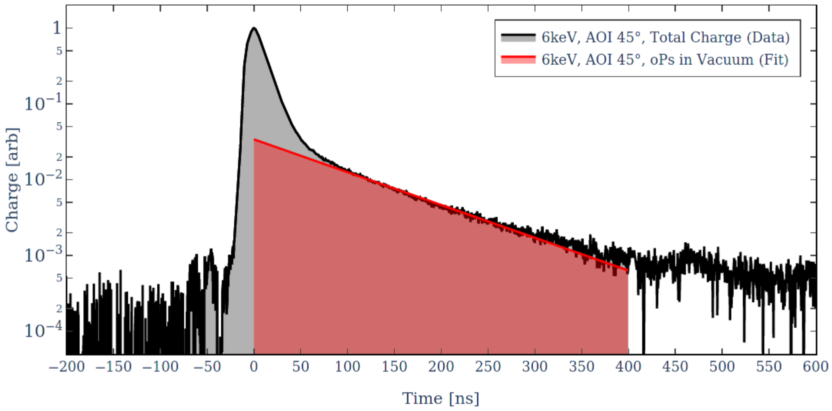

Figure 46: SSPALS spectrum obtained during run 2 using 6 keV implantation energy at 45° angle of incidence, which corresponds roughly to 5 keV when implanting perpendicular to the target. The time axis is referenced to the peak position and the height is normalized to unity. The data is shown in black and the shaded region (from −100 ns to +400 ns) corresponds to the total charge. Shown in red is the best fit for the oPs component of the spectrum fitted in the window from +100 ns to +400 ns. The red shaded region from 0 ns to +400 ns serves as an estimator of the charge deposited due to oPs decays.

background (mainly electrical switching noise) time spectra similar to PALS can be obtained.

This technique is used during measurements to keep track of the conversion efficiency to oPs. A sample SSPALS spectrum for both 1S-2S measurement runs each can be found in figures 45 and 46. While the absolute conversion efficiency can not be directly determined using these spectra, it is possible to extract values which are good estimators. For this work we employed a modified version[29] of the common delayed fraction approach [135], using

$$f = \frac{\int_0^b Q_{\mathrm{oPs}}(t)\,\mathrm{d}t}{\int_a^b Q(t)\,\mathrm{d}t} \tag{82}$$

where $Q(t)$ is the measured charge and $Q_{\mathrm{oPs}}(t)$ is the fit of the exponential long lifetime component representing oPs in vacuum (taken from 100 ns to 400 ns). The integral in the denominator is proportional to the total charge deposited by the positron bunch and the limits are chosen accordingly. The value $a = -100$ ns is taken conservatively to cover most of the incoming positron pulse and the value $b = 400$ ns is limited by ion feedback afterpulses in the PMT [133].

The first run was conducted using positrons with 4 keV implantation energy and 0° angle of incidence and the resulting SSPALS spectrum can be found in figure 45. The modified delayed fraction was found to be 18.7 %, which is in good agreement with

---

[29] The modification was introduced to reduce the sensitivity on changes in the time spread of the positron pulses. For short pulses the value agrees to within a few percent with the standard approach.

the expected oPs conversion efficiency. Similarly, the modified delayed fraction for the second run was found to be 13.9 %, where the implantation energy was increased to 6 keV at 45° angle of incidence, which would correspond to approximately 5 keV at 0° angle of incidence. The lower value is partly explained due to the higher implantation energy and partly due to the placement of the SSPALS scintillator further upstream (see discussion below).

It should be noted that the solid angle coverage of oPs is time-dependent due to its fast velocity of approximately 10^5 m/s and the placement of the scintillator. This is evidenced by the decay time of the fits of approximately 109 ns (figure 45) and 100 ns (figure 45), while oPs decays with 142 ns in vacuum (see section 1.1.2). The value obtained with equation 82 is therefore to be understood as a lower limit on the conversion efficiency.

3.3. Laser Excitation

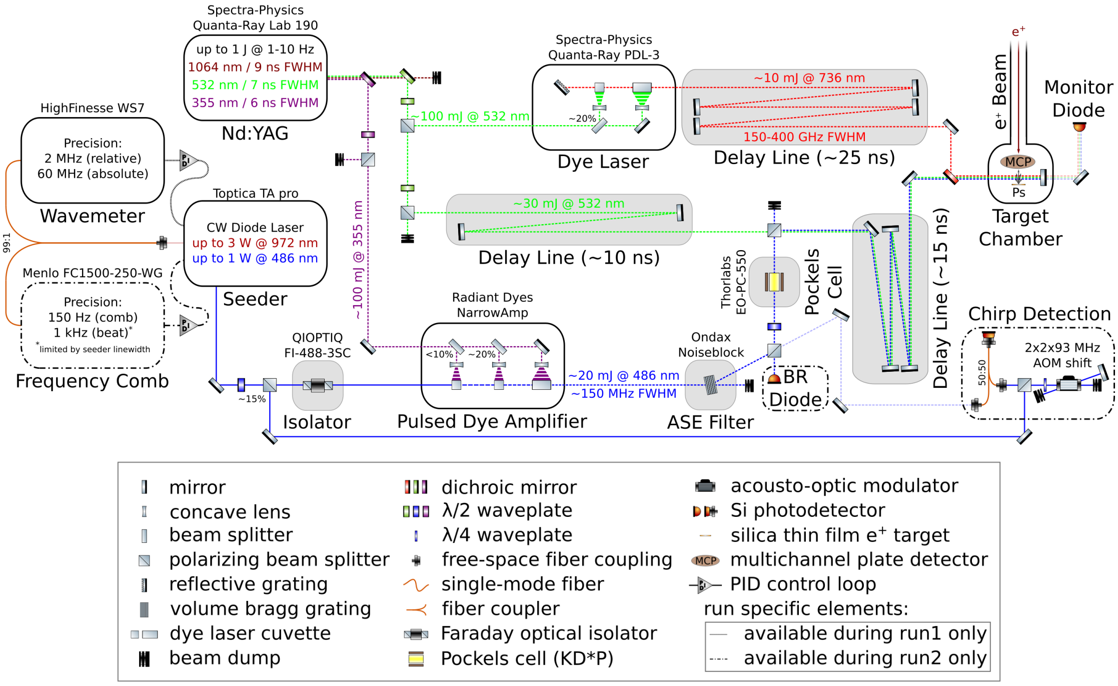

Figure 47: Schematic overview of the 1S-2S laser excitation system for both runs. Pulsed lasers are denoted as dotted and CW lasers as full lines. Not all elements are shown, e.g. pulse shaping optics, shutters etc. Positions, orientations and scales are arbitrary. A larger version of this figure is located in appendix A.

A schematic overview of the laser system employed to measure the 1S-2S transition can be found in figure 47. Three separate laser beams at different wavelengths (486 nm, 532 nm, and 736 nm) are generated, combined and used to excite and/or photo-ionize positronium atoms, which are produced in the experimental vacuum chamber (see section 3.2). As a source of pulsed light, a Spectra-Physics Quanta-Ray Lab 190 Nd:YAG solid state laser is used. This laser is capable of producing diffraction-limited pulses of up to 1 J at the fundamental wavelength of 1064 nm with a pulse length of approximately 9 ns (FWHM), achieved using a Q-switched Gaussian coupled resonator [136]. It is also equipped with an optional injection seeding [137] module reducing the line-width from approximately 30 GHz to below 90 MHz, which is required to produce narrow bandwidth output in subsequent dye laser stages. A temperature stabilized potassium dideuterium phosphate (KD*P) crystal is used for the generation of higher harmonics. This allows for the generation of 532 nm (second harmonic) of up to 500 mJ and 355 nm (third harmonic) of up to 250 mJ. This process reduces the pulse length by approximately 2 ns and 3 ns, respectively. Proper tuning of the polarization and crystal angles allows for the simultaneous generation of both higher harmonics at pulse energies in excess of 150 mJ each, which is used to directly photo-ionize positronium and to pump one of the two dye laser stages.

3.3.1. 1S-2S excitation (486 nm)

The 1S-2S transition frequency is approximately 1.2336×10^{15} Hz (see equation 25) which means that two counter-propagating photons of approximately 486 nm are required for Doppler free two-photon spectroscopy. The pulsed light at this wavelength is generated by a modified[30] Radiant Dyes NarrowAmp pulsed dye amplifier (PDA). In this device dye is circulated through three quartz cuvettes, which are pumped by simultaneously focusing the 355 nm output of the Nd:YAG laser into the cells, while expanding the beam to cover the length of the cells in the perpendicular axis.

The dye employed is Coumarin 102 [116] dissolved in ethanol, since both the absorption and fluorescence fit the application well (see figure 48). It is mixed to a concentration of 0.4 g/l and 0.15 g/l for the 20 mm and 40 mm dye cells respectively. While the conversion efficiency of this dye is excellent for this wavelength region (>20 % in our three stage setup) it has the significant drawback of rapid degradation. Photo-oxidation leads to the buildup of a reaction product of the coumarin dye that strongly absorbs around 486 nm. This process can be slowed by adding DABCO (1,4-Diazabicyclo[2.2.2]octan) at a concentration of 1-2 g/l [139]. It was found that using 100 mJ at 10 Hz repetition rate for pumping, the half-life of the dye mixture was approximately 2-3 days, even including the appropriate amount of DABCO. Therefore, the reservoirs of the circulator were enlarged by around a factor 6 and the repetition rate was reduced to 2 Hz. This increased the dye lifetime to 1-2 months, without significantly impacting the average rate of positrons provided by the trap (see section 2.3).

Seeding of the PDA is achieved using a frequency stabilized (see section 3.3.4) Toptica TA pro CW diode laser. It consists of a Fabry-Perot laser diode emitting around 972 nm and a piezo-tunable grating for frequency selection, which is amplified by a tapered amplifier up to 3 W output power. This is fed into a piezo controlled ring cavity containing

---

[30] The seed path was rebuilt using custom focal length optics and synthetic diamond pinholes mounted on 3-axis kinematic mounts. This modification allowed for significantly higher peak output powers and lower ASE ratios. Furthermore, the dye circulators were expanded by two 5 l reservoirs, from a total of approximately 1.6 l volume, which significantly improved the dye lifetime.

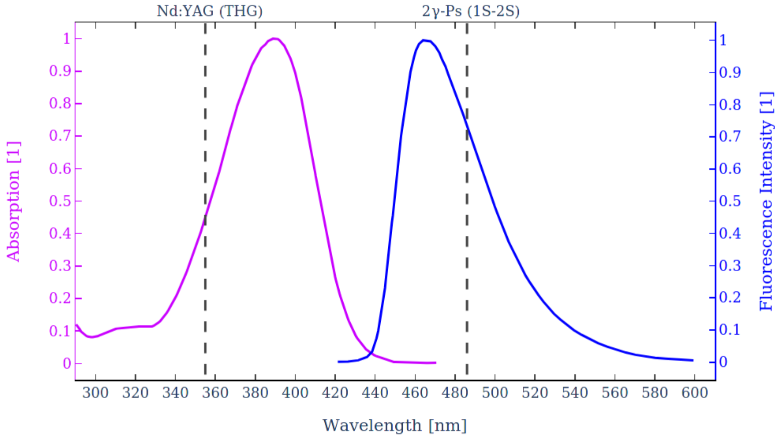

Figure 48: Absorption and Fluorescence Spectrum for Coumarin 102 dissolved in absolute ethanol (data from [138]). Both spectra are normalized to unity and the dotted lines show the pumping wavelength (355 nm) and the seeded wavelength (486 nm).

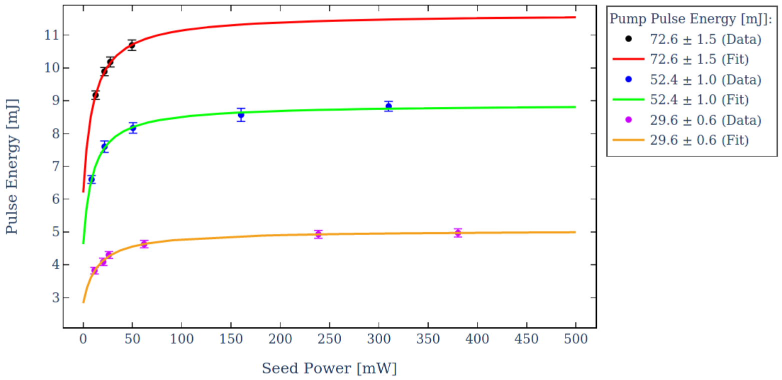

Figure 49: PDA output pulse energy for different pump and seed powers including best fits (data from [127]). This was taken with the coumarin 102 dye in a significantly degraded state and does therefore not represent the maximum output power of the PDA.

a lithium triborate (LBO) crystal to generate up to 1 W of 486 nm light with a line-width on the order of 200 kHz. After passing an optical isolator to protect the SHG cavity, the beam is focused with a long focal length lens through a 150 μm pinhole approximately 5 cm after the first dye cell. This allows for efficient seeding, while filtering out most unwanted amplified spontaneous emission (ASE), since there is virtually no seeded light generated outside of the CW beam path. The amplification and filtering in the second stage is completely analogous, with the only difference being a slightly larger pinhole diameter of 250 μm. Then the beam is collimated and amplified in the third stage without an additional pinhole.

Figure 49 shows the resulting output pulse energies for different pump pulse energies and seed powers. It was found that a good fit for the output pulse energy was given by the function[31]

$$E(P) = E_0 + \frac{E_{\mathrm{max}} - E_0}{1 + aP^{-1}} \tag{83}$$

where P is the seed power, E_0 is the PDA output without seeding given only by ASE, E_{max} is the PDA output with fully saturated seeding and a is an empirical saturation parameter. For efficient seeding, approximately 100-200 mW of CW power are required and the PDA output pulse energy $E(P)$ then roughly scales linearly with the pump pulse energy, showing no significant saturation in this regime.

Even for high seed powers the fraction of ASE is on the order of a few percent, centered around approximately 465 nm (see figure 48). While the FWHM of the gain profile is on the order of 50 nm, the ASE will not contribute significantly to the excitation of 2S states, but will photo-ionize those state quite efficiently. To avoid these losses, a volume Bragg grating (Ondax Noiseblock) is used as an ASE filter of approximately 0.1 nm bandwidth and diffraction efficiency of >90 %.

The PDA needs to be isolated from the pulse returning from the retro-reflection mirror in the experimental chamber. We found[32] that commonly used heavy flint glass in Faraday rotators (e.g. in a QIOPTIQ FI-488-3SC) exhibit thermally induced absorption around 486 nm for high incident power densities and is therefore not suitable for beam isolation. Instead, a Pockels cell can be used, where applying an appropriate voltage pulse rotates the polarization of the incoming pulse by 90°, while the returning pulse is unaffected by it. Due to the additional $\lambda/2$ waveplate, the returning pulse is dumped using a polarizing beamsplitter cube (see figure 47).

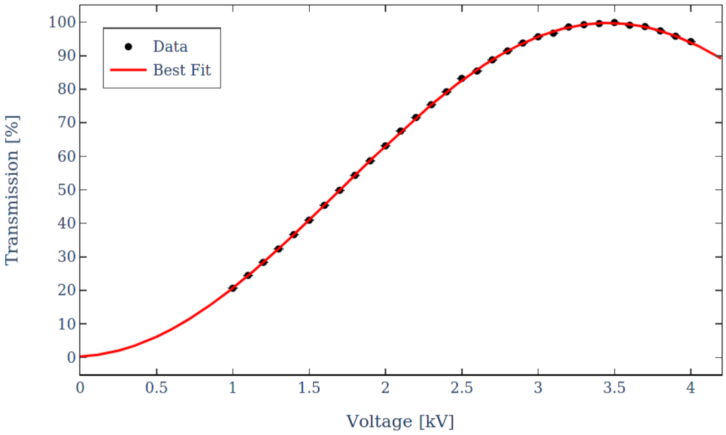

Figure 50: Transmission of the beamsplitter after the Pockels cell (see figure 47) for different applied voltages (black) including best fit for the transmission function given in equation 84 (red).

---

[31] Note that this form is not directly motivated by a specific model.

[32] To our knowledge this has not been reported in the literature to date.

Furthermore, the addition of the Pockels cell allows to vary the fraction of the blue pulse transmitted to the chamber by changing the peak-to-peak value of the voltage supplied to its electrodes. Since the polarization change depends linearly on the applied voltage, the transmission of the polarizing beam splitter after the Pockels cell follows

$$T\left(V_{\mathrm{pp}}\right) = 0.5 \cdot \left[1 + \mathrm{DOP} \cdot \sin\left(\frac{V_{\mathrm{pp}}}{V_{\mathrm{HW}}}\pi - \frac{\pi}{2} + d\right)\right] \quad , \tag{84}$$

where V_{pp} is the supplied voltage, V_{HW} is the Half-Wave Voltage, DOP is the degree of polarization of the light exiting the Pockels cell and d is the initial polarization phase. A measurement of the transmission function, taken during run 1, can be found in figure 50. The values[33] for the best fit are $V_{\mathrm{HW}} = (3505 \pm 15)$ V, DOP $= (99.52 \pm 0.76)$ %, and $d = 0.045 \pm 0.011$ (in radians). Continuously measuring the power transmitted to the experimental chamber allows for the long-term stabilization of the average pulse energy (e.g. to counter dye degradation) to better than 1 % and to scan over a wide range of pulse energies without changing the optical setup.

To efficiently suppress the back-reflection from the experimental chamber, the switch needs to ramp down close to 0 V before it arrives at the Pockels cell. To account for the fall time and possible jitter in the build-up time of the Nd:YAG pulse, a delay between incoming and returning pulse of approximately 25 ns is required. While for run 1 this was provided by the spatial separation of the laser generation and experimental chamber alone, a delay line of approximately 15 ns was added for run 2. This allows for extinction ratios on the order of 100:1, which is sufficient to protect optical elements of the PDA from damage induced by the retro-reflected pulse. To ensure proper alignment of the back-reflection, a diode (see BR diode in figure 47) with appropriate filter was added to monitor the reflected power for run 2. Due to the 7 mm beamsplitter used, this allows to limit the maximal beam misalignment between the incoming and retro-reflected beam axes to below 1.4 mrad for the beam path length of approximately 5 m.

3.3.2. 2S delayed photo-ionization (532 nm)

The ionization threshold of the 2S state is given to first order by equation 21:

$${E_I}^{2S} = -E_2 = \frac{3\alpha^2 m_e c^2}{8} \approx 1.7\,\mathrm{eV} \quad , \tag{85}$$

which means that single photons with a wavelength shorter than approximately 729 nm can be used to photo-ionize positronium in the 2S state. This is a quite efficient process compared to inducing the 1S-2S transition, since the ionization cross-section is around a factor 3 higher than the excitation cross-section (assuming the same laser power density) as can be seen in equations 105 and 103. A few tens of mJ for beam diameters on the order of a few mm provide ionization probabilities close to unity.

---

[33] Note that the voltages here correspond to the supply voltages on the HV switch and not the potential between the electrodes, which is likely lower. For this Thorlabs EO-PC-550 Pockels cell the Half-Wave voltage is specified to be approximately 3020 V.

While direct photo-ionization in the exciting laser (see section 3.3.1) can be used for detection, there is significant broadening and shift due to the AC-Stark effect (see section 3.5). Furthermore, this does not allow for the determination of surviving 2S states, since excitation and ionization are inextricably linked. To avoid these issues, part of the output at 532 nm of the Nd:YAG was used to photo-ionize, spatially and temporally separated from the laser driving the excitation. Since only up to approximately 100 mJ are used for pumping the Quanta-Ray PDL-3 dye laser, as described in the next section, there is sufficient power available.

After splitting off the appropriate fraction of the incoming laser pulse (approximately 30 mJ), the beam then passes a delay line of 10 ns, before being combined with the blue laser on a polarizing beamsplitter cube. It follows the same path as the 486 nm pulse through a 15 ns delay line and to the chamber. There it is retro-reflected to the same path, but contrary to the lasers driving the transition it is not required to exactly overlap. Therefore the alignment is slightly offset, such that the returning pulse is guided to a beam-dump before it reaches the Nd:YAG.

3.3.3. 2S-20P excitation (736 nm)

As an alternative to photo-ionization, the surviving 2S states can be excited to nP Rydberg states by efficient one-photon excitation. Since the annihilation lifetime depends on the overlap of the wavefunctions of positron and electron, decays of nP states are dominated by radiative transitions to lower lying states. Therefore, these states are quite long lived (see figure 7), which makes them suitable to be detected after flying several hundreds of nanoseconds (see section 3.4).

However, a competing loss mechanism for detecting Rydberg states are collisions on background gas atoms. Assuming the positronium atom is lost upon collision with a background gas atom, the probability for it to reach the MCP is

$$P_{\text{col}}(l) = e^{-l/\lambda} \tag{86}$$

where l is the length travelled by positronium and λ is the mean free path

$$\lambda = \frac{k_B T}{p\,\sigma_{\text{col}}} \tag{87}$$

with k_B being the Boltzmann constant, $T \approx 300\,\text{K}$ is the temperature and $p \approx 10^{-8}\,\text{mbar}$ the pressure of the background gas and σ_{col} the collision cross-section. Note that the usual relative velocity correction of $\sqrt{2}$ in the denominator of the mean free path should not be included, since background gas atoms appear essentially stationary for positronium. This can be understood by the fact that the velocity of oPs emitted from the target is on the order of $10^5\,\text{m/s}$, which is significantly larger than the average velocity of background gas atoms of approximately $500\,\text{m/s}$.

The cross-section σ_{col} can be estimated by assuming elastic collisions of two particle species with different radii, such that

$$\sigma_{\text{col}} = \pi\left(r_{gas} + r_{Ps}\right)^2 \tag{88}$$

where r_{Ps} is the radius of positronium and r_{gas} is the average radius of background gas molecules. The main gas species in the chamber is nitrogen reaching the chamber from the trap, for which the kinetic radius is $r_{\mathrm{N_2}} = 1.8 \times 10^{-10}\,\mathrm{m}$ [140]. For positronium the RMS radius

$$r_{\mathrm{RMS}} = \sqrt{\langle r^2 \rangle} = 2a_0\,\mathrm{n}\sqrt{\frac{5\mathrm{n}^2 - 3\mathrm{L}(\mathrm{L}+1) + 1}{2}} \quad , \tag{89}$$

which corresponds to the RMS radius of hydrogen [141] scaled with the reduced mass of positronium, is an appropriate approximation. We therefore find

$$\sigma_{\mathrm{col}}^{\mathrm{nP}}(\mathrm{n}) \approx \left(3.19 + 2.96\,\mathrm{n}\sqrt{\mathrm{n}^2 - 1}\right)^2 \times 10^{-20}\,\mathrm{m}^2 \tag{90}$$

for P states with arbitrary n.

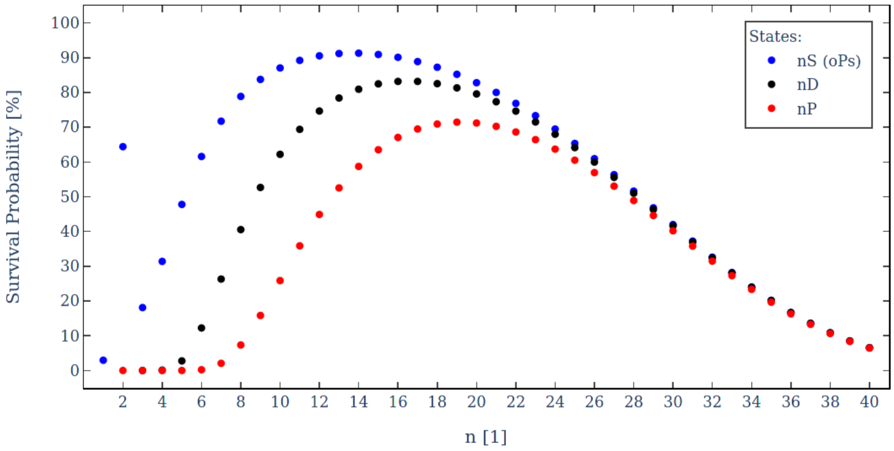

Figure 51: Survival probability of positronium for different principal quantum numbers in S, P and D states travelling 5 cm at a velocity of $10^5\,\mathrm{m/s}$ in vacuum with a background gas pressure of 10^{-8} mbar.

Combining the losses due to collisions with the decay probability yields

$$P^{\mathrm{nP}}(l,\mathrm{n}) = P_{\mathrm{col}}^{\mathrm{nP}}(l,\mathrm{n}) \cdot e^{-\frac{l}{v_{\mathrm{Ps}}\,\tau_{\mathrm{nP}}}} \tag{91}$$

for the probability of an atom with velocity v and lifetime τ_{nP} (see section 1.2.2) to reach the detector in the same state, after flying a distance of l. Figure 51 shows the survival probability for a pressure of $p = 10^{-8}$ mbar, velocity of $v_{\mathrm{Ps}} = 10^5\,\mathrm{m/s}$ and distance $l = 5$ cm, which corresponds to the approximate experimental parameters of both runs. The highest rate is therefore expected for n in the range from 18-20.

The final consideration for which specific n to use is the efficiency of field ionization on the detector. The field strengths achieved on the detector assembly are on the order of 2-4 kV/cm. For these field strengths, the probability of ionization is close to unity for $\mathrm{n} > 19$ (see section 3.4). Therefore, the 20P state was chosen for the Rydberg detection scheme. The transition frequency from the 2S to the 20P state is (see equation 25) $\nu_{2S-20P} = 4.0711 \times 10^{14}$ Hz or 736.39 nm in terms of wavelength.

Due to the large angular distribution of the oPs emission from the target (see section 3.2) the different paths have large Doppler shifts, since the transition is a single photon transition. The shift is given by

$$\Delta\nu = \nu_{2S-20P} \frac{v_{Ps}}{c} \cos\alpha \quad , \tag{92}$$

where α is the angle relative to the laser propagation axis, such that a path perpendicular to the target (the most probable emission) has $\alpha \approx 90°$. For the detector geometry (see section 3.4) in run 1 the angles covered by the MCP were approximately $90° \pm 30°$, while for run two it was somewhat smaller with $90° \pm 17°$ due to the smaller detector. Using equation 92 this amounts to a Doppler profile of 140 GHz (run 1) and 80 GHz (run 2), for $v_{Ps} = 10^5\,\mathrm{m/s}$.

Pulsed light to drive the 2S-20P transition is supplied by a modified Quanta-Ray PDL-3 dye laser, which is pumped by approximately 100 mJ of the SHG output of the Nd:YAG at 532 nm. Dye is circulated through 2 cuvettes (Oscillator and Amplifier) which are pumped with approximately 1:5 ratio. Frequency selection is achieved by retro-reflecting a narrow spectral region of the ASE of the oscillator on a grating. Additionally, a partially reflective output coupler builds a low finesse cavity around the first cell to seed the amplifier. In stock configuration, a prism system is used to illuminate the whole grating, resulting in very narrow linewidths below 1.5 GHz. To cover the Doppler profile this prism system was removed and the grating used directly. Depending on the alignment of the oscillator this results in approximately 200-400 GHz linewidth.

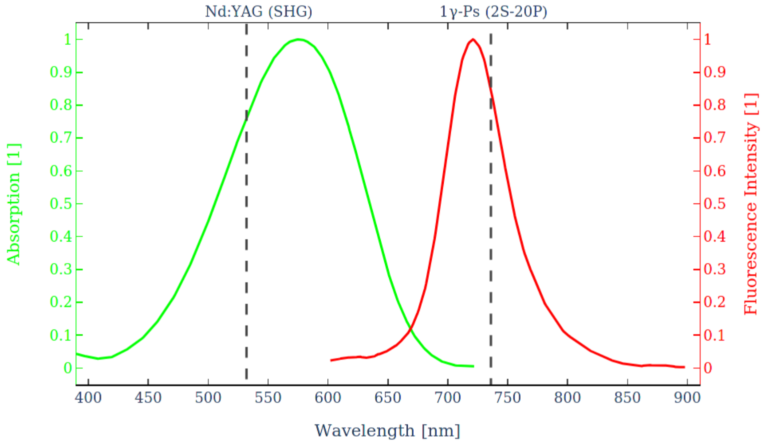

Figure 52: Absorption and Fluorescence Spectrum for Styryl 7 dissolved in ethanol (data from [142]). Both spectra are normalized to unity and the dotted lines show the pumping wavelength (532 nm) and the output wavelength (736.4 nm).

The employed dye is Styryl 7 [117], which absorption fits well with the SHG output of the Nd:YAG and the fluorescence peak is close to the 2S-20P transition wavelength. For the oscillator a concentration of 120 mg/l and for the amplifier of 60 mg/l is used. Contrary to Coumarin 102, the stability of the dye is excellent and the standard reservoir sizes (approximately 800 ml each) are appropriate for dye lifetimes of more than a month. The conversion efficiency is approximately 10 % resulting in pulses of up to 10 mJ at approximately 7 ns FWHM.

3.3.4. Frequency stabilization and measurement

To measure the 1S-2S transition with a precision on the MHz order, the frequency of the laser driving the transition needs to be known to the same or better precision. Additionally, it needs to be free from drift and able to be scanned over a few hundred MHz to cover the transition and systematic shift that can arise (see section 3.5.2). Conversely, the wavelength of the laser used for 2S-20P excitation only needs to be known to the order of the Doppler profile with 100 GHz. In the case of the delayed photo-ionization a measurement or stabilization is not necessary at all.

The wavelength and bandwidth of the output of the PDL-3 dye laser is regularly measured using a calibrated ASEQ Instruments HR1 spectrometer with 50 GHz resolution and shows no significant drift. The drive system for the grating used in the frequency selection of the PDL-3 system allows for changes with a repeatability of better than 5 GHz and frequency scans over a range of many nanometers.

A HighFinesse WL7 wavemeter is used to monitor the output of the Toptica TA pro diode laser used for seeding the PDA. While the device has a resolution of 2 MHz, this accuracy is only relevant for short term relative measurements. The absolute precision is specified to be 60 MHz, if it is frequently calibrated. For the first run the internal PID control of this device was used to stabilize and scan the frequency of the seed laser.

An issue often encountered in precision spectroscopy using pulsed lasers is frequency chirp [143, 144] which shifts the output of the pulsed dye amplifier from the frequency of the seed light due to the rapid change in refractive index of the gain medium [145]. The shift is time-dependent and can vary in sign and size, depending on the gain medium and pump energy, but is usually on the order of tens of MHz. An optical heterodyne technique to measure and correct for this shift was in fact developed for the measurement of the 1S-2S transition in positronium using pulsed lasers by Chu et al. [59–61]. This measurement was implemented for run 2 and an overview can be found in figure 47. A part of the seed light is shifted in frequency by a defined amount using an acousto-optic modulator (AOM) and mixed with the output of the PDA using a fiber-optic coupler. The resulting beatnote is then measured using a fast Thorlabs DET025AFC photodiode and a high bandwidth Teledyne LeCroy Waverunner 8104 oscilloscope. The laser bandwidth and instantaneous frequency shift can then be extracted with appropriate analysis (see section 3.6).

For the second run, a Menlo FC1500-250-WG optical frequency comb[34] was used as an absolute frequency standard. In this device a mode-locked femtosecond laser provides a well defined train of pulses, which form a periodic spectrum in frequency space [146].

---

[34] The comb was graciously provided by the group of Prof. Esslinger and was modified by Menlo to be used at 972 nm and to include several improvements of the newer FC1500-250-ULN model.

This allows to represent the series of peaks in frequency space (often called the frequency comb) as

$$\omega_k = k \cdot \omega_r + \omega_0 \quad , \tag{93}$$

where ω_r is the frequency difference between peaks, k is an integer multiple on the order of 10^6, and ω_0 is a frequency offset. The spacing ω_r is equivalent to the repetition rate of the pulsed laser (approximately 250 MHz in the case of this device), while ω_0 arises due to the difference in phase and group velocities of the mode-locked laser[35].

This effectively maps the optical range to two values in the RF range, which can easily be measured to very high precision. These frequencies are phase-locked to a stable reference (in our case to a precision GPS reference clock), by means of PID controls on the parameters of the mode-locked laser, e.g. the cavity length or temperature. Measuring the beatnote of the femtosecond laser with the seed laser then yields

$$\omega_{\text{beat}} = \omega_{\text{seed}} - \omega_k = \omega_{\text{seed}} - k\,\omega_r - \omega_0 \quad \Rightarrow \quad \omega_{\text{seed}} = k\,\omega_r + \omega_0 + \omega_{\text{beat}} \quad , \tag{94}$$

where the frequencies on the right hand side are stable and precisely measured. If k is known, this method allows for the measurement of the mean seed frequency on the order of a few kHz, which is mainly limited by the linewidth of the diode laser.

The integer value k (often called tooth number) can be determined by comparison with a coarse measurement of the seed laser with the wavemeter. Alternatively, if the seed laser is locked to an ultra-stable Fabry-Perot cavity, varying the repetition rate by a well-defined amount and measuring the beatnote allows for a tooth number determination without the need for another frequency reference. To cross-check the wavemeter, we developed an automatized technique, which allowed us to determine the tooth number with a high level of confidence (>95 %) even for a moderately drifting cavity ($\approx 20\,\mathrm{Hz/s}$), keeping the frequency comb locked and stable within a few hours [127].

In addition to measuring the frequency, the beatnote output can be used to lock the seed laser to a comb tooth. Not only does this counter possible drift, it also allows to scan over several 100 MHz by changing the repetition rate of the frequency comb. The lock is realized by feeding the bandwidth filtered beatnote signal into a MiniCurcuits RPD-1 analog phase detector both directly and delayed by approximately 4 ns. This produces an error signal by the phase detector [147], which is then used with a Toptica PID 110 lockbox to vary the grating angle of the laser diode in the seed laser.

3.4. Detection system

A schematic overview of the detection scheme for the 1S-2S transition can be found in figure 53. The implantation of positrons is monitored by the prompt peak in the SSPALS spectrum in a lead tungstate scintillator (see section 3.2) and by measuring backscattered positrons in an MCP that is placed at approximately 4 cm distance to the target. oPs emitted from the target can then be excited to the 2S state by a 486 nm laser and a significant fraction of the excited states are photo-ionized in the same laser. A

---

[35] Opposed to the repetition rate this quantity can not be directly measured. Instead, the beating of the original and the frequency doubled output yields ω_0.

small electric potential between the target and the detector assembly guides the resulting eV-scale positrons to the MCP, where they produce an electrical signal. Additionally, photons from the annihilation of the positron in the micro-channels of the MCP are picked up by the lead tungstate scintillator and contribute to the SSPALS spectrum.

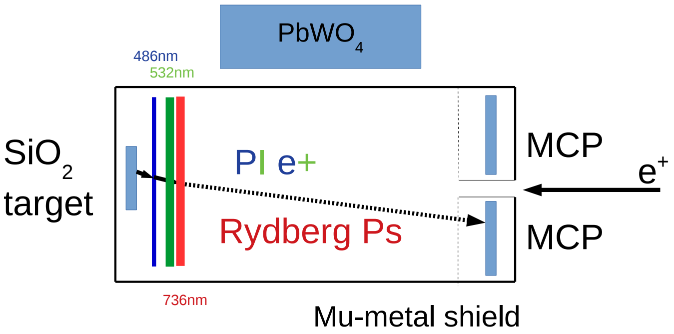

Figure 53: Sketch of positronium excitation and detection scheme: Positrons from the bunched positron beam are focused onto the silica thin film target. The created positronium is then laser excited to the 2S state by the 486 nm laser and can subsequently be ionized by a 532 nm laser or excited to the 20P state using a 736 nm laser. The positrons from photo-ionization or from field-ionization of the Rydberg atoms can either be detected on the MCP or via annihilation photons in a $PbWO_4$ scintillator.

Positronium atoms which do not ionize, do not produce a signal in the MCP directly and due to the small relative fraction and long lifetime, induce no significant change to the SSPALS spectrum. However, their presence can be detected by delayed photo-ionization in a 532 nm pulse. The detection for the positrons from delayed photo-ionization is analogous to direct photo-ionization, while being temporally well separated from the excitation.

Alternatively, positronium in the 2S state can be further excited to the 20P by the 736 nm laser. Afterwards, the atoms continue to propagate relatively undisturbed through the experimental chamber. Passing the bias grid in front of the MCP, they feel the electric field between the grid and the front plate, which is between 2-4 $^{\mathrm{kV}}/_{\mathrm{cm}}$, depending on the specific voltages set. In electric fields the Stark effect is responsible for mixing states with the same n and m, but different L. However, under a transformation into parabolic coordinates, there is a set of good quantum numbers consisting of the usual n, |m| (solutions in parabolic coordinates are degenerate for ±m) and the parabolic quantum numbers n_1, n_2, which are non-negative integers, representing the nodes of the wavefunctions in parabolic coordinates [38].

The quantum numbers are related by

$$\mathrm{n} = \mathrm{n}_1 + \mathrm{n}_2 + |\mathrm{m}| + 1 \quad , \tag{95}$$

which means that states with the quantum numbers n and m in zero field split into $\mathrm{n} - |\mathrm{m}|$ Stark states in an electric field. Those states acquire an energy splitting, which

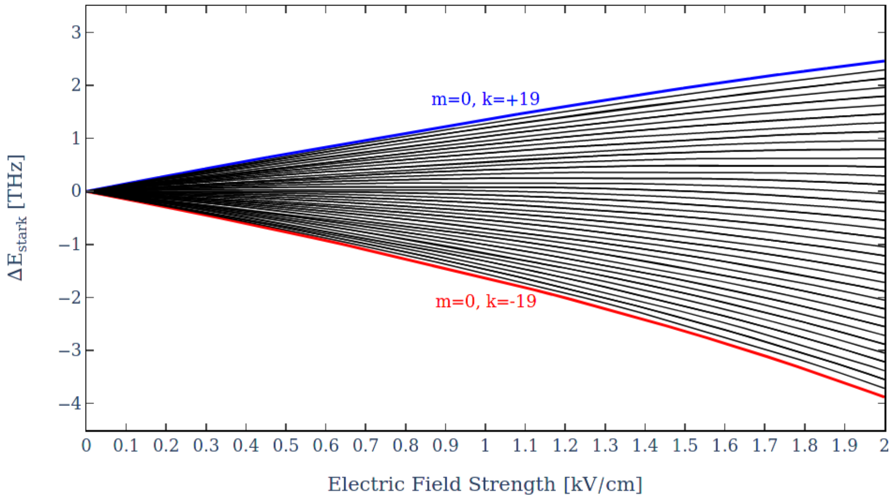

Figure 54: Stark splitting for the n = 20 state of positronium (|m| = 0, 1, 2) in a strong electric field. The states with the strongest positive (blue) and negative (red) shifts are marked.

is given to fourth order by [148]

$$\begin{aligned}\Delta E_{\text{Stark}} =& \, 3\,\mathrm{n}\,\mathrm{k}\,e\,a_0 F \\ & - \frac{\mathrm{n}^4 e^2 {a_0}^2 F^2}{2 m_e \alpha^2 c^2}\left(17\mathrm{n}^2 - 3\mathrm{k}^2 - 9\mathrm{m}^2 + 19\right) \\ & + \frac{3\mathrm{n}^7 e^3 {a_0}^3 F^3}{m_e^2 \alpha^4 c^4}\left(23\mathrm{n}^2 - \mathrm{k}^2 + 11\mathrm{m}^2 + 39\right) \\ & + \frac{\mathrm{n}^{10} e^4 {a_0}^4 F^4}{8 m_e^3 \alpha^6 c^6}\Big(5487\mathrm{n}^4 + 35182\mathrm{n}^2 - 1134\mathrm{m}^2\mathrm{k}^2 + 1806\mathrm{n}^2\mathrm{k}^2 - 3402\mathrm{n}^2\mathrm{m}^2 \\ & \qquad + 147\mathrm{k}^4 - 549\mathrm{m}^4 + 5754\mathrm{k}^2 - 8622\mathrm{m}^2 + 16211\Big) \quad , \end{aligned} \tag{96}$$

where F is the electric field strength and $\mathrm{k} = \mathrm{n}_1 - \mathrm{n}_2$. Figure 54 shows how the 20P states splits into states of the parabolic quantum number k, where the $|\mathrm{m}| = 0, 1, 2$ manifolds can be populated.

The field ionization rate, including tunneling, of these states is given by [148]

$$\begin{aligned}\Gamma_{\text{FI}} =& \frac{m_e c^2 \alpha^2 \,(4R)^{2\mathrm{n}_2 + |m| + 1}}{2\hbar\, \mathrm{n}^3\, \mathrm{n}_2!\,(\mathrm{n}_2 + |m|)!} \\ & \times \exp\left[-\frac{2R}{3} - \frac{4\,e\,a_0}{m_e c^2 \alpha^2}\left(34{\mathrm{n}_2}^2 + 34\mathrm{n}_2|\mathrm{m}| + 46\mathrm{n}_2 + 7\mathrm{m}^2 + 23|\mathrm{m}| + \frac{53}{3}\right)\right] \quad , \end{aligned} \tag{97}$$

where n_2 can be written as

$$\mathrm{n}_2 = \frac{\mathrm{n} - 1 - |\mathrm{m}| - \mathrm{k}}{2} \tag{98}$$

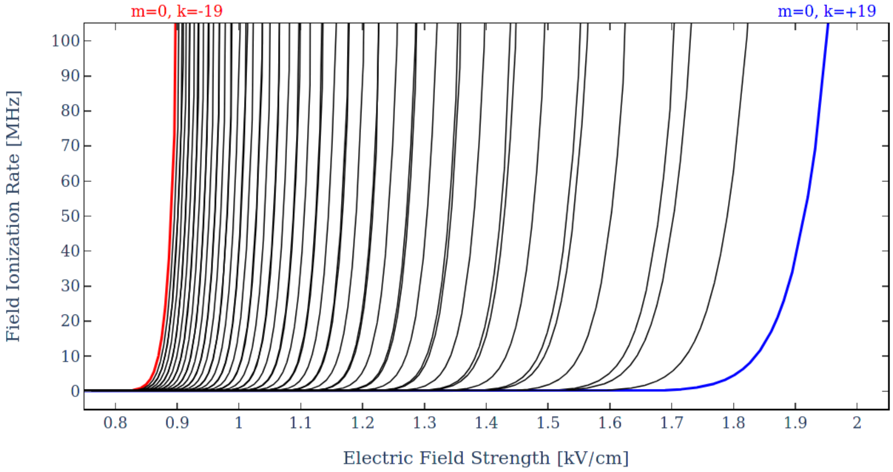

Figure 55: Field ionization rate for the n = 20 state of positronium ($|m| = 0, 1, 2$) in a strong electric field. The states with the highest (blue) and lowest (red) ionization rates are marked. They correspond to the marked states in figure 54.

for the allowed values of k. Figure 55 shows the ionization rate for the possible Stark states with $n = 20$ and $|m| = 0, 1, 2$. Of particular interest are the two states with the lowest and highest field ionization rate.

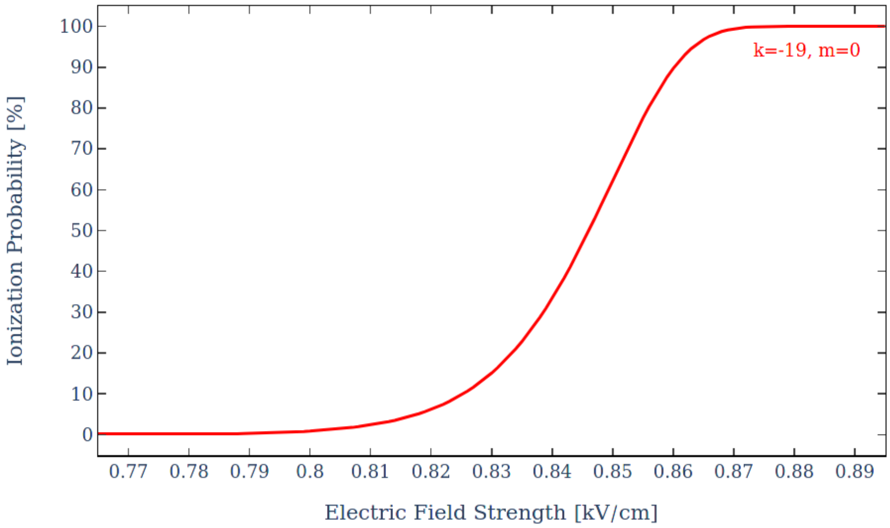

Figure 56: Field ionization probability for the $n = 20, k = -19, m = 0$ state propagating 5 cm at a velocity of $10^5\,\mathrm{m/s}$, corresponding to a positronium atom travelling from laser excitation to the bias grid on the detector.

When the atoms in Rydberg states propagate from laser excitation to the bias grid, the electric field should be small enough not to cause losses. Figure 56 shows the ionization probability for the most fragile state ($k = -19, m = 0$) for $n = 20$. From this it can be inferred that field ionization losses of the 20P state are negligible as long as the electric field strength is below approximately 800 V/cm in the region between the laser excitation and bias grid on the detector. In fact, this would even allow for a moderate voltage to be applied to the grid to bias off backscattered positrons.

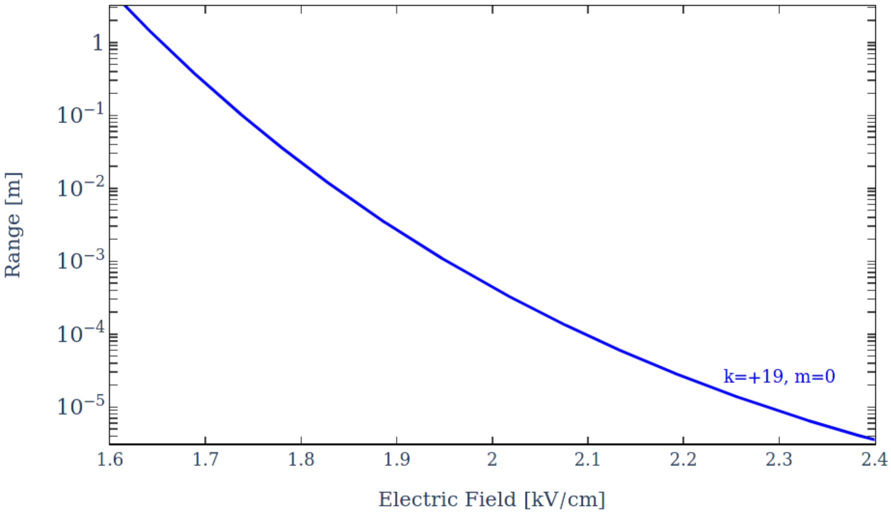

Figure 57: Mean range before ionization for the $n = 20, k = +19, m = 0$ state propagating at a velocity of 10^5 m/s. Note that this does not take annihilation or radiative decays into account.

On the other hand, after passing the bias grid the most stable state should ionize quickly to avoid a large uncertainty on the position – or equivalently the time – where the positron is freed. Figure 57 shows the range before ionization of the most stable state ($k = +19, m = 0$) for $n = 20$. It can be seen that most 20P atoms arriving at the bias grid will be ionized within less than 0.5 mm for electric fields above 2 kV/cm. Furthermore, that implies that the uncertainty on the arrival time of the positronium atom on the grid, given by the signal peak in the MCP, is below a few nanoseconds for velocities on the order of 10^5 m/s.

Figure 58 shows the detector and target assembly used during run 1. A matched set of two Photonis center-hole MCP plates are used in a chevron configuration, mounted in a custom assembly. A grounded tube through the center axis of the detector allows the positron beam to pass, which results in the active area being an annulus with 9.14 mm ID and 40 mm OD. The assembly incorporates two independent bias grids (92 % transmission), placed in approximately 3 mm and 13.5 mm distance from the the front plate, respectively. The center of the 486 nm laser axis and the center of the grid on which the 20P states field ionize are separated by (38.0 ± 1.0) mm. The kinetic energy of positrons implanted on the porous silica thin film target was 4 keV for this run.

For run 2 the detector geometry was modified to address some shortcomings that were identified with the original design. One such drawback is that a significant fraction of

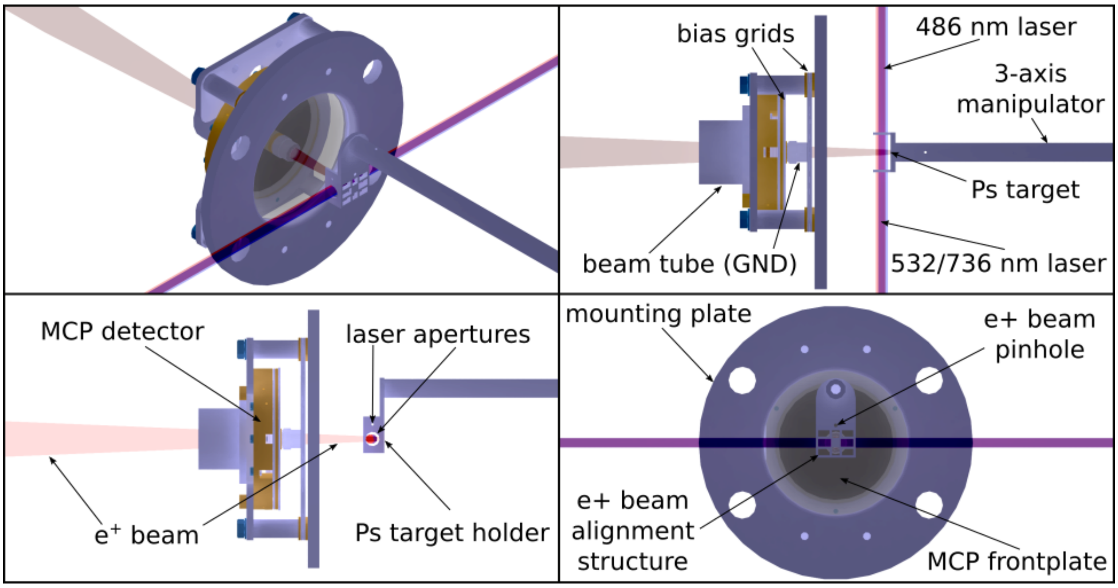

Figure 58: MCP detector and Ps conversion target assembly for run 1. Most parts of the mounting structure, magnetic shielding and vacuum chamber are not shown.

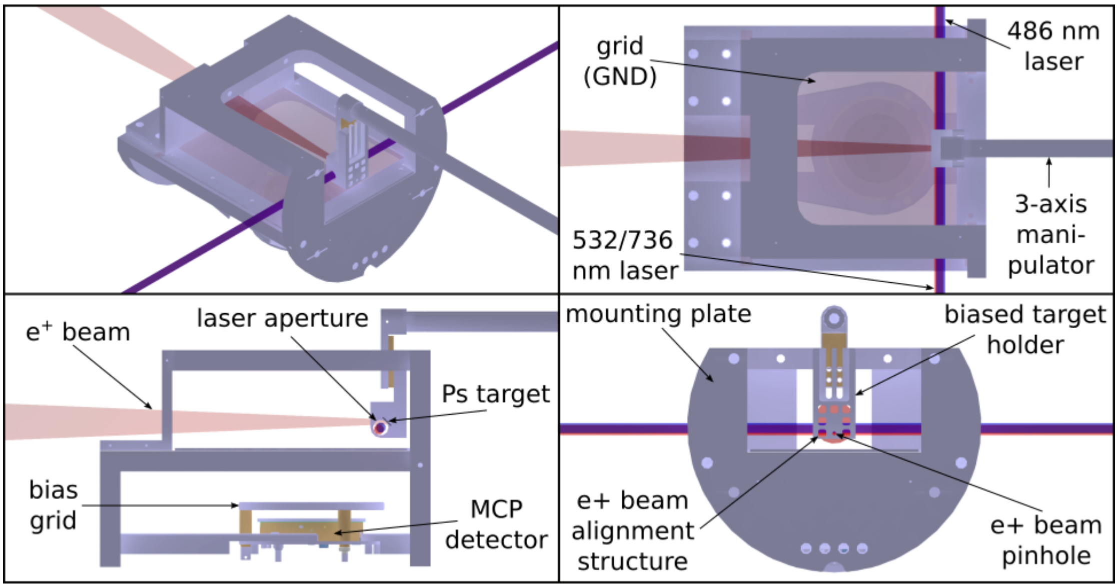

Figure 59: MCP detector and Ps conversion target assembly for run 2. Most parts of the mounting structure, magnetic shielding and vacuum chamber are not shown.

positrons incident on the target will backscatter and be picked up by the MCP. Earlier simulations with similar target geometries in GEANT4 show that approximately 6 % of the incident positrons are within the angular acceptance of the detector [149]. Due to ringing, which is a typical artifact in these kind of detectors (see figure 60), counting single events after the prompt peak induced by many backscattered positrons proves difficult. Furthermore, due to the $\cos\theta$-distribution of Ps emission angles (see section 3.2) and the overlap with the excitation lasers, losses in signal rate of more than 20 % through the center-hole in the MCP are expected. This might also lead to different collection efficiencies for positrons from photo-ionization and from 20P atoms ionizing in the electric field, which can cause a systematic frequency shift between those detection methods due to path-dependent AC stark shifts (see section 3.5).

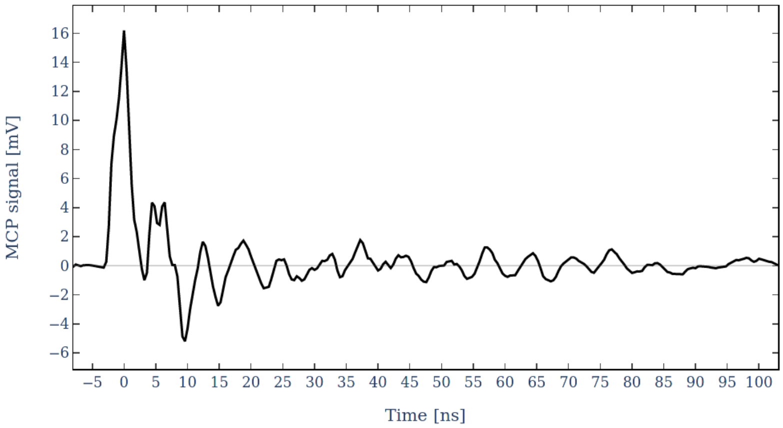

Figure 60: Average inverted single count MCP signal with ringing evident starting approximately 3 ns after the peak. Note that this was taken with the MCP configuration in run 2. The gain for the configuration during run 1 is approximately twice as high, with similar signal structure.

Figure 59 shows the updated detector setup used for run 2. Positrons are implanted at a 45° angle of incidence, while the detector is roughly centered on a line perpendicular to the target. It has been shown that positrons follow a specular-like reflection [150], i.e. the backscattering probability peaks where the angle of reflection equals the angle of incidence. Additionally, while the total fraction of backscattered positrons generally increases with higher angles of incidence, this effect is moderate for most materials at 45° [151]. Therefore, the fraction of positrons reaching an MCP, which is placed at approximately half the angle of incidence, is significantly reduced. Positronium atoms, which are implanted into the bulk of the porous silica structure and had time to cool down and diffuse to the surface before being emitted (see section 3.2), do not retain any information on the initial implantation angle. However, the kinetic energy of the impinging positrons must be increased according to equation 76 to achieve the same depth profile as for 0° angle of incidence. To further lower the mean energy of positronium being emitted into vacuum, the implantation energy was chosen to be 6 keV, which corresponds to implanting with approximately 5 keV perpendicular to the target.

The MCP used two matched GIDS plates with 25 mm quality diameter in a chevron configuration, mounted in a custom assembly. A bias grid is mounted at approximately 6 mm distance to the front plate of the MCP, while a second grid is placed on the grounded mounting structure in 27.5 mm distance. Both grids are tungsten wire meshes allowing for approximately 92 % transmission. However, due to the grid plane orientation of 45° to the target, an additional loss factor of $1/\sqrt{2}$ per grid is expected on average. The center of the 486 nm laser axis and the center of the grid, on which the 20P states field ionize, are separated by (41.8 ± 0.5) mm.

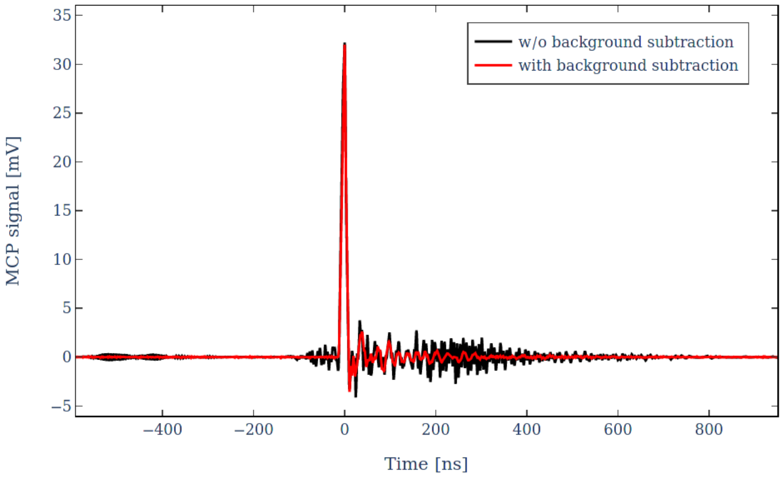

Figure 61: Average inverted MCP signal of backscattered positrons with superimposed switching noise (black) and signal after background subtraction (red).

Several devices close to the experimental chamber are switching voltages in the kilovolt range on a nanosecond time-scale within the measurement window, specifically the Nd:YAG Q-switch, the Pockels cell, and the elevator for implantation. This introduces unavoidable pick-up noise on the MCP readout in addition to the inherent ringing already present. However, the phase and amplitude of the switching noise is quite regular and can be subtracted. See figure 61 for the MCP signal due to backscattered positrons averaged over 3600 events and the corresponding noise subtraction. The background reference without positrons is taken while the moderator is regrown.

A shutter system is used in a periodic rotation, such that events are taken in sequence with and without laser interactions, which allows for the subtraction of a baseline without expected signal for the relevant process[36]. Figure 62 shows the average waveforms for direct and delayed photo-ionization for data taken during run 1 after baseline subtraction, while figure 63 shows the relevant average for field-ionization. Note that for photo-ionization the peak width is mainly given by the time-structure of the laser (approximately 6 − 7 ns FWHM), while the field-ionization signal is broadened due to the difference in time-of-flight from laser excitation to bias grid. This allows to infer properties of the initial velocity distribution (see section 3.6). The shaded regions in figures 62 and 63 mark the region of interest for the signal integration.

Alternatively, instead of integrating the average waveforms, it is also possible to count peaks, since most events of interest are due to a single positron and multiple overlapped

---

[36] The baseline includes other sources of signal, which are considered to be background for the analyses here, e.g. decay photons of positronium creating a charge on the MCP due to ionization.

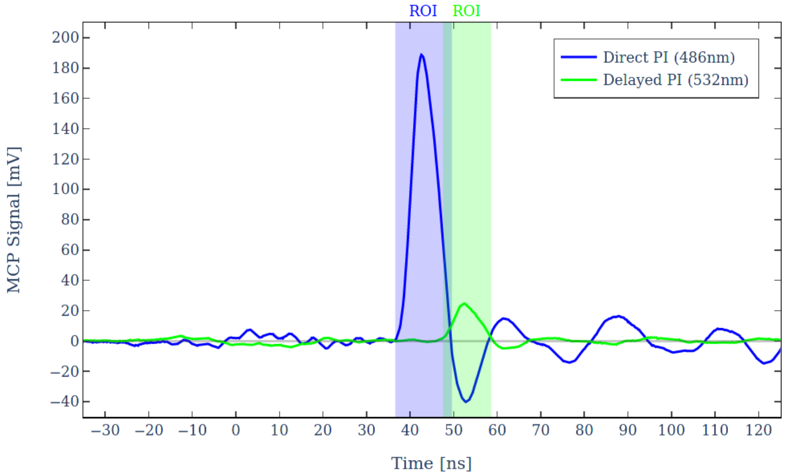

Figure 62: Average inverted MCP signal for direct and delayed photo-ionization after baseline subtraction taken during run 1. The time axis is relative to the prompt peak due to backscattered positrons. The shaded regions show the region of interest for signal integration.

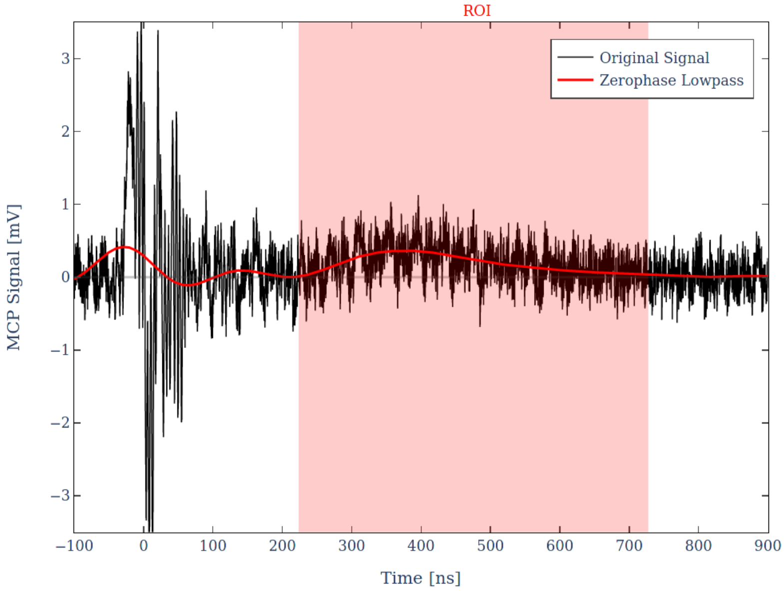

Figure 63: Average inverted MCP signal for Rydberg field-ionization after baseline subtraction taken during run 1. Additionally shown is the signal after filtering using a Butterworth zero phase low-pass filter [152, 153] with 7 MHz cutoff. The time axis is relative to the prompt peak due to backscattered positrons. The shaded regions show the region of interest for signal integration.

counts are rare. Counts are then extracted from the baseline to find the excess events due to a specific process, similar to the baseline subtraction described above. After using a Butterworth zero phase band-pass filter [152, 153] with 55 MHz and 400 MHz cutoffs, the counting algorithm uses a fixed trigger voltage to find peak times, heights and widths for all waveforms. In the case of photo-ionization events a higher threshold is used to be less sensitive on ringing introduced by backscattered positrons in the dataset of run 1. Furthermore, to avoid double counting single peaks, the algorithm uses 7 ns dead time after the peak position (see figure 60). Figures 64 and 65 show the time spectra of excess counts for photo-ionization and field ionization for the dataset of run 1. In general, counting is a more reliable method, if the events are spread out over a time-scale, which is significantly longer than a single pulse, as is the case for field ionization.

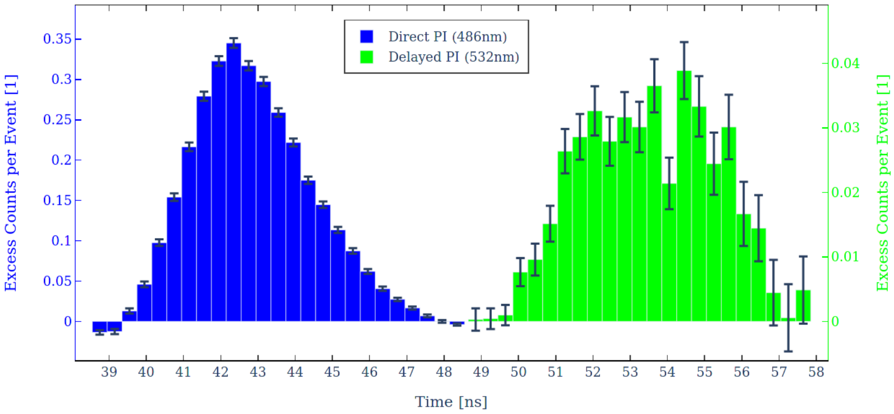

Figure 64: Histogram of excess MCP counts due to photo-ionization taken during run 1. A threshold of 25 mV was used for direct photo-ionization and 20 mV for delayed photo-ionization. The time axis is relative to the prompt peak due to backscattered positrons.

3.5. Theoretical background and simulation

To calculate the probability of exciting ground-state positronium to the 2S state, a density matrix approach for a two-level system [154] is used. This is done by solving the set of differential equations

$$\begin{aligned}\partial_t\,\rho_{gg}(t) &= -\Omega\ \mathrm{Im}(\rho_{ge}(t)) - \Gamma_{1S}\,\rho_{gg}(t)\\ \partial_t\,\rho_{ge}(t) &= -i\,\Delta\omega\,\rho_{ge}(t) + \frac{i\,\Omega}{2}(\rho_{gg}(t)-\rho_{ee}(t)) - \frac{\Gamma_i+\Gamma_{1S}+\Gamma_{2S}}{2}\,\rho_{ge}(t) \quad ,\\ \partial_t\,\rho_{ee}(t) &= \Omega\ \mathrm{Im}(\rho_{ge}(t)) - (\Gamma_i+\Gamma_{2S})\,\rho_{ee}(t)\end{aligned} \tag{99}$$

assuming that all positronium atoms are initially in the ground state. Equations (99) can be integrated numerically by using a suitable algorithm. To arrive at the simulation results presented in this thesis (see section 3.5.2) an adaptive Runge-Kutta method [155] was employed.

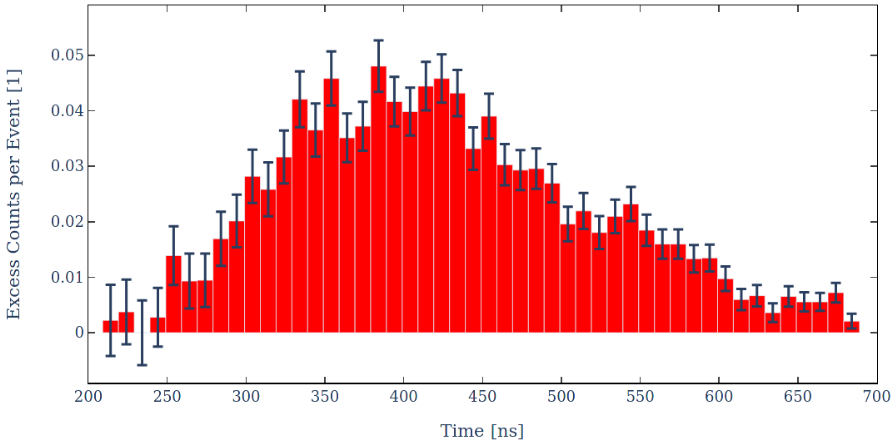

Figure 65: Histogram of excess MCP counts due to Rydberg field ionization taken during run 1. A threshold of 12.5 mV was used. The time axis is relative to the prompt peak due to backscattered positrons.

ρ_{gg} represents the state population of the ground state, while ρ_{ee} is the state population of the excited state. The annihilation decay rates read (see section 1.2.2)

$$\Gamma_{1S} = \frac{1}{\tau^a_{1^3\mathrm{S}_1}} \approx \frac{1}{142\,\mathrm{ns}} \tag{100}$$

and

$$\Gamma_{2s} = \frac{1}{\tau^a_{2^3\mathrm{S}_1}} \approx \frac{1}{1.14\,\mu\mathrm{s}} \;. \tag{101}$$

The spontaneous decay of the 2S states back into the ground state does not need to be included, since the the annihilation rate Γ_{2s} is many orders of magnitude larger. Ionization, however, needs to be included in the model, especially for higher power lasers, since the rate

$$\Gamma_i = 2\pi\,\beta_i\,I(t) \tag{102}$$

is directly proportional to the laser intensity $I(t)$. The ionization coefficient β_i is given by its value for hydrogen, taken from Haas et al. [154], after multiplying the proper rescaling factor

$$\beta_i = \frac{1}{Z^4}\left(\frac{m_e}{\mu}\right)^3 \cdot 1.20208 \times 10^{-4}\,\frac{\mathrm{Hz\,m^2}}{\mathrm{W}} = 9.61664 \times 10^{-4}\,\frac{\mathrm{Hz\,m^2}}{\mathrm{W}} \;, \tag{103}$$

where $Z = 1$ is the nuclear charge number and $\mu = {}^{m_e}\!/_2$ is the reduced mass.

The two-photon Rabi frequency

$$\Omega = 2\,(2\pi\,\beta_{ge})\,I(t) \tag{104}$$

used in equation (99) is proportional to the laser intensity $I(t)$ and a rescaled two-photon transition matrix element [154]

$$\beta_{ge} = \frac{1}{Z^4}\left(\frac{m_e}{\mu}\right)^3 \cdot 3.68111 \times 10^{-5}\,\frac{\mathrm{Hz\,m^2}}{\mathrm{W}} = 2.944888 \times 10^{-4}\,\frac{\mathrm{Hz\,m^2}}{\mathrm{W}} \;. \tag{105}$$

Finally, the excitation detuning is given by

$$\Delta\omega = 2\pi \left(2\,\nu_L - \nu_0 \left(1 + \frac{\vec{v}\cdot(\vec{e}_i + \vec{e}_r)}{2c} - \frac{v^2}{2c^2}\right) - \Delta\nu_{ac}^e + \Delta\nu_{ac}^g\right) \ , \tag{106}$$

where ν_L is the frequency of the laser used for excitation, ν_0 is the unperturbed transition frequency, which is shifted by the relativistic Doppler effect (shown to second order) and the AC Stark shift. The Doppler shift is given by the the positronium velocity $\vec{v}$ and the propagation axes of the incoming ($\vec{e}_i$) and reflected ($\vec{e}_r$) photons. In the case of perfectly overlapping retro-reflected laser beam profiles, $\vec{e}_i = -\vec{e}_r$ and the first order term cancels. Experimentally, this can be realized by employing a resonant Fabry-Perot cavity. Otherwise, there will be some residual first-order Doppler shift, depending on the angle between the counter-propagating wave fronts on the order of

$$\Delta\nu_{d1} \approx \pm 200\,\frac{\text{kHz}}{\mu\text{rad}} \ . \tag{107}$$

The AC Stark shifts are given by

$$\Delta\nu_{ac}^{e/g} = \beta_{ac}^{e/g}\, I(t) \ . \tag{108}$$

Analogous to the ionization coefficient and the transition matrix element, the AC Stark shift coefficients $\beta_{ac}^{e/g}$ are taken from Haas et al. [154], after multiplying the rescaling factor to yield

$$\beta_{ac}^{e} = \frac{1}{Z^4}\left(\frac{m_e}{\mu}\right)^3 \cdot 1.39927\times 10^{-4}\,\frac{\text{Hz}\,\text{m}^2}{\text{W}} = 1.119416\times 10^{-3}\,\frac{\text{Hz}\,\text{m}^2}{\text{W}} \tag{109}$$

and

$$\beta_{ac}^{g} = \frac{1}{Z^4}\left(\frac{m_e}{\mu}\right)^3 \cdot 2.67827\times 10^{-5}\,\frac{\text{Hz}\,\text{m}^2}{\text{W}} = 2.142616\times 10^{-4}\,\frac{\text{Hz}\,\text{m}^2}{\text{W}} \ . \tag{110}$$

Due to the relatively high velocities of positronium atoms produced with porous silica targets, they interact with the laser only for a very short period of time and the spatial and temporal profiles of the laser beam need to be taken into account. Assuming sufficiently collimated beams with Gaussian spatial profiles, the intensity can be written as

$$I(y,z) = \frac{2\,P}{\pi\,w}\, e^{-2\,\frac{y^2+z^2}{w^2}} \ , \tag{111}$$

where y and z are the time dependent coordinates of the positronium atom, with the propagation axis of the laser assumed to be parallel to the x-axis. The waist size w corresponds to the $1/e^2$-radius of the laser beam. While the Power P is assumed to be constant for a CW laser, for a pulsed laser a non-trivial temporal profile needs to be taken into account. It is given by a combination of the intrinsic Gaussian time profile of the incoming laser pulse

$$P_i(t) = \frac{E_p}{\sqrt{2\pi}\,\sigma}\, e^{-\frac{(t-t_{\text{off}})^2}{2\,\sigma^2}} \tag{112}$$

and the reflected laser pulse

$$P_r(t) = \frac{E_p}{\sqrt{2\pi}\,\sigma}\, e^{-\frac{(t+t_{\mathrm{ref}}-t_{\mathrm{off}})^2}{2\,\sigma^2}} \,, \tag{113}$$

where E_p is the pulse energy, t_{off} is the timing offset between positronium emission and the peak intensity of the laser pulse and t_{ref} is the round-trip time of the laser pulse to the mirror and back.

The combination required is the trivial superposition

$$P(t) = P_i(t) + P_r(t) \tag{114}$$

when used for the calculation of the ionization and Stark shift coefficients, since these are one-photon processes. However, excitation is strictly a two-photon resonant effect. This is taken into account by using the envelope of the two counter-propagating beams, which results in the expression

$$P(t) = 2\sqrt{P_i(t)P_r(t)}\ . \tag{115}$$

3.5.1. Description of Monte Carlo simulation

A Monte Carlo simulation was developed to accurately reproduce the lineshape for a given set of experimental parameters. This section will give a short introduction of which effects and parameters have been taken into account. Due to the slightly different experimental setup and improved measurement system run 1 and 2 use a different set of input parameters, which can be found in tables 3 and 4.

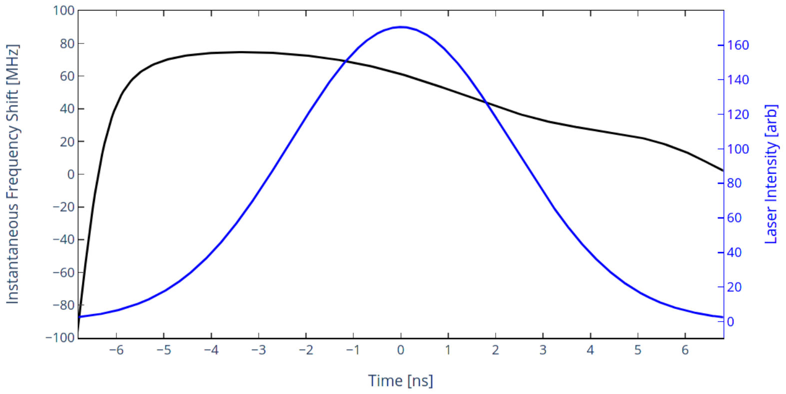

Figure 66: Average chirp profile (black) as taken during run 2 and simulated laser intensity time profile (blue) for a time spread of 5.5 ns (FWHM).

The effects of the laser chirp are included by modifying the instantaneous frequency according to the average of the chirp measurements taken during run 2 (see section 3.6 for a description of the method). Figure 66 shows the average shift from the laser detuning during the pulse length and the mean Gaussian time profile of the simulated intensity profile. This chirp profile is corrected by the intensity-weighted average chirp analogously to the method described in section 3.6, which amounts to

$$\overline{\Delta\nu_c} = 56.6\,\mathrm{MHz} \tag{116}$$

for the data shown in figure 66.

Variable Name	Typical Value	Description
WaistSize	2 mm	laser beam minimum waist radius
PulseEnergy	6.25 mJ	laser pulse energy
PulseFWHM	6.7 ns	FWHM of temporal pulse shape
LaserTimeOffset	28 ns	offset Ps creation / laser max.
MisalignmentY	0 mrad	angle between laser wave-fronts (XY-plane)
MisalignmentZ	2 mrad	angle between laser wave-fronts (XZ-plane)
PositroniumTemp	700 K	temperature for velocity distribution[37]
DistanceSourceLaserX	150 mm	X-axis distance target / mirror
DistanceSourceLaserY	0 mm	Y-axis distance target / laser
DistanceSourceLaserZ	3 mm	Z-axis distance target / laser
SigmaBeamX	1.5 mm	X-axis spread of Ps creation area
SigmaBeamY	1.5 mm	Y-axis spread of Ps creation area
SigmaEmission	20 ns	timing spread of Ps creation
DistanceMCPLaserX	0 mm	X-axis distance laser / MCP
DistanceMCPLaserY	0 mm	Y-axis distance laser / MCP
DistanceMCPLaserZ	38 mm	Z-axis distance laser / MCP
TargetAngle	0°	target angle relative to positron beam

Table 3: Experimental variables and typical values used in Monte-Carlo simulation (run 1)

Additionally, for run 2 the simulation is supplied with the spatial laser beam profile taken with a Thorlabs BP209-VIS beam profiler (see figure 67). It was found to be a slightly skewed elliptical Gaussian beam with waist sizes[38]

$$w_{\mathrm{hor}} = (2.91 \pm 0.01)\,\mathrm{mm} \tag{117}$$

$$w_{\mathrm{ver}} = (2.58 \pm 0.01)\,\mathrm{mm} \tag{118}$$

where the vertical axis lies parallel and the horizontal axis perpendicular to the target surface. However, due to pointing instability and the averaging nature of the measurement with a rotating slit beam profiler the true beam diameter is probably slightly lower. This has been taken into account in the simulation by including correction factors for the vertical and horizontal beam size (see table 4).

---

[37] Note the discussion in the text.

[38] Note that this value was calculated from the variance of a skewed Gaussian fit for reference. The simulation does not use this fit, but instead the complete measured profile as input.

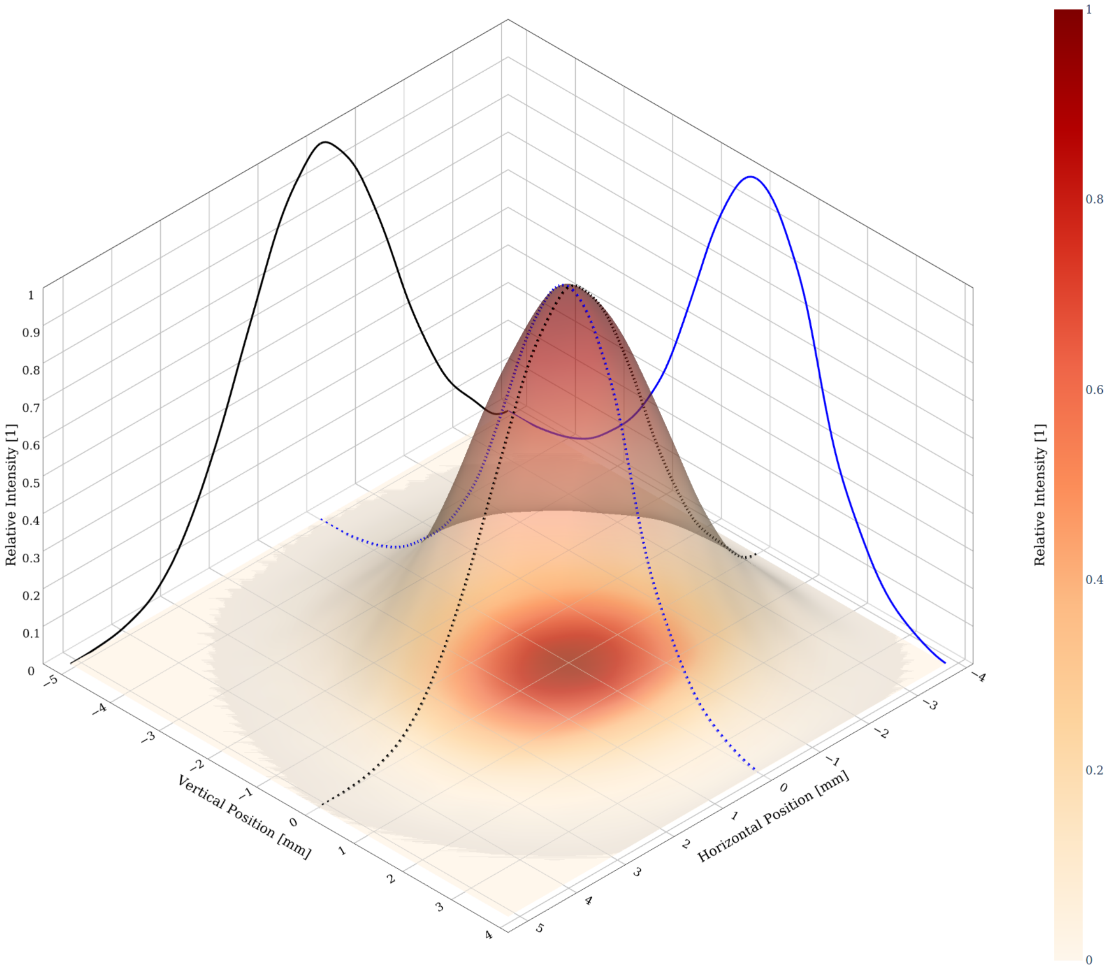

Figure 67: 3D surface plot of spatial laser beam profile taken during run 2, with 2D color space projection on the z-plane and 2D contour projections of the beam center for the horizontal (black) and vertical (blue) planes.

For each simulated atom, the primary positronium vertex is created according to an elliptical Gaussian profile of widths SigmaBeamX and SigmaBeamY. The coordinate system is chosen such that the X-axis corresponds to the propagation axis of the laser, while the Z-axis lies perpendicular to the target. The implantation and emission time profile is approximated by varying the creation time of the atom using a $\mathcal{N}(0, \text{SigmaEmission}^2)$ distribution.

In accordance with the emission described in section 3.2, the initial velocity vector is created with a $\cos\theta$-distribution [156] for the direction and a Maxwell-Boltzmann distribution [157] for the magnitude. It therefore reads

$$v^x{}_i = |v|_i \cdot ST_i \cdot \cos(2\pi P_i) \tag{119}$$

$$v^y{}_i = |v|_i \cdot ST_i \cdot \sin(2\pi P_i) \tag{120}$$

$$v^z{}_i = |v|_i \cdot \sqrt{1 - ST_i{}^2} \tag{121}$$

where ST_i and P_i are uniformly-distributed random variables in $(0, 1)$ and

$$|v|_i = \sqrt{\frac{k_B T}{2m_e}} \sqrt{VX_i{}^2 + VY_i{}^2 + VZ_i{}^2} \tag{122}$$

where VX_i, VY_i and VZ_i are standard normal distributed random variables.

Variable Name	Typical Value	Description
WaistMultiplierY	0.85	correction factor for measured beam size[39]
WaistMultiplierZ	0.85	correction factor for measured beam size[39]
PulseEnergy	6.0 mJ	laser pulse energy
PulseFWHM	5.5 ns	FWHM of temporal pulse shape
LaserTimeOffset	45 ns	offset Ps creation / laser max.
MisalignmentY	-1.2 mrad	angle between laser wave-fronts (XY-plane)
MisalignmentZ	0 mrad	angle between laser wave-fronts (XZ-plane)
PositroniumTemp	550 K	temperature for velocity distribution[39]
DistanceSourceLaserX	150 mm	X-axis distance target / mirror
DistanceSourceLaserY	0 mm	Y-axis distance target / laser
DistanceSourceLaserZ	3 mm	Z-axis distance target / laser
SigmaBeamX	1.5 mm	X-axis spread of Ps creation area
SigmaBeamY	2.0 mm	Y-axis spread of Ps creation area
SigmaEmission	40 ns	timing spread of Ps creation
DistanceMCPLaserX	0 mm	X-axis distance laser / MCP
DistanceMCPLaserY	-32.1 mm	Y-axis distance laser / MCP
DistanceMCPLaserZ	26.8 mm	Z-axis distance laser / MCP
TargetAngle	45°	target angle relative to positron beam

Table 4: Experimental variables and typical values used in Monte-Carlo simulation (run 2)

The relativistic Doppler shift (up to second order) for this specific path is then calculated using the velocity vector, MisalignmentY (δ_y) and MisalignmentZ (δ_z), which represent the misalignment angles with respect to the laser propagation axis along Y and Z. Since $\delta_y \ll 1$ and $\delta_z \ll 1$ it is given simply by

$$\Delta\nu^{DS}{}_i = \nu_0 \left(1 + \frac{v^y{}_i \delta_y + v^z{}_i \delta_z}{2c} - \frac{|v|_i{}^2}{2c^2}\right) \tag{123}$$

---

[39] Note the discussion in the text.

where ν_0 is the unperturbed transition frequency.

Since the atoms can only interact with the laser when passing the laser aperture of 6 mm diameter (see figure 58 and 59), the state populations in the 1S and 2S will only be calculated while they pass this region (see below). Otherwise they will be tracked and the populations corrected according to their decay rates. Positronium, which is photo-ionized, is assumed to be detected regardless of the path, since a small bias voltage on the target transports it towards the MCP. Within reasonable limits for the velocity of the positronium atoms, the pulse energy used for delayed photo-ionization is sufficiently large, such that the ionization rate is close to unity. Likewise, the pulse energy used for the 2S-20P excitation is expected to saturate the transition. Therefore these effects do not need be be modeled separately in the simulation.

Excited states, which are detected by field-ionization, are taken into account only if their path intersects with the active area of the MCP. For these states an additional correction for losses on passing the two grids of

$$\hat{\rho}_i = \rho_i \cdot \mathrm{OA}^2 \cdot (\vec{v}_i \cdot \vec{e}_g)^2 \tag{124}$$

is taken into account, where ρ_i are the state populations (see equation 99), OA = 92 % is the open area of the used mesh and $\vec{e}_g$ is the surface normal vector of the grid.

Variable Name	Unit	Description
LaserFrequency	MHz	excitation detuning (see eq. 106)[40]
PIProb	%	detection probability for direct PI on the MCP (mean)
Pop1S	%	fraction of ground state atoms reaching the MCP (mean)
Pop2S	%	fraction of excited state atoms reaching the MCP (mean)
HitTime	ns	Histogram of 2S atoms arrival time on the MCP
HitTheta	rad	Histogram of 2S atoms angle reaching the MCP
HitPop2S	%	Histogram of 2S atoms fraction reaching the MCP
Velocity	m/s	Histogram of 2S atoms velocity reaching the MCP

Table 5: Output variables of Monte-Carlo simulation

For each atom, the laser pulse energy and time spread is varied according to a Gaussian distribution, where the standard deviation was taken from data. For run 1 the spread was found to be 3.11% for the pulse energy and 4.7% for the time spread, while for run 2 the respective values were measured to be 3.68% and 3.44%.

The evolution of state populations are calculated by numerical integration of the optical Bloch equations (see equation 99) along the propagation path within the laser aperture. Before each integration step, the laser intensity seen by the atom at that moment (see equations 114 and 115), is calculated according to the spatial laser profile and the current time. Then the intensity dependent quantities governing the state

---

[40] While the chirp time profile is included in the simulation, it is corrected by the intensity-weighted average chirp to conform with the values given in the data analysis. Therefore the chirp does not significantly shift the resonance frequency in the simulation, while still inducing other effects on the lineshape.

evolution are determined, which includes the excitation rate (equation 104), ionization rate (equation 102) and AC Stark shift (equation 108). Finally, the excitation detuning (equation 106) is calculated including the current chirped laser detuning (corrected by the intensity-weighted average chirp), relativistic Doppler and AC stark shifts and the Bloch equations are integrated. This is continued until the atoms leave the region defined by the laser aperture on the target holder.

This process is repeated until the required number of events and laser detuning steps is reached. The simulation saves the results of each individual atom for later analysis. A list of the available output variables can be found in table 5.

3.5.2. Simulation results

This section will present the results of the simulation in general terms, what impact different effects have on the line shape, and the fitting procedures employed. Unless noted otherwise, the data shown corresponds to the best fit obtained for the analysis of run 1 (see section 3.6). Optimizing the amount of 2S states for subsequent microwave excitation will be discussed in the next chapter in section 4.3. Unless otherwise noted, frequency values given in this section usually refer to detuning in the excitation laser, which corresponds to half the value in the transition, since the excitation is a two-photon process.

Since the transition is determined both by direct photo-ionization in the exciting laser and by delayed ionization, two distinctly different line shapes are measured. Generally, direct photo-ionization produces a significantly broader line since it effectively limits the probed atoms lifetimes. Furthermore, the profile is generally more skewed, since the process strongly favors higher laser intensities (see also discussion of the AC Stark shift below).

The natural line width of the 1S-2S transition is dominated by the annihilation lifetimes and calculation yields

$$\Delta\omega_n \approx \gamma_{1s} + \gamma_{2s} \approx 2\pi \cdot 1.3\,\text{MHz}\ . \tag{125}$$

However, broadening of the line shape to at least $\Delta\nu \approx 100\,\text{MHz}$ in the transition is evident in all line shapes presented in this work. The main effects responsible for this and other features of the line shape will be explained in the following.

A major source of broadening is the limited interaction time of the positronium atoms with the light field, either due to spatial or temporal properties of the laser beam. For Gaussian profiles the time-bandwidth product reads

$$\Delta\nu \cdot \Delta t \approx 0.44 \tag{126}$$

which is just a consequence of the uncertainty principle. To give a numerical example, when a stationary atom interacts with a pulsed laser with Gaussian temporal profile and 5 ns FWHM, this equates to

$$\Delta\nu \approx \frac{0.44}{5\,\text{ns}} = 88\,\text{MHz} \tag{127}$$

broadening or equivalently to laser bandwidth. If the interaction time is limited by the atom propagating through the laser, this effect is commonly referred to as time-of-flight or transit-time broadening.

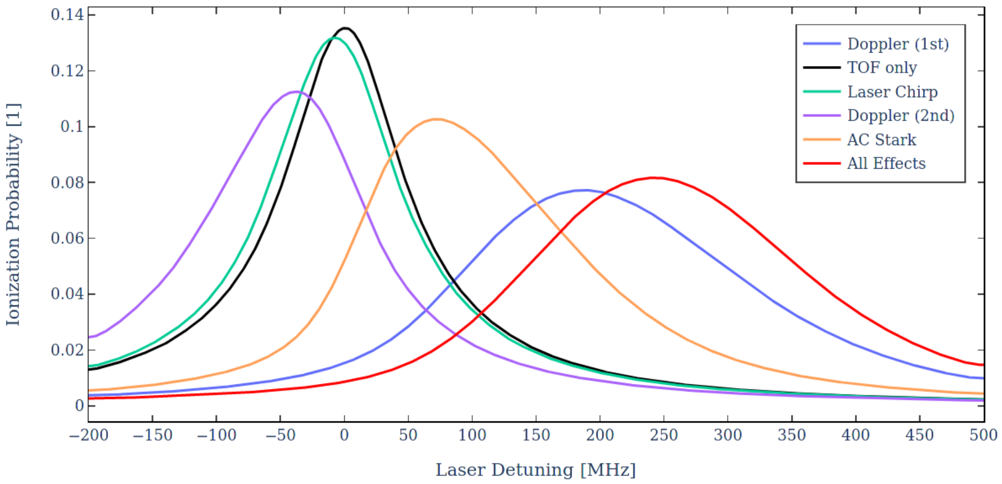

Figure 68: Impact on the direct photo-ionization line shape for effects included in the Monte-Carlo simulation shown for the parameters found as best fit to the data acquired during run 1.

Figures 68 and 69 shows the impact of other effects included in the simulation on the photo-ionization and transition line shapes. The graphs correspond to the best fit set of parameters determined for run 1 (see section 3.6). Run 2 shows analogous behavior unless otherwise noted. Different effects do not simply add up but can have a somewhat complex interaction. Nevertheless, the general effects on the line shape can be identified by studying their impact separately. To this end the plots show the strictly symmetric line shape, which includes TOF broadening only, in black as a staring point. In addition to the impact of the relevant effects included in the simulation shown separately, the final line shape with all effects combined is plotted.

Laser chirp introduces a slight shift and skew of the line shapes. Notably, it causes a red-shift for photo-ionization and a blue-shift for the excitation line, which can be explained by the fact that the chirp is larger for the high intensity part of the laser pulse (see figure 66). Excitation rates generally saturate significantly sooner at higher intensity than photo-ionization rates, which is why intensity-dependent effects generally affect the line-shapes differently.

The AC Stark effect always blue-shifts, broadens and positively skews the line. Similarly to chirp, the effect is more pronounced in photo-ionization, since it favors higher laser intensities, which makes it one of the major sources of broadening. The effects from second order Doppler shift are of similar magnitude, but opposite sign. While mono-energetic positronium would lead to a constant shift, the distribution of velocities leads to the broadening and skew of the line.

The impact of the residual first order Doppler shift is considerably more complex.

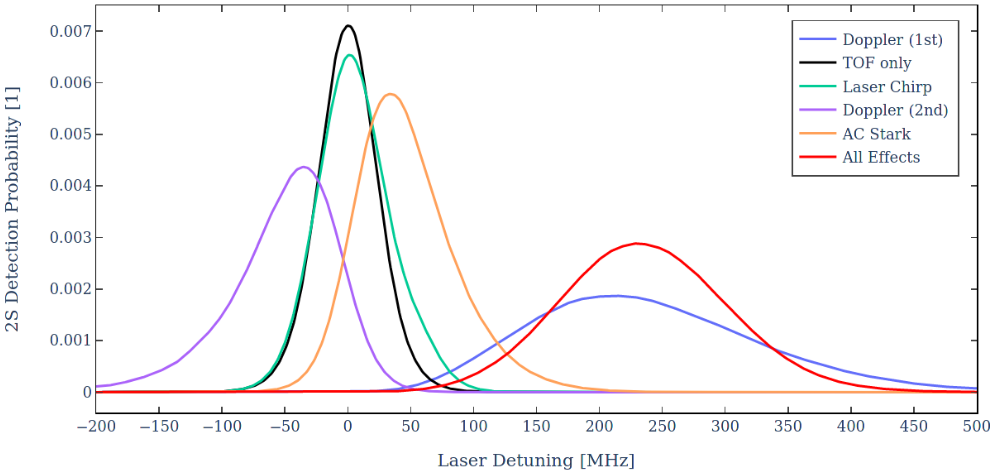

Figure 69: Impact on the excitation line shape for effects included in the Monte-Carlo simulation shown for the parameters found as best fit to the data acquired during run 1.

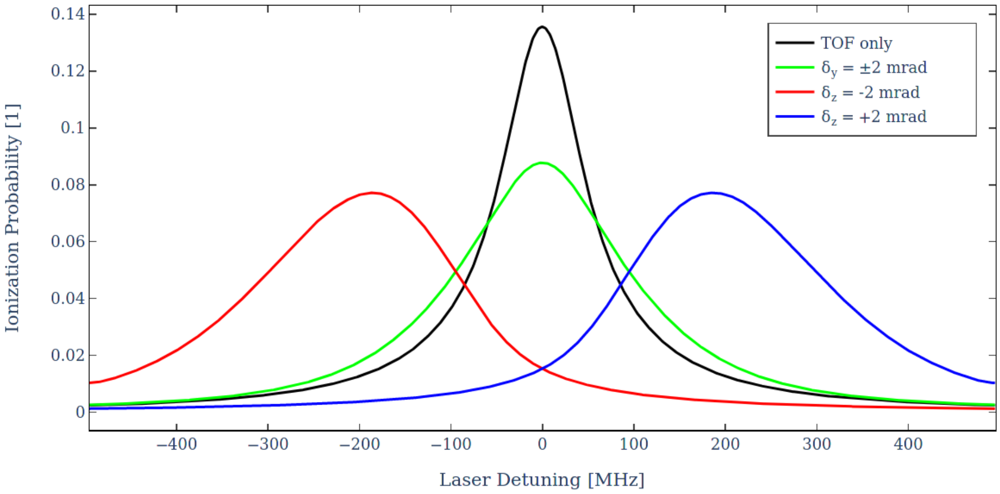

Figure 70: Impact of the residual first order Doppler shift for different magnitude and direction of misalignment on the direct photo-ionization line shape shown for the parameters found as best fit to the data acquired during run 1.

Generally, misalignment of the laser axis parallel to the target leads to broadening, but not shift (see exception below). The reason for this is that the $\cos\theta$-distribution of emission is axially symmetric, so for every blue-shifted velocity vector, there is an equally likely red-shifted velocity vector. However, this cancellation does not occur for misalignment perpendicular to the target, since all of the possible directions of emitted positronium have at least some velocity component in this direction. This leads to shifts which can have significant magnitude and arbitrary signs, depending on the direction of

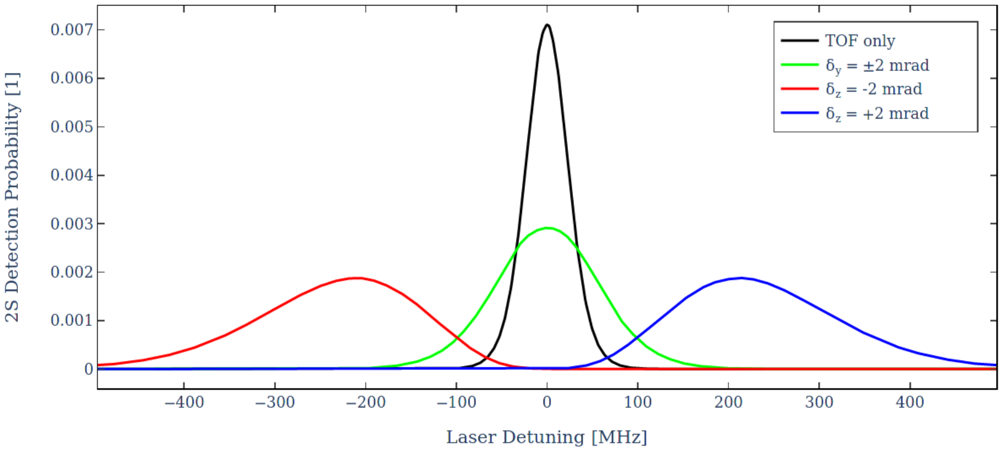

Figure 71: Impact of the residual first order Doppler shift for different magnitude and direction of misalignment on the excitation line shape shown for the parameters found as best fit to the data acquired during run 1.

the misalignment. The resulting shifts for a misalignment of 2 mrad for both signs along both axes can be found in figures 70 and 71. The shifts are qualitatively equivalent in both the photo-ionization and the excitation line shapes. However, the width of broadening in the XY-plane is reduced for the excitation line shape, depending on the angular acceptance of atoms undergoing field-ionization on the MCP. It is important to note that the symmetry of shifts for misalignments in the XY-plane is not just a consequence of the properties of the emission, but also of the detection. In fact, in the case of the experimental geometry used for run 2 this symmetry is broken, due to the angle and offset of the MCP relative to the target. This leads to a small, but significant shift in addition to the broadening in the excitation lineshape, as can be seen in figure 72. The reduced broadening due to smaller angular acceptance of the MCP, as described above, is also evident in this plot.

Ideally, each line would be simulated with very high statistics ($> 10^5$) for a very fine scan of laser detunings ($< 1\,\mathrm{MHz}$) over a wide range ($\approx 1\,\mathrm{GHz}$) to directly fit measurement data. However, while this might be feasible for a handful of parameters, it is clearly out of the scope for several thousand sets of parameters, as used for the data analysis presented in the next section. To severely reduce the required amount of computational resources, a fitting procedure was developed to convert simulation results to functional form. This allows for the fitting of data with arbitrary offsets, without further interpolation. While the fits give excellent agreement with the simulated line shapes, this introduces an error on the simulated line center, which has to be added to the experimental results.

To accurately model the features of the line shape an appropriate function is required. While the transition itself would present as a Lorentzian with a width corresponding to the natural linewidth, the effects discussed above change the shape significantly. If the broadening introduced is symmetric and due to a parameter with Gaussian distribution

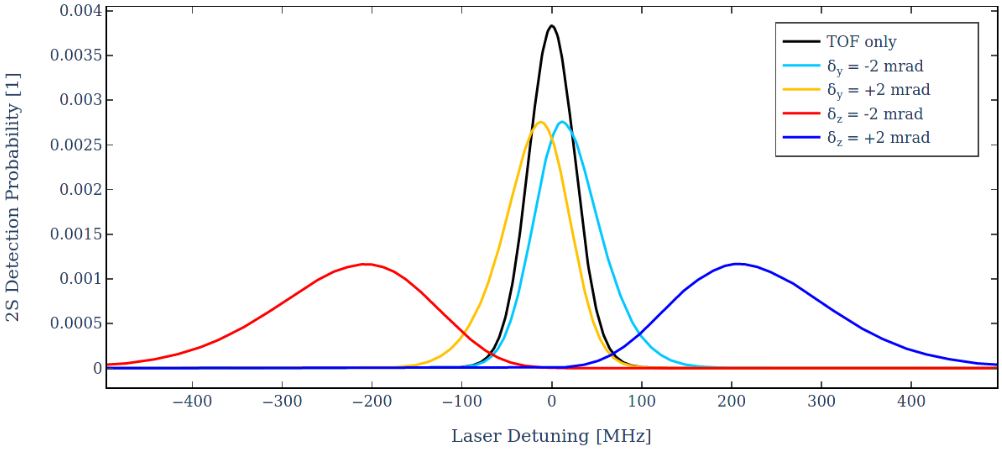

Figure 72: Impact of the residual first order Doppler shift for different magnitude and direction of misalignment on the excitation line shape shown for the geometry used during run 2.

(e.g. for time-of-flight broadening due to a Gaussian spatial profile), the appropriate function to fit would be a Voigt profile, which is given by the convolution of a Lorentzian and a Gaussian profile. However, most effects also introduce skewness to the line shape, which has to be taken into account. Several skewed variations of such profiles exist in the literature (e.g. the skew-normal distribution introduced in equation 44), however, most do not capture all relevant features. We found that using an extended approach based on efforts to model infrared absorption peaks [158] yielded excellent results for a wide range of parameters. Based on the Voigt profile

$$V(\nu,\sigma,\gamma)=\int_{-\infty}^{\infty}G(\nu',\sigma)L(\nu-\nu',\gamma)\,d\nu' \tag{128}$$

where

$$G(\nu,\sigma)=\frac{e^{-\nu^2/(2\sigma^2)}}{\sigma\sqrt{2\pi}} \tag{129}$$

is the Gaussian and

$$L(\nu,\gamma)=\frac{\gamma}{\pi(\mu^2+\gamma^2)} \tag{130}$$

is the Lorentzian distribution, a frequency dependence is included by sigmoidally varying the width parameters, such that

$$\sigma(\nu,\alpha)=\frac{2\sigma_0}{1+e^{\alpha\nu}} \tag{131}$$

and analogously

$$\gamma(\nu,\beta)=\frac{2\gamma_0}{1+e^{\beta\nu}} \tag{132}$$

where α and β are the skewness parameters.

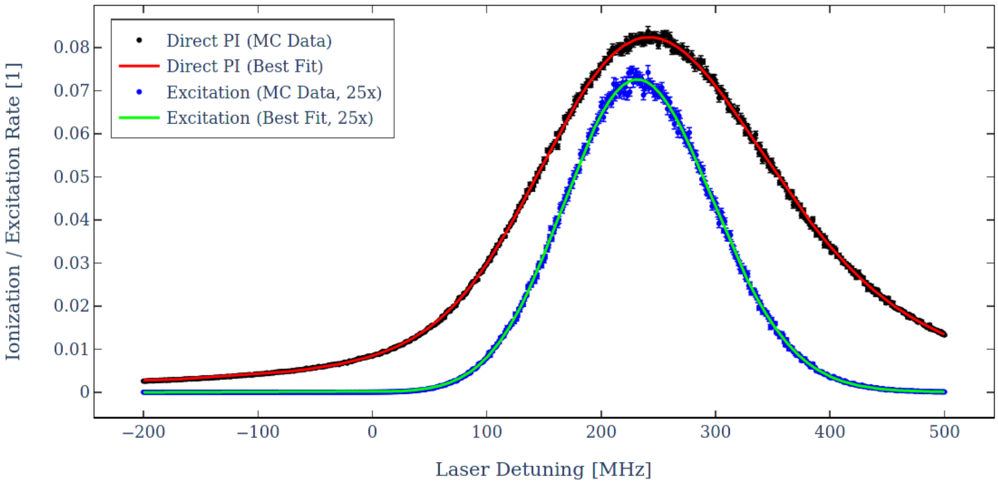

Figure 73: High statistics line shape simulation for direct photo-ionization (black) and excitation (blue), including best fits, using doubly skewed Voigt profiles for the most favoured parameter set during run 1.

Figure 73 shows the output and corresponding fits of a high statistics simulation for the best fit parameter set for run 1 (see section 3.6). The fits have the form

$$LS(\nu, \nu_{\text{loc}}, \sigma_0, \gamma_0, \alpha, \beta, A) = A \cdot V((\nu - \nu_{\text{loc}}), \sigma(\alpha), \gamma(\beta)) \tag{133}$$

where ν_{loc} is a location parameter, that corresponds to the mean value in the limit of no skewness and A is an overall amplitude scaling parameter. The set of parameters of the best fit shown in figure 73 of the photo-ionization line is given by

$$\begin{aligned}
{\nu_{\text{loc}}}^{\text{PI}} &= (247.98 \pm 0.14)\,\text{MHz} && (134)\\
\sigma^{\text{PI}} &= (80.0 \pm 0.53)\,\text{MHz} && (135)\\
\gamma^{\text{PI}} &= (54.78 \pm 0.82)\,\text{MHz} && (136)\\
\alpha^{\text{PI}} &= -2.564 \times 10^{-3} \pm 5.3 \times 10^{-5} && (137)\\
\beta^{\text{PI}} &= -6.2 \times 10^{-5} \pm 1.2 \times 10^{-4} && (138)\\
A^{\text{PI}} &= 26.431 \pm 0.066 && (139)
\end{aligned}$$

while the parameters for the best fit of the excitation lineshape read

$$\begin{aligned}
{\nu_{\text{loc}}}^{2\text{S}} &= (232.92 \pm 0.10)\,\text{MHz} && (140)\\
\sigma^{2\text{S}} &= (65.41 \pm 0.22)\,\text{MHz} && (141)\\
\gamma^{2\text{S}} &= (0.07 \pm 0.32)\,\text{MHz} && (142)\\
\alpha^{2\text{S}} &= -6.11 \times 10^{-4} \pm 6.5 \times 10^{-5} && (143)\\
\beta^{2\text{S}} &= -0.01 \pm 0.10 && (144)\\
A^{2\text{S}} &= 0.47604 \pm 8.7 \times 10^{-4} && (145)
\end{aligned}$$

where the error on the location parameter ν_{loc} corresponds approximately to the error of the line center (since $\alpha \ll 1$ and $\beta \ll 1$).

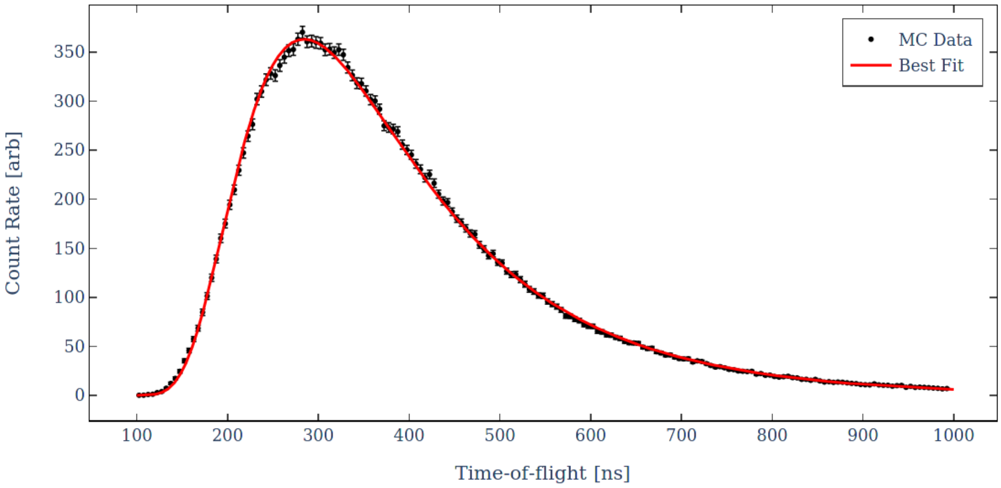

Figure 74: High statistics time-of-flight spectrum simulation (black), including best fit (red) using a χ-distribution for the most favored parameter set of run 1.

In addition to the line shape, the time-of-flight distribution is fitted to allow for direct comparison with measurement. It has been found that a χ-distribution

$$\chi(x,k) = \frac{x^{k-1}e^{-x^2/2}}{2^{k/2-1}\Gamma\left(k/2\right)} \tag{146}$$

with arbitrary (continuous) degrees of freedom k fits the spectra exceptionally well. Figure 74 shows the TOF spectrum corresponding to the line shapes of figure 73 using the function

$$\text{TOF}(t,l,s,k,B) = B \cdot \chi\left(\frac{1/t - l}{s}, k\right) \tag{147}$$

where the parameter l gives location, s time scaling and B overall amplitude. The best fit parameters were found to be

$$l = (5.31 \times 10^{-4} \pm 1.3 \times 10^{-5})\ 1/\text{s} \tag{148}$$

$$s = (1.7231 \times 10^{-3} \pm 4.7 \times 10^{-6})\ 1/\text{s} \tag{149}$$

$$k = 4.00 \pm 0.04 \tag{150}$$

$$B = 1079.5 \pm 3.0 \quad . \tag{151}$$

Note that the choice of distribution is motivated by the Maxwell-Boltzmann velocity profile, which corresponds to a χ-distribution with $k = 3$. However, the parameters do not have a direct physical correspondence since the distribution is a convolution of velocities, excitation and angular emission probabilities.

Several thousand combinations of parameters within experimental limits were used for the Monte-Carlo simulations to cover all possible parameter space for both experimental runs. Each line-shape was then fitted according to the description above, which provides a database of functions to fit experimental results, extract the transition frequency, and estimate the systematic errors of the measurement (see next section).

3.6. Results of the 1S-2S pulsed excitation measurement

Results of run 1: Figure 75 shows the the measured data-points taken during run 1. The results for direct photo-ionization and field-ionization were extracted by peak-counting, while for delayed photo-ionization the integral method was chosen. Due to the relatively short time delay of approximately 10 ns between direct and delayed photo-ionization, the peak-counting method was severely impacted by ringing suppression of the earlier events (see section 3.4) and showed significantly larger errors. The frequency shown corresponds to the value set via PID control on the wavemeter and the systematic error is omitted in the graph.

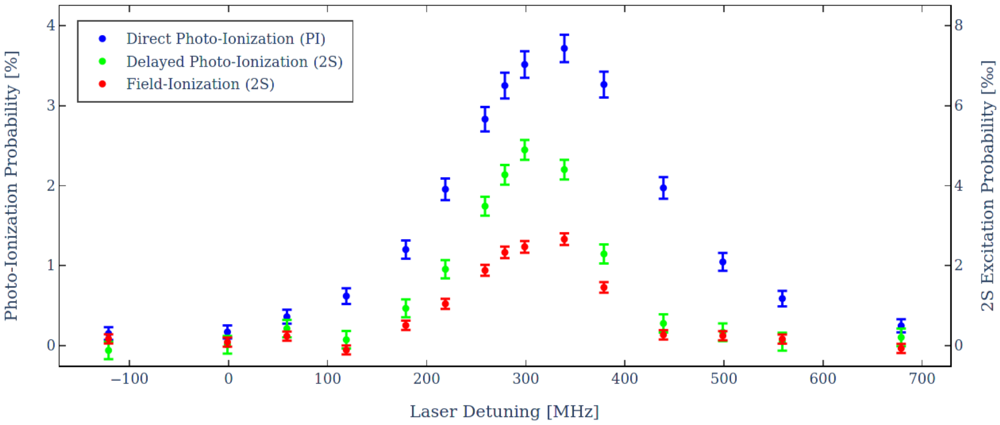

Figure 75: Positronium direct photo-ionization (blue) and 2S excitation probability measured via delayed photo-ionization (green) and field-ionization (red) as a function of laser detuning for data taken during run 1. Note that the laser detuning is given as set on the wavemeter and the systematic error is not shown. Furthermore, the chirp was not measured for this dataset and is therefore not corrected here.

The probabilities were calculated by taking the ratio of charge deposited by backscattered positrons to photo-ionized or field-ionized positronium and multiplying the normalization factor

$$N = \frac{P_{\mathrm{BS}}}{\varepsilon_c\,(1 - P_{\mathrm{BS}})} \approx 0.34\ , \tag{152}$$

where $\varepsilon_c \approx 18.7\%$ is the conversion efficiency of positrons to positronium on the target and $P_{\mathrm{BS}} \approx 0.06$ is the probability of a positron to back-scatter into the detector predicted by simulation (see section 3.4). The overall scale error associated with this normalization factor is not shown. Note that the approximate factor 2 between delayed photo-ionization and field-ionization is due to the fact that the 2S-20P transition is driven close to saturation, while the fraction of 2S atoms photo-ionized in the 532 nm laser is close to 1.

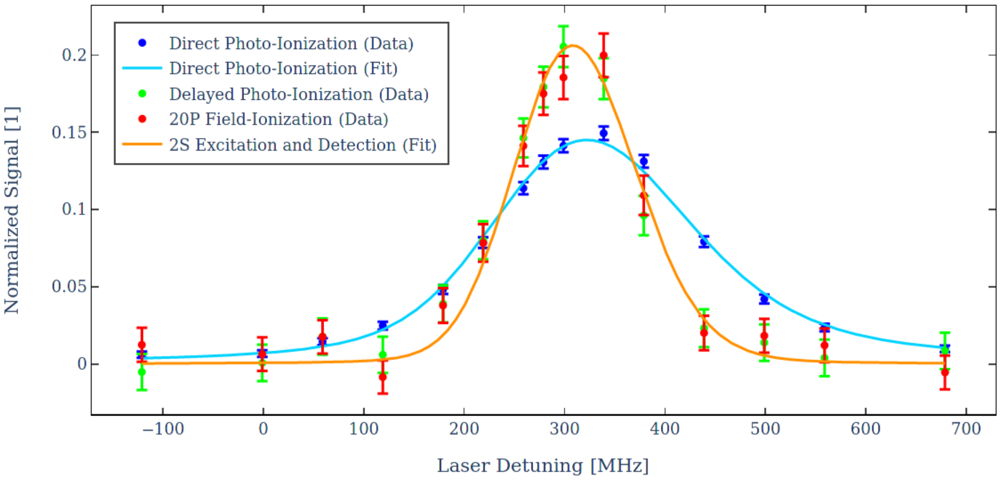

Figure 76: Normalized signal rates and best fit for all simulated parameter sets for run 1.

The process to extract the transition frequency from these results proceeds in three steps. The line-shape of each simulation is fitted simultaneously to all normalized data-points with the only free parameter, aside from the amplitude scaling, being a common offset from zero laser detuning. This allows to establish a correspondence of measured to simulated frequencies for this specific set of parameters. See figure 76 for the results of the best parameter set fit. Note that the data-points are sum-normalized and the fit is error-weighted.

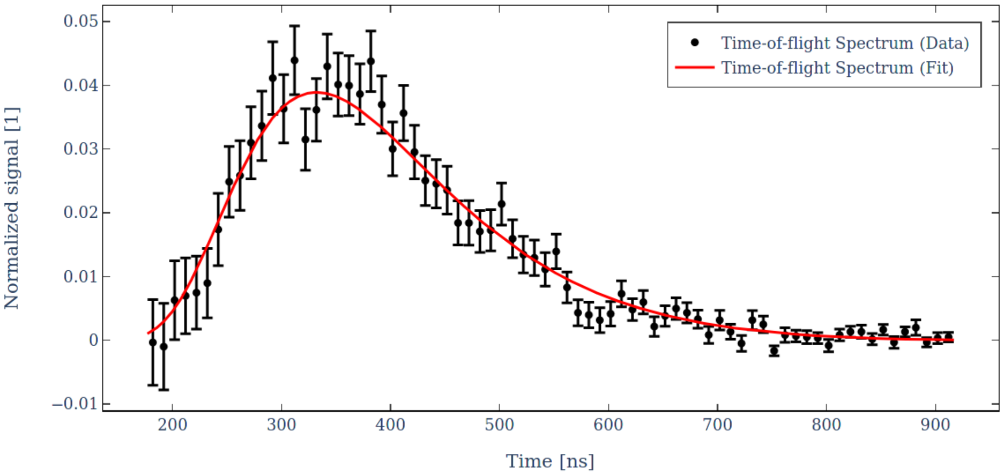

Figure 77: Normalized time-of-flight spectrum and best fit for all simulated parameter sets for run 1.

To achieve the best signal-to-noise ratio for the time-of-flight spectrum, a subset of frequency points around the peak of the transition is chosen to build the histogram. However, due to the Doppler shift the exact shape of the time-of-flight spectrum is unique for each frequency, since certain velocity components are favored for certain offsets. Therefore, the frequency correspondence established in step 1 of the fitting process allows to build the matching histogram from simulation. This histogram is then fitted with a χ-distribution as outlined in section 3.5.2 for each set of parameters available (see figure 74). Note that the simulated time-of-flight distribution assumes a Maxwell-Boltzmann distribution for the initial positronium velocity and the data shows excellent agreement. However, as mentioned in section 3.2, it should be reiterated that there is no reason to expect positronium to be intrinsically thermal at these energies.

Finally, the third step in the fitting procedure entails repeating the process of step one, additionally fitting the normalized time-of-flight spectrum obtained in the second step. The only free parameter in this additional fitting step is the overall amplitude. Figure 77 shows the fitted function of the best parameter set for the respective time-of-flight spectrum. This combined fitting procedure allows for generating a single χ^2 value, which is used to find the best fit for the complete set of parameters simulated.

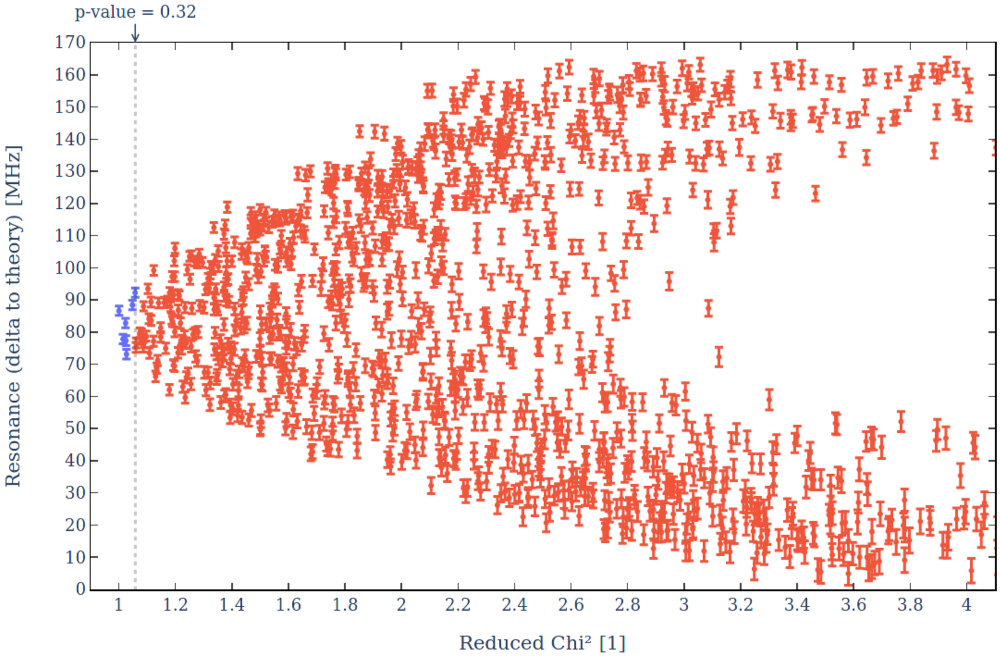

Figure 78: Plot of reduced χ^2 values for the fits of the dataset of run 1 to simulated line-shapes and TOF spectra. The cut-off for a p-value of 0.32 is shown as a dotted line. Fits below correspond to be within a 68% confidence interval and are taken into account for the estimation of the systematic error.

Aside from determining the best fitting set of parameters, this method allows for the extraction of an estimate for the systematic error as well. For each individual fit a

χ^2 test determines the quality-of-fit [159] to the simulated line-shape and time-of-flight spectrum. The reduced χ^2 parameter

$$\chi_r{}^2 = \frac{\chi^2}{\text{d.o.f.}} = \frac{1}{\text{d.o.f.}} \sum_i \frac{(O_i - F_i)^2}{\sigma_i^2} \tag{153}$$

is computed, where O_i and F_i correspond the the i-th observed and fit value, respectively. A cut-off on $\chi_r{}^2$ for a p-value of 0.32 then corresponds to selecting all simulated zero-detuning frequency values that fit the dataset with a confidence level of 68 %, which we will use as an estimator for the systematic error. However, since the true variance σ_i^2 for each data-point is not known a priori, this method can lead to underestimating the systematic error, due to partly unaccounted variance of the dataset or an effect that was not accounted for in the simulation. Therefore, in the case of $\min(\chi_r{}^2) > 1$, the dataset is corrected by multiplying an overall error scaling factor and repeating the fitting procedure, such that $\min(\chi_r{}^2) = 1$.

Magnitude	Description
1.4 MHz	Data Fitting Error
0.9 MHz	Simulation Fitting Error
9.6 MHz	Systematic Fitting Error
15.0 MHz	Chirp Estimation Error
60.0 MHz	Absolute Frequency Reference Error[41]
62.6 MHz	Quadrature Sum

Table 6: Sources and magnitude of statistical and systematic errors present in result for run 1.

Correcting for the chirp in the result is necessary, since our measurements showed chirp on the order of 60 MHz (see discussion of run 2 results below) for this laser system operated in a similar regime. The estimate should be correct to within approximately 25%, judging by the dataset gathered during run 2.

The final result for the resonance frequency in terms of laser detuning obtained during run 1 reads

$$616\,803\,638\,\text{MHz} \pm 63\,\text{MHz} \tag{154}$$

where the respective sources of error can be found in table 6.

This corresponds to a transition frequency of

$$1\,233\,607\,275\,\text{MHz} \pm 125\,\text{MHz} \tag{155}$$

or equivalently, this result differs from theory by

$$53\,\text{MHz} \pm 125\,\text{MHz} \pm 0.6\,\text{MHz} \tag{156}$$

---

[41] It should be noted, that the internal calibration lamp of the device was not functioning at the time of data-taking for run 1 and the device specification states that the absolute error of 60 MHz is guaranteed only if the device is frequently calibrated. However, operating the device in conjunction with a frequency comb over several months, we did not see long-term shifts above approximately 30 MHz from the stored calibration value.

where 0.6 MHz corresponds to the theoretical uncertainty in the 1S-2S interval at $m\alpha^6$ (see section 1.2.1).

Sources of systematic error and respective magnitudes: To ascertain the relative impact of different sources to the systematic error estimate of run 1, a set of additional simulations were produced, varying only individual parameters – in the case of misalignment of the incoming and retro-reflected laser beam, both angles in the XY and XZ plane were scanned. The systematic error corresponding to the respective parameter was then estimated analogously to the method described above.

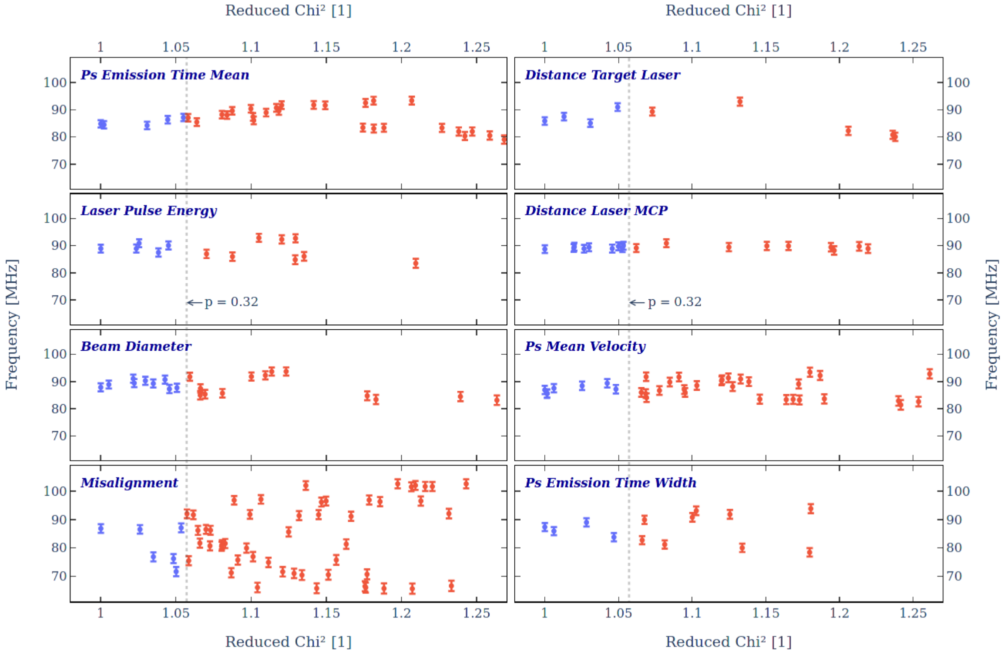

Figure 79: Plot of reduced Chi-Squared values for varying individual simulation parameters of run 1. The cut-offs for a p-value of 0.32 are shown as dotted lines. Fits below correspond to be within a 68% confidence interval and are taken into account for the estimation of the magnitude of the parameters influence on the systematic error.

Figure 79 shows the respective reduced χ^2 values for scans of the individual parameters. The extracted systematic errors can be found in table 7. Note that this method is limited in scope, since individual errors are in general not uncorrelated. A full scan of the parameter space (see figure 78) is necessary to extract a reliable estimate on the overall error. Furthermore, the estimation includes statistical errors due to the fitting procedure of the simulation output and will therefore be overestimated, especially for smaller contributions. However, these results allow to compare the relative impact of the parameter uncertainties on the systematic error.

The most significant contribution to the systematic error stems from the residual first

Magnitude	Parameter
7.7 MHz	Reflection Misalignment
2.9 MHz	Laser Position (relative to target)
2.6 MHz	Positronium Emission Time Spread
1.9 MHz	Positronium Mean Velocity
1.9 MHz	Laser Beam Waist Size
1.7 MHz	Laser Pulse Energy
1.5 MHz	Positronium Emission Time Mean
0.6 MHz	MCP Position (relative to laser)

Table 7: Sources of systematic fitting error for run 1.

order Doppler shift, which is directly proportional to the misalignment of the incoming and retro-reflected beam. Since it also scales linearly with positronium velocity, it is also partly responsible for the contribution from the timing and velocity profile of positronium emission.

Due to the short pulse length (relative to the transit time), the excitation laser preferentially probes a subset of velocities given by its spatial and temporal properties. This results in the second order Doppler shift contributing to the systematic error present on those parameters, as well as on parameters related to the emission profile. To a lesser degree, the AC-Stark shift similarly leads to systematic errors in parameters related to the spatial and temporal intensity profile seen by the positronium atoms, mainly due to uncertainties on the precise beam profile and pulse energy.

Description of laser chirp measurement: For run 2 a pulse-by-pulse chirp measurement was set up (see section 3.3) using an AOM in a second order double pass configuration operating at 92.96 MHz. Figure 80 shows a typical beatnote of a laser pulse and the 371.84 MHz shifted CW seed laser, which was taken with an oscilloscope with 1 GHz bandwidth at 20 GS/s sampling rate.

To extract the instantaneous frequency of the beatnote (which corresponds to the AOM shift plus laser chirp) the signal must first be filtered. Figure 81 shows the one-sided FFT, calculated from the beatnote shown in figure 80 before (black) and after (red) filtering. This is necessary to remove high frequency noise, components related to shifts other than twice the second order of the AOM and to the pulse envelope. To avoid any filter-induced delay, a zero-phase Butterworth band-pass filter is used [152, 153]. This ensures that the chirp calculated from the filtered signal does indeed correspond to the specific timing of the pulse.

After filtering, a Hilbert transformation [160] is used to extract both the instantaneous envelope and frequency (see figure 82). The chirp correction for a specific beatnote is obtained by averaging the instantaneous frequency weighted by the intensity profile. This is done on a pulse-by-pulse basis and each event is then re-binned according to the chirp corrected frequency.

The numerical value of this correction depends on the specific choice of cut-on and cut-

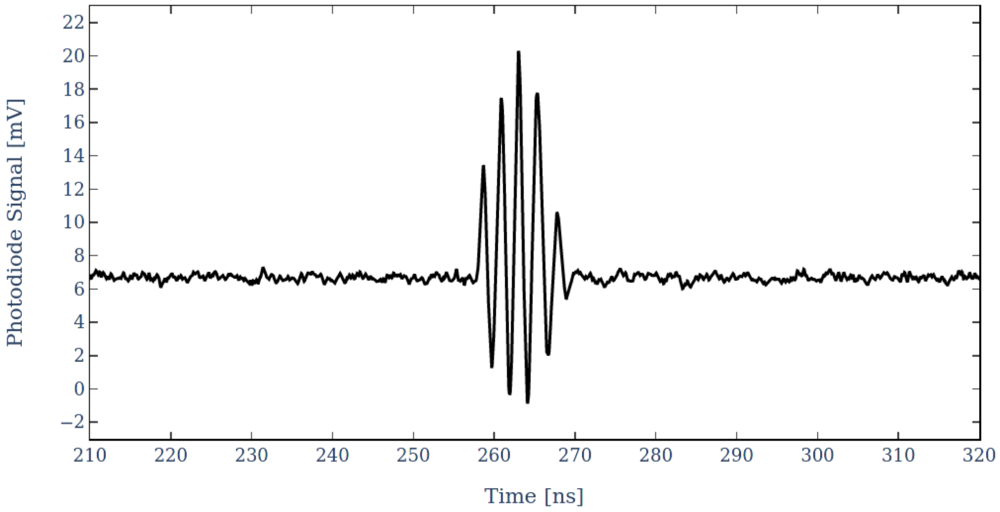

Figure 80: Typical chirp beatnote oscilloscope waveform taken during run 2.

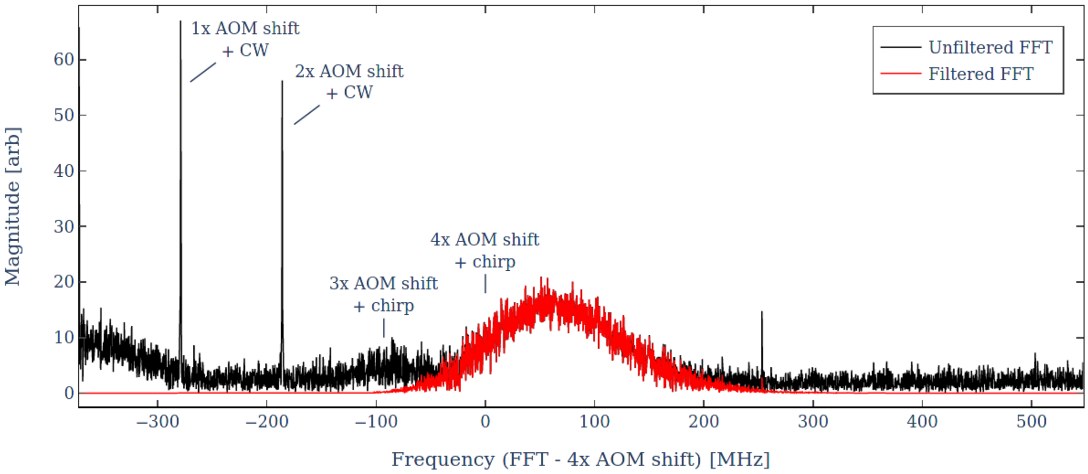

Figure 81: One-sided FFT spectrum of a typical chirp beatnote taken during run 2.

off frequency. These values need to be chosen narrow enough that parts of the frequency spectrum not related to the laser chirp are efficiently suppressed, without removing relevant frequencies. However, the choice is somewhat arbitrary and this limits the precision of the chirp correction. The chirp averaged over the dataset of run 2 was calculated for a reasonable range of filter settings and a standard deviation of 1.03 MHz was found.

Results of run 2: Figure 83 and 84 shows the dataset gathered during run 2 after chirp correction and re-binning, in addition to the best fit determined by χ^2 minimization analogous to run 1. Unfortunately, the statistical error is significantly larger in this

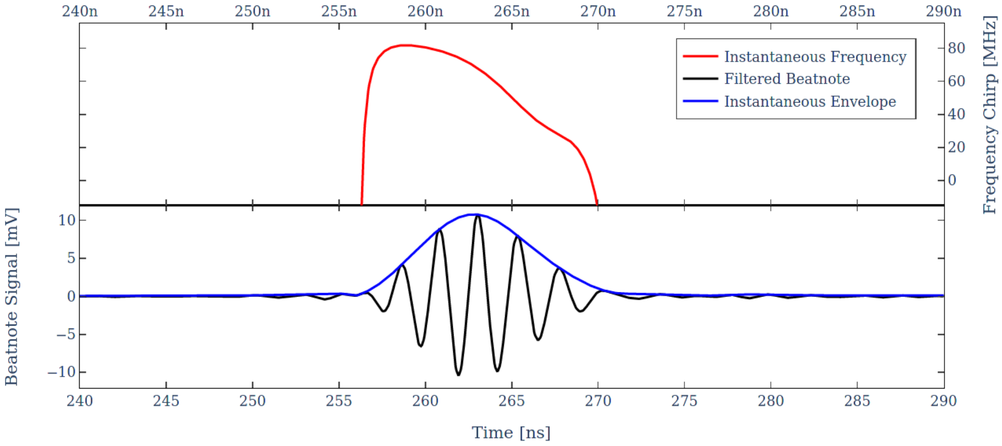

Figure 82: Filtered beatnote, instantaneous envelope and frequency, obtained via Hilbert transformation. Note that the instantaneous frequency is only well defined for times with appreciable pulsed laser intensity, which is why it is only shown here for intensities of at least 1% of the peak value.

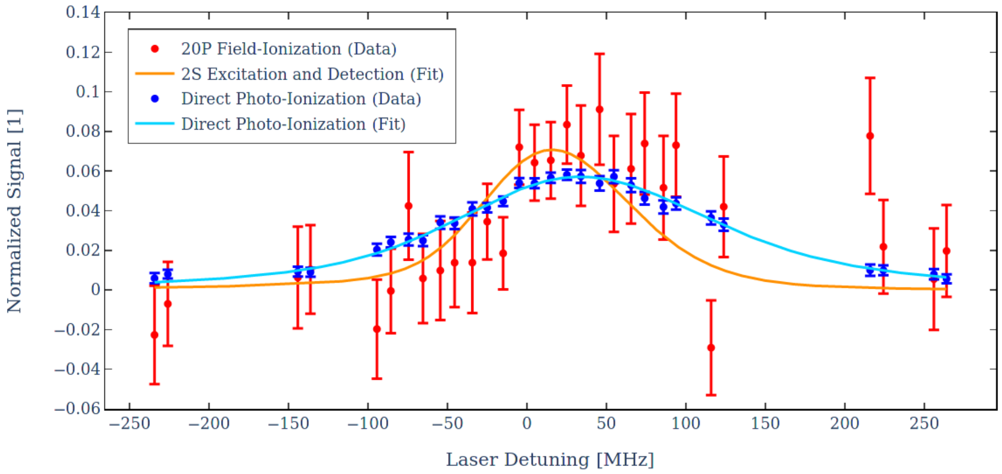

Figure 83: Normalized signal rates and best fit for all simulated parameter sets for run 2.

dataset. Firstly, the supplied positron rate is approximately a factor 2 smaller than for run 2, due to the decay of the sodium source. Furthermore, the solid angle acceptance of the MCP for field-ionization is approximately a factor 2 smaller, in addition to higher losses of the grids due to the shallower angle of incidence. Lastly, we found that the quantum efficiency of the detector for photons from positron decay was significantly higher in this arrangement, most likely due to the increased path length at an angle of 45°. This further decreased the signal-to-noise ratio for this dataset.

The estimation of the systematic error proceeds analogously to run 1. However, due

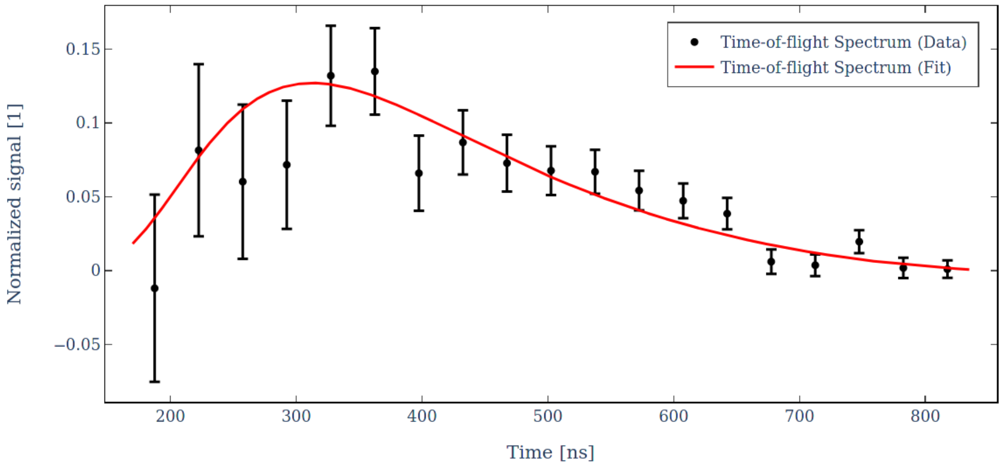

Figure 84: Normalized time-of-flight spectrum and best fit for all simulated parameter sets for run 2.

to larger errors in the data points, the line-shape and time-of-flight spectrum cannot be sampled as precisely and do not have the same impact on the quality-of-fit parameter. Therefore, the error estimate is correspondingly higher than in the case of run 1. The final result for the resonance frequency in terms of laser detuning obtained reads

$$616\,803\,599.2\,\mathrm{MHz} \pm 26.9\,\mathrm{MHz} \tag{157}$$

where the respective sources of error can be found in table 8.

Magnitude	Description
2.1 MHz	Data Fitting Error
0.8 MHz	Simulation Fitting Error
26.8 MHz	Systematic Fitting Error
1.0 MHz	Chirp Correction Error
0.2 MHz	Absolute Frequency Reference Error
26.9 MHz	Quadrature Sum

Table 8: Sources and magnitude of statistical and systematic errors present in result for run 2.

This corresponds to a transition frequency of

$$1\,233\,607\,198.4\,\mathrm{MHz} \pm 53.8\,\mathrm{MHz} \tag{158}$$

or equivalently, this result differs from theory by

$$-23.8\,\mathrm{MHz} \pm 53.8\,\mathrm{MHz} \pm 0.6\,\mathrm{MHz} \quad . \tag{159}$$

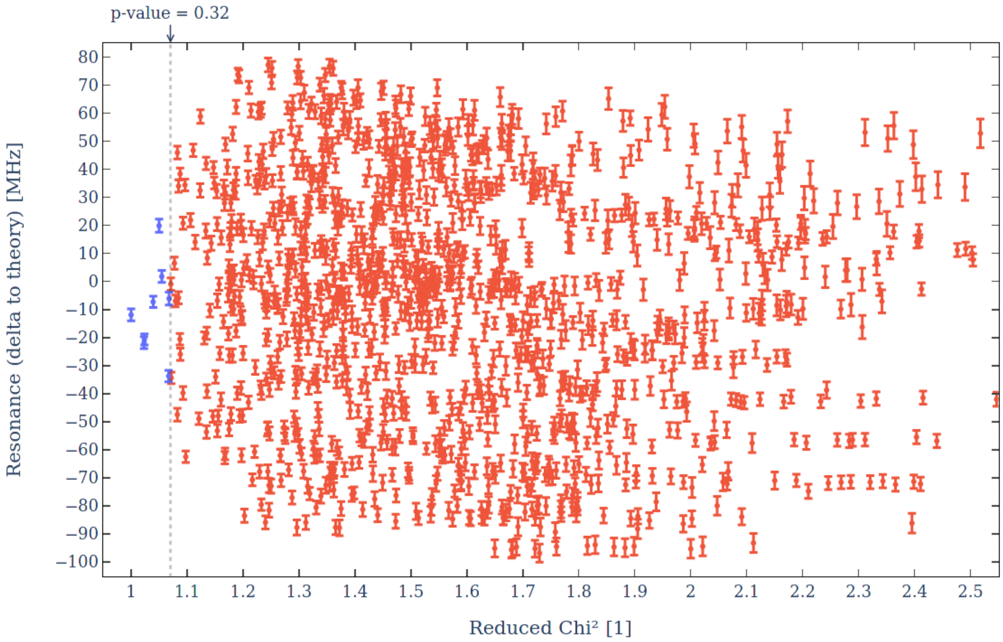

Figure 85: Plot of reduced Chi-Squared values for the fits of the dataset of run 2 to simulated line-shapes and TOF spectra. The cut-off for a p-value of 0.32 is shown as a dotted line. Fits below correspond to be within a 68% confidence interval and are taken into account for the estimation of the systematic error.

Combined result and summary: Assuming uncorrelated measurements, both results can be combined using the maximum likelihood estimator for the mean [159] given by

$$\bar{\mu} = \frac{\sum {}^{x_i}/_{{\sigma_i}^2}}{\sum {}^{1}/_{{\sigma_i}^2}} \tag{160}$$

where the uncertainty of the combined value is given by

$$\sigma_{\bar{\mu}} = \sqrt{\frac{1}{\sum {}^{1}/_{{\sigma_i}^2}}} \quad . \tag{161}$$

The weighted average for the resonance frequency in terms of laser detuning then yields

$$616\,803\,605.2\,\mathrm{MHz} \pm 24.8\,\mathrm{MHz} \tag{162}$$

which corresponds to a transition frequency of

$$1\,233\,607\,210.5\,\mathrm{MHz} \pm 49.6\,\mathrm{MHz} \tag{163}$$

or equivalently, this result differs from theory by

$$-\,11.7\,\mathrm{MHz} \pm 49.6\,\mathrm{MHz} \pm 0.6\,\mathrm{MHz} \quad . \tag{164}$$

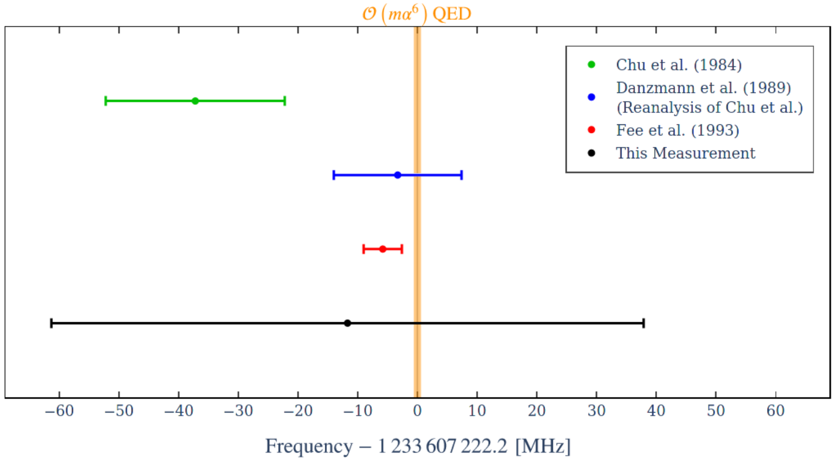

Figure 86: Summary of 1S-2S experimental results and most recent QED theory value and uncertainties. The dataset of Chu et al. (green) [60] was re-analyzed by Danzmann et al. (blue) [144]. The currently most precise experimental value was measured by Fee et al. [62] (red). The shaded orange band corresponds to the theoretical QED prediction at $\mathcal{O}\left(m\alpha^6\right)$ [161] including an error of 0.6 MHz.

Figure 86 shows the result presented here in the context of the most recent QED theory value and and previous experimental values. This measurement is an ongoing effort and improvements of up to two orders of magnitude are envisioned. This will allow to check QED calculations up to the current order $m\alpha^6$ and motivate further developments towards a full calculation of order $m\alpha^7$. Several of these upgrades are discussed in section 5.2.

4. Microwave spectroscopy of Positronium

4.1. Introduction

As outlined in chapter 1, positronium can be considered a precision test bench for bound state QED, due to the absence of effects stemming from the strong interaction in protonic atoms. In addition to the virtual electron-positron annihilation, recoil effects are strongly enhanced [162], which makes it particularly interesting to study not only the 1S-2S transition presented in chapter 2, but also the hyperfine and fine structure intervals.

This chapter will present ongoing efforts towards new high-precision measurements of both hyperfine and fine structure transitions in positronium using the pulsed slow positron beamline at ETH Zurich. While the experimental setup was developed for the measurement of the excited state hyperfine transition, minimal adaptations allow for the measurement of the fine structure, which recently came into focus due to a 4.5σ discrepancy of experiment and theory. The developments are therefore discussed in terms of the hyperfine structure measurement and relevant differences are noted where appropriate. Parts of these developments have been previously reported in earlier work [72, 163, 164] and are reproduced here.

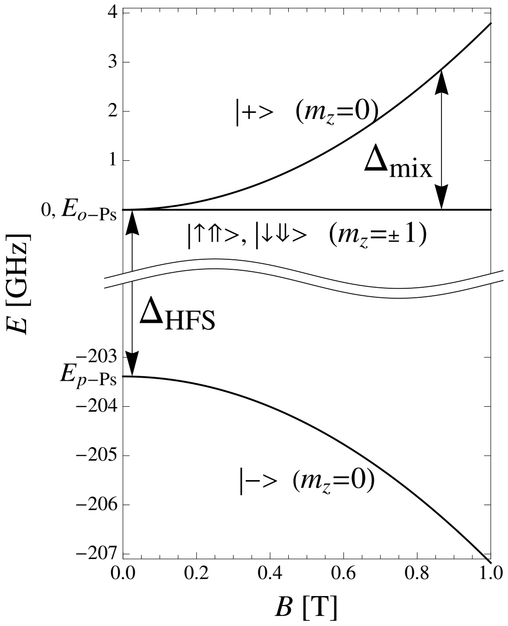

Figure 87: Ground state Zeeman splitting in positronium (*source:* [165])

Experimental Status – Hyperfine Structure Splitting: From the dawn of spectroscopic measurements in positronium, the hyperfine structure was of particular interest, starting in 1951 with measurements by Deutsch [41]. Many of the techniques he pioneered have been used for virtually all subsequent experiments. The most precise determinations of this transition were conducted by Ritter et al. [50] and Mills [49]. While they were all largely compatible with each other, they showed a deviation of almost 4σ from most recent bound state QED calculations.

These experiments share common experimental techniques, which were identified as possible sources of systematic error [166]. Due to the significant technical difficulties in producing the HFS transition frequency $\Delta_{\mathrm{HFS}} \approx 203\,\mathrm{GHz}$, the transition was not measured directly. Instead, it was extracted from the Zeeman splitting measured in a static magnetic field (see figure 87). Therefore, the uncertainty in the uniformity of the magnetic field in the experimental region directly contributes to the systematic error.

Recently, two experiments were conducted trying to minimize these systematic effects by using a very precisely determined magnetic field [165, 167] or by measuring the transition directly using novel millimeter microwave techniques [168]. While the former experiment yielded a result favoring the bound state QED calculations over the previous experimental average, a more precise measurement is needed to conclusively check the discrepancy with theoretical results. The latter experiment, while being completely free of this systematic effect, has very limited experimental sensitivity on the permill level due to the technical challenges involved and can therefore only be considered as a proof of principle.

Furthermore, all experiments conducted so far used gas as a target to form positronium. This influences the measured transition frequency Δ_{HFS} due to the Stark effect induced by local electric fields of the gas atoms. To obtain the HFS in vacuum, extrapolation to zero gas density is needed (see figure 88) – which in turn introduces another source of systematics.

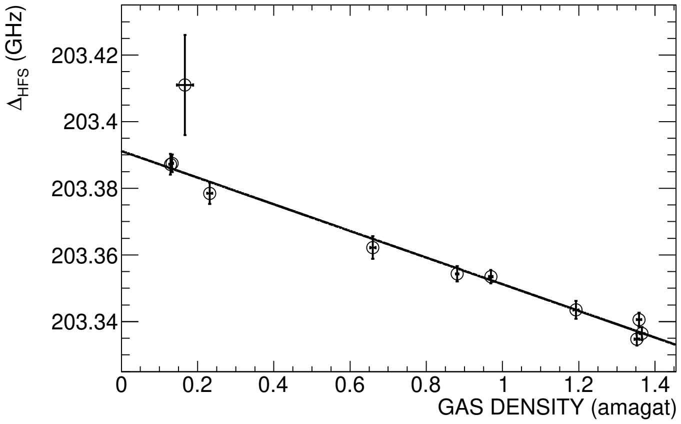

Figure 88: Dependence of measured Δ_{HFS} on the gas density as determined by Ishida et al. [167]

To conclusively resolve the discrepancy between previous experiments and QED calculations, a sufficiently precise direct measurement of the transition frequency in vacuum is needed.

Experimental Status – Fine Structure Splitting: Early measurements of the positronium fine structure relied on the direct generation of excited states on metal surfaces, which in addition to be quite inefficient ($\varepsilon_{2S} \approx 10^{-4}$), can only occur with epithermal positrons [57], which leads to significant Doppler shifts. Spanning two decades, these types of experiments [52–56] determined the fine structure splittings down to the MHz level or equivalently approximately 200 ppm accuracy.

The advent of mesoporous silica targets used with slow positron beams and high intensity laser sources allows experiments, where low energy positronium is efficiently laser-excited to the 2S state and subsequently undergoes fine structure transitions induced by microwave radiation. This allowed to improve a determination on the $2^3\mathrm{S}_1 \rightarrow 2^3\mathrm{P}_0$ interval by almost an order of magnitude to 33 ppm [58], showing a disagreement of 4.5σ with the most recent QED calculations.

This prompts further, more precise measurements probing this discrepancy. Since experimental requirements for fine and hyperfine structure in the excited state overlap in most areas, developments towards a new determination of the $2^3\mathrm{S}_1 \rightarrow 2^1\mathrm{S}_0$ transition can be directly applied for a more precise determination of the $2^3\mathrm{S}_1 \rightarrow 2^3\mathrm{P}_0$ as well.

4.2. Overview

Since the ground state HFS splitting is approximately 203 GHz, this leads to significant technological challenges. The low THz range is one of the last remaining largely undeveloped frequency regions, a fact which is referred to as the Terahertz gap [169]. As such, special devices for the production, manipulation and measurement of such radiation often have to be individually developed, built and characterized, potentially resulting in large systematic uncertainties.

However, as can be seen from equation 25, higher order corrections – among them the hyperfine splitting – roughly scale like n^{-3}. Therefore, exciting positronium atoms to the 2S state allows for the measurement of the $2^3\mathrm{S}_1 \rightarrow 2^1\mathrm{S}_0$ hyperfine transition (see figure 89). Due to the scaling this frequency is approximately 25.4 GHz, which can be generated, manipulated and characterized by using mostly commercially available products.

Instead of using gas as a target for positronium production, a mesoporous thin film silica target (see section 3.2) in conjunction with a slow positron beam (see section 2) can be used. This allows to employ laser excitation to efficiently excite positronium to the first excited state, as outlined in section 3.3. Subsequently the $2^3\mathrm{S}_1 \rightarrow 2^1\mathrm{S}_0$ hyperfine transition can be induced by using microwave radiation amplified by a resonator.

Since the singlet $2^1\mathrm{S}_0$ state decays with a lifetime of approximately 1 ns, positronium traverses only around 100 μm and decays within the resonator after the hyperfine transition is induced (see figure 90). The line-shape can therefore be measured by distinguishing two-photon decays from three-photon decays with high efficiency and measuring the ratio of the two rates. Finally, fitting the simulated lineshape to the data one can extract Δ_{HFS} and compare it to bound state QED theory results.

Contrary to the hyperfine transition, if the fine structure transition is driven, the

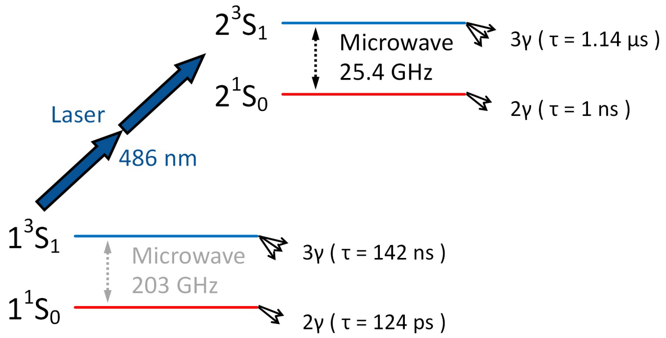

Figure 89: Overview of ground state and excited state hyperfine splittings, decay channels and lifetimes: The two-photon laser excitation is shown with bold arrows, while the hyperfine splitting is shown with dotted arrows. Next to the respective hyperfine states the decay channels and lifetimes can be found.

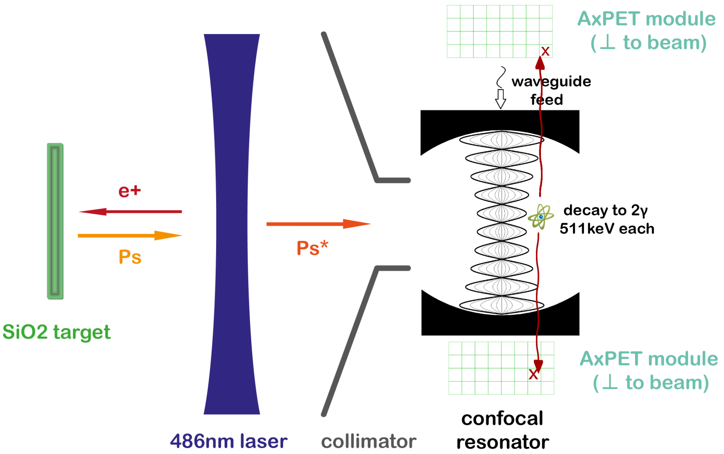

Figure 90: Simplified measurement scheme of the Ps hyperfine transition: Positrons from the bunched positron beam are focused onto the porous silica thin film target. The ejected positronium is then laser excited to the 2S state, spatially filtered and undergoes the hyperfine transition in the microwave field of the resonator. Subsequently, the back-to-back decay photons are picked up by two segmented scintillation detector modules.

annihilation decay channel does not change[42]. However, the 2P state decays radiatively back to the 1S state with a lifetime of approximately 3.2 ns. This leads to a significant increase in the 142 ns ground state decay component during and after traversing the resonator, which can be measured via SSPALS (see section 3.4). As long as the resonator can support both transition frequencies, the same experimental setup can be used for

---

[42] Note that while 2P states can indeed decay via 2 photon annihilation, the rate is negligible compared to radiative decay (see equation 28).

both the hyperfine and fine structure determination.

A collimator is used to reject positronium atoms which are not on paths intersecting the region with appreciable microwave power. This is necessary to increase the signal-to-noise ratio for both types of measurements.

4.3. Laser Excitation

The simulation of the laser excitation stage is based on the Monte-Carlo simulation presented in section 3.5, which was developed for the measurement of the $1^3\mathrm{S}_1 \rightarrow 2^3\mathrm{S}_1$ transition. The code was modified to implement a collimator and to calculate state probabilities entering the resonator, instead of the MCP.

Variable Name	Typical Value	Description
WaistSize	5.5 mm	laser beam minimum waist radius
PulseEnergy	16 mJ	laser pulse energy
PulseFWHM	5.5 ns	FWHM of temporal pulse shape
LaserTimeOffset	25 ns	offset Ps creation / laser max.
MisalignmentY	0 mrad	angle between laser wave-fronts (XY-plane)
MisalignmentZ	0 mrad	angle between laser wave-fronts (XZ-plane)
PositroniumTemp	645 K	temperature for velocity distribution
DistanceSourceLaserX	10 mm	X-axis distance target / mirror
DistanceSourceLaserY	0 mm	Y-axis distance target / laser
DistanceSourceLaserZ	3 mm	Z-axis distance target / laser
SigmaBeamX	1.5 mm	X-axis spread of Ps creation area
SigmaBeamY	1.5 mm	Y-axis spread of Ps creation area
SigmaEmission	17 ns	timing spread of Ps creation

Table 9: Laser excitation parameter set for best signal-to-noise ratio for HFS and FS measurements.

The available parameter space of experimental variables (see tables 3 and 4) was scanned, while the positronium emission profile was set to the best fit values obtained in the data-analysis for run 1 at 4 keV implantation energy. To optimize for signal-to-noise ratio, the best set of parameters is chosen such that the ratio of excited state to ground state fraction is maximized.

Figure 91 shows the probability for a positronium atom emitted into vacuum to reach the resonator either in the excited or ground state, depending on the laser detuning for this parameter set. Note that these probabilities already include the respective decay rates for both states, while propagating to the cavity. The peak 2S probability is approximately $P_{2\mathrm{S}} = 1.3\,\%$, which corresponds to a rate of

$$R_{\mathrm{res}}^{2\mathrm{S}} = N_{oPs} \cdot P_{2\mathrm{S}} = 4200 \cdot 1.3\,\% = 55 \tag{165}$$

of 2S atoms per second at the resonator, where the center-axis is placed at 52 mm distance to the laser. Similarly, the corresponding probability for 1S atoms to reach the resonator of approximately $P_{1S} = 1.0\,\%$ leads to a rate of

$$R_{\text{res}}^{1S} = N_{oPs} \cdot P_{1S} = 4200 \cdot 1.0\,\% = 42 \tag{166}$$

of remaining 1S atoms per second at the resonator.

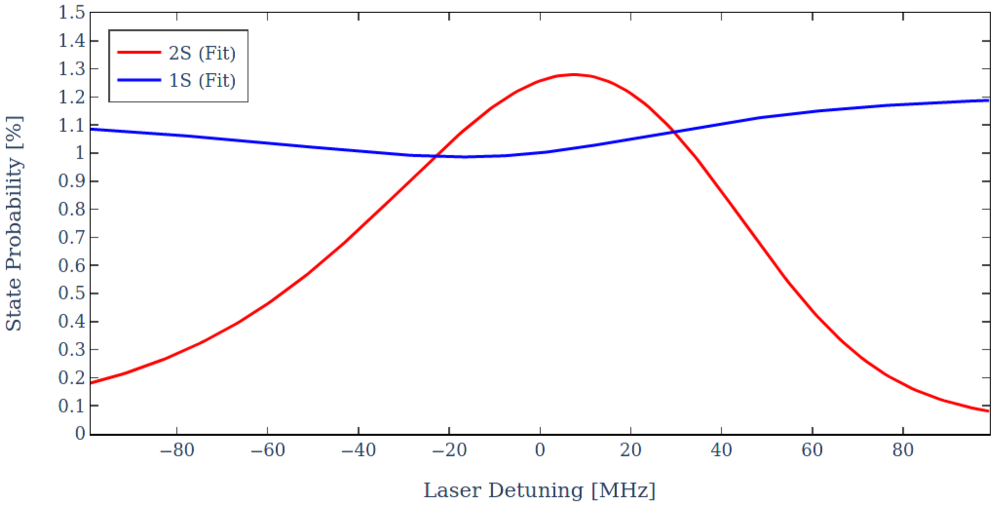

Figure 91: Probability of an emitted positronium atom to reach the resonator either in the excited or ground state. The remaining fraction is either filtered out by the collimator, photo-ionized or decayed while propagating to the cavity.

To ascertain the impact of specific parameters, the simulations were split in subsets for these parameters and the optimum settings for the best signal-to-noise ratio were extracted. The values therefore correspond to the best achievable performance, given a fixed value for one parameter. Note that due to the discrete spacing of the simulated parameter space, the resulting curves are not necessarily smooth.

The dependence of simulation results on the minimum waist size can be found in figure 92. As can be seen from this graph, the best excitation rate peaks at approximately 5.5 mm. Larger beams are generally advantageous due to the improved overlap with different velocity components of the emitted positronium. However, due to the limited pulse energy – up to 16 mJ was simulated, which corresponds roughly to the pulse energy that can be delivered to the experimental chamber after losses – there are diminishing returns for larger beams.

Therefore, higher power is generally preferable, as long as it can be offset with larger beam dimensions to achieve ideal intensities. This is the case if the intensity is high enough that the excitation is efficient without being overwhelmed by direct ionization. Since the simulation allows for comparably large beam diameters, figure 93 shows saturation for pulse energies above approximately 12 mJ. Note that the oscillatory behavior is an artifact of the discrete sampling of the waist size.

The excitation probability is also dependent on the timing between the creation of the positronium atoms and the temporal maximum of the laser pulse. To first order, the

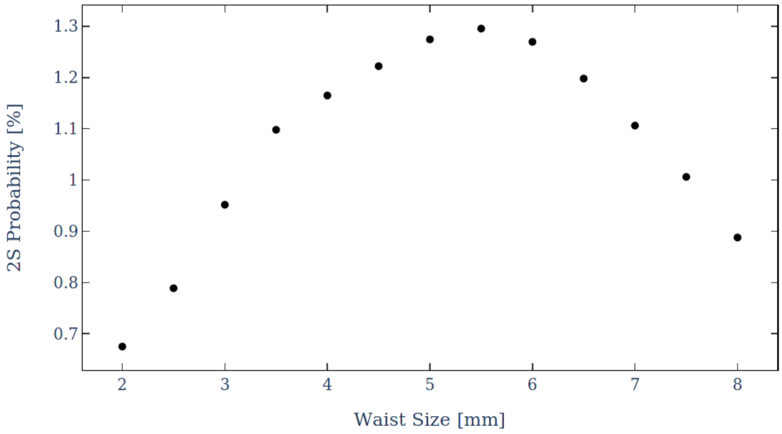

Figure 92: Excited state fraction for best signal-to-noise ratio vs. laser waist size

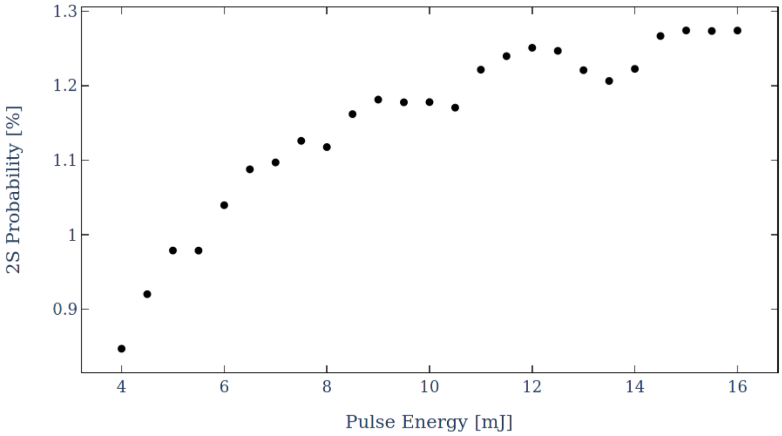

Figure 93: Excited state fraction for best signal-to-noise ratio vs. pulse energy

maximum is given by the most probable propagation time of the atoms from the target to the center axis of the laser. However, due to the relatively broad velocity distribution and large optimal waist sizes, the excitation efficiency is rather insensitive to the exact timing within 5-10 nanoseconds around the optimal value (see figure 94).

As can be seen from figure 95 the excited state fraction also depends on the exact position of the laser. This is a result of the laser aperture of 6 mm diameter on the target holder, as well as the fraction of ground state atoms decaying before reaching the laser. While shorter distances can be somewhat mitigated by timing and increased waist sizes, longer distances show significant losses due to decays.

4.4. Microwave Excitation

The hyperfine (M1) transition is achieved by using a time-varying magnetic field to resonantly flip the spin of either the electron or the positron. As mentioned in chapter

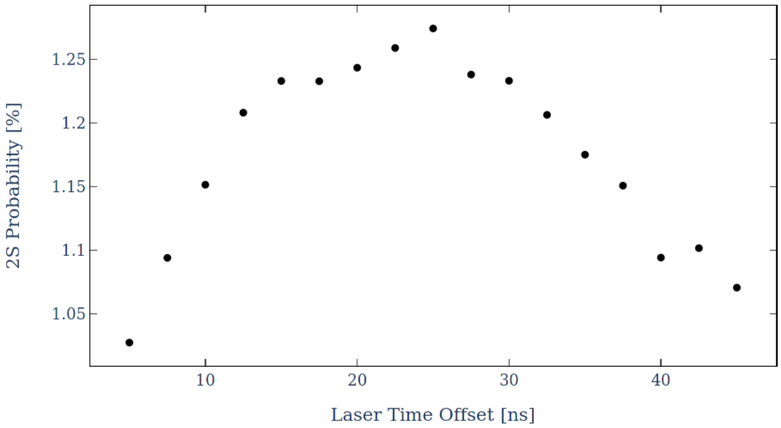

Figure 94: Excited state fraction for best signal-to-noise ratio vs. laser pulse delay

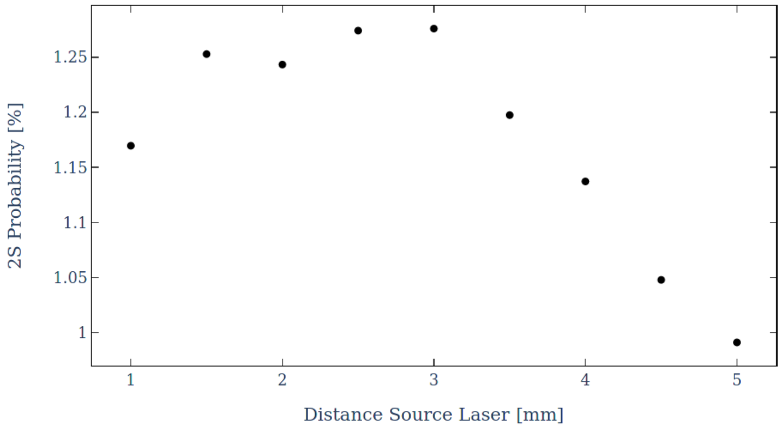

Figure 95: Excited state fraction for best signal-to-noise ratio vs. axial target-laser distance

4.2, the transition frequency is about 25.4 GHz, for which a resonant cavity can be used to form standing microwaves. Similarly, the electric field can impart angular momentum to induce the fine structure (E1) transition from 2S to 2P states, for which the frequencies are approximately 18.5 GHz, 13.0 GHz and 8.6 GHz. The attainable strength of the electromagnetic field in such a cavity is limited by the input power P_{in}, the coupling losses, and the quality factor Q of the cavity.

Usually, the laser excitation region and the resonant cavity are spatially separated, but this can lead to large losses, due to the limited lifetime and poor solid angle coverage. Ideally, one would use cryogenic positronium to mitigate these shortcomings and achieve longer interaction times, but this poses significant experimental challenges, some of which are discussed by Crivelli et al. in [170]. However, spatial separation brings with it the advantage of background suppression due to ground state decays and the option to use open confocal resonators, which can be built with extraordinarily high Q values.

On the other hand, as has been shown by Cooke et al., a tube-like geometry can be used to spatially confine positronium, where losses due to collisions with the walls are negligible [71]. This opens up the possibility to use a closed resonator to simultaneously induce transitions and confine positronium in the same volume. This would drastically increase the interaction time with the microwave radiation and therefore the transition probability.

This section will present two distinctly different possibilities to realize a resonant cavity, a closed rectangular waveguide design and an open confocal resonator design. While both options are viable and offer distinct advantages each, the confocal resonator design was chosen for the initial experimental setup, since it proved easier to implement and allows to use a single design for both the hyperfine and fine structure measurements. The final design of the confocal mirrors can be found in Appendix B.

Waveguide resonator: The simplest geometry for a resonator implementing a tube-like structure is a rectangular waveguide, close-circuited on both ends. To find its characteristics, it is first assumed that the walls are perfect conductors and only in a second step losses in the conducting walls are included to calculate its Q value.

To find the electric and magnetic fields in a box with width w, height h and length l, one makes the ansatz [171]

$$\vec{E} = \vec{E}_0(x, y, z)\, e^{-i\omega t} \quad \text{and} \quad \vec{B} = \vec{B}_0(x, y, z)\, e^{-i\omega t} \ , \tag{167}$$

with the boundary conditions

$$\vec{E}_{\parallel} = 0 \quad \text{and} \quad B_{\perp} = 0 \tag{168}$$

with respect to the perfectly conducting walls.

Using equations 167 in Maxwell's equations yields the time-independent set of differential equations

$$\begin{aligned} \nabla \cdot \vec{E}_0 &= 0 \\ \nabla \cdot \vec{B}_0 &= 0 \\ \nabla \times \vec{E}_0 &= i\omega \vec{B}_0 \\ \nabla \times \vec{B}_0 &= -\frac{i\omega}{c^2} \vec{E}_0 \end{aligned} \tag{169}$$

to which the most general solution for $\vec{E}_0$ is

$$\vec{E}_0 = \begin{pmatrix} (a_1 \sin k_x x + b_1 \cos k_x x)\,(c_1 \sin k_y y + d_1 \cos k_y y)\,(e_1 \sin k_z z + f_1 \cos k_z z) \\ (a_2 \sin k_x x + b_2 \cos k_x x)\,(c_2 \sin k_y y + d_2 \cos k_y y)\,(e_2 \sin k_z z + f_2 \cos k_z z) \\ (a_3 \sin k_x x + b_3 \cos k_x x)\,(c_3 \sin k_y y + d_3 \cos k_y y)\,(e_3 \sin k_z z + f_3 \cos k_z z) \end{pmatrix} \tag{170}$$

where

$$k_x^2 + k_y^2 + k_z^2 = -\frac{\omega^2}{c^2} \ . \tag{171}$$

Making use of the boundary conditions from equations 168, the electric field equations read

$$\begin{aligned} E_x &= 0 \quad \text{for } y = 0,\ z = 0,\ y = h \text{ and } z = l \\ E_y &= 0 \quad \text{for } x = 0,\ z = 0,\ x = w \text{ and } z = l \\ E_z &= 0 \quad \text{for } x = 0,\ y = 0,\ x = w \text{ and } y = h \end{aligned} \tag{172}$$

with integer values m, n and p for

$$k_x = \frac{m\pi}{w}, \quad k_y = \frac{n\pi}{h}, \quad k_z = \frac{p\pi}{l} \ . \tag{173}$$

From the first line in equation 169 it further follows that

$$A = C = E = 0 \quad \text{and} \qquad B k_x + D k_y + F k_z = 0 \ . \tag{174}$$

The full solution for the electric field therefore simplifies to

$$\vec{E} = \begin{pmatrix} B \, \cos k_x x \, \sin k_y y \, \sin k_z z \\ D \, \sin k_x x \, \cos k_y y \, \sin k_z z \\ F \, \sin k_x x \, \sin k_y y \, \cos k_z z \end{pmatrix} e^{-i\omega t} \ . \tag{175}$$

The solution for the magnetic field can be found by using the third relation in equation 169 resulting in

$$\vec{B} = \frac{1}{\omega} \begin{pmatrix} (D\, k_z - F\, k_y) \, \sin k_x x \, \cos k_y y \, \cos k_z z \\ (F\, k_x - B\, k_z) \, \cos k_x x \, \sin k_y y \, \cos k_z z \\ (B\, k_y - D\, k_x) \, \cos k_x x \, \cos k_y y \, \sin k_z z \end{pmatrix} e^{-i(\omega t - \pi/2)} \ . \tag{176}$$

The waveguide resonator allows for a wide range of resonant frequencies. They can be calculated from equation 171, using relation 173, to be

$$\omega = c\,\pi \sqrt{\frac{m^2}{w^2} + \frac{n^2}{h^2} + \frac{p^2}{l^2}} \ . \tag{177}$$

Dropping the restriction of perfectly conducting walls, it can be shown by using a perturbation technique, that the resonator does not only support discrete frequencies, but a continuous spectrum (see figure 96) [172]. Its FWHM is given by

$$\Gamma = \frac{\omega_0}{Q} \tag{178}$$

and the resonant frequency of the cavity is shifted by

$$\Delta\omega \approx -\frac{\omega_0}{2Q} \ . \tag{179}$$

Calculating the losses in the cavity walls and using relation 221, one finds the unloaded[43] Q factor for rectangular resonators to be [173]

$$Q = \frac{\pi\,\eta}{4\,R_S} \left(\frac{2h\ (w^2 + l^2)^{3/2}}{w\,l\ (w^2 + l^2) + 2h\ (w^3 + l^3)} \right) , \tag{180}$$

---

[43] The unloaded Q factor describes the quality of the cavity without taking coupling losses or absorption within the cavity into account.

where η is the wave impedance

$$\eta = \sqrt{\frac{\mu}{\varepsilon}} \xrightarrow{\text{vacuum}} \eta_0 = \sqrt{\frac{\mu_0}{\varepsilon_0}} = 376.730313\,\Omega \tag{181}$$

and the surface resistivity R_S is given by

$$R_S = \sqrt{\frac{\omega\,\mu_0\,\rho}{2}}\ , \tag{182}$$

with ρ being the specific resistivity of the wall material.

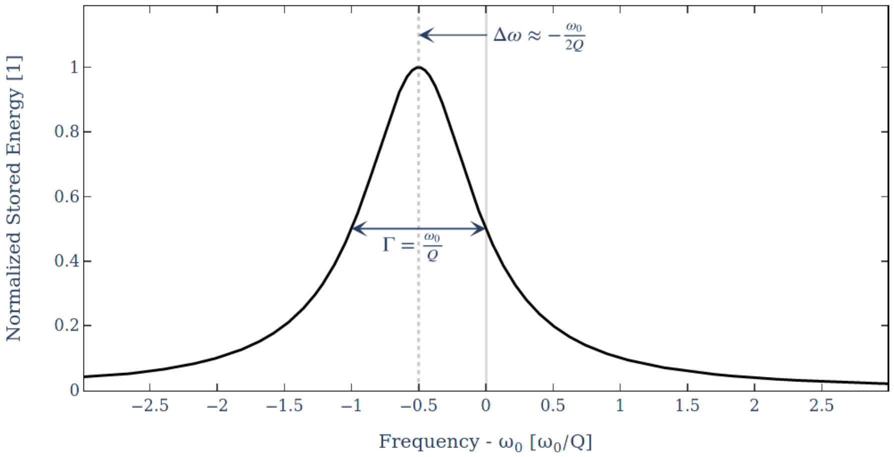

Figure 96: Resonance line shape of cavity with resistive losses including frequency shift $\Delta\omega$ and spread Γ (FWHM). The frequency axis represents the detuning from the unperturbed resonance, given in units of the resonance frequency ω_0 divided by the quality factor Q.

Confocal resonator: Strictly speaking, a confocal resonator consists of two spherical mirrors with identical bending radii placed in a distance d equal to their curvature R. Usually these resonators are used slightly off the confocal point to avoid instabilities and resonant frequency degeneracies. Such cavities are well known in laser physics, but they can be used equally well for microwaves in the centimeter range.

To find the field configurations in such a resonator, one makes the ansatz [174]

$$E = u(x, y, z)\, e^{-ikz}\, e^{i\omega t}\ , \tag{183}$$

for the potential of a wave traveling in the z direction.

One then uses equation 183 with the scalar wave equation

$$(\nabla^2 + k^2)\, E = 0 \tag{184}$$

to find the paraxial wave equation

$$\frac{\partial^2 u}{\partial x^2} + \frac{\partial^2 u}{\partial y^2} - 2ik\frac{\partial u}{\partial z} = 0\ , \tag{185}$$

where it was assumed that u varies very slowly with z.

One now looks for a solution of equation 185, given the boundary conditions of the mirrors confining the beam. For simplicity, a perfectly conducting smooth surface and infinite extent of the mirrors are assumed here. Solutions of the paraxial wave equation are well known and are usually categorized in Hermite-Gaussian and Laguerre-Gaussian modes. In this case the solutions of interest are the latter ones, because of the cylindrical symmetry of the mirrors. In cylindrical coordinates they read [175]

$$\begin{aligned} u_{n,p}(r,\phi,z) = & \frac{1}{w(z)}\sqrt{\frac{2n!}{\pi(|p|+n)!}} e^{i(2n+|p|+1)\Psi(z)} \left(\frac{\sqrt{2}\,r}{w(z)}\right)^{|p|} e^{-\frac{ikr^2}{2R_C(z)}+ip\phi-\frac{r^2}{w^2(z)}} \\ & \times L_n^{(p)}\left(\frac{2\,r^2}{w^2(z)}\right) \end{aligned} , \tag{186}$$

where n and p are the radial and azimuthal indices characterizing the specific mode and $w(z)$ is the waist size. Since it is usually preferable to only excite a single mode in a resonator and only the amplitude is of interest, equations 183 and 186 simplify to

$$|E(r,z)| = \frac{1}{w(z)}\sqrt{\frac{2n!}{\pi(|p|+n)!}} \left(\frac{\sqrt{2}\,r}{w(z)}\right)^{|p|} e^{-\frac{r^2}{w^2(z)}} L_n^{(p)}\left(\frac{2\,r^2}{w^2(z)}\right) , \tag{187}$$

where $L_n^{(p)}$ is the associated Laguerre polynomial.

Ideally, most of the amplitude should be concentrated on the z-axis. From the part

$$\left(\frac{\sqrt{2}\,r}{w(z)}\right)^{|p|} \tag{188}$$

it can be seen that the azimuthal mode number should then be chosen to be zero. By the same argument the radial mode number should be zero, such that the Laguerre polynomial gives only a constant part:

$$L_0^{(0)}\left(\frac{2\,r^2}{w^2(z)}\right) = 1 . \tag{189}$$

The resulting mode, using these preferred parameters,

$$|E(r,z)| = \sqrt{\frac{2}{\pi\,w^2(z)}}\, e^{-\frac{r^2}{w^2(z)}} , \tag{190}$$

is called the fundamental mode or Gaussian Beam.

The waist size is then given by

$$w(z) = w_0\sqrt{1+\left(\frac{z\,\lambda}{\pi\,w_0^2}\right)^2} , \tag{191}$$

where λ is the radiation wavelength and it was assumed that the minimum waist size is found at the origin, such that

$$w_0 = w(z=0) \ . \tag{192}$$

To find the waist size at the mirrors, equation 191 with $z = {}^{d}\!/_{2}$ is used to yield

$$w_m = w_0 \sqrt{1 + \left(\frac{2d\,c}{\omega\, w_0^2}\right)^2} \ , \tag{193}$$

where the following expression was used for the phase velocity of the radiation:

$$c = \frac{\lambda\,\omega}{2\pi} \ . \tag{194}$$

The minimum waist size of the Gaussian Beam is found at the point where the phase fronts are plane [174], to be

$$w_0 = \frac{c}{\omega}\sqrt{d(2R-d)} \ . \tag{195}$$

The resonance condition is given to first order by a multiple of the wavelength fitting in the resonator. For this reason the resonant frequencies are described in terms of the fundamental beat frequency

$$\omega_0 = \frac{c\,\pi}{d} \ . \tag{196}$$

However, due to different phase velocities of the respective modes, one needs to add the correction

$$\omega = \omega_0(m+1) + \omega_0\,\frac{1+n+p}{\pi}\,\arccos\left(1 - {}^{d}\!/_{R}\right) \ , \tag{197}$$

where m+1 gives the number of half-wavelengths fitting into the resonator or equivalently m gives the number of planes with zero amplitude along the z-axis.

Analogous to the waveguide cavity, the confocal resonator acquires a continuous spectral response if losses are included, such as ohmic losses or a finite extent of the mirrors (see equations 178, 179 and figure 96).[44]

To find the Q value of the confocal resonator, one first calculates the power losses per round-trip of the beam [176]. For a perfectly Gaussian mode the losses due to spillover are given by

$$\beta_D = e^{-\frac{D^2}{2w_m^2}} \ , \tag{198}$$

where D is the diameter of each mirror. The ohmic losses in the mirror walls are given by

$$\beta_\rho = 4\sqrt{2\,\omega\,\varepsilon_0\,\rho} \ , \tag{199}$$

where ρ is the specific resistivity of the mirror material.

To arrive at the unloaded Q value one then combines these losses to yield

$$Q = \frac{2\,\omega\,d}{c\,(\beta_D + \beta_\rho)} \ . \tag{200}$$

---

[44] Note that for finite mirror extents the Laguerre-Gaussian modes are actually only approximate solutions to the paraxial wave equation. However, the approximation is good as long as losses due to spillover can be neglected compared to other losses.

4.4.1. Electromagnetic field configuration

Eigenmodes of resonant cavities are usually denoted by which of the field components are zero in the transverse (by definition: z) direction. If $E_z = 0$, they are called TE_{mnp} (transverse electric) or TM_{mnp} (transverse magnetic), if $B_z = 0$. Note that TEM_{mnp} modes, for which $E_z = B_z = 0$, can not exist in waveguide resonators without an inner conductor, since the only configuration that is allowed by equation 174 with the condition $E_z = B_z = 0$, is $B = D = F = 0$ in equation 175 and therefore the resonator contains no field at all. Conversely, modes in confocal resonators are always of the TEM_{mnp} type, since all allowed solutions of the paraxial wave equation imply $E_z = B_z = 0$.

Waveguide resonator: Since the resonant frequency must match the respective fine or hyperfine transition of positronium, the dimensions are fixed by relation 177 for given m, n and p. Since m, n and p represent the number of extrema in the fields in each spatial direction, they can be chosen accordingly. From equation 175 it can be seen that at most one of those integers can be 0, otherwise the field would be 0 in all components. p is elected to be zero, to achieve constant magnetic fields over the length of the resonator, which is parallel to the exciting laser beam. From equation 176 follows that this is a TM mode.

Since the hyperfine transition is mediated via the magnetic field component, one value for either m or n needs to be even and the other odd, since the field would be zero in the center of the cavity otherwise. Under these considerations, the smallest values for m and n is chosen to maximize the flux density in the center and to keep the dimensions as small as possible. The two remaining options are either the mode TM_{120} or TM_{210}.

Conversely, for the fine structure transition, the electric field should be maximal in the center of the cavity, which is the case for the TM_{110} mode. Since both the width and height are free parameters in equation 177, we can choose the dimensions such that the cavity is resonant for two modes of different frequencies at the same time. Choosing the TM_{210} mode at the hyperfine transition frequency of 25.422 GHz and the TM_{110} mode to drive the $2^3\mathrm{S}_1 \rightarrow 2^3\mathrm{P}_0$ transition at 18.496 GHz, we find the dimensions by using the relation

$$\omega_{\mathrm{HFS}}{}^2 - c^2\pi^2\left(\frac{4}{w^2} + \frac{1}{h^2}\right) = \omega_{\mathrm{FS}}{}^2 - c^2\pi^2\left(\frac{1}{w^2} + \frac{1}{h^2}\right) \tag{201}$$

where we used the squared equation 177 and the respective values for m and n. Solving for the width we find

$$w = \frac{c\pi\sqrt{3}}{\sqrt{\omega_{\mathrm{HFS}}{}^2 - \omega_{\mathrm{FS}}{}^2}} = 14.89\,\mathrm{mm} \tag{202}$$

and therefore

$$h = \frac{2}{\sqrt{\left(\frac{\omega_{\mathrm{HFS}}}{c\pi}\right)^2 - \frac{1}{w^2}}} = \frac{1}{\sqrt{\left(\frac{\omega_{\mathrm{FS}}}{c\pi}\right)^2 - \frac{1}{w^2}}} = 9.66\,\mathrm{mm} \quad . \tag{203}$$

The resulting magnetic field for the hyperfine structure cavity configuration is shown in figure 97. The magnetic flux density in the center of the cavity is given by

$$|B| \approx \sqrt{P_{\mathrm{in}}} \cdot 1.55\,\frac{\mathrm{G}}{\mathrm{W}^{1/2}} \ , \tag{204}$$

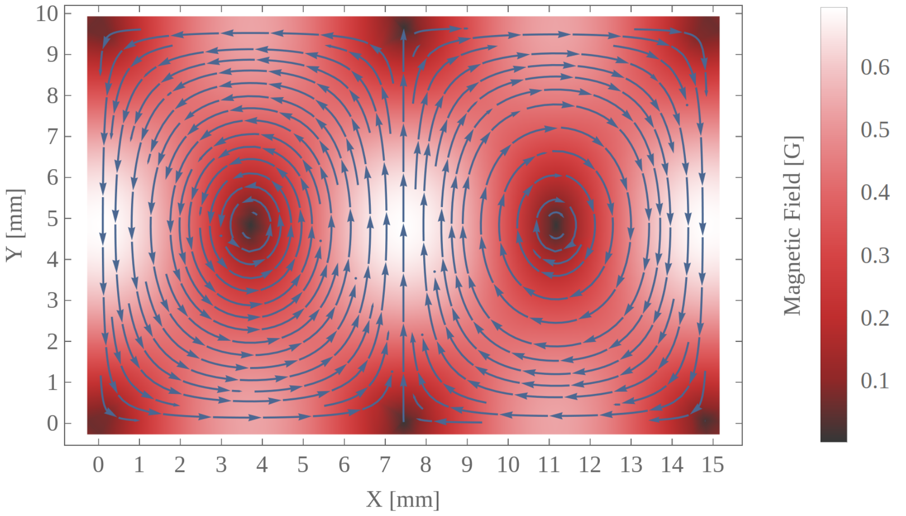

Figure 97: TM_{210} magnetic field configuration of resonant waveguide at 25.422 GHz using $P = 200\,\mathrm{mW}$ input power.

where P_{in} is the power coupled into the cavity. Furthermore, the unloaded Q factor of the cavity can be calculated, using equation 180 and the specific conductivity of copper at room temperature $\rho = 1.71 \times 10^{-8}\,\Omega\,\mathrm{m}$ to be

$$Q \approx 4400\ . \tag{205}$$

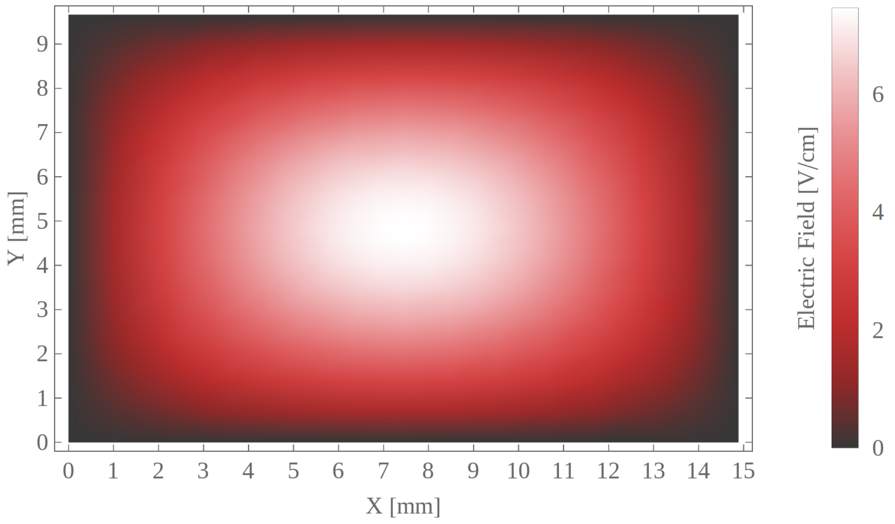

Figure 98: TM_{110} electric field configuration of resonant waveguide at 18.496 GHz using $P = 0.1\,\mathrm{mW}$ input power. Note that the direction of the electric field vector for this configuration is parallel to the z-axis and not shown here.

The resulting electric field for the fine structure cavity configuration is shown in figure 98 and the electric field strength in the center of the cavity is given by

$$|E| \approx \sqrt{P_{\text{in}}} \cdot 746 \, \frac{\text{V}}{\text{cm}\,\text{W}^{1/2}} \ . \tag{206}$$

The unloaded Q factor amounts to

$$Q \approx 5200 \ . \tag{207}$$

Confocal resonator: As has been argued in section 4.4, the respective TEM mode for the confocal resonator should have $n = 0$ and $p = 0$ to concentrate the field on the center axis of the resonator. Both the distance between the mirrors d and the bending radius R must then be chosen such that equation 197 gives the required transition frequency for arbitrary m.

Frequency	m	d [mm]	Q_0
25.422 GHz	6	43.33	52484
25.422 GHz	8	55.54	67022
25.422 GHz	10	67.52	80680
25.422 GHz	12	79.60	86359
18.496 GHz	4	43.35	35372
18.496 GHz	6	60.14	45960
18.496 GHz	8	76.90	38776

Table 10: Resonator length and unloaded Q value for various fundamental modes of the confocal cavity.

Due to the availability of mechanical tools at the manufacturing company, a radius of curvature of

$$R = 79.6\,\text{mm} \tag{208}$$

was chosen. The mode number m should be chosen even, such that the field in the center of the cavity, where the highest positronium flux is expected, is not zero. Furthermore, to realize a cavity of at least a few cm width (due to solid angle considerations), the fundamental mode number should be sufficiently large. Table 10 shows the resulting distances d between the mirrors and the unloaded Q factor – using the room temperature conductivity of $\rho = 1.71 \times 10^{-8}\,\Omega\,\text{m}$ – for a selection of reasonable mode numbers for both the hyperfine transition frequency of 25.422 GHz and the $2^3\text{S}_1 \rightarrow 2^3\text{P}_0$ transition at 18.496 GHz, given by equations 197 and 200. Note that due to coupling considerations (see section 4.4.2) other fine structure transitions are not supported with this setup.

To make sure only the specific fundamental modes would be excited, frequencies of all modes up to $m = n = p = 10$ were calculated. It was found that every mode was separated more than at least two times the FWHM of the spectral response from the relevant TEM_{m00} modes.

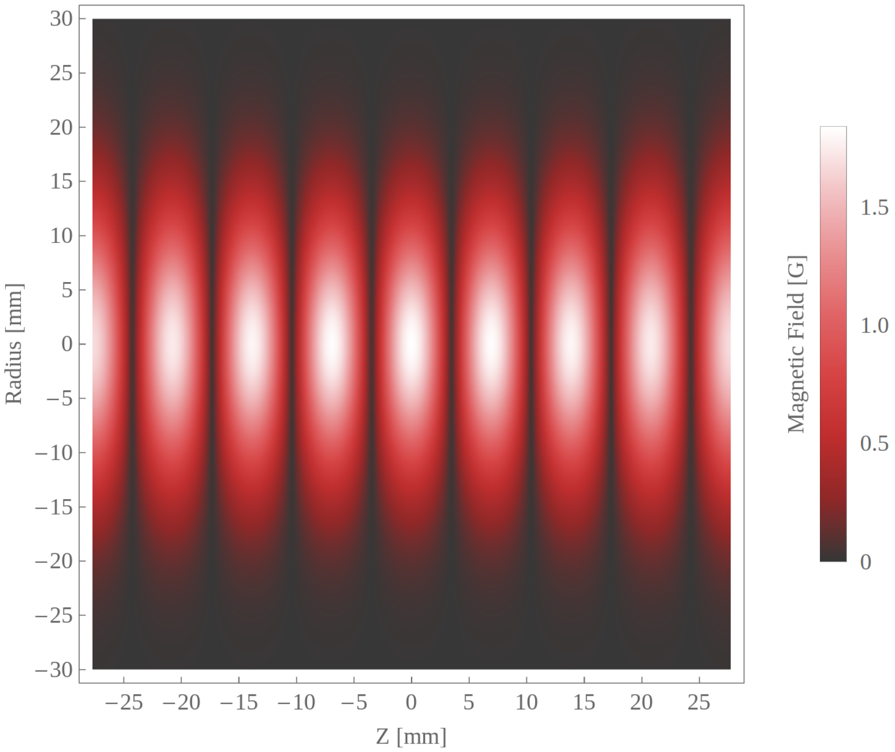

Figure 99: TEM_{800} magnetic field configuration of confocal resonator at 25.422 GHz using $P = 200\,\mathrm{mW}$ input power. Note that this is not the field in the cross-section of the cavity, but as viewed from the target.

The increased Q value leads to significantly stronger magnetic fields than in the waveguide cavity. Setting aside coupling losses for the moment, this would lead to magnetic flux densities for the TEM_{800} mode at 25.422 GHz in the center of the cavity of

$$|B| \approx \sqrt{P} \cdot 4.12\,\frac{\mathrm{G}}{\mathrm{W}^{1/2}}\ . \tag{209}$$

Similarly, the electric field for the fine structure configuration in the TEM_{600} mode at 18.496 GHz leads to

$$|E| \approx \sqrt{P} \cdot 983\,\frac{\mathrm{V}}{\mathrm{cm\,W}^{1/2}} \tag{210}$$

in the center of the cavity.

4.4.2. Further design considerations

The aforementioned resonator designs have some shortcomings, which need to be addressed in any final design. On one hand, a high Q value is needed to produce sufficient field strength to induce an appreciable amount of transitions (especially for the hyperfine measurement), on the other hand this introduces a problem for the measurement of the absolute frequency of the transition.

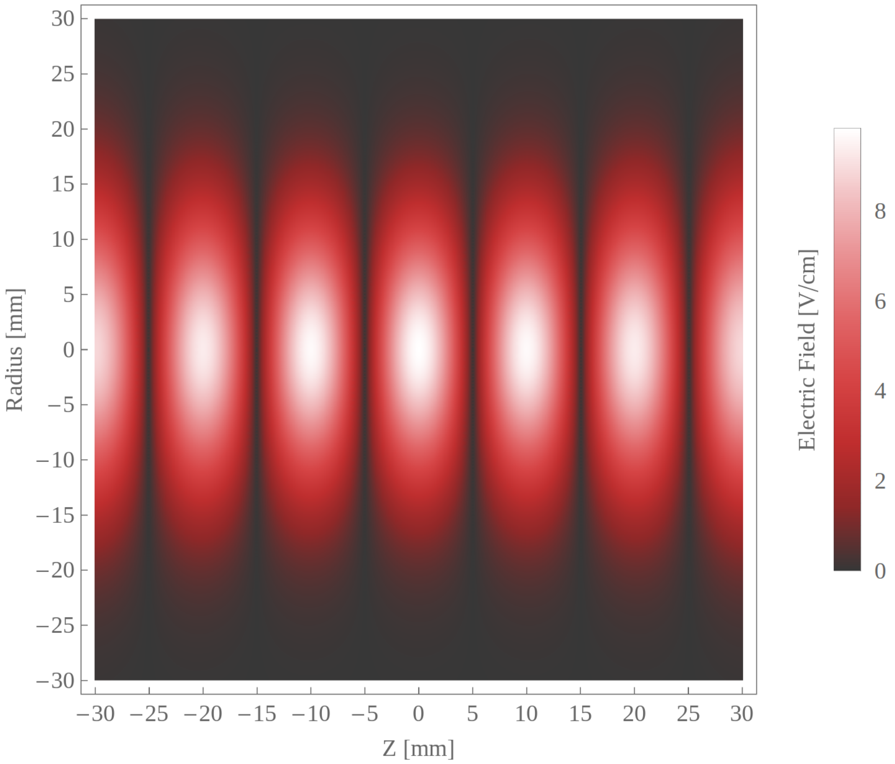

Figure 100: TEM_{600} electric field configuration of confocal resonator at 18.496 GHz using $P = 0.1\,\text{mW}$ input power. Note that this is not the field in the cross-section of the cavity, but as viewed from the target.

The resonance line shapes are broadened due to the short lifetime of positronium (see equation 216, acquiring a FWHM on the order of 100 MHz, while the FWHM of the cavity line shape is much smaller with

$$\frac{\Gamma_{WG}}{2\pi} = \mathcal{O}(10\,\text{MHz}) \tag{211}$$

for the waveguide cavity and

$$\frac{\Gamma_{CR}}{2\pi} = \mathcal{O}(1\,\text{MHz}) \tag{212}$$

for the confocal resonator.

This means that by scanning through the frequency on the input device, one effectively measures the cavity response and not the resonance line shape. This can be avoided by introducing a variable width in the cavities dimensions and locking this dimension with the input frequency. Furthermore, depending on the specific design, the coupling of the microwave source to the cavity can be problematic and introduce serious losses.

While both designs are viable to be used in the hyperfine and fine structure measurement, it was decided to use the confocal resonator design, at least to acquire first measurements. While it is expected that especially for the hyperfine measurement the waveguide design would feature significantly larger statistics [163] and (if it could be pulsed) a significantly better signal-to-noise ratio, it would undoubtedly represent a much more challenging endeavor. Some of the reasons for this are outlined in the remainder of this chapter.

Waveguide resonator: Scanning of the resonant frequency could in practice be achieved by cutting the cavity in two parts and join them with a flexible, highly conductive mesh. The distance could then be changed by a few hundred microns by a piezoelectric actuator, e.g. a PI P-603. This way the cavities frequency spectrum (see figure 96) can be locked to the input frequency, such that the maxima are always matched up. To scan over the FWHM of the hyperfine and fine structure transition line-shapes, changes in distance between the two parts of a few 100 μm would be required.

There is also a strong inhomogeneity in the magnetic flux density (see figure 97) in the waveguide cavity volume for the TM_{210} mode. If the positronium atoms could be confined to a region with relatively high energy density, then the (average) transition probability would increase drastically. This could be done by filling most of the cavity with a solid dielectric (see figure 101).

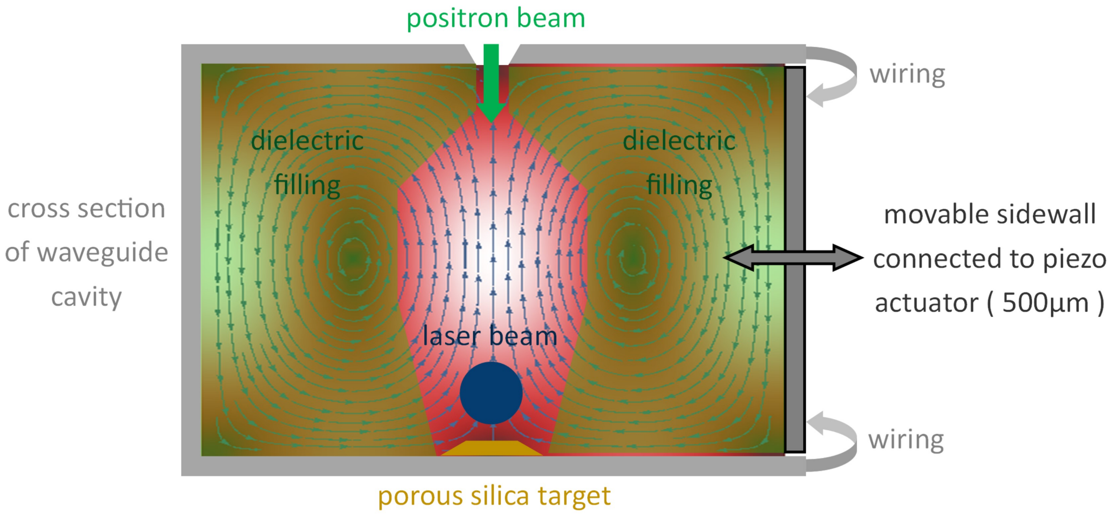

Figure 101: Schematic cross section of possible waveguide resonator design.

The choice of dielectric is problematic though and warrants further investigation. Ideally the dielectric constant should be close to $\varepsilon_r = 1$, such that it does not interfere with the electric field and the analytic solutions from section 4.4 are still good approximations. Most of the available materials with a low dielectric constant are plastics, which are problematic in a vacuum environment due to outgassing. Possible materials that could be investigated are, e.g HDPE [177, 178] or PTFE [179]. Another option would be to use some sort of glass, e.g. fused quartz. While this would be a superior choice regarding mechanic and vacuum properties, glasses typically have a dielectric constant around $\varepsilon_r = 4$ to $\varepsilon_r = 7$. For these materials the Maxwell's equations cannot be easily solved analytically, so one has to use simulation to investigate the field configurations. Preliminary simulations show that the magnetic flux density is decreased in the interaction region, but the homogeneity is enhanced [163]. Furthermore, it was found that the resonant frequencies are significantly shifted. If such a material was to be used, extensive further simulation would be necessary to characterize the specifications of such a cavity.

Furthermore, using a dielectric might lead to surface charges accumulating due to the positron bombardment. This could then lead to a deflection of the beam and therefore a loss in conversion efficiency. Also, the coupling into the cavity is not straightforward using this design and would need extensive simulation and testing.

The waveguide design is specific to a set of two resonant frequencies for the chosen modes and cannot easily be modified. Furthermore, the approximate inverse scaling of the resonator dimensions with the resonance frequency complicates efforts to implement interchangeable cavities to measure the $2^3\mathrm{S}_1 \rightarrow 2^3\mathrm{P}_2$ transition at 8.6 GHz and $2^3\mathrm{S}_1 \rightarrow 2^3\mathrm{P}_1$ transition at 13.0 GHz.

Confocal resonator: In contrast to the waveguide cavity, changing the resonant frequency does not need any altering of the design. One simply mounts one of the mirrors in a fixed location and the other mirror movable, such that the resonant frequency is tuned by changing the position.

As in the case of the waveguide resonator (see above), a piezoelectric actuator can be used to reliably tune the distance d between the mirrors. To scan over the FWHM of the HFS and FS transition line shapes a change in distance between the two halves of a few $100\,\mu$m is required, which was realized using a PI Q-521 linear piezo actuator.

Another significant advantage of a confocal resonator design is that it effectively functions in the same way as a pulsed resonator. During the time of flight of the positronium atoms from the source to the resonator region, a large fraction of the ground state will decay, while decays in the excited state occur with a decay rate, which is smaller by a factor of 8. The transit time of the arriving atoms through the microwave beam is then on the order of 100 ns. Additionally, a slit collimator can naturally be implemented between the laser beam and the resonator, filtering out remaining atoms which are not excited by the laser.

However, spatial separation of the conversion and interaction region still means significant losses of excited state atoms due to the limited geometric acceptance of the resonator. Furthermore, as can be seen in figures 99 and 100, the electromagnetic field is very inhomogeneous over the length of the resonator. While this problem is somewhat mitigated by the $\cos\theta$ distribution of the emitted positronium atoms, which effectively averages over the field, some losses have to be accepted.

To arrive at a final design one needs to include the coupling of the microwave input to the resonator. The most straightforward solution is a cylindrical through-hole in the center of one of the mirrors with a waveguide attached to it. Following Dunseith et al. [176] one finds that the ideal coupling hole diameter for critical coupling is approximately 2.9 mm, which depends on both the unloaded Q factor and resonant frequency. Table 11 shows the fraction of power coupled into the cavity C_p and loaded Q value Q_L for the modes shown in table 10. The circulating power in the cavity is the product of the Q factor, coupling efficiency and incident power on the coupling hole.

Frequency	m	C_p	Q_L
25.422 GHz	6	94 %	32607
25.422 GHz	8	89 %	44410
25.422 GHz	10	84 %	56476
25.422 GHz	12	77 %	66894
18.496 GHz	4	64 %	35372
18.496 GHz	6	50 %	45960
18.496 GHz	8	29 %	45088

Table 11: Fraction of power coupled into the resonator and loaded Q value for various fundamental modes of the confocal cavity.

While the resonator design can in principle accommodate a wide range of resonant frequencies – assuming low coupling efficiencies are not an issue – the waveguides used to feed the cavities do not. They generally have a lower and upper frequency cut-off and need to be operated within. The current mirrors are designed for WR-42, which supports frequencies between approximately 14 GHz and 28 GHz. Both the hyperfine and the $2^3\mathrm{S}_1 \rightarrow 2^3\mathrm{P}_0$ fine structure transition are therefore supported with this specific resonator design. However, since the overall dimensions of the resonator and waveguide feed do not change significantly, interchangeable mirrors with WR-75 waveguide feed offer a drop-in replacement to measure the two remaining fine structure transitions.

4.4.3. Experimental results on cavity performance:

The resonator parameters for the hyperfine transition were chosen such that the only excited mode is the fundamental with design values of a loaded Q factor of approximately 32600 at critical coupling (see preceding section) or equivalently a FWHM ≈ 0.8 MHz of the spectral response. This is significantly smaller than the transition line-shapes, which are broadened due to the short lifetime of positronium to the order of 100 MHz FWHM. Therefore, a piezo actuator is used to lock and stabilize the cavity to the input frequency, by controlling the distance between the two spherical mirrors. The stabilization and monitoring system is based on a simple custom scalar network analyzer (see figure 102) with a feedback loop to the piezo actuator, which allows for the cavity to be stabilized to the percent level while taking data [180].

The spectral response of our confocal resonator setup was measured to have a FWHM of about $\Gamma \approx 2\pi \cdot 1$ MHz and $Q \approx 26300$, which are close to the design value. However, as shown in figure 103, only about 70 % of the incident power is coupled into the cavity. This is likely due to a small mismatch of the coupling hole size at room temperature, since the ideal coupling hole size depends on the unloaded Q and therefore on the resistive losses in the cavity. In the final vacuum setup, the cavity is cooled and stabilized with thermoelectric elements. Furthermore, a second set of mirrors with a smaller coupling

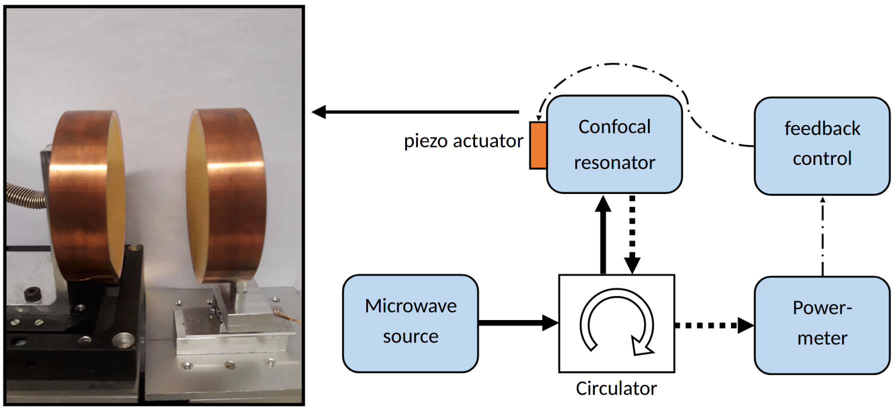

Figure 102: Left: Confocal resonator test setup including piezo actuator. Right: Schematic overview of the cavity monitoring and control system: The microwave radiation is directionally coupled via a circulator into the resonator, while the reflected power is directed into a powermeter. A feedback loop controls the piezo actuator used to stabilize the cavity.

hole diameter was produced and is available to be optimized for ideal coupling, e.g. by iteratively widening the coupling hole size via wire erosion.

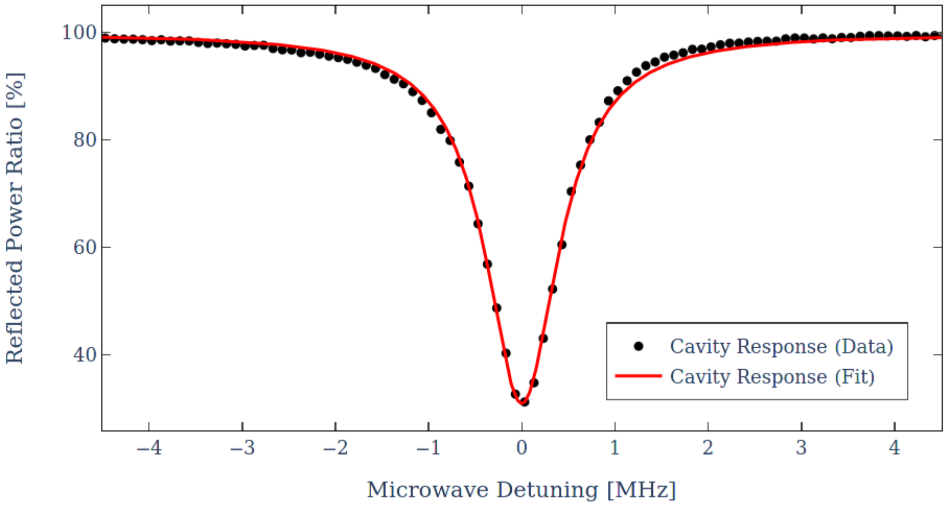

Figure 103: Measured spectral response of confocal resonator including Lorentzian simple fit for the TEM_{600} mode at 25.422 GHz. The data was calibrated offline to the spectral response of the system without the cavity.

Preliminary testing showed similar performance for the corresponding fine structure configuration using the TEM_{400} mode. A FWHM of $\Gamma \approx 2\pi{\cdot}0.6$ MHz and $Q \approx 34100$ was found. The incoupled fraction was not measured due to missing calibration references. However, since the fine structure transition is E1 as opposed to the M1 hyperfine transition, the excitation rate is approximately a factor $\alpha^{-2} \approx 2 \times 10^4$ higher. The required power is correspondingly lower and the resonator should be operated at approximately $\mathcal{O}(10\,\mathrm{mW})$ circulating power, which can be easily achieved, even with significantly degraded coupling.

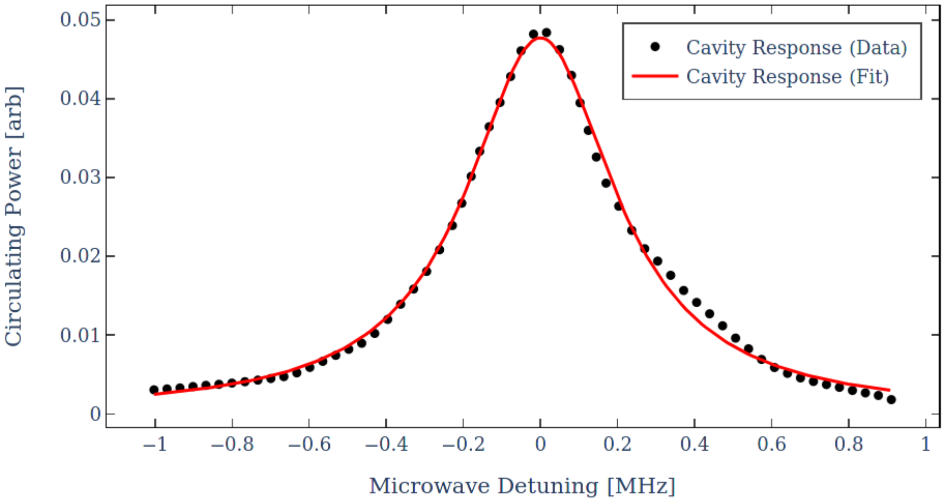

Figure 104: Measured spectral response of confocal resonator including Lorentzian simple fit for the TEM_{400} mode at 18.496 GHz. Since no calibration was available for this measurement, the fraction of power coupled into the cavity can not be extracted.

4.5. Detection system

4.5.1. Hyperfine structure detection system

To detect the two back-to-back[45] 511 keV photons of the annihilation of the 2^1S_0 state and to discriminate and reject the overwhelming background of three photon decays of the 2^3S_1 and 1^3S_1 states, excellent spatial and good temporal resolution is required of a detector. These and most other detector requirements are virtually the same for Positron Emission Tomography (PET), a medical imaging technique measuring positron annihilations in biological material.

Such a detector has been developed, amongst others, by the Group of Prof. Dissertori at ETH Zurich within the AX-PET collaboration as a demonstrator device [181] and was refurbished to be used for spectroscopic measurements at the slow positron beam facility[46]. The following sections will describe the detector, its readout system, signal and background characteristics in more detail and will present the results of a simulation, written using Geant4, to assess the performance of the detection system.

---

[45] The boost given by the positroniums kinetic energy can be neglected in an excellent approximation.

[46] We would like to express our sincere gratitude to Professor Dissertori for providing AxPET for these experiments.

AxPET demonstrator: The device consists of two identical modules (see figure 105) built up by six layers of eight 10 cm long LYSO crystals each, read out by Geiger-mode Avalanche Photo Diodes. The cross-section of the LYSO crystals of $3 \times 3\,\mathrm{mm}^2$, together with the distance of 3.5 mm and 7 mm between the crystals, defines the resolution of the detector in the X,Y-plane.

Each layer is additionally read out by 26 wavelength shifting strips (WLS) perpendicular to the crystals, connected to G-APDs as well. While the distance between the WLS is 3.2 mm, the precision in the Z-coordinate is on the order of 1 mm, since the signal can usually be seen on multiple WLS and one can use a weighted average to get a better spatial determination [181].

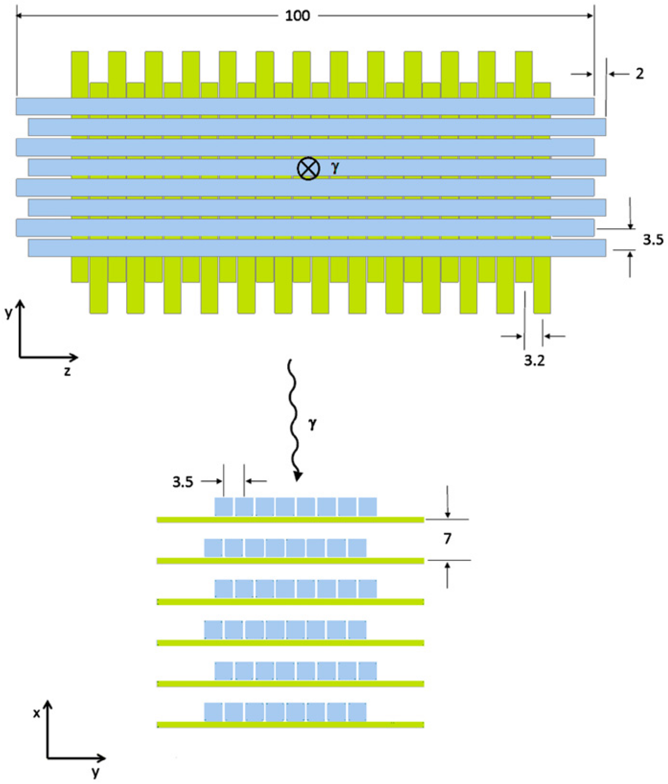

Figure 105: Schematic view of a detector module (*source:* [181]). The detector consists of 6 layers of LYSO crystals interspersed with perpendicular layers of wavelength shifting strips.

Detection method: The scintillating crystals are Saint-Gobain Prelude 420 Cerium doped Lutetium based scintillation crystals with a light yield of around 10 photons per contained decay photon. They are very fast with a decay time of approximately 40 ns and a time resolution on the order of 1 ns. They do however, contain a radioisotope resulting in background activity of around 250 cps per crystal (see figure 106 for the spectrum). The intrinsic energy resolution of the crystals was found [181] to be

$$\frac{\Delta E}{E} = (8.3 \pm 0.5)\,\% \tag{213}$$

for the FWHM for 511 keV photons. The wavelength shifting strips are Eljen EJ-280-10x, converting the blue photons not being totally reflected in the LYSO crystals to green light. They are based on the standard Polyvinyltoluene (PVT) product, but their dye content is enhanced to ten times the concentration.

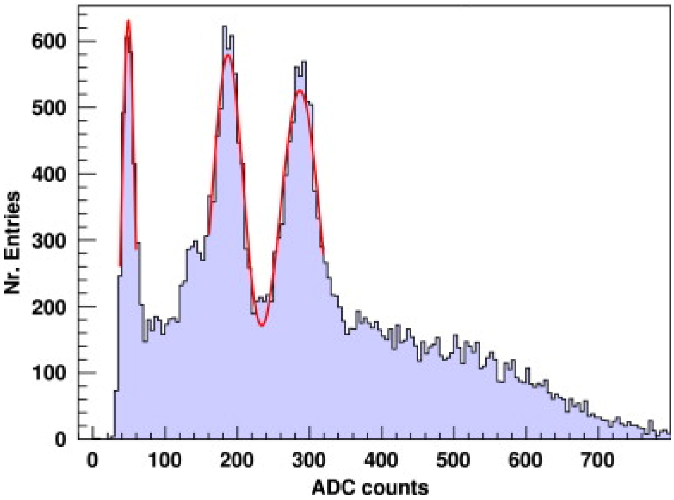

Figure 106: Spectrum of intrinsic radioactivity for a LYSO crystal of AxPET (*source:* [181])

Both the LYSO crystals and the WLS are coated with a reflective surface on one end and glued to Geiger-mode avalanche photo-diodes (also known as silica photo-multipliers (SiPM) or multi pixel photon counters (MPPC)) on the other. For the readout of the scintillating crystals Hamamatsu S10362-33-050C are used and custom-made devices are employed for the WLS readout.

Data acquisition method: The original data acquisition system used for the AxPET demonstrator could not be used for this experiment, since it provided neither a measurement of the energy, nor a timestamp for individual events. The large number of channels (408 MPPCs) made it challenging to design a cost-effective DAQ solution. For testing and characterization purposes, a CAEN DT5742 digitizer was used. While this provides excellent data readout, only 16 channels were available.

A sample energy spectrum of a ^{22}Na source taken with one of the crystals can be found in figure 108. They were taken using coincidence with a plastic scintillator, placed on the opposite side of the source. In addition to the internal radioactivity, the 511 keV decay photon peak and the 1275 keV peak from the subsequent ^{22}Ne* decay can be clearly seen.

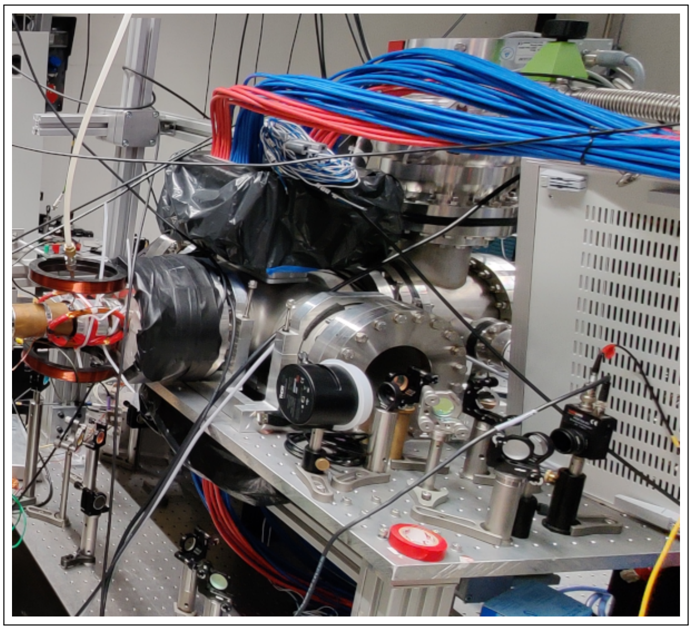

Figure 107: Photograph of AxPET detector mounted on the positronium spectroscopy chamber.

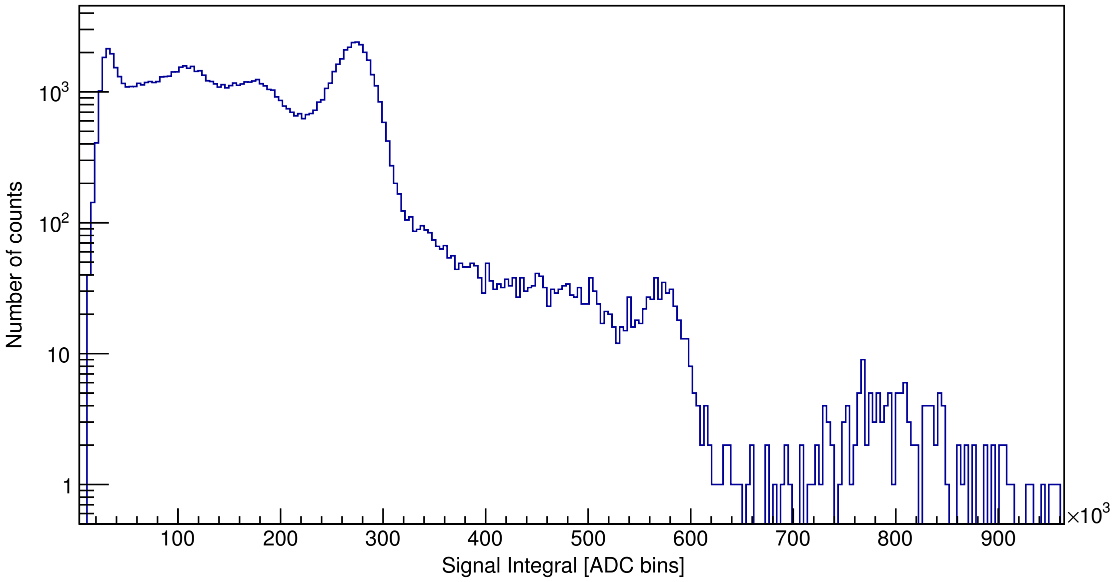

Figure 108: Spectrum of a ^{22}Na source taken with AxPET and CAEN digitizer.

To simultaneously read out all channels, a new DAQ was implemented based on the PETsys TOFPET2 readout system. This system comprises six independent ASIC chips measuring the timing and the deposited energy. The readout boards are connected by high speed Ethernet to a PC running the acquisition software. However, for this DAQ system to be used, every PCB and the cabling had to be redesigned due to severe problems with noise and to be able to use the internal power supply for the MPPCs. Figure 109 shows the spectrum of a ^{22}Na test source using a single crystal using TOFPET2. Note that this was taken without any additional required coincidence, which is why the intrinsic radiation is more pronounced than the contribution from the source.

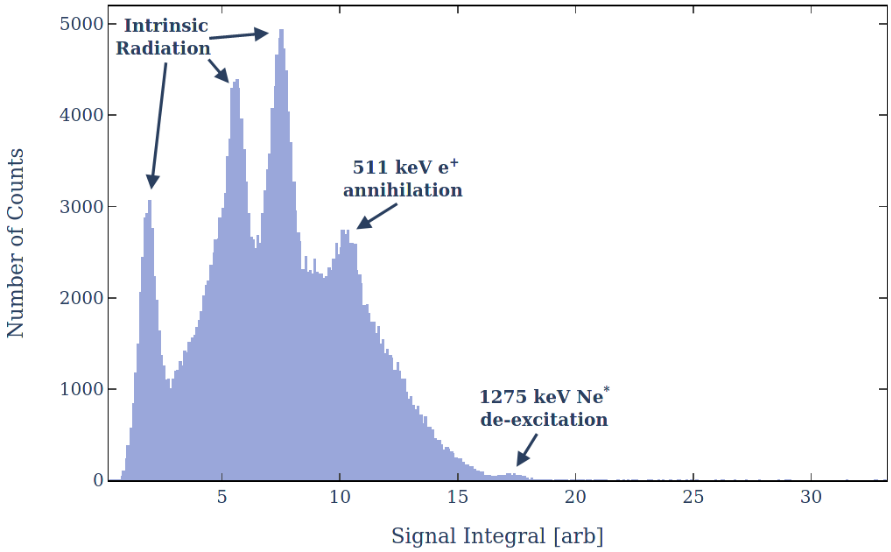

Figure 109: Spectrum of a ^{22}Na source taken with AxPET and the TOFPET2 DAQ.

Monte-Carlo simulation: To get an estimate of the detection efficiency, a simulation was developed [163, 182] using the Geant4 toolkit. It implements the detector module as 96 solid blocks of LYSO and records the time, position and energy of each deposition in the material. Furthermore, it tracks the particles and its daughter particles including all relevant decays and interactions in the material. If needed, every event can be rerun with the same initial conditions by saving and reusing all relevant random seeds during the simulation. This is particularly useful if a specific event warrants further investigation.

Signal and background characterization: A signal event consists of a 511 keV photon hit in both modules each from the decay of para-positronium. The matching of two compatible hits is verified by employing energy and timing cuts and a ray-tracing algorithm [183], which checks if the connecting ray between the two hit positions intersects with the resonator region. While this method strongly suppresses the misidentification of three photon events as two photon events, this is still an issue. In some of the triplet decays, two of the three photons are emitted within a small angle between each other and they will therefore show the same signature in the detector as a single photon. Similarly, if one of the three photons is soft, two hits close to 511 keV will be found in the detector. To maximize background rejection, the energy cuts in the analysis code can be tuned.

If this parameter is chosen too narrow on the other hand, then an appreciable fraction of real two photon hits is lost due to the statistical error of the energy measurement.

Table 12 shows the detection efficiency for two photon events $\varepsilon_{2\gamma}$ and the misidentification rate for three photon events as two photon events $\bar{\varepsilon}_{3\gamma}$ for different energy cuts and analysis techniques. The standard approach directly counts events found in the detector, while MLP (neural network) and BDTD (boosted decision tree) employ classifiers to further select events based on a supervised learning approach.

Required energy per crystal	Required energy per module	Analysis Method	$\varepsilon_{2\gamma}$ $[10^{-3}]$	$\bar{\varepsilon}_{3\gamma}$ $[10^{-4}]$	Ratio [1]
0 keV	0 keV	Standard	14.1 ± 0.4	52.0 ± 2.0	2.7
0 keV	0 keV	MLP	9.6 ± 0.3	10.8 ± 0.4	8.9
0 keV	0 keV	BDTD	11.5 ± 0.3	17.3 ± 0.7	6.7
100 keV	400 keV	Standard	6.2 ± 0.2	11.8 ± 1.1	5.3
100 keV	400 keV	MLP (v1)	5.7 ± 0.2	4.0 ± 0.4	14.1
100 keV	400 keV	BDTD (v1)	5.7 ± 0.2	3.8 ± 0.4	15.1
100 keV	400 keV	MLP (v2)	5.0 ± 0.2	2.7 ± 0.3	18.4
100 keV	400 keV	BDTD (v2)	5.2 ± 0.2	2.7 ± 0.3	19.2
100 keV	450 keV	Standard	6.1 ± 0.2	6.0 ± 0.7	10.2
100 keV	480 keV	Standard	5.6 ± 0.2	3.2 ± 0.6	17.5
400 keV	400 keV	Standard	6.0 ± 0.2	9.6 ± 1.0	6.25
450 keV	450 keV	Standard	5.8 ± 0.2	4.0 ± 0.6	14.5
480 keV	480 keV	Standard	5.4 ± 0.2	1.4 ± 0.4	38.6

Table 12: Simulated AxPET detection efficiencies for different energy cuts and analysis methods (data from [182])

4.5.2. Fine structure detection system

When the microwave resonator drives the transition from the $2^3\mathrm{S}_1$ to one of the $2^3\mathrm{P}_{0/1/2}$ states, a fraction of these atoms will decay with a lifetime of approximately 3.2 ns to the $1^3\mathrm{S}_1$ ground state. Since this constitutes a significant increase in the population in this state, this leads to a corresponding increase in annihilation decays for the 142 ns lifetime component.

This increase will occur well after the prompt and photo-ionization peaks, due to the time-of-flight of the positronium atoms from excitation to the microwave resonator (> 600 ns). This can be detected via counting of individual decays in AxPET with an oPs detection efficiency of 8.95 % [182]. Alternatively, SSPALS (see section 3.2) can be used with monolithic scintillators. A number of additional PbWO_4 crystals are available to be used for this experiment to enhance solid angle coverage. However, an issue that has to be addressed is ion feedback afterpulses that occur in PMTs usually used for this purpose (see figure 45), since they usually occur in the timing region of interest. A number of alternative types of photo-detectors, which do not exhibit these types of afterpulses, exist. Promising candidates are MPPCs (like used for AxPET), MCP-PMTs in which the dynode structure of PMTs is replaced by an MCP, or hybrid photo detectors in which a semiconductor is used for electron multiplication.

4.6. Expected sensitivity

4.6.1. Hyperfine structure measurement

To calculate the excited state hyperfine transition probability, a rate equation model [184] is employed, in which an independent two level system is assumed. This is a valid approximation in this case, since the spontaneous decay rates of the $2^3\mathrm{S}_1$ state are orders of magnitude smaller than the annihilation decay rate. Therefore, the model is conceptually the same as for the ground state hyperfine transition, but with different Einstein coefficients.

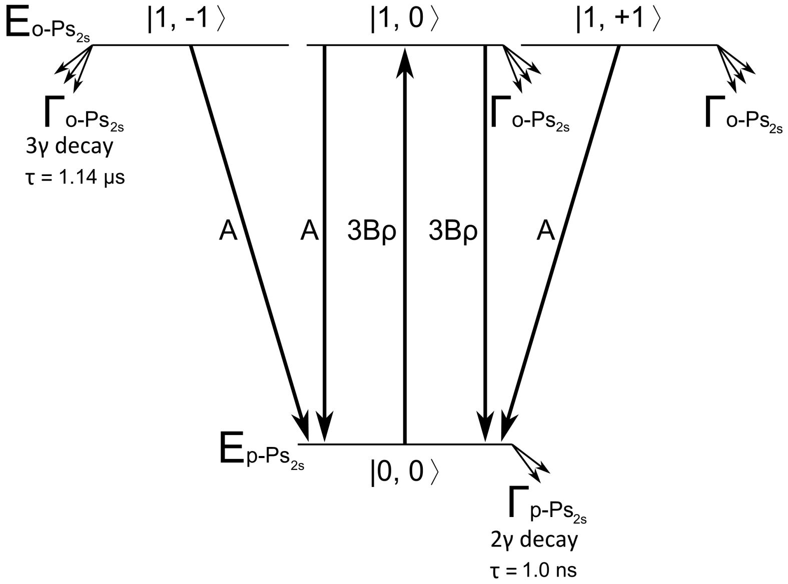

Figure 110: Level diagram of the 2S hyperfine structure of Ps (*adapted from source:* [184])

The magnetic field affects only the states to which the field vector is parallel to its spin angular momentum. Without loss of generality, this is assumed to be the $|1,0\rangle$ and $|0,0\rangle$ states. The transition rate between these states is proportional to the energy density ρ and the Einstein coefficient of induced emission

$$B(\omega) = A\frac{\pi^2\, c^3}{\hbar\,\omega_0^3}\, g(\omega)\ , \tag{214}$$

where A is the Einstein coefficient of spontaneous emission

$$A = \frac{4}{3}\frac{\hbar\,\alpha}{m_e^2\, c^4}\omega_0^3 \tag{215}$$

and $g(\omega)$ is the resonance line shape of the hyperfine transition (with the maximum at the transition frequency ω_n) given by

$$g(\omega)\,d\omega = {}^{1}\!/\!_{\pi} \frac{{}^{\Delta\omega_n}\!/\!_{2}}{(\omega-\omega_n)^2 + ({}^{\Delta\omega_n}\!/\!_{2})^2}\,d\omega\ , \tag{216}$$

with the FWHM given by

$$\Delta\omega_n = A + \gamma^a_{2^3\mathrm{S}_1} + \gamma^a_{2^1\mathrm{S}_0}\ , \tag{217}$$

where

$$\gamma^a_{2^1\mathrm{S}_0} = \frac{\gamma^a_{1^1\mathrm{S}_0}}{n^3} = \frac{1}{8\cdot 124.4\,\mathrm{ps}} \approx \frac{1}{1\,\mathrm{ns}} \tag{218}$$

is the decay rate of the singlet in the first excited state.

The transition rate is then given by

$$\gamma_{tr}(\omega_r) = \int_0^\infty 3\,B(\omega)\,\rho\,(\omega,\omega_r)\ d\omega\ , \tag{219}$$

where it was assumed that the cavity is locked to the resonance frequency ω_r.

For resonators with finite conductivity, the energy density ρ is generally given by a convolution of the energy input spectrum and the resonance line shape of the cavity (see section 4.4)

$$\frac{{}^{\omega_0}\!/\!_{Q}}{(\omega-\omega_0+{}^{\omega_0}\!/\!_{2Q})^2 + ({}^{\omega_0}\!/\!_{2Q})^2}\,d\omega\ , \tag{220}$$

where ω_0 is the eigenfrequency of the perfectly conducting cavity and the Q value is a measure for the quality of a cavity in terms of power losses. It is defined as

$$Q = \omega_0\,\frac{U}{P}\ , \tag{221}$$

where U is the electromagnetic energy stored in the cavity and P is the power dissipated by the different loss mechanisms. In the case of steady state operation P also equals the power input by the source.

However, the FWHM of the transition is on the order of 100 MHz (see equation 217) and the FWHM of the spectral response of typical cavities, as discussed in section 4.4, with Q values of a few thousand is on the order of 1 MHz. Since the spectral distribution of a typical microwave source is on the order of a few Hz, one can in an excellent approximation set the spectral energy density to a delta function, such that

$$\rho\,(\omega,\omega_r)\ d\omega = \eta(x,y,z)\,\delta(\omega-\omega_r)\,d\omega = \frac{\varepsilon_0}{2}\left|\vec{E}(x,y,z)\right|^2\delta(\omega-\omega_r)\,d\omega\ . \tag{222}$$

This leads to a simplification of the transition probability to

$$\gamma_{tr}(\omega_r) = B(\omega_r)\,\frac{\varepsilon_0}{2}\left|\vec{E}(x,y,z)\right|^2\ , \tag{223}$$

where γ_{tr} is dependent on the coordinates or equivalently on the time, given the direction and speed of a positronium atom. The explicit field configuration to be used in equation 223 can be found in section 4.4.1.

To find the state populations, the system of differential equations can be read off figure 110 yielding

$$\begin{aligned}
\partial_t N_{0,0}(t) &= -\,\gamma_{tr}\left(\omega_r\right)\left(N_{0,0}(t) - N_{1,0}(t)\right) + A\left(N_{1,-1}(t) + N_{1,0}(t) + N_{1,1}(t)\right) \\
&\quad -\,\gamma^{a}_{2^1\mathrm{S}_0} N_{0,0}(t) \\
\partial_t N_{1,0}(t) &= +\,\gamma_{tr}\left(\omega_r\right)\left(N_{0,0}(t) - N_{1,0}(t)\right) - \left(A + \gamma^{a}_{2^3\mathrm{S}_1}\right) N_{1,0}(t) \\
\partial_t N_{1,\pm1}(0) &= -\,\left(A + \gamma^{a}_{2^3\mathrm{S}_1}\right) N_{1,\pm1}(t)
\end{aligned} \tag{224}$$

with the related initial conditions

$$N_{1,0}(0) = N_{1,\pm1}(t) = {}^{1}\!/_{3} \quad \text{and} \quad N_{0,0}(0) = 0\ . \tag{225}$$

While explicit solutions can usually not be found, suitable algorithms allow for numerical integration.

The probability for a positronium atom in the $2S$ state to decay into two photons between time t_0 and t_1 is then given by

$$P_{2\gamma}(t_0, t_1) = \gamma^{a}_{2^1\mathrm{S}_0} \int_{t_0}^{t_1} N_{0,0}(t)\, dt\ , \tag{226}$$

while the probability[47] to observe a three photon decay in the same time-frame is given approximately by

$$P_{3\gamma}(t_0, t_1) = \int_{t_0}^{t_1} \gamma^{a}_{2^3\mathrm{S}_1}\left(N_{1,-1}(t) + N_{1,0}(t) + N_{1,1}(t)\right) + \frac{\rho_{gg}(t_0)}{\rho_{ee}(t_0)}\, \gamma^{a}_{1^3\mathrm{S}_1}\, e^{-\gamma_{1s} t}\, dt\ , \tag{227}$$

where the last term represents the additional decays resulting from ground state triplets, which remain in the 1S state after laser excitation. Since this rate is also directly proportional to the measured background events, it highlights the importance that the fraction excited by the laser is as large as possible.

With these values the signal-to-noise ratio is then given to a good approximation by

$$S/N = \frac{\varepsilon_{2\gamma}\, P_{2\gamma}(t_0, t_1)}{\bar{\varepsilon}_{3\gamma}\, P_{3\gamma}(t_0, t_1)}\ , \tag{228}$$

where $\varepsilon_{2\gamma}$ is the detection efficiency for a two photon event and $\bar{\varepsilon}_{3\gamma}$ is the probability that three photon events are wrongly detected as two photon events. Note that the signal-to-noise ratio is dependent on the time cuts and can be maximized by setting the times such that one only includes time of flight through the region of high microwave intensities in the resonator.

A simulation of the microwave excitation was written using Mathematica, which numerically averages over all possible trajectories through the resonator. For each path, the system of differential equations 224 is solved by numerical integration and a weighted average value is calculated. Figure 111 shows the resulting line-shape of the $2^3\mathrm{S}_1 \to 2^1\mathrm{S}_0$

---

[47] Note that this is not a probability in the strictest sense, since it can be larger than 1 for small t.

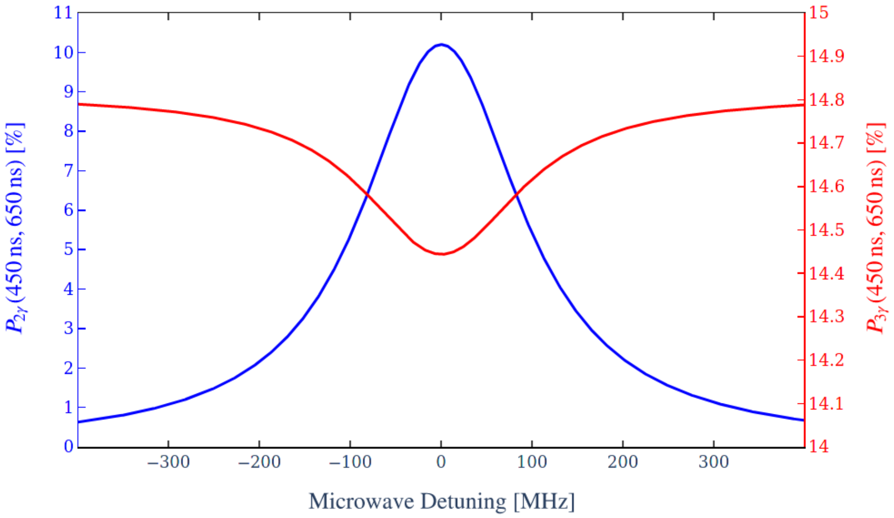

Figure 111: Hyperfine transition line shape for $P_{in} = 5\,\mathrm{W}$

transition for an input power[48] before coupling losses of 5 W. The values shown correspond to equations 226 and 227 with appropriate timing cuts.

According to these cuts we find a peak transition probability (see equation 226) of

$$P_{2\gamma} = 10.2\,\% \tag{229}$$

or equivalently an average rate of

$$R_{2\gamma} = R^{2\mathrm{S}}_{\mathrm{res}} \cdot P_{2\gamma} = 5.6 \tag{230}$$

for two-photon decays per second, using the optimized value of equation 165. The corresponding background probability (see equation 227) is found to be

$$P_{3\gamma} = 14.4\,\% \tag{231}$$

or equivalently an average rate of

$$R_{3\gamma} = R^{2\mathrm{S}}_{\mathrm{res}} \cdot P_{3\gamma} = 7.9 \tag{232}$$

three-photon decays per second. Note that due to the definition of equation 227, it is the excited state rate that is used here.

To arrive at the expected sensitivity, Poisson-distributed errors ($\mu = N$, $\sigma = \sqrt{N}$) are added to the simulated line-shape – using 21 frequency points spaced logarithmically around the center frequency – of the $2^3\mathrm{S}_1 \rightarrow 2^1\mathrm{S}_0$ transition, including detector sensitivity and background events. This is then fitted by a Lorentzian distribution, from which the precision is estimated by calculating the standard deviation of the center frequency of a set of 10000 iterations. Figure 112 shows one such line-shape including the best fit.

---

[48] An AnaPico APSIN26TP analog signal generator and an additional amplifier, e.g. a Microwave Town MTM1826-5, rated for 5 W P1dB output power, will be used to produce the microwave signal.

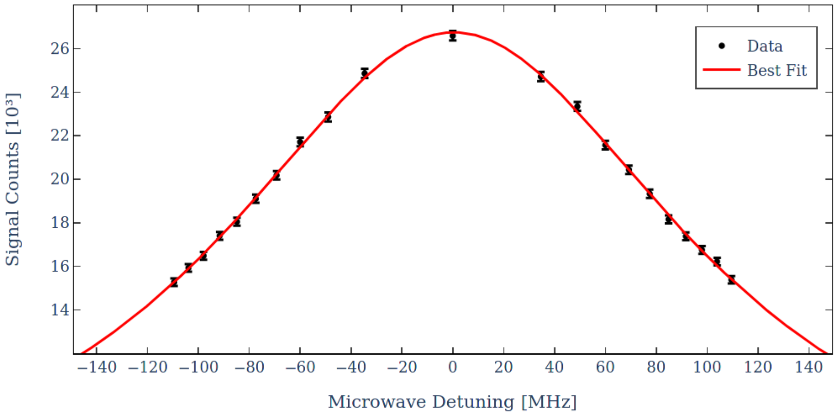

Figure 112: Simulated event count (blue) and best line shape fit (red) for 12 weeks of hyperfine transition data-taking

Required energy per crystal	Required energy per module	Analysis Method	Experimental Sensitivity (12 weeks data-taking)
0 keV	0 keV	Standard	10.6 ppm
0 keV	0 keV	MLP	10.5 ppm
0 keV	0 keV	BDTD	9.9 ppm
100 keV	400 keV	Standard	14.0 ppm
100 keV	400 keV	MLP (v1)	13.1 ppm
100 keV	400 keV	BDTD (v1)	13.0 ppm
100 keV	400 keV	MLP (v2)	13.7 ppm
100 keV	400 keV	BDTD (v2)	13.4 ppm
100 keV	450 keV	Standard	13.0 ppm
100 keV	480 keV	Standard	13.0 ppm
400 keV	400 keV	Standard	13.9 ppm
450 keV	450 keV	Standard	12.9 ppm
480 keV	480 keV	Standard	12.8 ppm

Table 13: Experimental sensitivity for different analysis parameters

Table 13 shows the result of this Monte-Carlo process for a total data-taking period of 12 weeks. Due to rather low expected signal rates, the best variant proves to be the boosted decision tree enhanced simple coincidence method without energy cuts, even with comparably low signal-to-noise performance. The resulting peak rates in the detector are expected to be

$$R_{signal} = 1.15\,\% \cdot 5.6 = 0.064 \tag{233}$$

signal events and

$$R_{bg} = 0.173\,\% \cdot 7.9 = 0.014 \tag{234}$$

background events registered in the detector per second. Equivalently, this gives a final signal-to-noise ratio (see equation 228) of

$$S/N = \frac{0.064}{0.014} = 4.7 \ . \tag{235}$$

For a data-taking period of 12 weeks, which can reasonably be achieved, the sensitivity is given by

$$\frac{\sigma_{2S-HFS}}{\nu_{2S-HFS}} \approx 9.9\,\mathrm{ppm} \ , \tag{236}$$

which corresponds to a 68 % confidence interval of ±252 kHz.

Further increases in the sensitivity can either be reached by impractically long data-taking periods or by improving the signal rate in the detector. Since the laser system is already optimized to yield the highest possible excitation efficiency, gains can be achieved by either installing a new positron source, using a higher power microwave source or increasing solid angle coverage of the detector (see chapter 5.3).

To estimate the systematic errors one, can compare the most recent indirect measurement by Ishida et al. [167] with the measurement presented in this thesis. Since this is a direct measurement conducted in vacuum, neither material effects, nor uncertainties introduced by the static magnetic field, play a role. The systematic errors stemming from the RF System and other sources are given by Ishida et al. to be 2 ppm and 1.9 ppm respectively. Similar values for these systematic errors can be assumed here, which corresponds to a total estimated systematic error of ±2.8 ppm or equivalently ±72 kHz.

Source	Errors in ν_{2S-HFS} [ppm]
RF System:	2
Others:	2
Quadrature sum	2.8

Table 14: Estimate of systematic errors for the hyperfine structure measurement (adapted from [167]).

A careful study of these sources of systematic error will have to be conducted, both in simulation and experiment, to verify the magnitudes estimated here. The combined simulations and estimations regarding systematic errors show the expected sensitivity of the measurement to be

$$\Delta\nu_{2S-HFS} = \pm\, 9.9\,\mathrm{ppm}\ \text{(statistical)}\ \pm\ 2.8\,\mathrm{ppm}\ \text{(systematic)} \tag{237}$$

which will constitute the first measurement of this transition and the first measurement of a hyperfine transition in vacuum altogether. Furthermore, it will allow to probe recent bound state QED calculations and to shed light on the discrepancy of earlier experiments with theoretical predictions.

4.6.2. Fine Structure Measurement

The three fine structure frequencies of interest can be found in table 15 along with the relative intensity of the transition lines. Due to the Clebsch-Gordan decomposition en-

Shorthand	Transition	Frequency	Natural Linewidth	Relative Intensity
ν_0	$2^3\mathrm{S}_1 \rightarrow 2^3\mathrm{P}_0$	18.496 GHz	49.88 MHz	1
ν_1	$2^3\mathrm{S}_1 \rightarrow 2^3\mathrm{P}_1$	13.011 GHz	49.88 MHz	2
ν_2	$2^3\mathrm{S}_1 \rightarrow 2^3\mathrm{P}_2$	8.625 GHz	49.88 MHz	3

Table 15: 2S Fine Structure transition frequencies, linewidths and relative intensities.

tering the electric dipole matrix elements, only the $M_J = 0$ sublevel can be depopulated for the ν_0 transition, while the ν_1 transition allows depopulating $M_J = \pm 1$ and all the sublevels for the ν_2 transition [56]. The natural linewidth is of the same size for all three transitions, since this only depends on the lifetime of the individual levels and not on the center frequency.

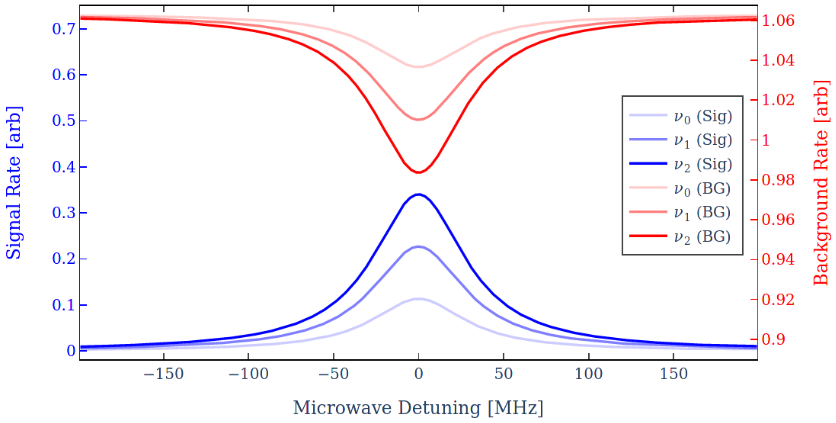

Figure 113: Estimated fine structure transition line shapes for 240 ns integration window after excitation.

Since the saturation intensity is on the order of a few tens of milliwatts and the achievable circulating powers in the resonators presented here (see section 4.4) is on the order of a few hundred watts, the transition can be driven arbitrarily close to saturation. We can therefore conservatively assume 50 % depopulation of the relevant sublevels as described above. To take possible broadening into account, e.g. due to transit-time, power and Doppler broadening, we also assume the line to be 30 % wider than the natural linewidth. These assumptions are also supported by earlier measurements of the ν_0 transition in a similar experimental setup, where the linewidth was found to be 66 MHz [58].

The signal manifests itself as an excess in oPs decays when the microwave excitation transfers the population of the 2S state to the 2P state and radiatively decays with 3.2 ns lifetime to the 1S state (see figure 113). Analogous to the method described above, a Monte-Carlo simulation was conducted to estimate the projected sensitivity for the measurement of each of the fine structure transitions. Figure 114 shows one such ν_2 line-shape out of the Monte-Carlo sample including the best fit.

For a data-taking period of 12 weeks the sensitivities are given by

$$\frac{\sigma_0}{\nu_0} \approx 7.2\,\mathrm{ppm} \tag{238}$$

$$\frac{\sigma_1}{\nu_1} \approx 6.8\,\mathrm{ppm} \tag{239}$$

$$\frac{\sigma_2}{\nu_2} \approx 5.5\,\mathrm{ppm} \tag{240}$$

which corresponds to a 68 % confidence interval of

$$\sigma_0 \approx \pm 132\,\mathrm{kHz} \tag{241}$$

$$\sigma_1 \approx \pm 89\,\mathrm{kHz} \tag{242}$$

$$\sigma_2 \approx \pm 47\,\mathrm{kHz} \quad . \tag{243}$$

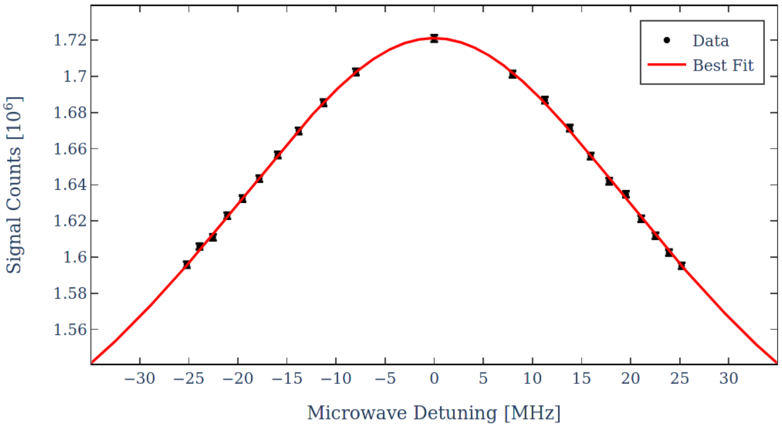

Figure 114: Simulated event count (blue) and best line shape fit (red) for 12 weeks of ν_2 transition data-taking

Similar to the hyperfine measurement, the sensitivity can either be increased by impractically long data-taking periods or by improving the signal rate in the detector. However, since both the laser and microwave system are already optimized to yield the highest possible excitation efficiencies, gains can be realized by installing a new positron source or by increasing the solid angle coverage of the detector (see chapter 5.3).

To estimate the systematic errors for this measurement, a comparison with the most recent fine structure measurement by Gurung et al. [58] can be made. While the general setup is similar, a key difference is the use of a confocal resonator. Due to the standing waves in the cavity, each path shifts symmetrically around the center frequency. A mismatch of axes therefore only leads to broadening, which might decrease the experimental sensitivity, but will not introduce systematic errors. Furthermore, due to the extraction of positrons from the magnetic field and subsequent shielding of the experimental region, the motional Stark shift is highly suppressed and no extrapolation to zero field is necessary. Due to the significantly larger dimensions of the resonator as opposed to

Source	Errors in ν_0 [kHz]
Stray electric fields	< 7
Second order Doppler	1
AC Stark	7
Quadrature sum	9.95

Table 16: Estimate of systematic errors for the ν_0 fine structure measurement (adapted from [58]).

positronium confined to a waveguide, electrical stray fields should in principle also be less of a concern.

Table 16 shows the relevant sources of systematic error. It can therefore be estimated to be on the order of 10 kHz for the ν_0 or equivalently – since these sources scale with the unperturbed transition frequency – 0.54 ppm for each of the fine structure measurements.

A careful study of these sources of systematic error will have to be conducted, both in simulation and experiment, to verify the magnitudes estimated here. The combined simulations and estimations regarding systematic errors show the expected sensitivities of the measurements to be

$$\Delta\nu_0 = \pm\, 7.2\,\text{ppm (statistical)} \;\pm\; 0.5\,\text{ppm (systematic)} \tag{244}$$

$$\Delta\nu_1 = \pm\, 6.8\,\text{ppm (statistical)} \;\pm\; 0.5\,\text{ppm (systematic)} \tag{245}$$

$$\Delta\nu_2 = \pm\, 5.5\,\text{ppm (statistical)} \;\pm\; 0.5\,\text{ppm (systematic)} \quad , \tag{246}$$

which will not only allow to check the 4.5σ discrepancy of the most recent fine structure measurement by Gurung et al. with bound state QED calculations, but also probe these transitions on the level of the current theoretical uncertainty. Experimentally this would also constitute a 5-fold improvement on the current best value for ν_0 and improvements of a factor 20-30 for ν_1 and ν_2.

5. Conclusion and future prospects

As outlined in chapter 1, positronium represents an ideal system to probe for new physics beyond the Standard Model. Spectroscopic precision measurements allow us to stringently test bound-state Quantum Electrodynamics, without the complications presented by the finite size effect of protonic atoms. Especially the advent of pulsed slow positron beams has led to many advancements in this field. Chapter 2 presented one such beamline operating at ETH Zurich and the efforts to monitor and optimize its performance. Section 5.1 contains a summary and possible future improvements on the setup.

Over the last few decades measurements in positronium have been a driver for many theoretical developments and vice-versa. However, the currently most precise measurement, which is the determination of the $1^3\mathrm{S}_1 \rightarrow 2^3\mathrm{S}_1$ transition by Fee et al. [61] at a level of 2.6 ppb, is still almost an order of magnitude less precise than the most recent calculations. The current status of an effort towards a determination of this interval on the level of current theory results was discussed in chapter 3 and preliminary results and future prospects are presented in section 5.2.

During the history of positronium physics more than one interesting puzzle has arisen, i.e. the – now apparently solved – ortho-positronium lifetime puzzle, but also discrepancies in the hyperfine and fine structure transitions. The developments towards precision laser spectroscopy can be naturally applied to experiments determining these transitions. These efforts and the current status was outlined in chapter 4 and section 5.3 contains a summary and outlooks for these measurements.

5.1. Pulsed slow positron beamline

The pulsed slow positron beamline at ETH Zurich is a fundamental prerequisite for the spectroscopic measurements of positronium presented in this thesis. Not only does the event rate scale linearly with the number of positrons supplied, but final properties of the extracted pulses – like time spread and spot size – can have a crucial influence on subsequent experimental stages.

After optimization, a moderation efficiency of

$$\varepsilon_m = (0.519 \pm 0.078)\,\% \tag{247}$$

was found, which is comparable to other experiments using similar moderation stages.

The trapping efficiency was found to be

$$\varepsilon_t = (5.4 \pm 0.1)\ \% \quad , \tag{248}$$

which is in the expected range for these types of commercial buffer gas traps used with a neon moderator.

However, two sources of losses in positron flux have been identified. Firstly, approximately 10 % of positrons annihilate on a pumping restriction in the source region due to slight misalignment with the magnetic field. This can potentially be rectified when the source is removed for maintenance by careful alignment.

Secondly, around 25 % of positrons are lost by magnetic mirroring on the trap inlet, due to the mismatch of the strength of the magnetic field in the source and trapping regions. This could be significantly reduced by implementing new coils producing higher fields at the source. However, due to thermal constraints this requires a significant redesign, implementing a new cooling mechanism.

Furthermore, it was found that the trapping efficiency degrades with a half-life of approximately 22 hours, which is significantly smaller than the lifetime of the moderator. This limits the overall rate of positrons that can be extracted due to the requirement of frequent moderator regrowth procedures. The two mechanisms responsible for this fast decay of trapping efficiency were identified as a decrease in mean energy and increase in energy spread in positrons supplied by the moderator. Significant improvements could potentially be made by continually varying the trapping potentials to accommodate these changes. However, the exact procedure would require extensive research, testing and continuous monitoring.

A new system to transfer, time bunch and extract positrons to the field-free experimental region – placed at approximately 7 m distance from the trap – was developed. It was found to conform to specifications, providing well timed bunches, with below 10 ns (FWHM) time spread. Monte-Carlo simulations show this could be further improved to approximately 2 ns incurring only minor losses on the order of 10 %.

Finally, the most significant improvement for the pulsed slow positron beamline would be to install a new ^{22}Na source. For the type of capsule used in this experiment, activities of approximately 1.85 GBq can be provided by the manufacturer. This would increase the positron rate by more than one order of magnitude and would allow to drastically reduce the required data-taking period or improve on the statistical error for the spectroscopic measurements presented in this thesis. In fact, the required amount of data for the proposed 2S hyperfine and fine structure measurements (see below) could be acquired within a few days instead of 12 weeks.

5.2. Precision measurement of the 1S-2S transition

Chapter 3 presented the progress towards a new high precision measurement of the $1^3\mathrm{S}_1 \rightarrow 2^3\mathrm{S}_1$ transition. Two sets of measurements have been conducted within the scope of this thesis, with the combined result given by

$$1\,233\,607\,210.5\,\mathrm{MHz} \pm 49.6\,\mathrm{MHz} \quad . \tag{249}$$

This represents a difference from theory of

$$-\,11.7\,\mathrm{MHz} \pm 49.6\,\mathrm{MHz} \pm 0.6\,\mathrm{MHz} \quad , \tag{250}$$

where the second error is the uncertainty of the theoretical QED calculation to $\mathcal{O}(m\alpha^6)$.

Source of systematic error: The largest source of systematic error present in the early stages of the experiment was caused by the use of a wavemeter to determine the absolute frequency of the seed laser. The addition of a frequency comb (see section 3.3.4) reduced this error by more than two orders of magnitude to well below the MHz level, limited by the seed laser linewidth. Further improvements down to the kHz level would be possible by current-locking the seed laser to an ultra-stable reference cavity.

The second largest systematic error was caused by frequency chirping of the pulsed dye amplifier, which was addressed by employing an online pulse-to-pulse chirp measurement at a precision of approximately 1 MHz, which is mainly limited by the separation of the chirp spectrum in frequency space (see figure 81) due to the limited frequency shift – approximately 370 MHz in a second order double pass configuration – of the AOM. To improve this separation, a new Isomet M1250T260L0p45VA 260 MHz AOM was acquired, which will allow shifts up to 1.04 GHz depending on the configuration and should allow determinations of the frequency chirp to the sub-MHz level. However, this level of accuracy will require substantial efforts, especially if an additional Fabry-Pérot cavity is used [61].

The remaining systematic uncertainties arise not in the determination of the absolute wavelength of the exciting laser, but in the shifts experienced by the atom. By far the largest contribution of these effects (see table 7) is the residual first order Doppler shift, which is caused by alignment mismatch of the retro-reflected laser beams. However, this effect can be highly suppressed by employing a stable Fabry-Pérot resonator to build up a Gaussian beam with well defined position and size in the excitation region. In this case virtually all power is in a mode with perfectly overlapping wave-fronts with no residual misalignment.

Such a cavity was built using supermirrors with more than 99.999 % transmission to be used directly with the Toptica DL pro CW laser without any additional pulsed amplification for this experiment [71, 185]. While such high-finesse cavities are able to build up extraordinarily high circulating powers – we observed more than 3 kW intra-cavity for approximately 500 mW input power – two key problems have been identified. Firstly, we observed significant mirror degradation on the timescale of hours, even for relatively low circulating powers. While this effect on the mirrors seems to be somewhat reversible with proper cleaning, it requires breaking the vacuum, which makes prolonged measurements extremely challenging. Secondly, even with such high circulating powers, the excitation rate is approximately two orders of magnitude smaller than for the pulsed excitation. It was found that the micro-channel plate detectors showed a higher quantum efficiency for decay photons from positronium annihilation than expected, which – coupled with the small excitation efficiency – leads to overwhelming background. While using such a cavity shows great promise, these issues have to be overcome, which involves significant investigation of the degradation mechanism and low-noise detection methods.

Another option involves using a low-finesse cavity with the pulsed laser setup presented here (see section 3.3.1). Such resonators have been shown to work well in the nanosecond regime [186]. In fact, this has the additional advantage that the pulse length is stretched according to the finesse of the cavity. Not only would this reduce the time-of-flight broadening, but it would also significantly reduce the impact of the temporal emission profile of positronium on the systematic uncertainty. Furthermore, the position and size of the beam is well constrained by the parameters of the resonator – section 4.4 discusses the analog for the microwave case – and the pulse energy can be precisely measured using the transmission on the out-coupling mirror.

If such a cavity would be employed, the largest remaining uncertainty would be arising due to the second order Doppler shift and the knowledge of the velocity profile of positronium emitted from the target. The addition of a position sensitive MCP would allow to infer the emission angle and path length, which, in addition to careful scans of the laser delay, yields a determination of the velocity profile.

These improvements will result in systematic errors below the MHz level, which would pave the way to stringently test bound state QED calculation and improve on earlier measurements by a factor 3-5. To achieve the necessary statistical sensitivity, at least an order of magnitude more signal events as taken during the second run – specifically in the field-ionization channel – would be necessary.

Experimental sensitivity using MCP detectors: Aside from increasing the positron flux by installing a new source (see above) several other improvements are envisioned from the current experimental setup (see description for run 2 in section 3). Approximately a factor 4-5 can be gained by installing a larger MCP with the detector plates parallel to the target plane. This would reduce transmission losses on the grids, allow for more solid angle coverage and reduce the quantum efficiency for photons from oPs decay.

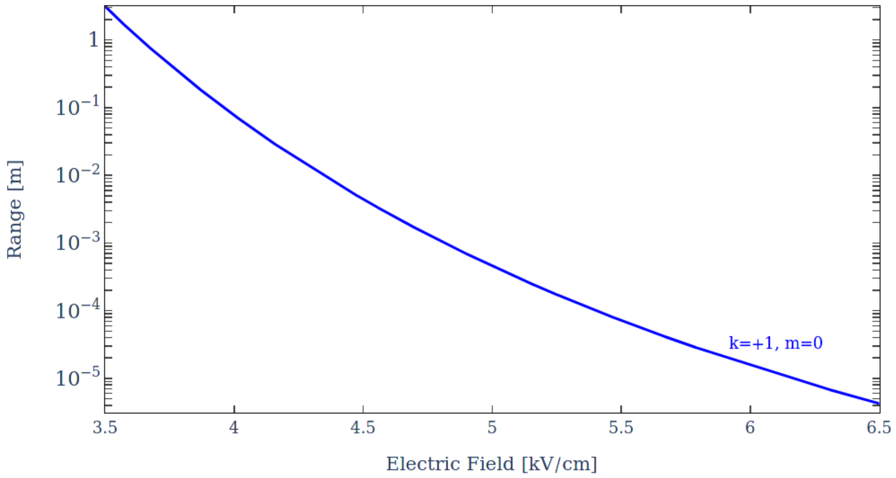

Figure 115: Mean range before ionization for the $\mathrm{n} = 2, \mathrm{k} = +1, \mathrm{m} = 0$ state propagating at a velocity of 10^5 m/s. Note that this does not take annihilation or radiative decays into account.

Furthermore, instead of exciting the 2S to the 20P states to be field-ionized on the MCP grid, the 2S state could be used directly. If electric fields on the order of 5 kV/cm could be reached, the calculations of section 3.4 show that the most stable $n = 2$ state has similar ionization rates as the most stable $n = 20$ state at 2 kV/cm. Since the survival probabilities during propagation to the MCP are similar for both the 2S and the 20P state (see figure 51), this would increase the signal rate by approximately a factor 2, since there is no additional laser excitation needed. However, a competing mechanism is Stark mixing of 2S and 2P, which leads to radiative decays of the excited state under the emission of a Lyman-α photon. While this is irrelevant if the ionization rate is high enough, simulations have to be conducted to ascertain if fields leaking through the ionization grid will lead to significant losses, before the atoms reach the region of high fields.

If these improvements were to be implemented, approximately 8 weeks of data-taking without improvements on the positron rates or around 5 days with a new sodium source would be necessary to reach the required statistical sensitivity.

Experimental sensitivity using AxPET: A very intriguing alternative to the use of MCPs for the detection of the 1S-2S transition is the use of the AxPET detector as described for the detection of the 2S hyperfine and fine structure transitions. This would allow to use the same experimental setup for three separate transitions – 1S-2S, 2S-HFS, and 2S-FS (ν_0) – without any changes.

Essentially, one could operate the experiment in either the hyperfine or fine structure detection mode, but scan the laser detuning and keep the resonator on the microwave transition resonance. Since the transition line-shapes have similar widths, similar absolute statistical uncertainties as for the respective microwave transition can be achieved. This would allow for a determination of the line center within a few hundreds of kHz.

In fact, if the hyperfine transition is used, this would even provide position and timing information for individual events, since the vertex of the pPs decay can be tracked due to the back-to-back nature of the decay photons. However, extensive simulation integrating laser excitation, microwave excitation and detection would be required to ascertain if the systematic error due to the second order Doppler shift could be controlled to the required level.

5.3. Precision measurement of the 2S hyperfine and fine structure splittings

Chapter 4 presented the current efforts towards the first measurement of the 2S hyperfine structure and new, improved measurements of the 2S fine structure. For the initial setup, a microwave resonator, which can be operated both at 25.422 GHz for the hyperfine and at 18.496 GHz for the ν_0 fine structure transition, was designed and characterized. All other relevant parts have been produced and are ready to be installed.

2S hyperfine structure measurement: The projected sensitivity for the determination of the hyperfine structure in the excited state is

$$\Delta\nu_{2S-HFS} = \pm\, 9.9\,\text{ppm (statistical)} \;\pm\; 2.8\,\text{ppm (systematic)} \tag{251}$$

for a data-taking period of twelve weeks, or approximately one week if a new sodium source is installed. This would constitute the first measurement of this transition and the first measurement of a hyperfine transition of positronium in vacuum altogether. Furthermore, it would help to shed light on the discrepancy of earlier measurements of the ground state hyperfine transition with most recent bound state QED results.

Further improvements could be achieved either by increasing the hyperfine transition probability or by increasing the solid angle acceptance of the detector. While higher circulating powers could potentially increase the signal rate by up to 50 %, the cooling system for the confocal resonator will already be operating close to its design capacity. Further increases would require a substantial redesign and extensive testing.

Due to the relatively small size of the AxPET detector, large gains in signal rate could be achieved by increasing the solid angle coverage. While the cost of large PET-style detectors is usually preventative, there have been several efforts in recent years to design and produce smaller, cost-effective detectors, e.g. by the ETH spin-off Positrigo AG, which aims to commercialize PET brain scanners. Potential increases in detection efficiency by one order of magnitude would be feasible with such a device.

2S fine structure measurement: The experimental sensitivity for the respective fine structure transitions were found to be

$$\Delta\nu_0 = \pm\,7.2\,\text{ppm (statistical)} \ \pm\ 0.5\,\text{ppm (systematic)} \tag{252}$$

$$\Delta\nu_1 = \pm\,6.8\,\text{ppm (statistical)} \ \pm\ 0.5\,\text{ppm (systematic)} \tag{253}$$

$$\Delta\nu_2 = \pm\,5.5\,\text{ppm (statistical)} \ \pm\ 0.5\,\text{ppm (systematic)} \tag{254}$$

for a data-taking period of 12 weeks or approximately one week with the addition of a new positron source. This would allow to improve on earlier measurements by a factor 5 for the ν_0 transition and more than an order of magnitude for the others.

The recent emergence of a 4.5σ discrepancy between measurement and theory for the ν_0 transition [58] might hold hints that the fine structure could constitute a window for potential physics beyond the standard model. Since these measurements will be limited by statistical uncertainty, further improvements could provide stringent tests for our current understanding of QED and motivate further developments in this direction.

Since both the two-photon excitation to the 2S state and the microwave excitation from 2S to 2P are driven close to saturation, further improvements are only possible by covering more solid angle with the scintillation detectors. However, in this case it is not required to measure individual events separately or identify the decay channel. Therefore, a detector with fewer large crystals could be used to take an SSPALS spectrum with high detection efficiency. As outlined in section 4.5.2 several large $PbWO_4$ scintillators are available to build such a detector. Due to the afterpulses present in standard PMTs, further research is required to identify a suitable type of photo-detector.

List of Figures

List of Tables

References

[1] P. A. M. Dirac. The quantum theory of the electron. *Proc. R. Soc. Lond. A*, 117:610–624, 1928.

[2] P. A. M. Dirac. Quantised singularities in the electromagnetic field. *Proc. R. Soc. Lond. A*, 133:60–72, 1931.

[3] C. D. Anderson. The Positive Electron. *Phys. Rev.*, 43:491–494, 1933.

[4] C. Weiner. Interview of Carl Anderson. *Niels Bohr Library & Archives, American Institute of Physics*, 1966.

[5] S. Mohorovičić. Möglichkeit neuer Elemente und ihre Bedeutung für die Astrophysik. *Astronomische Nachrichten*, 253:94, 1934.

[6] A. E. Ruark. Positronium. *Phys. Rev.*, 68:278–278, 1945.

[7] M. Deutsch. Evidence for the Formation of Positronium in Gases. *Phys. Rev.*, 82:455–456, 1951.

[8] W. Bernreuther and O. Nachtmann. Weak interaction effects in positronium. *Zeitschrift für Physik C Particles and Fields*, 11(3):235–245, 1981.

[9] G. S. Adkins and F. R. Brown. Rate for positronium decay to five photons. *Phys. Rev. A*, 28:1164–1165, 1983.

[10] J. A. Wheeler. Polyelectrons. *Annals of the New York Academy of Sciences*, 48(3):219–238, 1946.

[11] J. Pirenne. Le champ propre et l'interaction des particules de Dirac : suivant l'électrodynamique quantique. *Archives des sciences physiques et naturelles*, 28:233, 1946.

[12] G. S. Adkins, N. M. McGovern, R. N. Fell, and J. Sapirstein. Two-loop corrections to the decay rate of parapositronium. *Phys. Rev. A*, 68:032512, 2003.

[13] A. H. Al-Ramadhan and D. W. Gidley. New precision measurement of the decay rate of singlet positronium. *Phys. Rev. Lett.*, 72:1632–1635, 1994.

[14] A. Ore and J. L. Powell. Three-Photon Annihilation of an Electron-Positron Pair. *Phys. Rev.*, 75:1696–1699, 1949.

[15] G. S. Adkins, R. N. Fell, and J. Sapirstein. Two-Loop Correction to the Orthopositronium Decay Rate. *Annals of Physics*, 295(2):136 – 193, 2002.

[16] R. S. Vallery, P. W. Zitzewitz, and D. W. Gidley. Resolution of the Orthopositronium-Lifetime Puzzle. *Phys. Rev. Lett.*, 90:203402, 2003.

[17] O. Jinnouchi, S. Asai, and T. Kobayashi. Precision measurement of orthopositronium decay rate using SiO_2 powder. *Physics Letters B*, 572(3):117 – 126, 2003.

[18] Y. Kataoka, S. Asai, and T. Kobayashi. First test of $O(\alpha^2)$ correction of the orthopositronium decay rate. *Physics Letters B*, 671(2):219 – 223, 2009.

[19] C. G. Parthey, A. Matveev, J. Alnis, B. Bernhardt, A. Beyer, R. Holzwarth, A. Maistrou, R. Pohl, K. Predehl, T. Udem, T. Wilken, N. Kolachevsky, M. Abgrall, D. Rovera, C. Salomon, P. Laurent, and T. W. Hänsch. Improved Measurement of the Hydrogen $1S-2S$ Transition Frequency. *Phys. Rev. Lett.*, 107:203001, 2011.

[20] A. Matveev, C. G. Parthey, K. Predehl, J. Alnis, A. Beyer, R. Holzwarth, T. Udem, T. Wilken, N. Kolachevsky, M. Abgrall, D. Rovera, C. Salomon, P. Laurent, G. Grosche, O. Terra, T. Legero, H. Schnatz, S. Weyers, B. Altschul, and T. W. Hänsch. Precision Measurement of the Hydrogen $1S-2S$ Frequency via a 920-km Fiber Link. *Phys. Rev. Lett.*, 110:230801, 2013.

[21] R. Ley and G. Werth. Positronium: Theory Versus Experiment. In *The Hydrogen Atom*, pages 407–418. Karshenboim, S.G., Pavone, F.S., Bassani, F., Inguscio, M., Hänsch, T.W., 2001.

[22] G. W. F. Drake and R. A. Swainson. Bethe logarithms for hydrogen up to n = 20, and approximations for two-electron atoms. *Phys. Rev. A*, 41:1243–1246, 1990.

[23] U. D. Jentschura and P. J. Mohr. Calculation of hydrogenic Bethe logarithms for Rydberg states. *Phys. Rev. A*, 72:012110, 2005.

[24] H. A. Bethe and E. E. Salpeter. *Quantum mechanics of one- and two-electron atoms,*. Springer; Academic Press, Berlin; New York, 1957.

[25] A. Rich. Recent experimental advances in positronium research. *Rev. Mod. Phys.*, 53(1):127–165, 1981.

[26] A. Czarnecki, K. Melnikov, and A. Yelkhovsky. Positronium hyperfine splitting: analytical value at $\mathcal{O}(m\alpha^6)$. *Phys. Rev. Lett.*, 82:311–314, 1999.

[27] M. Baker, P. Marquard, A. A. Penin, J. Piclum, and M. Steinhauser. Hyperfine splitting in positronium to $\mathcal{O}(\alpha^7 m_e)$: one-photon annihilation contribution. *Phys. Rev. Lett.*, 112:120407, 2014.

[28] G. S. Adkins and R. N. Fell. Positronium hyperfine splitting at order $m\alpha^7$: Light-by-light scattering in the two-photon-exchange channel. *Phys. Rev. A*, 89:052518, 2014.

[29] Michael I. Eides and Valery A. Shelyuto. Hard nonlogarithmic corrections of order $m\alpha^7$ to hyperfine splitting in positronium. *Phys. Rev. D*, 89:111301, 2014.

[30] G. S. Adkins, C. Parsons, M. D. Salinger, R. Wang, and R. N. Fell. Positronium energy levels at order $m\alpha^7$: Light-by-light scattering in the two-photon-annihilation channel. *Phys. Rev. A*, 90:042502, 2014.

[31] Michael I. Eides and Valery A. Shelyuto. Hard three-loop corrections to hyperfine splitting in positronium and muonium. *Phys. Rev. D*, 92:013010, 2015.

[32] G. S. Adkins, C. Parsons, M. D. Salinger, and R. Wang. Positronium energy levels at order $m\alpha^7$: Vacuum polarization corrections in the two-photon-annihilation channel. *Phys. Lett. B*, 747:551–555, 2015.

[33] G. S. Adkins, M. Kim, C. Parsons, and R. N. Fell. Three-Photon-Annihilation Contributions to Positronium Energies at Order $m\alpha^7$. *Phys. Rev. Lett.*, 115:233401, 2015.

[34] G. S. Adkins, L. M. Tran, and R. Wang. Positronium energy levels at order $m\alpha^7$: Product contributions in the two-photon-annihilation channel. *Phys. Rev. A*, 93:052511, 2016.

[35] Michael I. Eides and Valery A. Shelyuto. Hyperfine splitting in muonium and positronium. *Int. J. Mod. Phys. A*, 31(28n29):1645034, 2016.

[36] Michael I. Eides and Valery A. Shelyuto. One more hard three-loop correction to parapositronium energy levels. *Phys. Rev. D*, 96:011301, 2017.

[37] A. Sen and Z. K. Silagadze. Two-photon decay of P-wave positronium: a tutorial. *Canadian Journal of Physics*, 97(7):693–700, 2019.

[38] T. F. Gallagher. *Electric fields*, page 70–102. Cambridge Monographs on Atomic, Molecular and Chemical Physics. Cambridge University Press, 1994.

[39] O. Jitrik and C. F. Bunge. Transition Probabilities for Hydrogen-Like Atoms. *Journal of Physical and Chemical Reference Data*, 33(4):1059–1070, 2004.

[40] M. Göppert-Mayer. Über Elementarakte mit zwei Quantensprüngen. *Ann. Phys.*, 401(3):273–294, 1931.

[41] M. Deutsch and E. Dulit. Short Range Interaction of Electrons and Fine Structure of Positronium. *Phys. Rev.*, 84(3):601–602, 1951.

[42] R. Weinstein, M. Deutsch, and S. Brown. Fine structure of positronium. *Phys. Rev.*, 98:223(A), 1955.

[43] V. W. Hughes, S. Marder, and C. S. Wu. Hyperfine Structure of Positronium in Its Ground State. *Phys. Rev.*, 106(5):934–947, 1957.

[44] E. D. Theriot, R. H. Beers, V. W. Hughes, and K. O. H. Ziock. Precision Redetermination of the Fine-Structure Interval of the Ground State of Positronium and a Direct Measurement of the Decay Rate of Parapositronium. *Phys. Rev. A*, 2(3):707–721, 1970.

[45] E. R. Carlson, V. W. Hughes, M. L. Lewis, and I. Lindgren. Higher-Precision Determination of the Fine-Structure Interval in the Ground State of Positronium, and the Fine-Structure Density Shift in Nitrogen. *Phys. Rev. Lett.*, 29(16):1059–1061, 1972.

[46] A. P. Mills and G. H. Bearman. New Measurement of the Positronium Hyperfine Interval. *Phys. Rev. Lett.*, 34(5):246–250, 1975.

[47] E. R. Carlson, V. W. Hughes, and I. Lindgren. Precision determination of the fine-structure interval in the ground state of positronium. III. *Phys. Rev. A*, 15:241–250, 1977.

[48] P. O. Egan, V. W. Hughes, and M. H. Yam. Precision determination of the fine-structure interval in the ground state of positronium. IV. Measurement of positronium fine-structure density shifts in noble gases. *Phys. Rev. A*, 15(1):251–260, 1977.

[49] A. P. Mills. Line-shape effects in the measurement of the positronium hyperfine interval. *Phys. Rev. A*, 27:262–267, 1983.

[50] M. W. Ritter, P. O. Egan, V. W. Hughes, and K. A. Woodle. Precision determination of the hyperfine-structure interval in the ground state of positronium. V. *Phys. Rev. A*, 30:1331–1338, 1984.

[51] K. F. Canter, A. P. Mills, and S. Berko. Observations of Positronium Lyman-α Radiation. *Phys. Rev. Lett.*, 34:177–180, 1975.

[52] A. P. Mills, S. Berko, and K. F. Canter. Fine-Structure Measurement in the First Excited State of Positronium. *Phys. Rev. Lett.*, 34(25):1541–1544, 1975.

[53] S. Hatamian, R. S. Conti, and A. Rich. Measurements of the $2^3\mathrm{S}_1$-$2^3\mathrm{P}_\mathrm{J}$ (J=0,1,2) fine-structure splittings in positronium. *Phys. Rev. Lett.*, 58(18):1833–1836, 1987.

[54] R. S. Conti, S. Hatamian, L. Lapidus, A. Rich, and M. Skalsey. Search for C-violating, P-conserving interactions and observation of $2^3\mathrm{S}_1$ to $2^1\mathrm{P}_1$ transitions in positronium. *Physics Letters A*, 177(1):43–48, 1993.

[55] D. Hagena, R. Ley, D. Weil, G. Werth, W. Arnold, and H. Schneider. Precise measurement of n=2 positronium fine-structure intervals. *Phys. Rev. Lett.*, 71(18):2887–2890, 1993.

[56] R. Ley, D. Hagena, D. Weil, G. Werth, W. Arnold, and H. Schneider. Spectroscopy of excited state positronium. *Hyperfine Interactions*, 89(1):327–341, 1994.

[57] D. B. Cassidy. Experimental progress in positronium laser physics. *The European Physical Journal D*, 72(3):53, 2018.

[58] L. Gurung, T. J. Babij, S. D. Hogan, and D. B. Cassidy. Precision Microwave Spectroscopy of the Positronium $n = 2$ Fine Structure. *Phys. Rev. Lett.*, 125(7):073002, 2020.

[59] S. Chu and A. P. Mills. Excitation of the Positronium $1^3S_1 \rightarrow 2^3S_1$ Two-Photon Transition. *Phys. Rev. Lett.*, 48(19):1333–1337, 1982.

[60] S. Chu, A. P. Mills, and J. L. Hall. Measurement of the Positronium $1^3S_1 - 2^3S_1$ Interval by Doppler-Free Two-Photon Spectroscopy. *Phys. Rev. Lett.*, 52:1689–1692, 1984.

[61] M. S. Fee, K. Danzmann, and S. Chu. Optical heterodyne measurement of pulsed lasers: Toward high-precision pulsed spectroscopy. *Phys. Rev. A*, 45:4911–4924, 1992.

[62] M. S. Fee, A. P. Mills, S. Chu, E. D. Shaw, K. Danzmann, R. J. Chichester, and D. M. Zuckerman. Measurement of the positronium 1^3S_1-2^3S_1 interval by continuous-wave two-photon excitation. *Phys. Rev. Lett.*, 70(10):1397–1400, 1993.

[63] M. S. Fee, S. Chu, A. P. Mills, R. J. Chichester, D. M. Zuckerman, E. D. Shaw, and K. Danzmann. Measurement of the positronium 1^3S_1-2^3S_1 interval by continuous-wave two-photon excitation. *Phys. Rev. A*, 48(1):192–219, 1993.

[64] CMS Collaboration. Observation of a new boson at a mass of 125 GeV with the CMS experiment at the LHC. *Physics Letters B*, 716(1):30 – 61, 2012.

[65] ATLAS Collaboration. Observation of a new particle in the search for the Standard Model Higgs boson with the ATLAS detector at the LHC. *Physics Letters B*, 716(1):1 – 29, 2012.

[66] M. Ahmadi, B. X. R. Alves, C. J. Baker, W. Bertsche, E. Butler, A. Capra, C. Carruth, C. L. Cesar, M. Charlton, S. Cohen, R. Collister, S. Eriksson, A. Evans, N. Evetts, J. Fajans, T. Friesen, M. C. Fujiwara, D. R. Gill, A. Gutierrez, J. S. Hangst, W. N. Hardy, M. E. Hayden, C. A. Isaac, A. Ishida, M. A. Johnson, S. A. Jones, S. Jonsell, L. Kurchaninov, N. Madsen, M. Mathers, D. Maxwell, J. T. K. McKenna, S. Menary, J. M. Michan, T. Momose, J. J. Munich, P. Nolan, K. Olchanski, A. Olin, P. Pusa, C. Ø. Rasmussen, F. Robicheaux, R. L. Sacramento, M. Sameed, E. Sarid, D. M. Silveira, S. Stracka, G. Stutter, C. So, T. D. Tharp, J. E. Thompson, R. I. Thompson, D. P. van der Werf, and J. S. Wurtele. Observation of the 1S-2S transition in trapped antihydrogen. *Nature*, 541(7638):506–510, 2017.

[67] M. Ahmadi, B. X. R. Alves, C. J. Baker, W. Bertsche, E. Butler, A. Capra, C. Carruth, C. L. Cesar, M. Charlton, S. Cohen, R. Collister, S. Eriksson, A. Evans, N. Evetts, J. Fajans, T. Friesen, M. C. Fujiwara, D. R. Gill, A. Gutierrez, J. S. Hangst, W. N. Hardy, M. E. Hayden, C. A. Isaac, A. Ishida, M. A. Johnson, S. A. Jones, S. Jonsell, L. Kurchaninov, N. Madsen, M. Mathers, D. Maxwell,

J. T. K. McKenna, S. Menary, J. M. Michan, T. Momose, J. J. Munich, P. Nolan, K. Olchanski, A. Olin, P. Pusa, C. Ø. Rasmussen, F. Robicheaux, R. L. Sacramento, M. Sameed, E. Sarid, D. M. Silveira, S. Stracka, G. Stutter, C. So, T. D. Tharp, J. E. Thompson, R. I. Thompson, D. P. van der Werf, and J. S. Wurtele. Observation of the hyperfine spectrum of antihydrogen. *Nature*, 548(7665):66–69, 2017.

[68] The ALPHA Collaboration. Investigation of the fine structure of antihydrogen. *Nature*, 578(7795):375–380, 2020.

[69] E. Widmann, C. Amsler, S. Arguedas Cuendis, H. Breuker, M. Diermaier, P. Dupré, C. Evans, M. Fleck, A. Gligorova, H. Higaki, Y. Kanai, B. Kolbinger, N. Kuroda, M. Leali, A. M. M. Leite, V. Mäckel, C. Malbrunot, V. Mascagna, O. Massiczek, Y. Matsuda, D. J. Murtagh, Y. Nagata, A. Nanda, D. Phan, C. Sauerzopf, M. C. Simon, M. Tajima, H. Spitzer, M. Strube, S. Ulmer, L. Venturelli, M. Wiesinger, Y. Yamazaki, and J. Zmeskal. Hyperfine spectroscopy of hydrogen and antihydrogen in ASACUSA. *Hyperfine Interactions*, 240(1):5, 2018.

[70] P. Crivelli, D. Cooke, and M. W. Heiss. Antiproton charge radius. *PRD*, 94(5):052008, 2016.

[71] D. A. Cooke, P. Crivelli, J. Alnis, A. Antognini, B. Brown, S. Friedreich, A. Gabard, T.W. Haensch, K. Kirch, A. Rubbia, and V. Vrankovic. Observation of positronium annihilation in the 2S state: towards a new measurement of the 1S-2S transition frequency. *Hyperfine Interactions*, pages 1–7, 2015.

[72] M. W. Heiss, G. Wichmann, A. Rubbia, and P. Crivelli. The positronium hyperfine structure: Progress towards a direct measurement of the $2^3S_1 \to 2^1S_0$ transition in vacuum. *Journal of Physics: Conference Series*, 1138:012007, 2018.

[73] P. Petit, M. Desaintfuscien, and C. Audoin. Temperature Dependence of the Hydrogen Maser Wall Shift in the Temperature Range 295-395 K. *Metrologia*, 16(1):7–14, 1980.

[74] N. Bezginov, T. Valdez, M. Horbatsch, A. Marsman, A. C. Vutha, and E. A. Hessels. A measurement of the atomic hydrogen Lamb shift and the proton charge radius. *Science*, 365(6457):1007, 2019.

[75] E. Widmann, M. Diermaier, B. Juhász, C. Malbrunot, O. Massiczek, C. Sauerzopf, K. Suzuki, B. Wünschek, J. Zmeskal, S. Federmann, N. Kuroda, S. Ulmer, and Y. Yamazaki. Measurement of the hyperfine structure of antihydrogen in a beam. *Hyperfine Interactions*, 215(1):1–8, 2013.

[76] G. Lüders. On the equivalence of invariance under time reversal and under particle-antiparticle conjugation for relativistic field theories. *Dan. Mat. Fys. Medd.*, 28(5):1–17, 1954.

[77] W. Pauli. Exclusion Principle, Lorentz Group and Reflection of Space-Time and Charge. In *Niels Bohr and the Development of Physics*. Pauli, W. and Rosenfeld, L. and Weisskopf, V., 1955.

[78] G. Lüders. Proof of the TCP theorem. *Annals of Physics*, 2(1):1–15, 1957.

[79] V. A. Kostelecký and R. Potting. Expectation values, Lorentz invariance, and CPT in the open bosonic string. *Physics Letters B*, 381(1):89 – 96, 1996.

[80] D. Colladay and V. A. Kostelecký. CPT violation and the standard model. *PRD*, 55(11):6760–6774, 1997.

[81] A. V. Manohar. Effective field theories. In H. Latal and W. Schweiger, editors, *Perturbative and Nonperturbative Aspects of Quantum Field Theory*, pages 311–362, Berlin, Heidelberg, 1997. Springer Berlin Heidelberg.

[82] V. A. Kostelecký. Gravity, Lorentz violation, and the standard model. *Phys. Rev. D*, 69:105009, 2004.

[83] O. W. Greenberg. *CPT* Violation Implies Violation of Lorentz Invariance. *Phys. Rev. Lett.*, 89(23):231602, 2002.

[84] V. A. Kostelecký and N. Russell. Data tables for Lorentz and *CPT* violation. *RMP*, 83(1):11–31, 2011.

[85] V. A. Kostelecký and A. J. Vargas. Lorentz and *CPT* tests with hydrogen, antihydrogen, and related systems. *Phys. Rev. D*, 92:056002, 2015.

[86] A. Wagner, M. Butterling, M. O. Liedke, K. Potzger, and R. Krause-Rehberg. Positron annihilation lifetime and Doppler broadening spectroscopy at the ELBE facility. *AIP Conference Proceedings*, 1970(1):040003, 2018.

[87] T. Kurihara, A. Yagishita, A. Enomoto, H. Kobayashi, T. Shidara, A. Shirakawa, K. Nakahara, H. Saitou, K. Inoue, Y. Nagashima, T. Hyodo, Y. Nagai, M. Hasegawa, Y. Inoue, Y. Kogure, and M. Doyama. Intense positron beam at KEK. *Nuclear Instruments and Methods in Physics Research Section B: Beam Interactions with Materials and Atoms*, 171(1):164–171, 2000.

[88] C. Hugenschmidt, B. Löwe, J. Mayer, C. Piochacz, P. Pikart, R. Repper, M. Stadlbauer, and K. Schreckenbach. Unprecedented intensity of a low-energy positron beam. *Nuclear Instruments and Methods in Physics Research Section A: Accelerators, Spectrometers, Detectors and Associated Equipment*, 593(3):616–618, 2008.

[89] A. van Veen, H. Schut, F. Labohm, and J. de Roode. Positron extraction and transport in a nuclear-reactor-based positron beam. *Nuclear Instruments and Methods in Physics Research Section A: Accelerators, Spectrometers, Detectors and Associated Equipment*, 427(1):266–270, 1999.

[90] M. P. Unterweger. Half-life measurements at the National Institute of Standards and Technology. *Applied Radiation and Isotopes*, 56(1):125–130, 2002.

[91] R. Krause-Rehberg, N. van der Walt, L. Büttner, and F. Börner. A ^{22}Na positron source for use in UHV. *Nuclear Instruments and Methods in Physics Research Section B: Beam Interactions with Materials and Atoms*, 221:165–167, 2004.

[92] O. Nähle, K. Kossert, and R. Klein. Activity standardization of ^{22}Na. *Applied Radiation and Isotopes*, 66(6):865–871, 2008.

[93] P. J. Schultz and K. G. Lynn. Interaction of positron beams with surfaces, thin films, and interfaces. *RMP*, 60(3):701–779, 1988.

[94] A. Vehanen, K. G. Lynn, Peter J. Schultz, and M. Eldrup. Improved slow-positron yield using a single crystal tungsten moderator. *Applied Physics A*, 32(3):163–167, 1983.

[95] H. M. Weng, C. C. Ling, C. D. Beling, S. Fung, C. K. Cheung, P. Y. Kwan, and I. P. Hui. Tungsten mesh as positron transmission moderator in a monoenergetic positron beam. *Nuclear Instruments and Methods in Physics Research Section B: Beam Interactions with Materials and Atoms*, 225(3):397–401, 2004.

[96] A. P. Mills and E. M. Gullikson. Solid neon moderator for producing slow positrons. *Appl. Phys. Lett.*, 49(17):1121–1123, 1986.

[97] S. Marjanović, A. Banković, D. Cassidy, B. Cooper, A. Deller, S. Dujko, and Z. L. Petrović. A CF_4 based positron trap. *Journal of Physics B: Atomic, Molecular and Optical Physics*, 49(21):215001, 2016.

[98] R. Khatri, M. Charlton, P. Sferlazzo, K. G. Lynn, A. P. Mills, and L. O. Roellig. Improvement of rare-gas solid moderators by using conical geometry. *Appl. Phys. Lett.*, 57(22):2374–2376, 1990.

[99] S. Mukhopadhyay. Plastic gamma sensors: an application in detection of radioisotopes. In *Hard X-Ray and Gamma-Ray Detector Physics V*, volume 5198, 2004.

[100] H. Xiao, W. Hajdas, B. Wu, N. Produit, T. Bao, T. Bernasconi, F. Cadoux, Y. Dong, K. Egli, N. Gauvin, M. Kole, R. Kramert, S. Kong, L. Li, Z. Li, J. Liu, X. Liu, R. Marcinkowski, D. K. Rybka, M. Pohl, H. Shi, L. Song, J. Sun, S. Xiong, J. Szabelski, P. Socha, R. Wang, X. Wen, X. Wu, L. Zhang, P. Zhang, S. Zhang, X. Zhang, Y. Zhang, and A. Zwolinska. In-flight energy calibration of the space-borne Compton polarimeter POLAR. *Astroparticle Physics*, 103:74–86, 2018.

[101] G. I. Britvich, V. V. Brekhovskikh, V. K. Semenov, and S. A. Kholodenko. The main characteristics of polystyrene scintillators produced at the institute of high-energy physics and detectors on their basis. *Instruments and Experimental Techniques*, 58(2):211–220, 2015.

[102] R. G. Greaves and C. M. Surko. Solid neon moderator for positron-trapping experiments. *Can. J. Phys.*, 74(7-8):445–448, 1996.

[103] C. D. Molek, C. M. Lindsay, and M. E. Fajardo. A combined matrix isolation spectroscopy and cryosolid positron moderation apparatus. *Review of Scientific Instruments*, 84(3):035106, 2013.

[104] J. P. Merrison, M. Charlton, B. I. Deutch, and L. V. Jørgensen. Studies of positron moderation in surface charged rare gas solids. *Hyperfine Interactions*, 76(1):305–308, 1993.

[105] A. O'Hagan and T. O. M. Leonard. Bayes estimation subject to uncertainty about parameter constraints. *Biometrika*, 63(1):201–203, 1976.

[106] S. Ghosh, J. R. Danielson, and C. Surko. Energy distribution and adiabatic guiding of a solid-neon-moderated positron beam. *Journal of Physics B: Atomic, Molecular and Optical Physics*, 2020.

[107] D. B. Cassidy, S. H. M. Deng, R. G. Greaves, and A. P. Mills. Accumulator for the production of intense positron pulses. *Review of Scientific Instruments*, 77(7):073106, 2006.

[108] B. S. Cooper, A. M. Alonso, A. Deller, T. E. Wall, and D. B. Cassidy. A trap-based pulsed positron beam optimised for positronium laser spectroscopy. *Review of Scientific Instruments*, 86(10):103101, 2015.

[109] J. H. Malmberg and J. S. deGrassie. Properties of Nonneutral Plasma. *Phys. Rev. Lett.*, 35:577–580, 1975.

[110] C. M. Surko, M. Leventhal, and A. Passner. Positron Plasma in the Laboratory. *Phys. Rev. Lett.*, 62:901–904, 1989.

[111] J. P. Marler and C. M. Surko. Positron-impact ionization, positronium formation, and electronic excitation cross sections for diatomic molecules. *Phys. Rev. A*, 72:062713, 2005.

[112] J. R. Danielson, D. H. E. Dubin, R. G. Greaves, and C. M. Surko. Plasma and trap-based techniques for science with positrons. *Rev. Mod. Phys.*, 87:247–306, 2015.

[113] R. G. Greaves and J. M. Moxom. Compression of trapped positrons in a single particle regime by a rotating electric field. *Physics of Plasmas*, 15(7):072304, 2008.

[114] D. A. Cooke, G. Barandun, S. Vergani, B. Brown, A. Rubbia, and P. Crivelli. Positron extraction to an electromagnetic field free region. *J. Phys. B: At., Mol. Opt. Phys.*, 49(1):014001, 2016.

[115] M. R. Natisin, J. R. Danielson, and C. M. Surko. Formation of buffer-gas-trap based positron beams. *Physics of Plasmas*, 22(3):033501, 2015.

[116] S. A. Tuccio, K. H. Drexhage, and G. A. Reynolds. CW Laser Emission from Coumarin Dyes in the Blue and Green. *Optics Communications*, 7(3):248–252, 1973.

[117] K. Kato. High-efficiency, high-power difference-frequency generation at 2-4 µm in LiNbO3. *IEEE Journal of Quantum Electronics*, 16(10):1017–1018, 1980.

[118] M. W. Heiss, G. Wichmann, B. Radics, and P. Crivelli. Excitation of positronium from 2S to 20P state. *arXiv e-prints*, page arXiv:1809.07854, 2018.

[119] L. Liszkay, C. Corbel, P. Perez, P. Desgardin, M.-F. Barthe, T. Ohdaira, R. Suzuki, P. Crivelli, U. Gendotti, A. Rubbia, M. Etienne, and A. Walcarius. Positronium reemission yield from mesostructured silica films. *Appl. Phys. Lett.*, 92(6):063114, 2008.

[120] S. Valkealahti and R. M. Nieminen. Monte-Carlo calculations of keV electron and positron slowing down in solids. *Applied Physics A*, 32(2):95–106, 1983.

[121] J. Algers, P. Sperr, W. Egger, G. Kögel, and F. H. J. Maurer. Median implantation depth and implantation profile of 3–18 keV positrons in amorphous polymers. *Phys. Rev. B*, 67:125404, 2003.

[122] J. Dryzek and P. Horodek. GEANT4 simulation of slow positron beam implantation profiles. *Nuclear Instruments and Methods in Physics Research Section B: Beam Interactions with Materials and Atoms*, 266(18):4000 – 4009, 2008.

[123] P. Crivelli, U. Gendotti, A. Rubbia, L. Liszkay, P. Perez, and C. Corbel. Measurement of the orthopositronium confinement energy in mesoporous thin films. *Phys. Rev. A*, 81:052703, 2010.

[124] S. J. Tao. The formation of positronium in molecular substances. *Applied physics*, 10(1):67–79, 1976.

[125] O. E. Mogensen. Spur reaction model of positronium formation. *The Journal of Chemical Physics*, 60(3):998–1004, 1974.

[126] Y. Nagashima, Y. Morinaka, T. Kurihara, Y. Nagai, T. Hyodo, T. Shidara, and K. Nakahara. Origins of positronium emitted from SiO_2. *Phys. Rev. B*, 58:12676–12679, 1998.

[127] L. de Sousa Borges. Positronium spectroscopy: 1^3S_1–2^3S_1 by pulsed excitation and Rydberg detection. Master thesis, ETH Zurich, 2020. unpublished.

[128] S. Mariazzi, A. Salemi, and R. S. Brusa. Positronium cooling into nanopores and nanochannels by phonon scattering. *Phys. Rev. B*, 78:085428, 2008.

[129] D. B. Cassidy, P. Crivelli, T. H. Hisakado, L. Liszkay, V. E. Meligne, P. Perez, H. W. K. Tom, and A. P. Mills. Positronium cooling in porous silica measured via Doppler spectroscopy. *Phys. Rev. A*, 81:012715, 2010.

[130] A. Deller, B. S. Cooper, T. E. Wall, and D. B. Cassidy. Positronium emission from mesoporous silica studied by laser-enhanced time-of-flight spectroscopy. *New Journal of Physics*, 17(4):043059, 2015.

[131] Y. Huang and H. Thomann. Critique and correction of the currently accepted solution of the infinite spherical well in quantum mechanics. *EPL (Europhysics Letters)*, 115(6):60001, 2016.

[132] A. M. Alonso, L. Gurung, B. A. D. Sukra, S. D. Hogan, and D. B. Cassidy. State-selective electric-field ionization of Rydberg positronium. *Phys. Rev. A*, 98:053417, 2018.

[133] V. B. Brudanin, V. A. Morozov, and N. V. Morozova. Ion Feedback Afterpulses in FEU-130 and XP2020 Photomultipliers. *Instruments and Experimental Techniques*, 47(6):783–790, 2004.

[134] H. Peng, W. E. Frieze, R. S. Vallery, D. W. Gidley, D. L. Moore, and R. J. Carter. Revealing hidden pore structure in nanoporous thin films using positronium annihilation lifetime spectroscopy. *Applied Physics Letters*, 86(12):121904, 2005.

[135] D. B. Cassidy, S. H. M. Deng, H. K. M. Tanaka, and A. P. Mills. Single shot positron annihilation lifetime spectroscopy. *Appl. Phys. Lett.*, 88(19):194105, 2006.

[136] S. De Silvestri, P. Laporta, V. Magni, and O. Svelto. Solid-state laser unstable resonators with tapered reflectivity mirrors: the super-Gaussian approach. *IEEE Journal of Quantum Electronics*, 24(6):1172–1177, 1988.

[137] Y. Park, G. Giuliani, and R. Byer. Single axial mode operation of a Q-switched Nd:YAG oscillator by injection seeding. *IEEE Journal of Quantum Electronics*, 20(2):117–125, 1984.

[138] Fangyuan Han, Weimin Liu, Liangdong Zhu, Yanli Wang, and Chong Fang. Initial hydrogen-bonding dynamics of photoexcited coumarin in solution with femtosecond stimulated Raman spectroscopy. *J. Mater. Chem. C*, 4:2954–2963, 2016. Electronic Supplementary Information (ESI).

[139] R. Von Trebra and T. H. Koch. Dabco stabilization of coumarin dye lasers. *Chemical Physics Letters*, 93(4):315–317, 1982.

[140] A. F. Ismail, K. C. Khulbe, and T. Matsuura. Gas Separation Membrane Materials and Structures. In *Gas Separation Membranes: Polymeric and Inorganic*, pages 37–192. Springer International Publishing, Cham, 2015.

[141] R. Shankar and R. Shankar. The Hydrogen Atom. In *Principles of Quantum Mechanics*, pages 353–371. Springer US, New York, NY, 1994.

[142] S. Udayan, R. Sha M M, M. Sebastian, V. P. N. Nampoori, and S. Thomas. Two photon induced amplified spontaneous emission at low threshold from Styryl 7 dye incorporated DNA template. *Optical Materials*, 86:492 – 497, 2018.

[143] C. Wieman and T. W. Hänsch. Precision measurement of the $1S$ Lamb shift and of the $1S-2S$ isotope shift of hydrogen and deuterium. *Phys. Rev. A*, 22:192–205, 1980.

[144] K. Danzmann, M. S. Fee, and Steven Chu. Doppler-free laser spectroscopy of positronium and muonium: Reanalysis of the 1S-2S measurements. *Phys. Rev. A*, 39:6072–6073, 1989.

[145] I. Reinhard, M. Gabrysch, B. Fischer von Weikersthal, K. Jungmann, and G. zu Putlitz. Measurement and compensation of frequency chirping in pulsed dye laser amplifiers. *Applied Physics B*, 63(5):467–472, 1996.

[146] T. Udem, R. Holzwarth, and T. W. Hänsch. Optical frequency metrology. *Nature*, 416(6877):233–237, 2002.

[147] U. Schünemann, H. Engler, R. Grimm, M. Weidemüller, and M. Zielonkowski. Simple scheme for tunable frequency offset locking of two lasers. *Review of Scientific Instruments*, 70(1):242–243, 1999.

[148] S. D. Hogan. Calculated photoexcitation spectra of positronium Rydberg states. *Phys. Rev. A*, 87:063423, 2013.

[149] C. Vigo. *Search for Invisible Decay Channels of Positronium Confined in a Vacuum Cavity.* PhD thesis, ETH Zurich, 2017.

[150] G. R. Massoumi, W. N. Lennard, Peter J. Schultz, A. B. Walker, and Kjeld O. Jensen. Electron and positron backscattering in the medium-energy range. *Phys. Rev. B*, 47:11007–11018, 1993.

[151] X. Lai, X. Jiang, X. Cao, X. Zhang, Z. Zhang, X. Cao, G. Xiang, B. Wang, and L. Wei. Simulation of positron backscattering on Al, Cu, Ag and Au targets using GEANT4 code. *Surf. Interface Anal.*, 49(5):457–463, 2017.

[152] A. V. Oppenheim, J. R. Buck, and R. W. Schafer. *Discrete time signal processing.* Prentice-Hall, Inc, New Jersey, 1998.

[153] F. Gustafsson. Determining the initial states in forward-backward filtering. *IEEE Transactions on Signal Processing*, 44(4):988–992, 1996.

[154] M. Haas, U. D. Jentschura, C. H. Keitel, N. Kolachevsky, M. Herrmann, P. Fendel, M. Fischer, Th. Udem, R. Holzwarth, T. W. Hänsch, M. O. Scully, and G. S. Agarwal. Two-photon excitation dynamics in bound two-body Coulomb systems including ac Stark shift and ionization. *Phys. Rev. A*, 73:052501, 2006.

[155] W. H. Press. *Numerical recipes in C++ : the art of scientific computing.* Cambridge University Press, 2005.

[156] J. Greenwood. The correct and incorrect generation of a cosine distribution of scattered particles for Monte-Carlo modelling of vacuum systems. *Vacuum*, 67(2):217 – 222, 2002.

[157] N. M. A. Mohamed. Efficient Algorithm for Generating Maxwell Random Variables. *Journal of Statistical Physics*, 145(6):1653–1660, 2011.

[158] A. L. Stancik and E. B. Brauns. A simple asymmetric lineshape for fitting infrared absorption spectra. *Vibrational Spectroscopy*, 47(1):66 – 69, 2008.

[159] P. R. Bevington and D. K. Robinson. *Data reduction and error analysis for the physical sciences; 3rd ed.* McGraw-Hill, New York, NY, 2003.

[160] H. Luo, X. Fang, and B. Ertas. Hilbert Transform and Its Engineering Applications. *AIAA Journal*, 47(4):923–932, 2009.

[161] K. Pachucki and S. G. Karshenboim. Complete Results for Positronium Energy Levels at Order $m\alpha^6$. *Phys. Rev. Lett.*, 80:2101–2104, 1998.

[162] G. S. Adkins. Higher order corrections to the hyperfine splitting of positronium. *Hyperfine Interactions*, 233(1):59–66, 2015.

[163] M. W. Heiss. Feasibility of Ps-HFS Measurement: $2^3\mathrm{S}_1 \rightarrow 2^1\mathrm{S}_0$ transition in vacuum. Project thesis, ETH Zurich, 2015. unpublished.

[164] M. W. Heiss. Simulation and optimization of an experiment to measure the positronium hyperfine structure: $2^3\mathrm{S}_1 \rightarrow 2^1\mathrm{S}_0$ transition in vacuum. Master thesis, ETH Zurich, 2016. unpublished.

[165] A. Ishida, Y. Sasaki, G. Akimoto, T. Suehara, T. Namba, S. Asai, T. Kobayashi, H. Saito, M. Yoshida, K. Tanaka, and A. Yamamoto. Precise measurement of positronium hyperfine splitting using the Zeeman effect. *Hyperfine Interactions*, 212(1-3):133–140, 2012.

[166] S. Asai, Y. Kataoka, T. Kobayashi, T. Namba, T. Suehara, G. Akimoto, A. Ishida, M. M. Hashimoto, H. Saito, T. Idehara, and M. Yoshida. Precision measurements of positronium decay rate and energy level. *AIP Conference Proceedings*, 1037(1):43–55, 2008.

[167] A. Ishida, T. Namba, S. Asai, T. Kobayashi, H. Saito, M. Yoshida, K. Tanaka, and A. Yamamoto. New Precision Measurement of Hyperfine Splitting of Positronium. *Physics Letters B*, 734:338–344, 2014.

[168] A. Miyazaki, T. Yamazaki, T. Suehara, T. Namba, S. Asai, T. Kobayashi, H. Saito, Y. Tatematsu, I. Ogawa, and T. Idehara. First millimeter-wave spectroscopy of ground-state positronium. *Progress of Theoretical and Experimental Physics*, 2015(1), 2015.

[169] R. Kleiner. Filling the Terahertz Gap. *Science*, 318(5854):1254–1255, 2007.

[170] P. Crivelli, D. A. Cooke, and S. Friedreich. Experimental considerations for testing antimatter antigravity using positronium 1S-2S spectroscopy. *International Journal of Modern Physics: Conference Series*, 30:1460257, 2014.

[171] D. J. Griffiths. *Introduction to Electrodynamics*. Prentice Hall, 1999.

[172] J. D. Jackson. *Classical electrodynamics*. Wiley, New York, 3rd edition, 1999.

[173] S. Ramo, J. R. Whinnery, and T. Van Duzer. *Fields and waves in communication electronics*. Wiley, New York, 1994.

[174] H. Kogelnik and T. Li. Laser Beams and Resonators. *Appl. Opt.*, 5(10):1550–1567, 1966.

[175] A. E. Siegman. *Lasers*. University Science Books, Sausalito, CA, 1986.

[176] D. P. Dunseith, S. Truppe, R. J. Hendricks, B. E. Sauer, E. A. Hinds, and M. R. Tarbutt. A high quality, efficiently coupled microwave cavity for trapping cold molecules. *Journal of Physics B: Atomic, Molecular and Optical Physics*, 48(4):045001, 2015.

[177] K. Seeger. Microwave measurement of the dielectric constant of high-density polyethylene. *Microwave Theory and Techniques, IEEE Transactions on*, 39(2):352–354, 1991.

[178] L. N. Dinh, J. Sze, M. A. Schildbach, S. C. Chinn, R. S. Maxwell, P. Raboin, and W. McLean. Vacuum outgassing of high density polyethylene. *Journal of Vacuum Science & Technology A*, 27(2):376–380, 2009.

[179] K. F. Poole and M. M. Michaelis. Hialvac and Teflon outgassing under ultra-high vacuum conditions. *Vacuum*, 30(10):415 – 417, 1980.

[180] I. El-Maïs. Design of the vacuum chamber and test of the microwave cavity for the measurement of the positronium hyperfine splitting. Master thesis, ETH Zurich, 2018. unpublished.

[181] P. Beltrame, E. Bolle, A. Braem, C. Casella, E. Chesi, N. Clinthorne, R. De Leo, G. Dissertori, L. Djambazov, V. Fanti, M. Heller, C. Joram, H. Kagan, W. Lustermann, F. Meddi, E. Nappi, F. Nessi-Tedaldi, J.F. Oliver, F. Pauss, M. Rafecas, D. Renker, A. Rudge, D. Schinzel, T. Schneider, J. Seguinot, P. Solevi, S. Stapnes, and P. Weilhammer. The AX-PET demonstrator – Design, construction and characterization. *Nuclear Instruments and Methods in Physics Research Section A: Accelerators, Spectrometers, Detectors and Associated Equipment*, 654(1):546 – 559, 2011.

[182] B. Banto Oberhauser. Simulation and Integration of the AxPET Detector for the PHySES Experiment. Master thesis, ETH Zurich, 2020. unpublished.

[183] A. Williams, S. Barrus, R. K. Morley, and P. Shirley. An Efficient and Robust Ray-Box Intersection Algorithm. *J. Graphics Tools*, 10(1):49–54, 2005.

[184] A. Miyazaki. *Direct Measurement of the Hyperfine Structure Interval of Positronium Using High-Power Millimeter Wave Technology.* Springer Theses. Springer Japan, 2015.

[185] G. Wichmann. *Measurement of the Positronium 1S-2S Transition and Implications for that of Muonium.* PhD thesis, ETH Zurich, 2018.

[186] R. Tanaka, T. Matsuzawa, H. Yokota, T. Suzuki, Y. Fujii, A. Mio, and M. Katsuragawa. Stable confinement of nanosecond laser pulse in an enhancement cavity. *Opt. Express*, 16(23):18667–18674, 2008.

A. Schematic overview of the 1S-2S laser excitation system

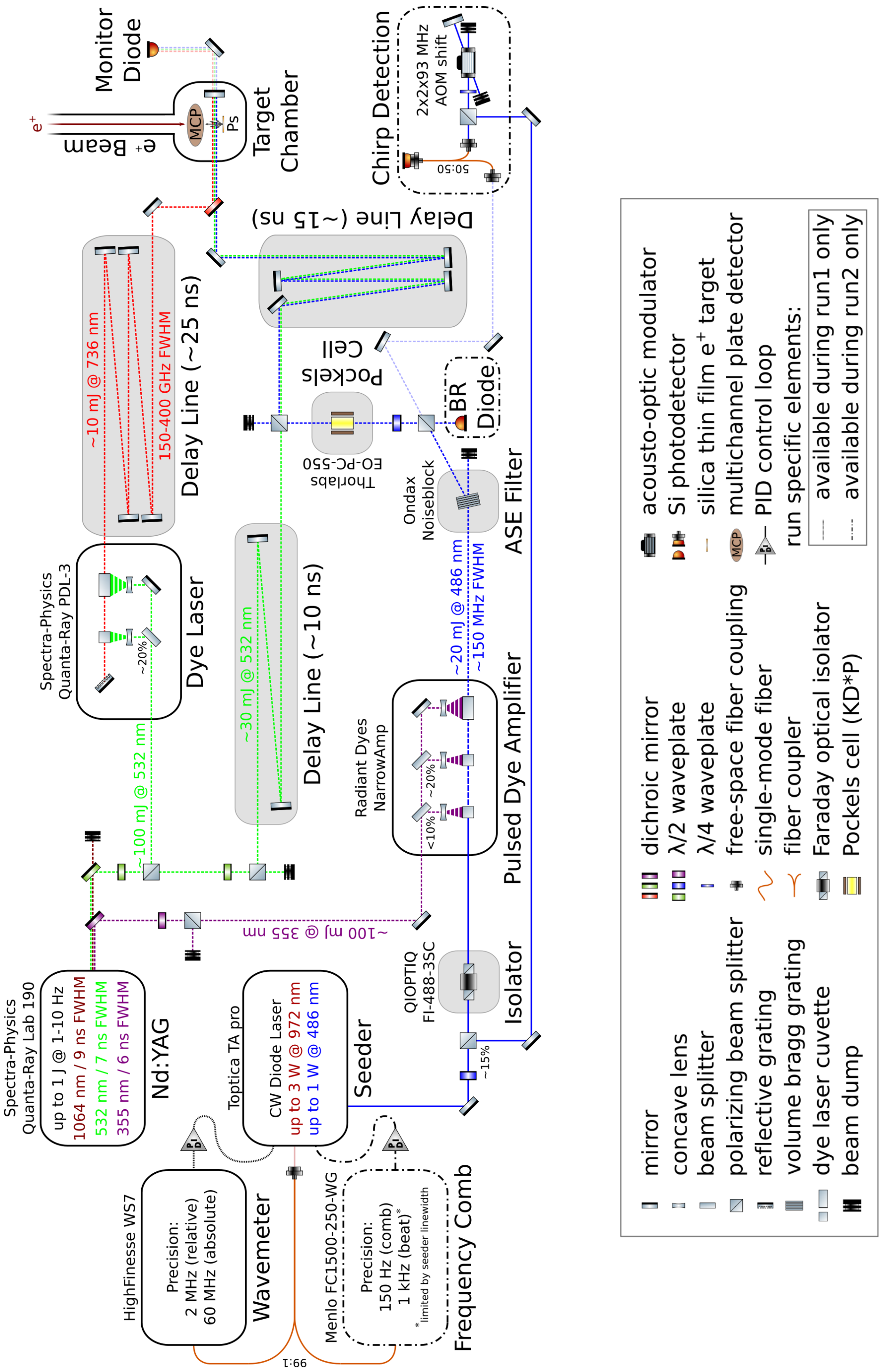

Figure 116: Schematic overview of the 1S-2S laser excitation system (enlarged).

B. Technical drawings of confocal mirrors

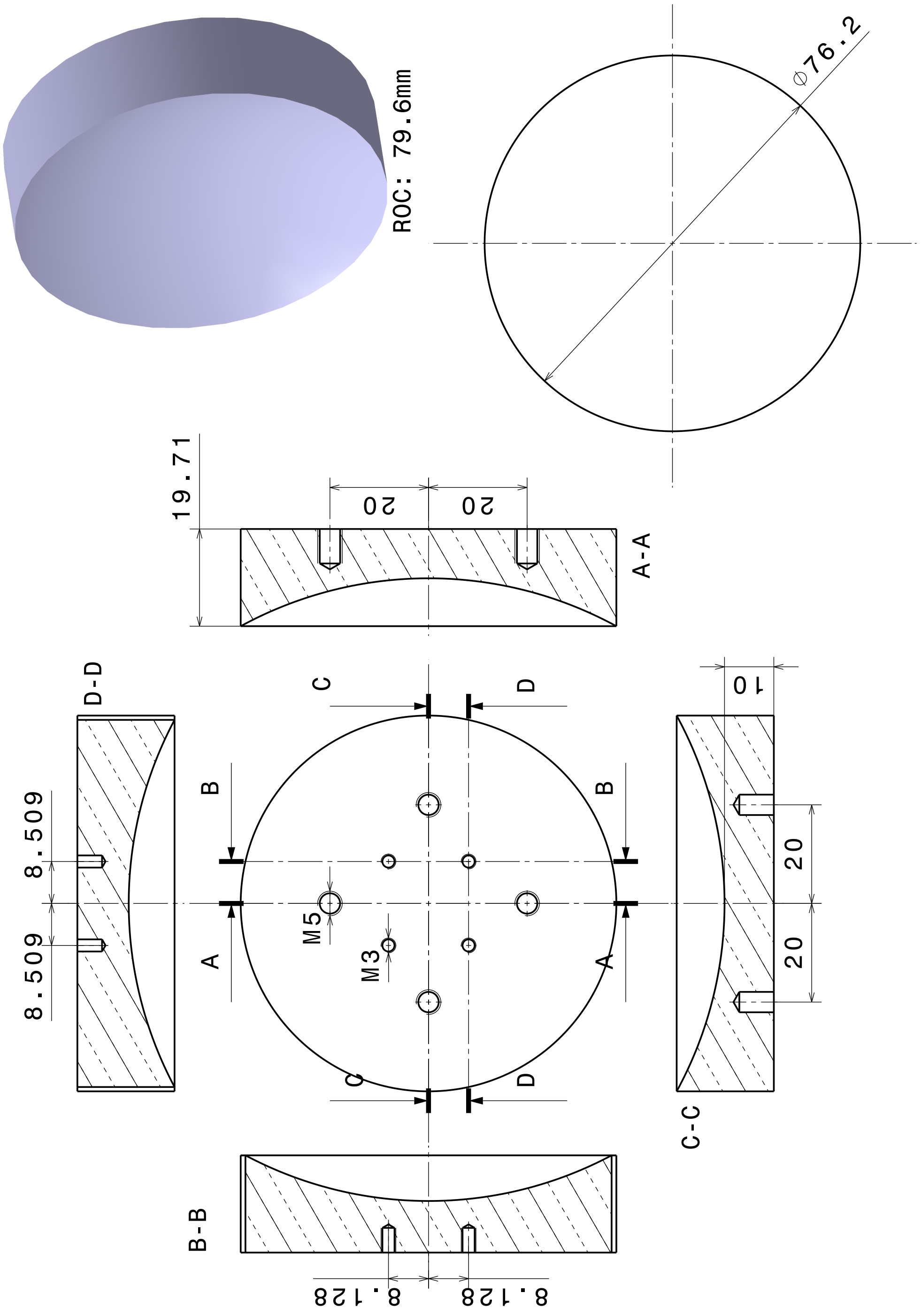

Figure 117: Technical drawing of confocal mirror (mounting side)

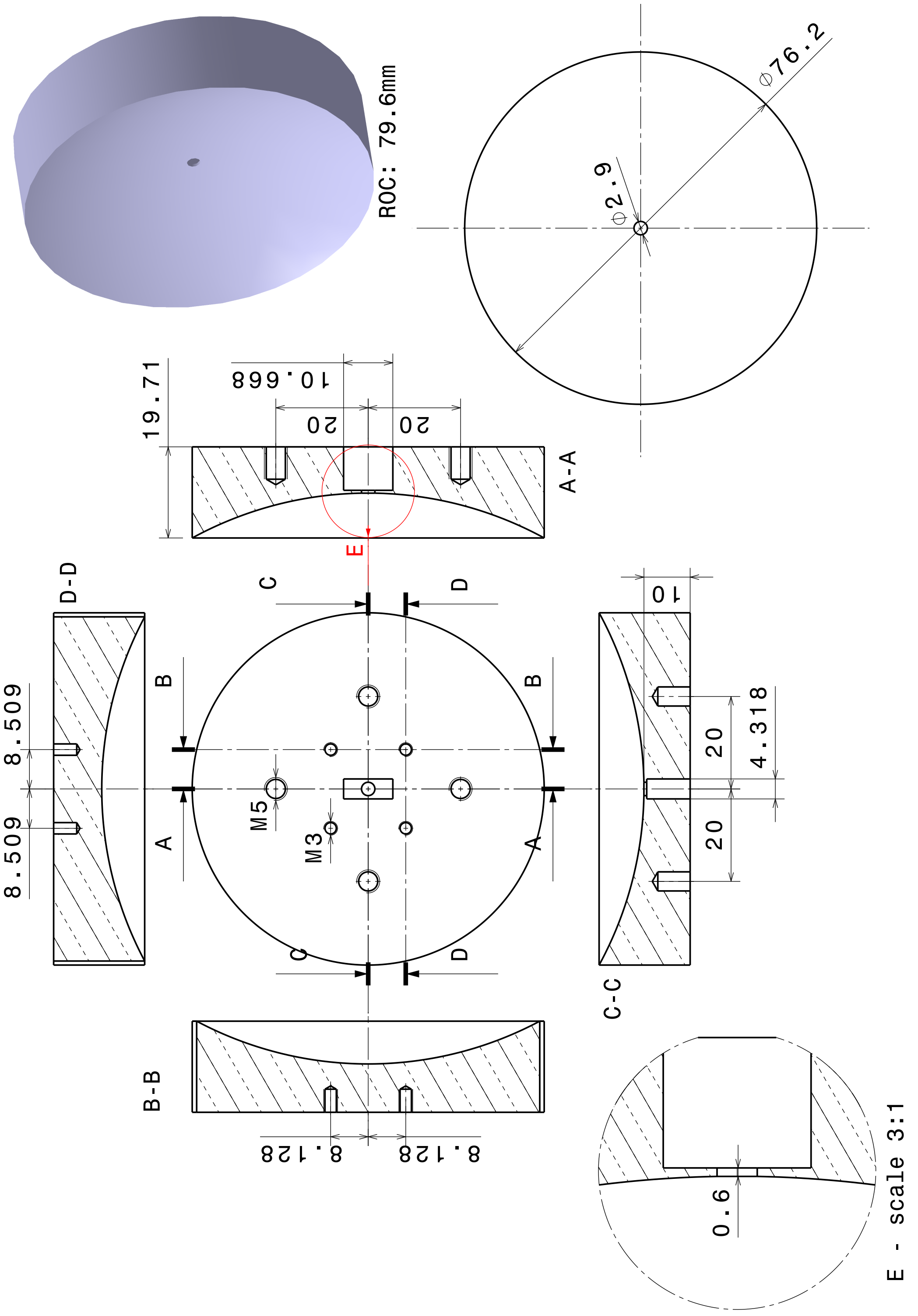

Figure 118: Technical drawing of confocal mirror (coupling side, non-cryogenic)

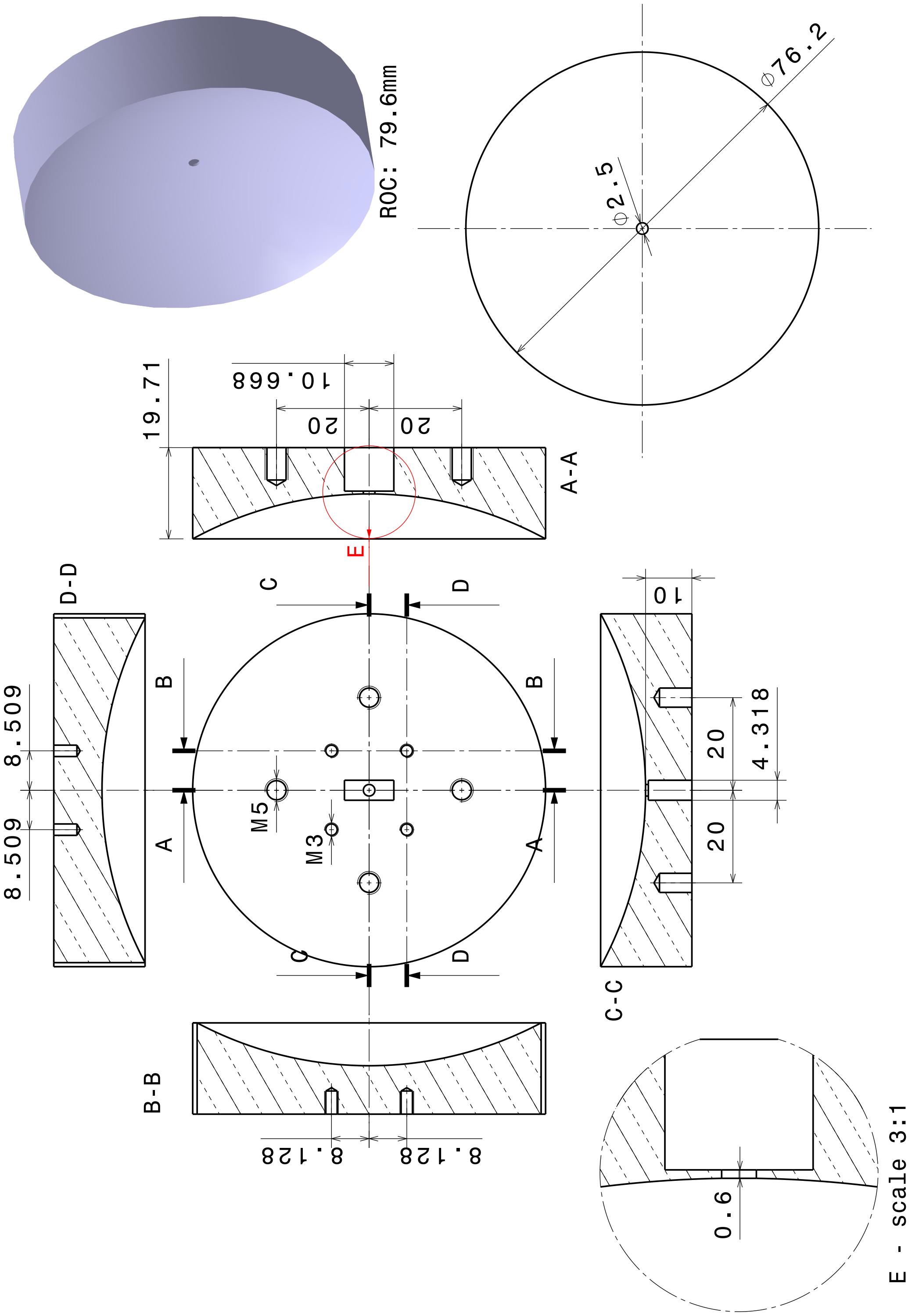

Figure 119: Technical drawing of confocal mirror (coupling side, cryogenic)

C. Schematics of time-buncher and elevator

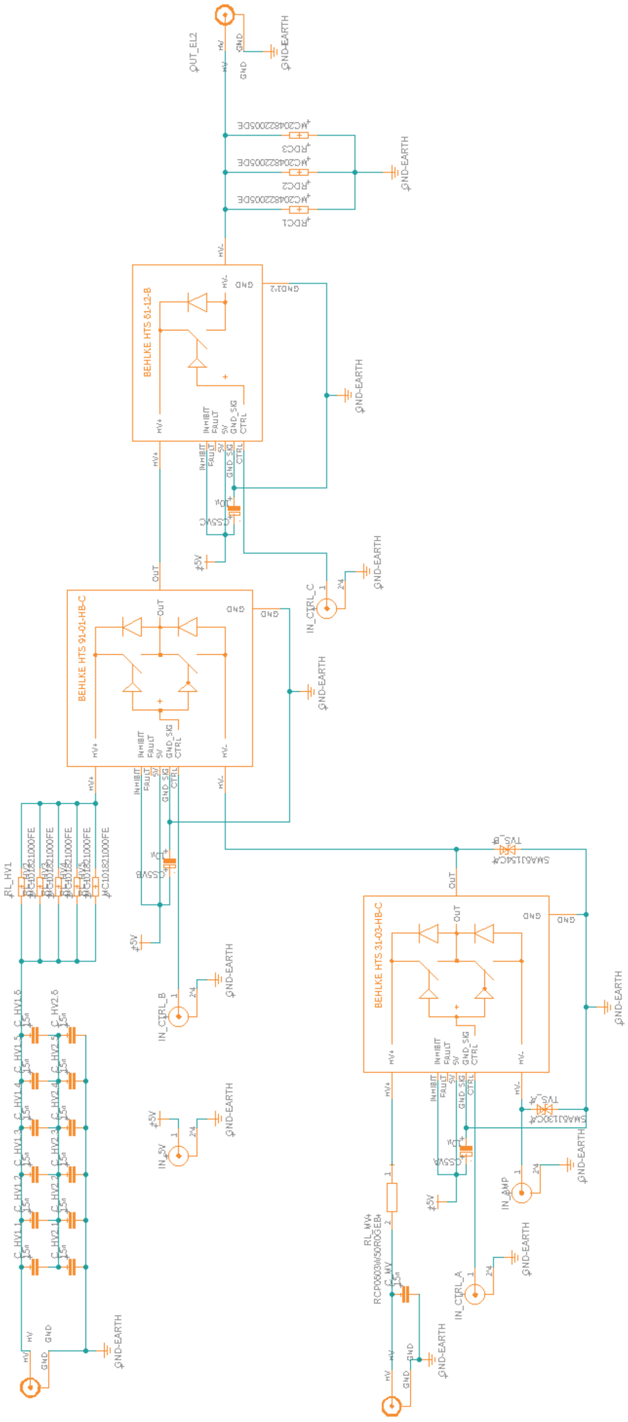

Figure 120: High voltage buncher and elevator schematic.